Amplitude analysis of $D^0 \to K^+K^-\pi^+\pi^-$ and its subsequent use in measuring the CKM phase γ through $B^\pm \to D(\to K^+K^-\pi^+\pi^-)K^\pm$ decays at LHCb

by

Nicola Skidmore

A thesis submitted to the University of Bristol in accordance
with the requirements for award of the
degree of Doctor of Philosophy

in the
Faculty of Science
School of Physics

June 2017

Word count: 71,995

Abstract

An amplitude analysis of the 4-body charmed decay $D^0 \to K^+K^-\pi^+\pi^-$ has been performed using data collected from symmetric electron-positron collisions at the CLEO experiment. Both flavour tagged and *CP* tagged data are utilised in the analysis, making it unique among amplitude analyses performed at other experiments and providing extra sensitivity to the phases of the amplitude components. This analysis uses a data driven regularisation method to determine which of the multitude of possible amplitude components to include in the amplitude model. The dominant contributions are found to be $D^0 \to \phi(1020)\,\rho^0(770)$, $D^0 \to K^-\,K_1(1270)^+$ and $D^0 \to K^-\,K_1(1400)^+$. Tests for *CP* violation in the D system are performed using the amplitude model; no evidence for *CP* violation is found. The amplitude model obtained is crucial input for a model-dependent measurement of the *CP*-violating phase γ using $B^\pm \to D(\to K^+K^-\pi^+\pi^-)K^\pm$ decays, which remains one of the least constrained parameters of the Standard Model. Significant progress has been made towards this measurement using the full Run 1 LHCb dataset corresponding to 3 fb^{-1} of integrated luminosity. This includes: data selection including the use of a multivariate classifier, fits to mass distributions to obtain event-by-event signal and background weights and an investigation into potential biases in the extraction of γ from $B^\pm \to D(\to K^+K^-\pi^+\pi^-)K^\pm$ decays using the control channel $B^\pm \to D(\to K^+K^-\pi^+\pi^-)\pi^\pm$.

Declaration of authorship

I, Nicola Skidmore, declare that the work in this dissertation was carried out in accordance with the requirements of the University's Regulations and Code of Practice for Research Degree Programmes and that it has not been submitted for any other academic award. Except where indicated by specific reference in the text, the work is the candidate's own work. Work done in collaboration with, or with the assistance of, others, is indicated as such. Any views expressed in the dissertation are those of the author.

Signed: ______________________________

Date: ______________________________

Acknowledgements

Over the last four years I have received support from many people.

Firstly I would like to thank my supervisor Jonas, who has been a constant source of both academic and personal support and with whom I have thoroughly enjoyed working. It is because of him that I am so proud of this thesis.

Secondly, my two post-docs, Jeremy and Paras. Their relentless supply of help with these analyses made them possible. They have also made the PhD experience a lot of fun; I was lucky enough to share an office with both of them at one point or another. In the same breath I would also like to thank Sam who helped me on so many occasions.

I also must mention my two tea buddies, Sophie and Gen, who also happen to share my interest in life risking obstacle courses. Hopefully we can find a way to continue both the tea breaks and these crazy challenges.

My biggest thanks goes to my parents, who have been with me every step of the way and my siblings who have always been a source of inspiration for achieving great things.

The best experience of my PhD has been meeting Siphiwe, who has taught me more than any book could, and with whom I have shared some amazing adventures.

Finally, thank you to the whole of the Bristol particle physics group for creating such a great atmosphere to work in.

Author's contribution

The author's contributions to the work presented in this thesis are as follows:

- Chapter 4: The amplitude analysis of $D^0 \to K^+K^-\pi^+\pi^-$ decays uses data collected by the CLEO detector. The CLEO collaboration performed reconstruction of decays and produced samples of simulated data for use in the analysis. This work is a continuation of that presented in the paper *Amplitude Analysis of* $D^0 \to K^+K^-\pi^+\pi^-$ published by the CLEO collaboration in 2012 [1]. Taken from this previous analysis is part of the data selection including data tagging, as well as analysis of the background fractions for *CP* tagged data. This is clearly indicated and referenced within the text. Work reported from section 4.4 onwards and all analysis of the data is the author's. This analysis has since been published [2] and has been accepted by a peer reviewed journal. The author of this thesis is a corresponding author on the paper.

- Chapter 5: This chapter uses data collected by the LHCb experiment and is the author's own work. Collaboration wide software was used to reconstruct decays for analysis and produce samples of simulated data. Various tools available to the collaboration have been used in the selection of the data and the treatment of simulated data samples, these tools are indicated and referenced in the text.

Both the analyses presented in this thesis use the 3- and 4-body decay event generator and amplitude model fitter, MINT [3], developed at the University of Bristol.

Contents

List of Figures

List of Tables

Chapter 1

CP-violation in the Standard Model

The observed imbalance between matter and antimatter in the universe, formally known as the baryon asymmetry problem, remains one of the most fundamental problems in physics, bridging cosmology and particle physics. Baryon number distinguishes between matter and antimatter with baryons, such as the proton, being assigned baryon number $B = 1$ and anti-baryons, such as the anti-proton, being assigned $B = -1$. Immediately after the big bang the universe is thought to have been baryon-symmetric, with baryon number $B = 0$. Since, there has been a baryon excess generated where $B > 0$. The creation of a baryon asymmetry with $B > 0$ from an initial $B = 0$ state is referred to as Baryogenesis. At this point we introduce three discrete transformation operators C, P and T. The charge conjugation operator C interchanges a particle with its antiparticle. The parity transformation with operator P inverts the spatial coordinates a of a system

$$P\psi(x, y, z, t) = \psi(-x, -y, -z, t).$$

Finally the time reversal operator T reverses the time coordinate

$$T\psi(x, y, z, t) = \psi(x, y, z, -t).$$

The combination of these operators, CPT, is believed to be an exact symmetry of nature based on fundamental assumptions such as Lorentz invariance and causality. Experimentally, no violation of CPT symmetry has been observed.

In the paper *Violation of CP invariance, C asymmetry, and baryon asymmetry of the universe* (1967) [4] Sakharov described a minimal set of conditions for baryogenesis:

1. At least one B-violating process
2. C- and CP-violation
3. Interactions outside of thermal equilibrium

The first of the Sakharov conditions insists on a process

$$X \to YZ$$

that has an overall positive gain in baryon number in order to break the initial baryon symmetry i.e. $B(X) < B(Y + Z)$. If however, C remains a symmetry then the decay rate of this process and its charge conjugate decay are equal

$$\Gamma(X \to YZ) = \Gamma(\bar{X} \to \bar{Y}\bar{Z}).$$

This leads to any increase in B being negated by an equal decrease in B. Consider further if the B-violating process decays to left handed particles $X \to Y_L Z_L$. If CP is a symmetry then the CP conjugate of this decay $\bar{X} \to \bar{Y}_R \bar{Z}_R$ proceeds at the same rate and we again find that the net change in B is zero. Hence not only C but CP must be violated for baryogenesis. Note that the violation of CP symmetry implies violation of T symmetry. The final condition considers interactions in thermal equilibrium. For a process in thermal equilibrium the rate of the forward reaction is equal to the rate of the inverse reaction

$$\Gamma(X \to YZ) = \Gamma(YZ \to X).$$

Therefore for baryon asymmetry to be established processes must occur outside of thermal equilibrium.

This thesis will focus on the second Sakharov condition, *CP* violation. Fifty years on from Sakharov's paper current knowledge of *CP* violation in the Standard Model fails to accommodate the observed baryon asymmetry by several orders of magnitude [5]. This suggests additional sources of *CP*-violation beyond the Standard Model of particle physics.

1.1 The Standard Model of particle physics

The Standard Model (SM) of particle physics is the current, best theory to describe fundamental particles and their interactions. It is a Quantum Field Theory that interprets physical particles as excitations of underlying fields. The connection between the symmetries of a system and conservation laws was first established by Noether in the paper *Invariante Variationsprobleme* (1918) [6]. The SM is a gauge theory based on the symmetry group SU(3)$\otimes$SU(2)$\otimes$U(1), the enforcement of which derives the electromagnetic, strong and weak interactions with corresponding conservation of electric, colour and isospin charge. Table 1.1 shows the fundamental particles of the SM grouped into quarks, leptons and bosons. Quarks and leptons are known as fermions with spin 1/2 and are divided into three generations. Each quark generation has an up-type and a down-type quark with electric charge $+2/3$ and $-1/3$ respectively, whilst lepton generations each have an electron-type and neutrino-type particle with charge -1 and 0 respectively. Quarks also carry colour charge and so partake in strong interactions. Bosons have integer spin and are the force carriers of the SM; 8 massless gluons couple to colour charge C and mediate the strong interaction, one massless photon couples to electric charge Q and mediates the electromagnetic interaction and three massive bosons; $W^{\pm}$ and Z, couple to a combination of weak isospin T and hypercharge Y mediating the weak interaction [7]. A spin-0 boson known as the Higgs boson completes the model and is responsible for the masses of fundamental particles.

	I	II	III	
Quarks	u	c	t	
	d	s	b	
Leptons	e	μ	τ	
	ν_e	ν_μ	ν_τ	
Bosons	γ	Z	$W^\pm$	H

Table 1.1: Fundamental particles of the Standard Model

1.1.1 Quantum Electrodynamics: U(1) abelian local gauge theory

The Dirac Lagrangian density describes free, relativistic, spin-$\frac{1}{2}$ particle fields. The Dirac spinor, ψ, represents a particle field with mass m and with Lagrangian density

$$\mathcal{L} = \bar{\psi}(i\gamma^\mu \partial_\mu - m)\psi. \tag{1.1}$$

where $\bar{\psi} = \psi^\dagger \gamma^0$ and where γ^μ are the four Dirac matrices. All physical quantities of ψ such as charge density current $q\bar{\psi}\gamma^\mu\psi$ are invariant under local phase transformations where $\psi \to \psi' = e^{iq\theta(x)}\psi$ and $\bar{\psi} \to \bar{\psi}' = \bar{\psi}e^{-iq\theta(x)}$, also known as a local U(1) gauge transformation. The Lagrangian must also be invariant under such local phase transformations, however the derivative $\partial_\mu\psi$ transforms as

$$\partial_\mu\psi \to (\partial_\mu\psi)' = \partial_\mu(e^{iq\theta(x)}\psi) = e^{iq\theta(x)}(\partial_\mu\psi + iq\partial_\mu\theta(x)\psi).$$

For local invariance we require a derivative term, D_μ, that transforms like the particle fields ψ,

$$D_\mu \to D'_\mu = e^{iq\theta(x)}D_\mu.$$

This can be achieved by introducing a spin-1 gauge field, A_μ, that transforms as $A_\mu \to A'_\mu = A_\mu + \partial_\mu\theta(x)$ and a covariant derivative

$$D_\mu = \partial_\mu - iqA_\mu \tag{1.2}$$

The condition then for local U(1) gauge invariance is the interaction between the Dirac particle field and the vector field A_μ which couple via q. This is the description of

Quantum Electrodynamics (QED) and therefore QED is the result of U(1) abelian local gauge theory [7]. To describe the free propagation of the electromagnetic field we add a gauge-invariant kinetic term for A_μ, $F_{\mu\nu} = \frac{i}{q}[D_\mu, D_\nu] = \partial_\mu A_\nu - \partial_\nu A_\mu$ where $F_{\mu\nu}$ is the electromagnetic field strength. Finally we have the QED Lagrangian density,

$$\mathcal{L} = \bar{\psi}(i\gamma^\mu D_\mu - m)\psi - \frac{1}{4}F_{\mu\nu}F^{\mu\nu} \tag{1.3}$$

A mass term for the gauge field of the form $\propto M^2 A^\mu A_\mu$ would break the gauge invariance and so $M = 0$ i.e. the photon is predicted to be massless. By applying the Euler-Lagrange equation for fields

$$\frac{\partial \mathcal{L}}{\partial \psi^n} - \partial_\mu \left(\frac{\partial \mathcal{L}}{\partial(\partial_\mu \psi^n)} \right) = 0$$

to the Lagrangian density in 1.3 we can derive the Dirac equation for a particle in an electromagnetic field [8]

$$(i\gamma^\mu \partial_\mu - m)\psi - q\gamma^\mu A_\mu \psi = (i\gamma^\mu D_\mu - m)\psi = 0. \tag{1.4}$$

1.1.2 Electroweak theory: SU(2)⊗U(1) local gauge theory

The symmetry group SU(2)⊗ U(1)[1] is used to describe the electroweak interaction; the unified description of electromagnetism and the weak interaction. In the electroweak interaction left-handed L, and right-handed R, fermions behave differently. For this reason left-handed up-type and down-type quarks are arranged together in SU(2) doublets and right-handed up-type and down-type quarks are arranged in SU(2) singlets. Analogous terms exist for left-handed neutrinos and electrons and for right-handed electrons[2][10],

[1]The S of SU(2) stands for *special* meaning the generators of the group have determinant equal to 1.

[2]Right-handed neutrinos have not yet been observed, however their existance could be responsible for phenomena such as neutrino oscillations for which there is no explanation within the SM [9].

$$
\begin{aligned}
Q_{Li} &= \begin{pmatrix} u_{Li} \\ d_{Li} \end{pmatrix} \qquad (u_{Ri}) \qquad (d_{Ri}) \\
L_{Li} &= \begin{pmatrix} \nu_{Li} \\ e_{Li} \end{pmatrix} \qquad (e_{Ri})
\end{aligned}
\tag{1.5}
$$

where the index i runs over the 3 fermion generations. As with QED we wish to have invariance under local U(1) gauge transformations for SU(2) doublets and SU(2) singlets. As well as invariance under local U(1) gauge transformations, $\beta(x)$, we now also demand invariance under SU(2) gauge transformations, $\boldsymbol{\alpha}(x)$, for the SU(2) doublets such that

$$
\begin{aligned}
\Psi_L &\rightarrow \Psi'_L = e^{iY_L\beta(x)}e^{i\boldsymbol{\tau}\boldsymbol{\alpha}(x)}\Psi_L \\
\psi_R &\rightarrow \psi'_R = e^{iY_R\beta(x)}\psi_R.
\end{aligned}
\tag{1.6}
$$

where the generator Y is known as the hypercharge and $\boldsymbol{\tau} = \frac{\boldsymbol{\sigma}}{2}$ where $\boldsymbol{\sigma}$ are the 3 generators of the SU(2) group i.e. the Pauli matrices

$$
\begin{pmatrix} 0 & 1 \\ 1 & 0 \end{pmatrix} \qquad \begin{pmatrix} 0 & -i \\ i & 0 \end{pmatrix} \qquad \begin{pmatrix} 1 & 0 \\ 0 & -1 \end{pmatrix}
\tag{1.7}
$$

Following the prescription above this requires the replacement $\partial_\mu \rightarrow D_\mu$ where D_μ is a covariant derivative acting on Ψ_L and ψ_R

$$
\begin{aligned}
D_\mu\Psi_L &= (\partial_\mu - ig\widetilde{W}_\mu - ig'Y_LB_\mu)\Psi_L \\
D_\mu\psi_R &= (\partial_\mu - ig'Y_RB_\mu)\psi_R
\end{aligned}
\tag{1.8}
$$

B_μ is the gauge field needed for U(1) invariance with coupling g' and hypercharge Y. $\widetilde{W}_\mu(x) \equiv \boldsymbol{\tau}\boldsymbol{W}_\mu(x)$ denotes three SU(2) gauge fields with coupling g and weak-isospin charge $\boldsymbol{T} = \boldsymbol{\tau}$ [11]. The values of hypercharge are fixed such that the sum of hypercharge and the third component of weak-isospin charge gives the electric charge of the fermion, $Q = T^3 + Y$. For a left handed doublet $T^3 = \pm\frac{1}{2}$ and for right handed singlets $T^3 = 0$

(the reason for this will become clear later). Table 1.2 gives the values of Y, Q and T^3 for the fermion singlets and doublets.

Table 1.2: Values of hypercharge Y, weak isospin T^3 and electric charge Q for fermions of the Standard Model.

	Y	T^3	Q
Doublets			
u_L	$+1/6$	$+1/2$	$+2/3$
d_L	$+1/6$	$-1/2$	$-1/3$
ν_L	$-1/2$	$+1/2$	0
e_L	$-1/2$	$-1/2$	-1
Singlets			
u_R	$+2/3$	0	$+2/3$
d_R	$-1/3$	0	$-1/3$
e_R	-1	0	-1

As before, the covariant derivative must transform like the particle field and so, defining $U_L(x) \equiv e^{i\boldsymbol{\tau\alpha}(x)}$ for brevity, the gauge fields must transform as

$$\begin{aligned} B_\mu \to B'_\mu &= B_\mu + \frac{1}{g'}\partial_\mu \beta(x) \\ \widetilde{W}_\mu \to \widetilde{W}'_\mu &= U_L(x)\widetilde{W}_\mu U_L^\dagger(x) - \frac{i}{g}(\partial_\mu U_L(x))U_L^\dagger(x) \end{aligned} \tag{1.9}$$

To describe propagation of the 4 gauge fields we need gauge invariant kinetic terms for the fields. As for QED

$$B_{\mu\nu} = \frac{i}{g'}[D_\mu, D_\nu] = \partial_\mu B_\nu - \partial_\nu B_\mu.$$

However due to the non commutation of $\widetilde{W}_\nu$ and $\widetilde{W}_\mu$ (SU(2) is a non-abelian group) the SU(2) case yields

$$\widetilde{W}_{\mu\nu} = \frac{i}{g}[D_\mu, D_\nu] = \partial_\mu \widetilde{W}_\nu - \partial_\nu \widetilde{W}_\mu - ig[\widetilde{W}_\mu, \widetilde{W}_\nu]$$

which can be written in component form

$$\widetilde{W}_{\mu\nu} = [\partial_\mu W^i_\nu - \partial_\nu W^i_\mu + g\varepsilon^{ijk} W^j_\mu W^k_\nu]\tau_i = W^i_{\mu\nu}\tau_i$$

where ε^{ijk} is the antisymmetric tensor. Noting the analogy between this and the U(1) case a gauge invariant kinetic term can be written $\propto W^i_{\mu\nu}W^{\mu\nu}_i$. The total Lagrangian is then given by

$$\mathcal{L} = \bar{\psi}(i\gamma^\mu(\partial_\mu - ig\tau_i W^i_\mu - ig'YB_\mu)\psi) - \frac{1}{4}W^i_{\mu\nu}W^{\mu\nu}_i - \frac{1}{4}B_{\mu\nu}B^{\mu\nu} \tag{1.10}$$

Notice again that in the Lagrangian of 1.10 there can be no mass terms for the gauge bosons. Mass terms for the fermions are also forbidden in the Lagrangian as a term such as $m\bar{\psi}\psi = m[(\bar{\psi_L} + \bar{\psi_R})(\psi_L + \psi_R)] = m(\bar{\psi_L}\psi_R + \bar{\psi_R}\psi_L)$ causes mixing of right handed particles that transform as SU(2) singlets and left handed particles that transform as SU(2) doublets. A term like this is not therefore invariant under SU(2)$\otimes$U(1) transformations.

1.1.3 The Higgs mechanism

To obtain massive Z and W bosons we introduce the Higgs mechanism and spontaneous symmetry breaking [12]. The Goldstone theorem states that for each broken generator of a global symmetry group a massless spin-zero particle will appear, known as a *Goldstone boson*. This theorem is integral to the following. Consider an SU(2) doublet of complex scalar fields known as the Higgs field

$$\phi(x) \equiv \begin{pmatrix} \phi^+(x) \\ \phi^0(x) \end{pmatrix} \tag{1.11}$$

with hypercharge of 1/2 and a potential $V(\phi) = -\mu^2(\phi^\dagger\phi) + \frac{\lambda}{4}(\phi^\dagger\phi)^2$. The Higgs field's contribution to the Lagrangian is

$$\mathcal{L}_{Higgs} = (D^\mu\phi)^\dagger(D_\mu\phi) - V(\phi) \tag{1.12}$$

where D^μ is the covariant derivative in equation 1.8. In the case where $\lambda > 0$ and $\mu^2 > 0$, the potential the has a Mexican hat shape whereby there is a local maximum at $\phi^T(x) = (0, 0)$ and an infinite number of degenerate minima. The classical minimum of this potential is at points where $(\phi^\dagger\phi)_{min} = 2\mu^2/\lambda \equiv v^2/2$ which has the quantum interpretation of a vacuum expectation value (vev) of $\langle 0|\phi^\dagger\phi|0\rangle = v^2/2$ where $|0\rangle$ is a ground state. The choosing of a particular ground state causes the SU(2)$\otimes$ U(1) symmetry to be spontaneously broken. The ground state suggested by Weinberg [7] is

$$\phi_0(x) \equiv \begin{pmatrix} 0 \\ v/\sqrt{2} \end{pmatrix}.$$

It should be noted that although the SU(2)$\otimes$ U(1) generators are broken by the vev, the combination of generators $(T^3 + Y)$ remains unbroken as $(T^3 + Y)\phi_0(x) = Q\phi_0(x) = 0$ [3] [13] (this will later be associated to the photon, the carrier of electromagnetism). Hence after symmetry breaking we have SU(2)$\otimes$ U(1)$\rightarrow$U(1).

Expansion about the ground state can be parameterised as

$$\phi(x) = e^{i\boldsymbol{\zeta}(x)\cdot\boldsymbol{\tau}/2v} \begin{pmatrix} 0 \\ \frac{1}{\sqrt{2}}(v + H) \end{pmatrix} \tag{1.13}$$

where the 3 ζ fields together with H are the 4 degrees of freedom of the Higgs field. However by using an appropriate choice of local gauge transformation under SU(2) (known as the unitary gauge) the ζ components can be eliminated. Letting $\boldsymbol{\alpha}(x) = \boldsymbol{\zeta}(x)/v$ the ground state to expand around becomes

$$\phi(x) \rightarrow e^{-i\boldsymbol{\alpha}(x)\boldsymbol{\tau}/2}\phi(x) = \begin{pmatrix} 0 \\ \frac{1}{\sqrt{2}}(v + H) \end{pmatrix}.$$

The mass terms of the fields in the Lagrangian in equation 1.12 become

$$\mathcal{L}_{\text{mass}} = -\mu^2 H^2 + \frac{v^2}{8}\Big[g^2(W^1_\mu W^{1\mu} + W^2_\mu W^{2\mu}) + (gW^3_\mu - g'B_\mu)^2\Big].$$

The first term shows that the scalar field H has developed a mass, this corresponds to the Higgs boson discovered by the ATLAS and CMS experiments in 2012 [14], [15]. We

[3] If a transformation is invariant then $e^{i\alpha Z}\phi = \phi$ where Z is the generator of the transform. For infinitesimal transformations $(1 + i\alpha Z)\phi = \phi$ and so $\alpha Z\phi = 0$.

can define the charged $W^{\pm}$ bosons as superpositions of W_μ^1 and W_μ^2 and the neutral A_μ and Z_μ bosons as superpositions of the W_μ^3 and B_μ,

$$\begin{aligned} W_\mu^{\pm} &= \frac{1}{\sqrt{2}}(W_\mu^1 \mp iW_\mu^2) \\ A_\mu &= \frac{1}{\sqrt{g^2+g'^2}}(g'W_\mu^3 + gB_\mu) \\ Z_\mu &= \frac{1}{\sqrt{g^2+g'^2}}(gW_\mu^3 - g'B_\mu) \end{aligned} \tag{1.14}$$

By examining 1.10, $W_\mu^{\pm}$ couple to weak isospin and now A_μ and Z_μ couple to the combination of the third component of weak isospin and hypercharge. We can rewrite $\mathcal{L}_{mass}$ in terms of the physical gauge bosons $W^{\pm}, Z$ and A,

$$\mathcal{L}_{mass} = -\mu^2 H^2 + \frac{v^2}{8}\Big[g^2(W_\mu^+)^2 + g^2(W_\mu^-)^2 + (g^2+g'^2)Z_\mu^2 + 0\cdot A_\mu^2\Big].$$

The $W^{\pm}$ and Z have acquired a mass and the photon has remained massless. The masses of the bosons arise from the 3 degrees of freedom that were gauged away in 1.13 using the local symmetries of the group. The 3 ζ fields represent the massless Goldstone bosons arising due to the broken symmetry group, the use of the unitary gauge gauged away these Goldstone bosons that then reappeared as a longitudinal degree of freedom for the 3 weak gauge bosons and as such they acquire a mass. It is said that the Goldstone bosons have been eaten by the gauge fields to become massive.

1.1.4 Yukawa couplings

As discussed, a mass term $m\bar{\psi}\psi$ for fermions is forbidden in the Lagrangian as it would not be gauge invariant [12]. However using the Higgs doublet introduced previously we can form a singlet that is invariant under SU(2)⊗U(1). Taking the quark doublets and singlets,

$$\mathcal{L}^d_{\text{Yukawa}} = -\lambda_d[\bar{Q}_{Li}\phi d_{Ri} + \bar{d}_{Ri}\bar{\phi}Q_{Li}]$$

where λ_d is known as the Yukawa coupling. This term only gives mass to down-type fermions however. Defining $\widetilde{\phi}^c = -i\sigma_2\phi^*$ we can also write a term

$$\mathcal{L}^u_{\text{Yukawa}} = -\lambda_u[\bar{Q}_{Li}\widetilde{\phi}^c u_{Ri} + \bar{u}_{Ri}\bar{\widetilde{\phi}}^c Q_{Li}]$$

giving mass terms to up-type fermions. Most generally, the Yukawa couplings are matrices, after spontaneous symmetry breaking the quark mass term of the Lagrangian for the 3 generations of quarks can be written using Yukawa coupling matrices Y_{ij} as

$$\mathcal{L}_{\text{Yukawa}} = -Y^d_{ij}\frac{1}{\sqrt{2}}\bar{Q}_{Li}\begin{pmatrix} 0 \\ (v+H) \end{pmatrix} d_{Rj} - Y^u_{ij}\frac{1}{\sqrt{2}}\bar{Q}_{Li}\begin{pmatrix} (v+H) \\ 0 \end{pmatrix} u_{Rj} + h.c \quad (1.15)$$

where $h.c$ stands for hermitian conjugate. Not only does this give rise to the desired fermion mass terms $Y^d_{11}(v/\sqrt{2})\bar{d}d$ but also to mixed mass terms such as $Y^d_{12}(v/\sqrt{2})\bar{d}s$. In order to relate fields to physical particles there must be well defined mass terms. From above we have that

$$\begin{aligned}\mathcal{L}_{\text{Yukawa}} &= -\frac{v}{\sqrt{2}}Y^d_{ij}\bar{d}_{Li}d_{Rj} - \frac{v}{\sqrt{2}}Y^u_{ij}\bar{u}_{Li}u_{Rj} + h.c + \text{higgs interaction terms} \\ &\equiv -\bar{d}_{Li}M^d_{ij}d_{Rj} - \bar{u}_{Li}M^u_{ij}u_{Rj} + h.c + \text{higgs interaction terms}\end{aligned} \quad (1.16)$$

Diagonalising the matrices M^d and M^u with unitary matrices[4] V so that $M^d_{diag} = V^d_L M^d V^{d\dagger}_R$ and $M^u_{diag} = V^u_L M^u V^{u\dagger}_R$ gives

$$\begin{aligned}-\mathcal{L}_{\text{Yukawa}} &= \bar{d}_{Li}V^{d\dagger}_L V^d_L M^d_{ij} V^{d\dagger}_R V^d_R d_{Rj} + \bar{u}_{Li}V^{u\dagger}_L V^u_L M^u_{ij} V^{u\dagger}_R V^u_R u_{Rj} + h.c + \text{higgs interaction terms} \\ &= \bar{d}^{mass}_{Li}(M^d_{ij})_{diag}d^{mass}_{Rj} + \bar{u}^{mass}_{Li}(M^u_{ij})_{diag}u^{mass}_{Rj} + h.c + \text{higgs interaction terms}\end{aligned} \quad (1.17)$$

where we have defined

$$d^{mass}_{Li} = (V^d_L)_{ij}d_{Lj}, \quad d^{mass}_{Ri} = (V^d_R)_{ij}d_{Rj}$$

[4]The unitarity condition is required to conserve the sum of the quark coupling probabilities

and

$$u_{Li}^{mass} = (V_L^u)_{ij} u_{Lj}, \quad u_{Ri}^{mass} = (V_R^u)_{ij} u_{Rj}.$$

The mass eigenstates are now linear superpositions of the interaction or weak eigenstates and only terms of unmixed mass eigenstates are present.

CP-violation in the SM is possible through weak charged current interactions which mix the up and down type weak quark states. The interaction term of the Lagrangian that gives rise to charged-current interactions for quarks is

$$\mathcal{L}_{CC} = g\bar{Q}_{Li}\gamma^{\mu}\boldsymbol{\tau}\boldsymbol{W}_{\mu}Q_{Li}$$

where

$$\begin{aligned}
\boldsymbol{\tau}\boldsymbol{W}_{\mu} &= \frac{1}{2}\Big[\begin{pmatrix} 0 & 1 \\ 1 & 0 \end{pmatrix} W_{\mu}^1 + \begin{pmatrix} 0 & -i \\ i & 0 \end{pmatrix} W_{\mu}^2 + \begin{pmatrix} 1 & 0 \\ 0 & -1 \end{pmatrix} W_{\mu}^3\Big] \\
&= \frac{1}{\sqrt{2}}\begin{pmatrix} \sqrt{2}W_{\mu}^3 & (W_{\mu}^1 - iW_{\mu}^2) \\ (W_{\mu}^1 + iW_{\mu}^2) & -\sqrt{2}W_{\mu}^3 \end{pmatrix} \\
&= \frac{1}{\sqrt{2}}\begin{pmatrix} \sqrt{2}W_{\mu}^3 & W_{\mu}^+ \\ W_{\mu}^- & -\sqrt{2}W_{\mu}^3 \end{pmatrix}
\end{aligned} \tag{1.18}$$

which results in a term

$$\mathcal{L}_{CC} = \frac{g}{\sqrt{2}}\Big[\bar{u}_{Li}\gamma^{\mu}W^+ d_{Li} + \bar{d}_{Li}\gamma^{\mu}W^- u_{Li}\Big].$$

This describes quark mixing within weak eigenstate generations. Rewriting this in terms of mass eigenstates we have quark mixing between mass generations

$$\begin{aligned}
\mathcal{L}_{CC} &= \frac{g}{\sqrt{2}}\bar{u}_{Li}^{mass}(V_L^u V_L^{d\dagger})_{ij}\gamma_{\mu}W^{+\mu}d_{Lj}^{mass} \\
&+ \frac{g}{\sqrt{2}}\bar{d}_{Li}^{mass}(V_L^d V_L^{u\dagger})_{ij}\gamma_{\mu}W^{-\mu}u_{Lj}^{mass}
\end{aligned} \tag{1.19}$$

We are free to allow $u_{Li} = u_{Li}^{mass}$ and $d_{Lj} = (V_L^u V_L^{d\dagger})_{ij} d_{Li}^{mass}$, where the matrix $(V_L^u V_L^{d\dagger})_{ij}$ is known as the Cabibbo-Kobayashi-Maskawa (CKM) matrix. The charged current interaction term can now be written as

$$\begin{aligned}\mathcal{L}_{CC} = \frac{g}{\sqrt{2}}(\bar{u}_L, \bar{c}_L, \bar{t}_L)_{mass}\gamma^{\mu}W_{\mu}^{+}(V^{CKM}) \begin{pmatrix} d_L \\ s_L \\ b_L \end{pmatrix}_{mass} \\ + \frac{g}{\sqrt{2}}(\bar{d}_L, \bar{s}_L, \bar{b}_L)_{mass}\gamma^{\mu}W_{\mu}^{-}(V^{CKM})^{\dagger} \begin{pmatrix} u_L \\ c_L \\ t_L \end{pmatrix}_{mass}\end{aligned} \tag{1.20}$$

clearly displaying that the up type quarks couple to a superposition of down type quarks, with couplings proportional to the elements of the CKM matrix. Complex Yukawa couplings allow *CP*-violation in the Standard Model. Taking 1.20 and performing a *CP* transformation gives

$$\mathcal{L}_{CC}^{CP} = \frac{g}{\sqrt{2}}\bar{d}_L{}^{mass}\gamma^{\mu}W_{\mu}^{-}(V^{CKM})^{T}u_L^{mass} + \frac{g}{\sqrt{2}}\bar{u}_L^{mass}\gamma^{\mu}W_{\mu}^{+}(V^{CKM\dagger})^{T}d_L^{mass} \tag{1.21}$$

and so the Lagrangian remains invariant under *CP* transformations if and only if $V_{ij} = V_{ij}^{*}$. If there are complex terms in (V_{CKM}) however there can be *CP*-violation in the weak sector of the SM.

1.1.5 Quantum Chromodynamics: SU(3) non-abelian local gauge theory

The final component of the SM, responsible for the strong interaction, is born out of enforcing local gauge invariance of the SU(3) group, the generators of which are 8 3×3 Gell-Mann matrices [16]. This introduces 8 new massless bosons known as gluons which couple to SU(3) triplets of colour charge that comes in 3 types; red, green and blue. Quarks and gluons carry colour charge and are SU(3) triplets whereas leptons have no colour charge and so are SU(3) singlets. All physical states are required to be colourless and so quarks are never observed in isolation due to the colour confinement principle, rather they are grouped together to form colourless hadrons. To understand the colour confinement principle consider a quark and antiquark in a bound state. Due to gluon-gluon interactions as the separation between the two is increased there comes a point at which it is energetically favourable for a new quark-antiquark pair to form. This results in 2 quark-antiquark pairs. This process is known as hadronisation and is how jets of mesons and baryons are formed in particle detectors. Before 2009 the only observed hadrons were quark-antiquark pairs known as mesons and quark or antiquark triplets known as baryons. In 2013 however both the BES III collaboration and the Belle experiment confirmed the first observation of a tetraquark, formed of two quarks and two anti-quarks, in the $J/\psi\pi^{\pm}$ channel, now known as $Z_C(3900)$ [17][18]. Later in 2015 LHCb found evidence for pentaquarks; composed of four quarks and one antiquark, in the study of Λ_b^0 decays[19].

1.2 The CKM matrix

The CKM matrix shown in equation 1.22 transforms the quarks from their weak eigenstates into their physical mass eigenstates and, as demonstrated in 1.20, describes the strengths of flavour changing weak decays or quark-mixing.

$$\begin{pmatrix} d \\ s \\ b \end{pmatrix}_{\text{weak}} = V_{CKM} \begin{pmatrix} d \\ s \\ b \end{pmatrix}_{\text{mass}} = \begin{pmatrix} V_{ud} & V_{us} & V_{ub} \\ V_{cd} & V_{cs} & V_{cb} \\ V_{td} & V_{ts} & V_{tb} \end{pmatrix} \begin{pmatrix} d \\ s \\ b \end{pmatrix}_{\text{mass}} \tag{1.22}$$

A complex $n \times n$ matrix has $2n^2$ real parameters. The unitarity condition, $VV^{\dagger} = I$, imposes n^2 constraints on these parameters; n for the condition on diagonal elements and $n^2 - n$ for the condition on off-diagonal elements. For the CKM matrix specifically, where n is now the number of quark generations, all observables are invariant under phase changes of the quark fields [20]. Hence one phase of the CKM matrix can be absorbed into each of the quark fields, however there remains one overall common phase that is unobservable and so only $2n - 1$ free parameters are removed from the CKM matrix. This leaves $(n - 1)^2$ free, real parameters of which $n(n - 1)/2$ are magnitudes and $(n-1)(n-2)/2$ are phases. For 3 quark generations we have 3 magnitudes and a single phase; it is this phase that permits *CP*-violation in the standard model. It should be noted that 3 generations is the minimum required for *CP*-violation in the standard model as 2 generations results in zero phases and therefore no complex Yukawa couplings. This insight led Kobayashi and Maskawa to predict the existence of a third generation of quarks following the observation of *CP*-violation in the decays of kaons.

There are various parameterisations of the CKM matrix [21], a standard representation uses 3 Euler angles denoted θ_{12} (the Cabibbo angle), θ_{23} and θ_{13} and one complex *CP*-violating phase δ_{13}. Cosines and sines of the angles are denoted c_{ij} and s_{ij} respectively.

$$\begin{aligned}\mathbf{V}_{CKM} &= \begin{pmatrix} c_{12} & s_{12} & 0 \\ -s_{12} & c_{12} & 0 \\ 0 & 0 & 1 \end{pmatrix}\begin{pmatrix} c_{13} & 0 & s_{13}e^{-i\delta_{13}} \\ 0 & 1 & 0 \\ -s_{13}e^{i\delta_{13}} & 0 & c_{13} \end{pmatrix}\begin{pmatrix} 1 & 0 & 0 \\ 0 & c_{23} & s_{23} \\ 0 & -s_{23} & c_{23} \end{pmatrix} \\ &= \begin{pmatrix} c_{12}c_{13} & s_{12}c_{13} & s_{13}e^{-i\delta_{13}} \\ -s_{12}c_{23} - c_{12}s_{23}s_{13}e^{i\delta_{13}} & c_{12}c_{23} - s_{12}s_{23}s_{13}e^{i\delta_{13}} & s_{23}c_{13} \\ s_{12}s_{23} - c_{12}c_{23}s_{13}e^{i\delta_{13}} & -c_{12}s_{23} - s_{12}c_{23}s_{13}e^{i\delta_{13}} & c_{23}c_{13} \end{pmatrix}\end{aligned} \tag{1.23}$$

Experimentally it is found that s_{ij} are small and that $s_{12} > s_{23} > s_{13}$. Wolfenstein proposed the approximate parameterisation

$$s_{12} = \lambda, \qquad s_{23} = A\lambda^2, \qquad s_{13}e^{-i\delta_{13}} = A\lambda^3(\rho - i\eta)$$

where A, ρ and η are of order unity and λ is the sine of the Cabibbo angle and approximately 0.23[22]. The CKM matrix to $\mathcal{O}(\lambda^3)$ in the Wolfenstein parameterisation is

$$\mathbf{V}_{CKM} = \begin{pmatrix} 1-\lambda^2/2 & \lambda & A\lambda^3(\rho - i\eta) \\ -\lambda & 1-\lambda^2/2 & A\lambda^2 \\ A\lambda^3(1-\rho-i\eta) & -A\lambda^2 & 1 \end{pmatrix} + \mathcal{O}(\lambda^4). \tag{1.24}$$

This parameterisation is particularly popular as it clearly indicates the relative strengths of the Yukawa couplings.

Using the unitarity property of the matrix we can obtain six orthogonality relationships between the couplings. Relevant to this analysis is the relation

$$V_{ud}V_{ub}^* + V_{cd}V_{cb}^* + V_{td}V_{tb}^* = 0. \tag{1.25}$$

Dividing 1.25 through by $|V_{cd}V_{cb}^*|$ results in a relation that when represented in the complex plane forms the CKM unitarity triangle with one side along the real axis normalised to unity. This gives rise to three CKM phases; α, β and γ as shown in figure 1.1, where the apex of the triangle $(\bar{\rho}, \bar{\eta})$ is

$$\bar{\rho} + i\bar{\eta} \equiv \rho(1 - \frac{1}{2}\lambda^2) + i\eta(1 - \frac{1}{2}\lambda^2)$$

and the angles α, β and γ are

$$\alpha \equiv \arg\Big[-\frac{V_{td}V_{tb}^*}{V_{ud}V_{ub}^*}\Big], \qquad \beta \equiv \arg\Big[-\frac{V_{cd}V_{cb}^*}{V_{td}V_{tb}^*}\Big], \qquad \gamma \equiv \arg\Big[-\frac{V_{ud}V_{ub}^*}{V_{cd}V_{cb}^*}\Big].$$

It should be noted that the sides of this triangle are all of comparable size resulting in large α, β and γ angles which is experimentally advantageous. In the Wolfenstein parameterisation to $\mathcal{O}(\lambda^3)$ the elements V_{ub} and V_{td} have complex components and $V_{cd}V_{cb}^*$ is negative. Using the CKM triangle it can be seen that $-\arg(V_{td}) = \beta$ and $-\arg(V_{ub}) = \gamma$ and hence the CKM matrix can be given as

$$\mathbf{V}_{CKM} = \begin{pmatrix} |V_{ud}| & |V_{us}| & |V_{ub}|e^{-i\gamma} \\ -|V_{cd}| & |V_{cs}| & |V_{cb}| \\ |V_{td}|e^{-i\beta} & -|V_{ts}| & |V_{tb}| \end{pmatrix} + \mathcal{O}(\lambda^4). \tag{1.26}$$

The Standard Model does not give predictions for Yukawa couplings, all the elements of the CKM matrix must be determined experimentally. Constraining all parameters of the CKM unitary triangle allows for a test of the unitarity condition. A deviation from this would indicate evidence of new physics not described by the Standard Model. The

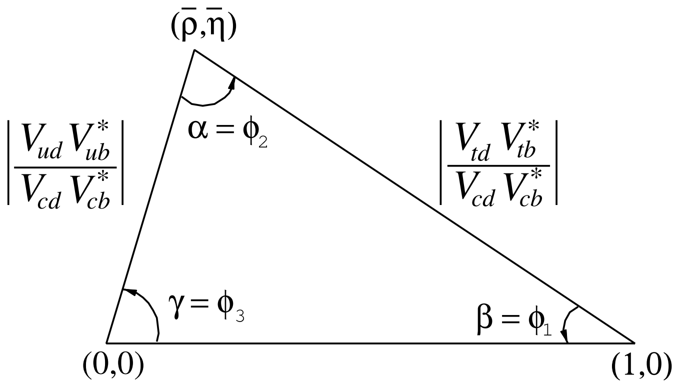

Figure 1.1: The CKM unitary triangle arising from the orthogonality relation $V_{ud}V_{ub}^* + V_{cd}V_{cb}^* + V_{td}V_{tb}^* = 0$ divided through by $|V_{cd}V_{cb}^*|$ which normalises one of the sides to unity. Taken from reference [23].

current constraints on the CKM triangle are shown in figure 1.2. The CKM phase γ remains the least well constrained of the CKM parameters. As can be seen in the figure the error on γ prevents the determination of whether or not the CKM parameters form a closed triangle i.e. conform to the unitarity condition.

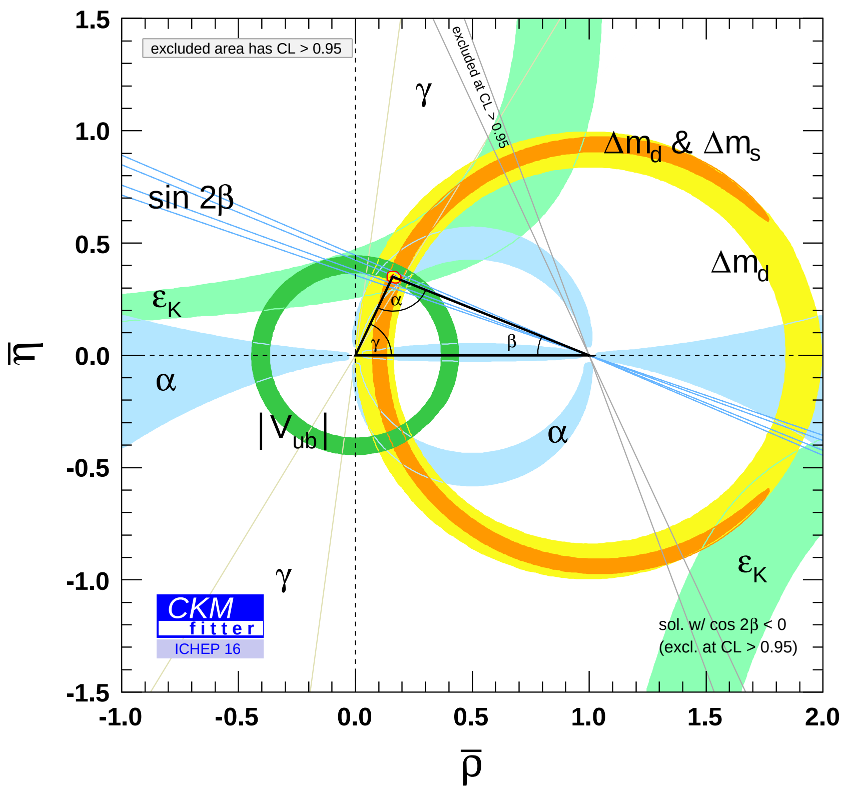

Figure 1.2: The CKM unitary triangle with global average constraints on parameters as determined by the CKM Fitter group. Taken from reference [24].

The phase γ is unique from the other CKM parameters in that it can be measured entirely from tree level amplitudes as well as from processes including loop amplitudes such as $B_s^0 \to K_S^0\pi^+\pi^-$. Amplitudes involving loops are highly sensitive to the effects of new physics as particles at mass scales far greater than those accessible in direct searches can enter into the loops as virtual particles [5] [25]. Exclusively tree level measurements of γ (such as the one presented in this thesis) are expected to be unaltered by new physics. A precision tree level measurement of γ can act as a Standard Model standard candle to which measurements involving loop processes can be compared [26]. A significant difference between the two measurements will be strong evidence of new physics.

Another sign of new physics would be a discrepancy between the direct and indirect measurements of γ. Whereas direct measurements measure γ in the fit, indirect measurements determine γ from measurements of the phase β and sides of the CKM triangle assuming the SM holds. The current best indirect measurement of γ is $\gamma = 65.33^{+0.96}_{-2.54}$[24] degrees whilst the current best direct measurement is $\gamma = 72.1^{+5.4}_{-5.8}$. Therefore to compare the two measurements the uncertainty on the direct measurement must be significantly reduced.

1.3 Measuring *CP*-violation in the *D* system

This thesis focuses on decays of D mesons. There are three ways in which *CP*-violation in the D system can manifest; direct, indirect via mixing and indirect via interference between mixing and a decay. Direct *CP*-violation occurs when a decay and its *CP* conjugate decay have different decay amplitude magnitudes. The decays must have contributions from two amplitudes with different *CP* conserving strong phases and *CP*-violating weak phases [27]. For instance, consider a decay $D \to f$ with amplitude $A = |A|e^{i\delta}e^{i\theta}$ where δ is a strong *CP* conserving phase and θ is a weak *CP*-violating phase. The amplitude for the decay $\bar{D} \to \bar{f}$ is $\bar{A} = |A|e^{i\delta}e^{-i\theta}$, however any physical quantity that is measured for either decay is proportional to $|A|^2$. Now let there be two indistinguishable paths to the same final state that can interfere with each other such

[5] Virtual particles are referred to as off mass-shell as they do not obey the energy-momentum relationship $E^2 - p^2 = m^2$

that

$$A = |A_1|e^{i\delta_1}e^{i\theta_1} + |A_2|e^{i\delta_2}e^{i\theta_2}$$

and

$$\bar{A} = |A_1|e^{i\delta_1}e^{-i\theta_1} + |A_2|e^{i\delta_2}e^{-i\theta_2}.$$

Now the difference in decay rates between the two decays is

$$|A|^2 - |\bar{A}|^2 = -4|A_1||A_2|\sin(\theta_1 - \theta_2)\sin(\delta_1 - \delta_2) \tag{1.27}$$

which can be observed by experiment [21].

Indirect *CP*-violation arises from particle-antiparticle oscillation through weak interactions in the $D^0 - \bar{D}^0$ system, also known as mixing. The Feynman diagram for this process is shown in figure 1.3.

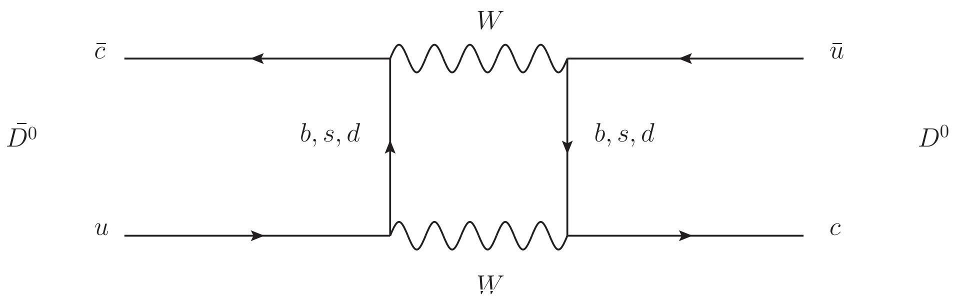

Figure 1.3: Feynman diagram of mixing in the $D^0 - \bar{D}^0$ system.

The physical eigenstates $|D_{1,2}\rangle$ are a linear combination of the interaction eigenstates

$$|D_1\rangle = p|D^0\rangle + q|\bar{D}^0\rangle$$

$$|D_2\rangle = p|D^0\rangle - q|\bar{D}^0\rangle$$

where p and q are complex mixing parameters with *CP*-violating phases and ratio

$$\frac{q}{p} = \left|\frac{q}{p}\right| e^{-i\phi}.$$

CP-violation in mixing occurs if the probability for $D^0 \to \bar{D}^0$ is different to that of $\bar{D}^0 \to D^0$ [28] i.e. if

$$\left|\frac{q}{p}\right| \neq 1.$$

Mixing can also cause *CP*-violation through its interference with a decay where D^0 and $\bar{D}^0$ have access to the same final state f. A D^0 meson can decay to f via two possible paths; directly by $D^0 \to f$ or by mixing to $\bar{D}^0$ and then decaying $D^0 \to \bar{D}^0 \to f$, with an analogous argument for $\bar{D}^0 \to \bar{f}$ decays[29]. As shown in equation 1.27 it is then possible for a difference in decay rates between $D^0 \to f$ and $\bar{D}^0 \to \bar{f}$ if $\phi + \arg\left(\frac{A_{\bar{D}^0 \to f}}{A_{D^0 \to f}}\right) \neq 0$. The contribution of mixing to *CP*-violation in the D^0 system is predicted to be unobservably small and so any observed *CP*-violation in D decays is expected to be dominated by direct contributions.

Singly Cabibbo suppressed D meson decay amplitudes are sensitive to direct *CP*-violation [30]. These amplitudes are dominated by $c \to s$ or $c \to d$ transitions occurring at tree-level and involving only the first two generations of quarks, this results in *CP* conserving amplitudes. However, direct *CP*-violation can occur in the SM through interference with loop amplitudes containing virtual b quarks in gluonic penguin diagrams as shown in figure 1.4 for $D^0 \to K^+K^-$ decays. These amplitudes involve $c \to u\bar{q}q$ transitions that are suppressed by the CKM matrix element $V_{cb}^{*}V_{ub}$ [31]. The standard model prediction for *CP*-violation in D meson decays is of the order 10^{-3}, a level that is currently experimentally unobservable. The loop diagrams however are sensitive to the effects of new physics that can enhance the level of *CP*-violation, hence any measured *CP*-violation is a clear indicator of physics beyond the SM. These penguin contributions cannot affect the Cabibbo favoured $c \to s\bar{d}u$ or doubly Cabibbo suppressed $c \to d\bar{s}u$ decays and no *CP*-violation is predicted by the SM for these decays.

Direct *CP*-violation in the D system can be observed in the following two ways. First, the global direct *CP* asymmetry can be measured using decay rates,

$$\mathcal{A}_{CP} \equiv \frac{\Gamma(D^0 \to f) - \Gamma(\overline{D}^0 \to \bar{f})}{\Gamma(D^0 \to f) + \Gamma(\overline{D}^0 \to \bar{f})}. \tag{1.28}$$

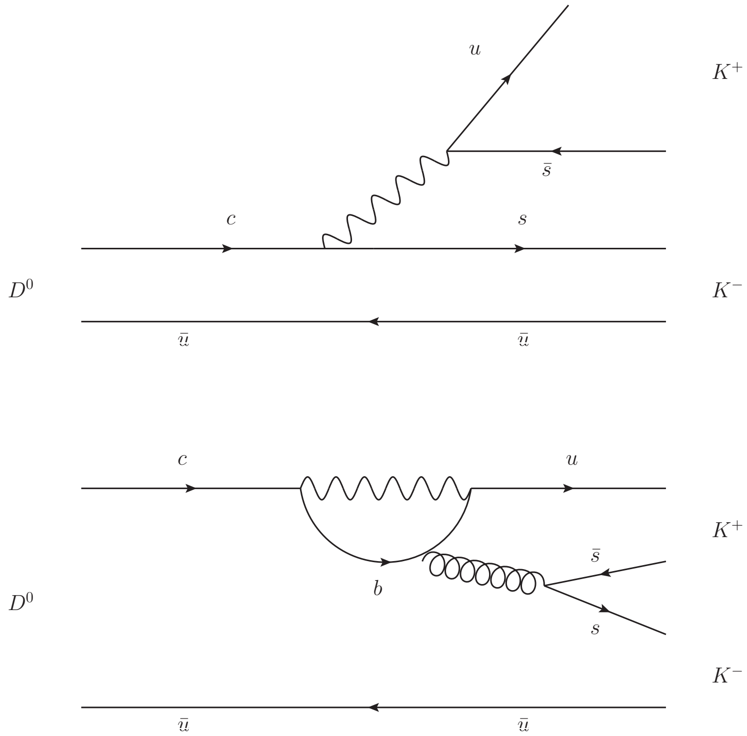

Figure 1.4: Singly Cabibbo suppressed $D^0 \to K^+K^-$ tree-level diagram (top) and penguin diagram (bottom).

In this measurement *CP*-violating effects can be diluted as they are integrated over phasespace. The second method searches for *CP*-violation at the amplitude component level by studying the intermediate states via which decays and their *CP* conjugate decays proceed. For this an amplitude analysis (as described in section 2) is performed on both the decay and its *CP* conjugate decay. Asymmetries in the fitted amplitude model parameters for a decay and its *CP* conjugate decay are indicative of *CP*-violation.

1.4 CKM phase γ from $B^\pm \to D(\to f)K^\pm$ Decays at LHCb

This thesis uses input from the amplitude analysis of D meson decays to make a measurement of the CKM phase γ. The precision measurement of γ is a main goal of the LHCb experiment [32]. The phase γ can be measured using the interference between $b \to u(c\bar{s}) \propto V_{ub}V_{cs}^*$ and $b \to c(u\bar{s}) \propto V_{cb}V_{us}^*$ quark transitions, the former of which is sensitive to γ. Colour favoured $B^- \to D^0K^-$ and colour suppressed $B^- \to \bar{D}^0K^-$ decays where the D decays[6] to the same final state f are studied [33][34][35]. These

[6]Here and throughout this thesis D denotes either D^0 or $\bar{D}^0$

decays are shown in figure 1.5. $B^{\pm} \to DK^{\pm}$ decays are favourable as they have the theoretically cleanest SM determination of γ with $|\delta\gamma| < 10^{-7}$, as they only have tree-level amplitude contributions and not loop (penguin) amplitude contributions [36]. They are also produced in large amounts at the LHCb experiment.

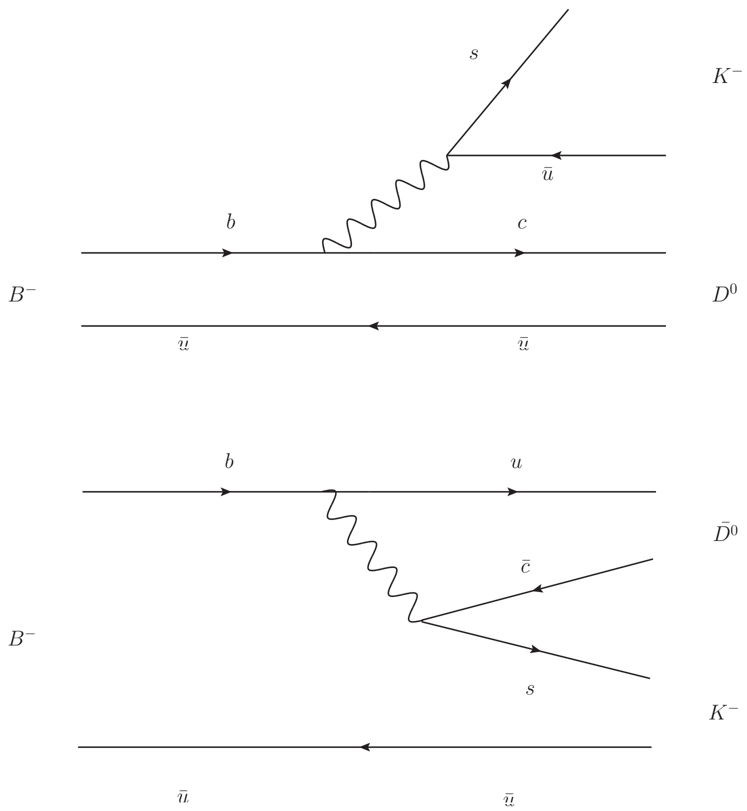

Figure 1.5: Feynman diagrams for the $B^- \to D^0K^-$ decay (top) and $B^- \to \bar{D}^0K^-$ decay (bottom).

Using the CKM matrix representation in 1.26 the ratio of the colour favoured and colour suppressed decays can be most generally written, separating the strong and weak contributions, as

$$\frac{A(B^- \to \bar{D}^0K^-)}{A(B^- \to D^0K^-)} = \frac{|A_{B\to\bar{D}^0K}|e^{i\delta_{B\to\bar{D}^0K}}}{|A_{B\to D^0K}|e^{i\delta_{B\to D^0K}}} \cdot \frac{|V_{cs}||V_{ub}|e^{-i\gamma}}{|V_{cb}||V_{us}|}$$

where A and δ are the magnitude and phase of the strong part of the amplitudes respectively. We can absorb the magnitudes of the CKM elements into the A parameters and let

$$r_B = \frac{|A_{B\to\bar{D}^0K}|}{|A_{B\to D^0K}|}$$

$$\delta_B = \delta_{B\to\bar{D}^0K} - \delta_{B\to D^0K}$$

such that r_B is the ratio of the magnitudes of the amplitudes and δ_B is the difference in the strong phases of the amplitudes.

For final states of 3 or more particles the amplitude of the decay $D^0 \to f$ is dependent on the position of the final state particles in phasespace, p. Different intermediate resonant states are accessible depending on the final state p and hence the amplitude of $D^0 \to f$ is a function of p. The full amplitude for the $B^- \to D^0(\to f)K^-$ decay is then

$$A(p)^- = A_{D^0}(p) + r_B e^{i(\delta_B - \gamma)} A_{\bar{D}^0}(p).$$

Under a *CP* transformation the strong parameters of the decay remain invariant, however as shown in section 1.1.4 the Yukawa coupling is conjugated and so for a B^+ meson the full amplitude is given by

$$A(p)^+ = A_{\bar{D}^0}(p) + r_B e^{i(\delta_B + \gamma)} A_{D^0}(p).$$

Therefore, if we can assume no *CP*-violation in the D decay (an assumption that can be confirmed from an amplitude analysis), by using amplitude models for $D^0 \to f$ and $\bar{D}^0 \to f$ as a function of p and by fitting $|A^+(p)|^2$ and $|A^-(p)|^2$ to $B^+ \to D^0(\to \bar{f})K^+$ and $B^- \to D^0(\to f)K^-$ decays respectively, values for r_B, δ_B and γ can be obtained.

The analysis presented in this thesis uses a 4 body generalisation of the Giri-Grossman-Soffer-Zupan (GGSZ) method [37] which uses a self-conjugate final state f. The $K^+K^-\pi^+\pi^-$ final state is chosen[38], this final state is particularly suited to LHCb due to the excellent kaon and pion identification provided by the Ring Imaging CHerenkov (RICH) detectors.

The following thesis comprises two parts. Section 4 details the amplitude analysis of $D^0 \to K^+K^-\pi^+\pi^-$ decays with new physics searches performed in the study of *CP*-violation in the D system. In section 5, using the amplitude model from section 4, an assessment of potential biases in the model-dependent measurement of γ using $B^\pm \to D(\to K^+K^-\pi^+\pi^-)K^\pm$ decays is performed. This is achieved by performing the measurement on a control channel for which the value of r_B is an order of magnitude smaller than that in $B^\pm \to D(\to K^+K^-\pi^+\pi^-)K^\pm$ decays, as such we expect to see no CP-violation for this channel. The following section will introduce the formalism used for the amplitude analysis and section 3 will describe both the CLEO and LHCb detectors from which the data used in these analyses is collected.

Chapter 2

Amplitude analyses

This section describes the formalism used in the amplitude analysis presented in this thesis as well as the MINT amplitude fitter package used.

2.1 Differential decay rates

The differential partial decay rate (or decay width) of a D meson decaying to n final state pseudoscalar particles can be given as a function of any set of ν independent variables $\mathbf{x} = (x_1, ..., x_\nu)$ by

$$d\Gamma \propto |A_D|^2 d\Phi_n \tag{2.1}$$

The differential element $d\Phi_n$ is given by

$$d\Phi_n = \phi_n(\mathbf{x}) d^\nu x$$

where $\phi_n(\mathbf{x})$ is the density of states in the phasespace element $d^\nu x$. The term A_D is the amplitude of the decay, it contains all of the decay dynamics [39]. A decay $D \to f$ can proceed directly (a non-resonant decay) or, more commonly, via various intermediate states. Relevant examples are $D^0 \to \phi(1020)\,(\pi^+\pi^-)$ where $\phi(1020) \to (K^+K^-)$, $D^0 \to \rho^0(770)\,(K^+K^-)$ where $\rho^0(770) \to (\pi^+\pi^-)$ and $D^0 \to \phi(1020)\,\rho^0(770)$, where $\phi(1020) \to (K^+K^-)$ and $\rho^0(770) \to (\pi^+\pi^-)$. Here, ϕ and ρ here are known as resonance states. An amplitude analysis is the study of the relative contribution of intermediate resonance states via which a decay can occur. An amplitude analysis attempts to parameterise A_D.

2.2 The 3-body case

Consider the 3-body decay, $D \to abc$, where a, b and c are pseudoscalar particles. This decay can occur via 2-body resonances such as $D \to rc, r \to ab$ [40]. Similar to Young's double slit experiment where light particles with multiple possible paths to a position in space produce quantum mechanical interference effects on a screen, so too do multiple, indistinguishable decay paths to the same final state f due to phase differences in the contributing decay path amplitudes. These interference effects can be seen as regions of higher (constructive interference) and lower (destructive interference) population density in the phasespace of the final state particles. For three body decays these effects are commonly illustrated on a Dalitz plot.

2.2.1 Dalitz plots

A Dalitz plot is a visual representation of the resonant substructure of the decay of a spin-less particle to three spin-less particles. It is a scatter plot with axes equal to the square of invariant mass combinations of the final state particles. The Dalitz plot traditionally refers only to the 3-body decay case (however in this thesis its use is extended to 4-body decays). For a 3-body decay only 2 independent invariant mass variables are needed to fully describe the decay as can be seen by the relation

$$m_{ab}^2 + m_{bc}^2 + m_{ac}^2 = m_D^2 + m_a^2 + m_b^2 + m_c^2$$

where $m_{ab}^2 = (p_a + p_b)^2$. As such the Dalitz plot for a 3-body decay is 2-dimensional. The number of independent variables needed to describe an n-body decay i.e. the value of ν in 2.1, can be explained through

- **4n** variables for each particle's 4-momentum

- **-n** for the known masses of the final state particles
- **-4** for conservation of energy and momentum in the decay
- **-3** for arbitrary rotation

This generalises to $3n$-7 independent variables. The boundaries of the allowed phasespace for a decay are dictated by the conservation of 4-momentum between the decaying particle and the decay products, this is what gives the Dalitz plot its unique shape. For example, for $D \to abc$, the kinematically allowed values of m^2_{bc} are in the range $(m_b + m_c)^2 \leq m^2_{bc} \leq (m_D - m_a)^2$ with the minimum and maximum value occurring when b and c are parallel or anti-parallel, respectively

$$m^2_{bc} = (p_b + p_c)^2 = m^2_b + m^2_c + 2E_bE_c - 2\mathbf{p}_b \cdot \mathbf{p}_c.$$

A Dalitz plot can be used to infer the resonances present in a decay, the interference (phase difference) between resonances and also a resonance's spin. Consider a single amplitude component contributing to a decay with amplitude $A(p) = A_1(p)e^{i\theta_1(p)}$. The observable as seen on the Dalitz plot will be $|A_1(p)|^2$ and hence we will be able to infer its presence by a band of higher event population - a resonance band. However, we have lost all information about the phase of the decay. Consider now the case of two contributing amplitude components that can interfere. Now the Dalitz plot will show contributions of

$$|A(p)|^2 = |A_1(p)|^2 + |A_2(p)|^2 + 2|A_1(p)||A_2(p)|\cos(\theta_1(p) - \theta_2(p)).$$

Here we have access to phase information of the amplitude components which manifests in constructive interference and destructive interference. To see how we can infer the spin of a resonance we introduce some more formalism. The decay $D \to rc, r \to ab$ has an amplitude, $A_D(p)$, which is normalised relative to all other amplitudes for the decay of $D \to abc$. $A_D(p)$ consists of

- A term Z describing the angular distribution of the decay accounting for conservation of total angular momentum

- A form factor, B_L, for each decaying particle to account for finite size
- A propagator or lineshape, T_R, to represent each unstable (resonance) particle

These factors combine to form,

$$A(p) = Z(J, L, l, \bar{p}, \bar{q}) B_L^D(|\bar{p}|) B_L^r(|\bar{q}|) T_r(m_{ab}) \tag{2.2}$$

Here, J is the total angular momentum (sum of orbital momentum and spin) of the D^0 particle which is zero. Between the resonance r and final particle c there can exist an orbital angular momentum L and between final state particles a and b there can exist an orbital angular momentum l. The momenta of c and a are given in the rest frame of r as $\bar{p}$ and $\bar{q}$ respectively.

For pseudoscalar to pseudoscalar decays the orbital angular momentum between r and c, denoted L, is necessarily the spin of r. The quantum mechanical orbital angular momentum operator, $\hat{L}^2$, has eigenfunctions equal to the spherical harmonics $Y_l^m(\theta, \phi)$ [41]. The first 3 spherical harmonics (up to a relative D wave) have the form

$$\begin{aligned} Y_0^0(\theta, \phi) &= \frac{1}{2}\sqrt{\frac{1}{\pi}} \\ Y_1^0(\theta, \phi) &= \frac{1}{2}\sqrt{\frac{3}{\pi}}\cos\theta \\ Y_2^0(\theta, \phi) &= \frac{1}{4}\sqrt{\frac{5}{\pi}}(3\cos^2\theta - 1) \end{aligned} \tag{2.3}$$

Defining θ as the angle between particle a and c in the rest frame of the resonance we can see how spin S of the resonance r contributes a $\cos^S(\theta)$ dependence to the amplitude. Hence the spin of a resonance can be inferred by gaps in the Dalitz plot resonance band.

The Dalitz plot for the decay $D^0 \to K_S^0\pi^+\pi^-$ can be seen figure 2.1 with axes $s_+ = m_+^2 = (p_{K_S} + p_{\pi^+})^2$ and $s_- = m_-^2 = (p_{K_S} + p_{\pi^-})^2$ [42]. Bands of high density indicate the presence of intermediate resonance states, the $D^0 \to K^*(892)^-(\to K_S^0\pi^-)\pi^+$ resonance decay is clearly visible as a band at constant m_-^2. In the $D^0 \to K^*(892)^-(\to K_S^0\pi^-)\pi^+$

decay there must be a P (L=1) relative wave between the $K^*(892)^-$ and the bachelor π^+ to conserve total angular momentum. A single gap in the resonance band can be seen.

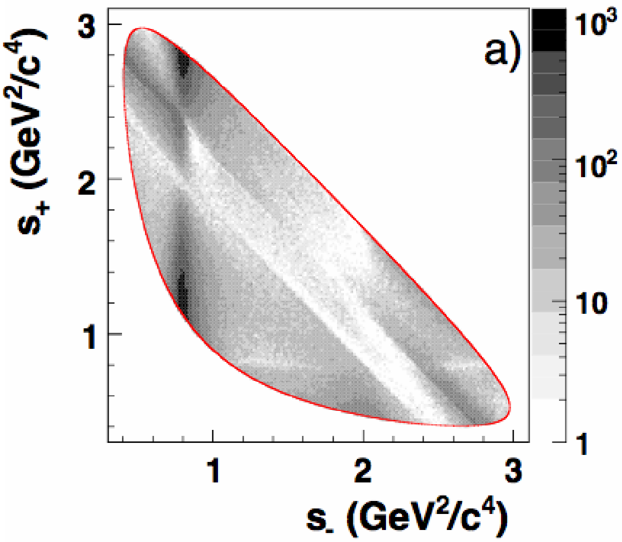

Figure 2.1: Dalitz plot for $D^0 \to K^0_S\pi^+\pi^-$. Taken from reference [42].

The amplitude in equation 2.2 is phenomenological and as such there exists different formalisms for Z, B_L and T_r. The next section details how these are formulated in this analysis for 4-body decays.

2.3 The 4-body case

There are several complications in 4-body Dalitz analyses that are not present in the 3-body case. In 4-body decays 5 independent variables are required to describe the decay kinematics, the 4-body generalisation of the Dalitz plot is then 5 dimensional. In the following analyses we use the labelling scheme $j = 1, 2, 3, 4$ corresponding to the K^+, K^-, π^+, π^- of the D decay respectively. The 5 independent variables chosen are $s_{12} = (p_{K^+} + p_{K^-})^2$, $s_{23} = (p_{K^-} + p_{\pi^+})^2$, $s_{34} = (p_{\pi^+} + p_{\pi^-})^2$, $s_{123} = (p_{K^+} + p_{K^-} + p_{\pi^+})^2$ and $s_{234} = (p_{K^-} + p_{\pi^+} + p_{\pi^-})^2$. In the 3-body case the parity operation can be expressed simply as a rotation of the decay plane and so there are no parity violating kinematic observables (assuming rotational invariance in decays). For 4-body decays however, where there is no such single decay plane, these parity even invariant-mass-squared variables are not sufficient to unambiguously describe a decay. For the construction of the amplitudes however we use the 4-momenta of the final state particles rather than these 5 variables which are used primarily for showing projections of the 5 dimensional D decay phasespace.

Unlike for 3-body decays the phasespace density for 4-body decays is not uniform in any set of 5 variables, rather it is proportional to the reciprocal of the square root of the Grahm determinant [1], where $x_{ij} = p_i \cdot p_j$,

$$\phi_4 = \frac{d\Phi_4}{ds_{12}ds_{23}ds_{34}ds_{123}ds_{234}} = \frac{\pi^2}{32m_D^2}\left[-\begin{vmatrix} x_{11} & x_{12} & x_{13} & x_{14} \\ x_{21} & x_{22} & x_{23} & x_{24} \\ x_{31} & x_{32} & x_{33} & x_{34} \\ x_{41} & x_{42} & x_{43} & x_{44} \end{vmatrix}\right]^{-\frac{1}{2}}$$

During the normalisation process of Probability Density Functions (PDFs) used to fit the data this varying phasespace density must be taken into account and is denoted as $R_4(p)$ in the following where p is a point in the D decay phasespace.

For 3-body pseudoscalar to pseudoscalar decays only single resonance decays are possible and each has only one possible orbital angular momentum configuration. For 4-body decays there can be:

- Single resonance decays eg. $D^0 \to \phi(1020)\,(\pi^+\pi^-)_S$
- Double resonance decays eg. $D^0 \to \phi(1020)\,\rho^0(770)$
- Cascade decays eg. $D^0 \to K^-\,[K_1(1270)^+ \to \pi^+\,K^{*0}(892)]$

The double resonance and cascade decay is illustrated in figure 2.2. These decays can have multiple associated amplitudes depending on the orbital angular momentum state involved. For instance in the double resonance decay $D^0 \to \phi(1020)\,\rho^0(770)$ the intermediate particles are vector particles (spin 1) and as such they can be in an S, P or D relative wave, each of which has its own amplitude to consider [1]. These are denoted in the following as $D^0[S,P,D] \to \phi(1020)\,\rho^0(770)$. Particles that do not originate from a resonance like the two pion system in $D^0 \to \phi(1020)\,(\pi^+\pi^-)_S$, can also be in a state of relative orbital angular momentum. We refer to these as non-resonant states and denote them by surrounding the particles with brackets and indicating the partial wave state with a subscript. For example, for this decay $(\pi^+\pi^-)_S$ refers to a non-resonant 2 pion system in a relative S wave.

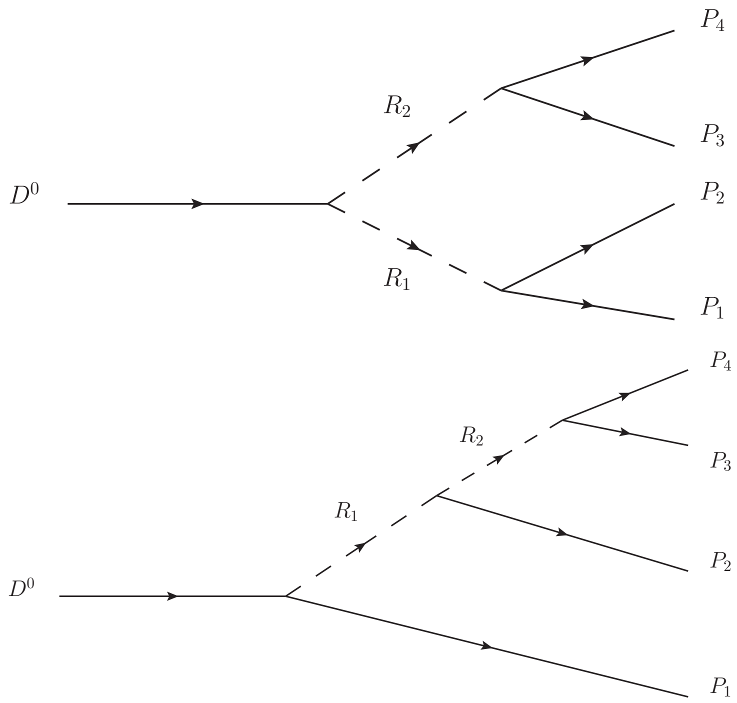

Figure 2.2: A double resonance decay (top) and cascade decay (bottom) of a D meson to 4-final state particles where dashed lines represent unstable resonance particles.

2.4 Isobar model

The Isobar model is used to parameterise an amplitude model for $D^0 \to K^+K^-\pi^+\pi^-$ decays in the form $A_{D^0}(p) = |A_{D^0}(p)|e^{i\delta_D(p)}$ where $\delta_D(p)$ describes the phase motion over the D decay phasespace. The isobar model assumes that 4-body decay amplitudes can be factorised into sequential two-body decay amplitudes. Recalling equation 2.2, consider the processes $D \to R_1(\to ab)R_2(\to cd)$ and $D \to d[R_1 \to c(R_2 \to ab)]$. The relative amplitude is expressed as

$$A_D(p) = B_L^D(p)[B_L^{R_1}(p)T_{R_1}(p)][B_L^{R_2}(p)T_{R_2}(p)]Z(p) \tag{2.4}$$

The parameterisations of these terms is described in the following, beginning with the lineshape T_R which includes a description of the 2 and 3-body energy dependent widths, $\Gamma(s)$.

2.4.1 Lineshape, T_R

The resonance lineshape is by default given by the relativistic Breit-Wigner which is suitable for describing resonances that are non-overlapping and far from the threshold of other decay channels. Consider now, a resonance R decaying to particles R_1 and R_2. The Breit-Wigner amplitude is given by

$$T_R(s) = \frac{1}{m_R^2 - s - im_R\Gamma(s)} \tag{2.5}$$

where $s = p_R^2$ and m_R is the pole mass of R. $\Gamma(s)$ is known as the energy-dependent width and has the form

$$\Gamma(s) = \Gamma_0 \left(\frac{q}{q_R}\right)^{2L+1} \left(\frac{m_R}{\sqrt{s}}\right) \frac{B_L(q)^2}{B_L(q_R)^2}. \tag{2.6}$$

Here, the particle width Γ_0 is multiplied by factors representing the energy-dependent 2-body phasespace available to the decaying particle. These factors are normalised such that for a resonance decaying at its pole mass, $(s = m_R^2)$ $\Gamma(s) = \Gamma_0$. The parameter q is the magnitude of the momenta of R_1 and R_2 in the resonance rest frame, also known as the breakup momentum,

$$|q| = \sqrt{\frac{\left(s - (\sqrt{p_{R_1}^2} + \sqrt{p_{R_2}^2})^2\right)\left(s - (\sqrt{p_{R_1}^2} - \sqrt{p_{R_2}^2})^2\right)}{4s}}. \tag{2.7}$$

q_R is the breakup momentum evaluated when $s = m_R^2$. The orbital angular momentum between R_1 and R_2 is represented by L and parameter B_L is given in equation 2.11 and discussed later.

For the cascade topology, where either R_1 or R_2 is a resonance, the energy-dependent width must take into account the full 3-body phase space available to the decaying resonance R. It is also possible that $m_R^2 < \left(\sqrt{p_{R_1}^2} + \sqrt{p_{R_2}^2}\right)^2$ whilst $s \geq \left(\sqrt{p_{R_1}^2} + \sqrt{p_{R_2}^2}\right)^2$ due to the width of R [1]. Using the 2-body description for the energy dependent width given above would result in an undefined breakup momentum. For cascade decays then, the energy-dependent width of a 3-body decay can be found using the integral of the differential partial width equation in 2.1 for all possible decay channels open to the resonance. In other words the partial width

$$\Gamma_{R\to f}(s) = \frac{1}{2\sqrt{s}} \int |A_{R\to f}(s)|^2 d\Phi_3$$

is found for each decay channel of R where the 3-body amplitude $A_{R\to f}$ is parameterised using the 3-body formalism. To find the total width we sum over all partial widths

$$\Gamma(s) = \sum_i g_i \Gamma_i(s),$$

where g_i is the coupling strength to channel i. The set of g_i couplings for all decay channels of a resonance R can be found from their branching fractions through a fit to

$$\mathcal{B}_i = \int_{s_{min}}^{\infty} \frac{g_i\, m_R\, \Gamma_i(s)}{|m_R^2 - s - i\, m_R \sum_j g_j\, \Gamma_j(s)|^2}\, \mathrm{d}s. \tag{2.8}$$

In the following analyses the resonant particles occurring in such cascade decays are the $K_1(1270)$ and $K_1(1400)$ mesons and the $K^*(1410)$ and $K^*(1680)$ mesons. For the $K_1(1270)$ and $K_1(1400)$ mesons the $K\rho(770)^0$, $K^*(892)\pi$, $K_0^*(1430)\pi$, $Kf_0(1370)$ and $K\omega$ channels are taken into account at the lowest possible angular momentum state only. For the $K^*(1410)$ and $K^*(1680)$ mesons decay channels $K\rho(770)^0$, $K^*(892)\pi$ and $K\pi$ are considered. For the purpose of approximating $\mathcal{B}_i$ in equation 2.8 using measured branching fractions the contributions are considered incoherent. For example the energy dependent width of $K^*(1680)$ is given by

[1]This is not possible in 2-body decays as R_1 and R_2 are final state particles where $p_{R_1}^2 = m_{R_1}^2$ and $p_{R_2}^2 = m_{R_2}^2$

$$\begin{aligned}\Gamma_{K^*(1680)}(s) = {} & g_{K\rho(770)^0}\Gamma_{K^*(1680)\to K\rho(770)^0}(s) \\ & + g_{K\pi}\Gamma_{K^*(1680)\to K\pi}(s) \\ & + g_{K^*(892)\pi}\Gamma_{K^*(1680)\to K^*(892)\pi}(s)\end{aligned}$$

where the g_i values are found from their respective branching fractions. These energy-dependent width values are calculated once, before the amplitude fit, and stored in histograms that are accessed at run time. The histograms are produced by scanning over values of s and evaluating $\Gamma(s)$, values can be taken for any value of s through the interpolation of these results. Figure 2.3 and 2.4 shows the energy-dependent width histograms used for the following analyses.

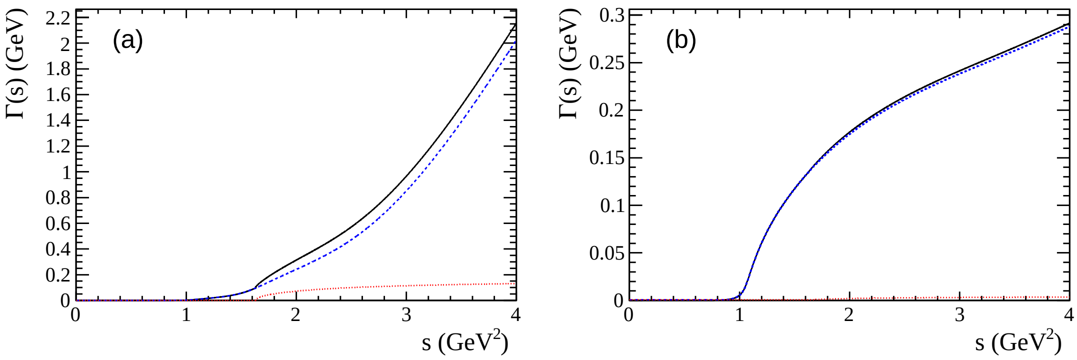

Figure 2.3: Energy dependent width for a) $K_1(1270)$ and b) $K_1(1400)$ resonances. The black line shows the total width, the partial widths of channels $K\pi\pi$ and $K\omega$ are shown in dashed blue and red respectively. Taken from reference [2].

Besides the Breit-Wigner lineshape the Flatté distribution is used to model resonances where a second decay channel opens close to the resonance such as the $f_0(980)$. In the Breit-Wigner equation (2.5), $\Gamma(s)$ is replaced by the sum of the partial widths to the $\pi\pi$ and KK channels

$$\Gamma_{f_0(980)}(s) = g_{\pi\pi}\Gamma_{f_0(980)\to\pi\pi}(s) + g_{KK}\Gamma_{f_0(980)\to KK}(s).$$

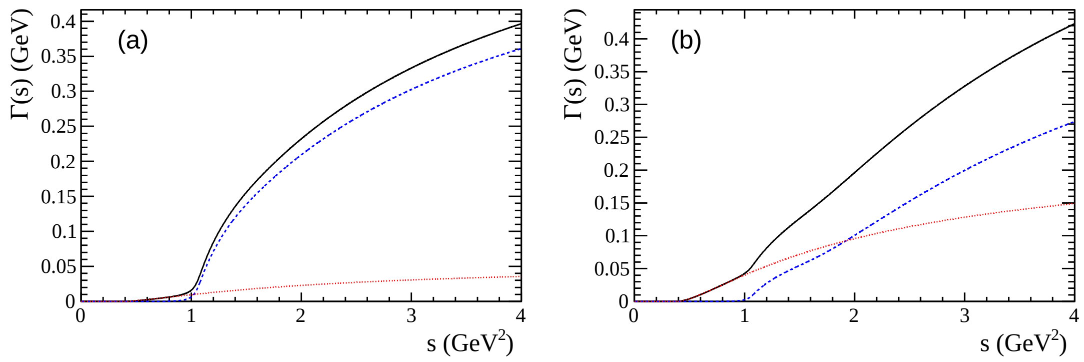

Figure 2.4: Energy dependent width for a) $K^*(1410)$ and b) $K^*(1680)$ resonances. The black line shows the total width, the partial widths of channels $K\pi\pi$ and $K\pi$ are shown in dashed blue and red respectively. Taken from reference [2].

The $g_{\pi\pi}$ and g_{KK} values as well as the mass and width parameters needed for the evaluation of $\Gamma_{f_0(980)\to\pi\pi}(s)$ and $\Gamma_{f_0(980)\to KK}(s)$ (using the 2-body energy-dependent width 2.6) are taken from a measurement performed by the BES collaboration [43].

For particles that do not originate from a resonance but are in a state of relative orbital angular momentum the lineshape is set to unity.

2.4.2 Angular distribution component, Z

The angular distribution component, Z, (also known as the spin factor or spin amplitude) is a Lorentz-invariant quantity that enforces total angular momentum conservation and the correct parity transformation of the wavefunction. In quantum mechanics, the total angular momentum of a particle, $\bar{J}$, is the vector sum of orbital angular momentum, $\bar{L}$ and spin angular momentum, $\bar{S}$. Spin and orbital angular momentum must be projected into the same subspace in order to ensure total angular momentum conservation. Following the isobar formalism, where 4-body decays are factorised into 2-body decays, the construction of the spin amplitude for a decay $R \to R_1 R_2$ involves 3 objects; polarisation tensors, spin projection tensors and orbital angular momentum tensors.

Polarisation tensors

A massive, spin-1 particle with momentum p and spin projection along the z axis, s_z, can be represented by a polarisation vector $\varepsilon^{\mu}_{(1)}(p, s_z)$. This vector must be orthogonal to the momentum of the particle as spin is an angular momentum like quantity. The time component, $\varepsilon^{0}_{(1)}(p, s_z)$, must also be equal to zero as spin does not evolve over time. Given these conditions there are 3 independent solutions for $\varepsilon^{\mu}_{(1)}(p, s_z)$ that for illustration can be interpreted as the 3 polarisation states of a spin-1 particle along the z-axis in the particle rest frame[44]; the longitudinal polarisation

$$\varepsilon^{\mu}_{(1)}(0) = (0, 0, 0, 1)$$

and transverse polarisations, analogous to left and right circular polarisation states for plane waves

$$\varepsilon^{\mu}_{(1)}(\pm 1) = \mp \frac{1}{\sqrt{2}}(0, 1, \pm i, 0).$$

This analysis also considers particles of spin 2. For spin-2 and higher particles, polarisation tensors must meet two more conditions forming the set of three Rarita-Schwinger conditions [45]. These state that the polarisation tensor for a spin-S particle must be:

- Orthogonal to the momentum of the particle (as stated above)

$$\varepsilon^{\mu_1 \ldots \mu_s}_{S}(p, s_z) p_{\mu_1} = 0$$

- Symmetric

$$\varepsilon^{\ldots \mu_i \ldots \mu_j \ldots}_{S}(p, s_z) = \varepsilon^{\ldots \mu_j \ldots \mu_i \ldots}_{S}(p, s_z)$$

- Traceless

$$g_{\mu_i \mu_j} \varepsilon^{\ldots \mu_i \ldots \mu_j \ldots}_{S}(p, s_z) = 0$$

A particle of spin-S has 2S+1 degrees of freedom (or spin projections), the Rarita-Schwinger conditions reduce the 4^S elements of the polarisation tensor to 2S+1 independent elements.

Spin projection tensors

The spin-L projection operator, $P_{(L)}^{\mu_1 \ldots \mu_L}(p_R)$, projects any 4-vector into the spin-L subspace spanned by the 2L+1 polarisation vectors orthogonal to p_R. For $L = 0$, $P_{(0)}(p_R) = 1$. For $L = 1$,

$$P_{(1)}^{\mu\nu}(p_R) = -g^{\mu\nu} + \frac{p_R^\mu p_R^\nu}{s} = \sum_{s_z} \varepsilon^\mu(p_R, s_z)\varepsilon^{*\nu}(p_R, s_z)$$

where $g^{\mu\nu}$ is the Minkowski metric. For the $L = 2$ case,

$$\begin{aligned} P_{(2)}^{\mu_1\mu_2\nu_1\nu_2}(p_R) = &\frac{1}{2}\Big[P_1^{\mu_1\nu_1}(p_R)P_1^{\mu_2\nu_2}(p_R) + P_1^{\mu_1\nu_2}(p_R)P_1^{\mu_2\nu_1}(p_R)\Big] \\ &- \frac{1}{3}\Big[P_1^{\mu_1\mu_2}(p_R)P_1^{\nu_1\nu_2}(p_R)\Big] \end{aligned}$$

Orbital angular momentum tensor

The orbital angular momentum tensor[46] projects the rank-L relative momenta tensor, $q_R^{\nu_1} \ldots q_R^{\nu_L}$, where $q_R = p_{R_1} - p_{R_2}$, onto the spin-L subspace orthogonal to p_R using again the spin-L projection operator

$$L_L^{\mu_1 \ldots \mu_L}(p_R, q_R) = (-1)^L P_L^{\mu_1 \ldots \mu_L \nu_1 \ldots \nu_L}(p_R) q_{R_{\nu_1}} \ldots q_{R_{\nu_L}}$$

The polarisation tensors, spin projection tensors and orbital angular momentum tensors are contracted to form a Lorentz scalar for each decay vertex [2]. The steps to form the spin amplitude for a decay $R \to R_1 R_2$ with relative wave, L, between the decay products are

- Assign a polarisation tensor to the decaying particle R and to each decay product R_1 and R_2 (for decay products the complex conjugate of the polarisation tensor is taken)

- Project the polarisation tensors of the decay products onto the spin-L subspace that is orthogonal to p_R using the spin-L projection operator
- Project the relative momenta tensor $q_R^{\nu_1}...q_R^{\nu_L}$ onto the same spin-L subspace using the orbital angular momentum tensor
- Contract all of the above with the polarisation tensor of the decaying particle to give a Lorentz scalar.

A specific example relevant to this analysis is the decay of a pseudoscalar particle D to vector particles R_1 and R_2, $D \to R_1 R_2$, followed by the subsequent decay of R_1 and R_2 to pseudoscalar particles, $R_1 \to ab$ and $R_2 \to cd$. This is the form of decays such as $D^0[S,P,D] \to \phi(1020)\,\rho^0(770)$. There are 3 orbital angular momentum configurations possible for this decay where the relative wave between particles R_1 and R_2 can be L=[0, 1, 2], each has its own associated spin amplitude. The construction of these will now be shown.

For the initial $D \to R_1 R_2$ decay a complex conjugated polarisation vector is assigned to each decay particle,

$$\varepsilon^{*a}_{(1)}(p_{R_1}, s_{R_{1z}})\varepsilon^{*b}_{(1)}(p_{R_2}, s_{R_{2z}}).$$

The decaying particle has no spin component and thus no polarisation tensor. In the case of $L = 0$, there is no relative orbital angular momentum to consider so we simply contract the polarisation vectors of the decay products together.

$$Z_{\langle D \to R_1 R_2 | L=0 \rangle} = \sum_{s_{R_{1z}}, s_{R_{2z}}} \varepsilon^{*a}(p_{R_1}, s_{R_{1z}})\varepsilon^{*}_{a}(p_{R_2}, s_{R_{2z}})$$

In the case of $L = 1$, we must also consider the parity of the $R_1 R_2$ system which is given by

$$\eta = (-1)^L \eta_{R_1} \eta_{R_2}$$

where η is the eigenvalue of the parity operator. The parity of this system is odd ($\eta = -1$) and as such it's wavefunction must behave as an odd eigenstate of the parity operator. The antisymmetric Levi-Civita tensor contracted with the 4-momentum of D,

$\varepsilon_{\alpha\beta\gamma\delta}p_D^{\delta}$, is used to ensure the correct parity transformation of the total wavefunction. For the $L = 1$ case then,

$$Z_{\langle D\to R_1R_2|L=1\rangle} = \sum_{s_{R_1Z},s_{R_2Z}} L_{1e}(p_D, q_D)P^{ea}_{(1)}(p_D)\varepsilon_{abcd}\varepsilon^{*b}(p_{R_1}, s_{R_{1z}})\varepsilon^{*c}(p_{R_2}, s_{R_{2z}})p_D^d$$

and finally for the $L = 2$ case,

$$Z_{\langle D\to R_1R_2|L=2\rangle} = \sum_{s_{R1Z},s_{R2Z}} L_{2ab}(p_D, q_D)P^{abcd}_{(2)}(p_D)\varepsilon^*_c(p_{R_1}, s_{R_{1z}})\varepsilon^*_d(p_{R_2}, s_{R_{2z}})$$

The spin amplitudes of the subsequent decays, $R_1 \to ab$ and $R_2 \to cd$ are far simpler to evaluate. The relative wave between two pseudoscalar decay products must always be equal to the spin of the decaying particle, in this case spin-1. The decay products have no polarisation tensor and the decaying particle has polarisation tensor $\varepsilon^{*\mu}_{(1)}(p_{R_1}, s_{R_{1z}})$. This is simply contracted with the angular momentum tensor that projects the relative momentum between the decay products onto the spin-1 subspace

$$Z_{\langle R_1\to ab|L=1\rangle} = \sum_{s_{R_1Z}} \varepsilon^{\mu}(p_{R_1}, s_{R_{1z}})L_{1\mu}(p_{R_1}).$$

For brevity we introduce the following notation,

$$\begin{aligned}
\varepsilon_{(S)}(R) &\equiv \varepsilon_{(S)}(p_R, s_{R_z}),\\
P_{(S)}(R) &\equiv P_{(S)}(p_R),\\
L_{(L)}(R) &\equiv L_{(L)}(p_R, q_R).
\end{aligned} \tag{2.9}$$

and for each value of L we can write the spin factor for the decay $D \to R_1(\to AB)R_2(\to CD)$ as

$$\sum_{s_{R_1Z}, s_{R_2Z}} S_{D\to R_1R_2}(\mathbf{p}|L_{R_1R_2}; s_{R_1Z}, s_{R_2Z})\, S_{R_1\to AB}(\mathbf{p}|L_{AB}; s_{R_1Z})\, S_{R_2\to CD}(\mathbf{p}|L_{CD}; s_{R_2Z}), \tag{2.10}$$

where

$$S_{D\to R_1R_2}(\mathbf{p}|L_{R_1R_2}; s_{R_1Z}, s_{R_2Z}) = L_{(L_{R_1R_2})}(D)P_{(L_{R_1R_2})}(D)\varepsilon^*_{(S_{R_1})}(R_1)\varepsilon^*_{(S_{R_2})}(R_2)$$

(for $L = 1$ we also include the Levi-Civita tensor) and

$$S_{R_1\to AB}(\mathbf{p}|L_{AB}; s_{R_1Z}) = \sum_{s_{R_1Z}} \varepsilon_{(S_{R_1})}(R_1)L_{(L_{AB})}(R_1)$$

$$S_{R_2\to CD}(\mathbf{p}|L_{CD}; s_{R_2Z}) = \sum_{s_{R_2Z}} \varepsilon_{(S_{R_2})}(R_2)L_{(L_{CD})}(R_2)$$

The full set of spin amplitudes used in this analysis along with particle orderings is given in appendix A.1.

2.4.3 Barrier factors, B_L

A form factor or barrier factor is assigned to each decaying particle and takes the form given by Blatt and Weisskopf [47]. These factors depend on the break-up momenta of the decay products as well as the impact parameter d (or meson radius) which is taken as 5 GeV^{-1} for the D meson and 1.5 GeV^{-1} for all other particles. The barrier factors for resonances with relative angular momentum L between decay products are given by

$$\begin{aligned} B_L(q)(L=0) &= 1 \\ B_L(q)(L=1) &= \sqrt{\frac{1}{1+(qd)^2}} \\ B_L(q)(L=2) &= \sqrt{\frac{1}{9+3(qd)^2+(qd)^4}} \end{aligned} \tag{2.11}$$

2.5 Amplitude construction

The full amplitude A_D in equation 2.1 for $D^0 \to K^+K^-\pi^+\pi^-$ decays can be expressed as $A_{D^0}(p) = |A_{D^0}(p)|e^{i\delta_D(p)}$ where $\delta_D(p)$ describes the phase motion over the D decay phasespace. $A_{D^0}(p)$ is the coherent sum over all intermediate state amplitudes, $A_i(p)$, also known as isobars. The amplitudes $A_i(p)$ are weighted by complex factors, $a_i = |a_i|e^{i\phi}$, describing their relative contribution to the decay, as shown,

$$A_{D^0}(p) = \sum_i a_i A_i(p) \tag{2.12}$$

The complex factors, a_i, are determined from a fit to data where for one isobar (the *anchor* isobar) $a = 1$ and all other a_i are determined relative to this. The *CP* conjugate amplitude to $A_i(p)$, $\bar{A}_i(p)$, is given by

$$\bar{A}_i(p) = A_i(\bar{p})$$

where $\bar{p}$ is the *CP* transformed phasespace point p, obtained by swapping particle charges and reversing 3-momenta. For the total amplitude of the $\bar{D^0}$ decay

$$A_{\bar{D}^0}(p) = \sum_i \bar{a}_i \bar{A}_i(p) = \sum_i \bar{a}_i A_i(\bar{p}).$$

Unless stated otherwise, we assume that there is no *CP*-violation in the D^0 decay such that $\bar{a}_i = a_i$ and so

$$A_{\bar{D}^0}(p) = \sum_i a_i A_i(\bar{p}).$$

2.6 Fit fractions and interference fractions

The real and imaginary parts (or magnitude and phase) of the complex coefficients, a_i, are difficult to interpret in terms of physically meaningful parameters. They are dependent on the parameterisation/formalism used for the amplitude model and are only relative to all other a_i parameters. To provide insightful and meaningful quantities, fit fractions and interference fractions are constructed. The fit fraction of an amplitude component is defined as

$$F_i \equiv \frac{\int |a_i\, A_i(p)|^2\ R_4(p)\mathrm{d}p}{\int |A_{D^0}(p)|^2\ R_4(p)\mathrm{d}p}, \tag{2.13}$$

and can be interpreted as the branching fraction of amplitude i if no interference effects between amplitude components are considered. The interference fraction is given by

$$I_{ij} \equiv \frac{\int 2\,\Re[a_i a_j^*\, A_i(p) A_j^*(p)]\ R_4(p)\mathrm{d}p}{\int |A_{D^0}(p)|^2\ R_4(p)\mathrm{d}p}, \tag{2.14}$$

which measures the interference between amplitude components i and j and can take positive (constructive interference) or negative (destructive interference) values. Because of interference effects the fit fractions of an amplitude model will not necessarily sum to unity. However it can be seen that

$$\sum_i F_i + \sum_{j<k} I_{j,k} = 1$$

must hold.

2.7 MINT package

The analyses in this thesis use the Minuit INTerface package known as MINT [3]. MINT is a 3- and 4-body decay event generator and amplitude model fitter. This section will explain how MINT normalises PDFs and generates events for a 4-body amplitude model given the complexities detailed in section 2.3.

2.7.1 Normalising PDFs: Monte Carlo Integration

Monte Carlo integration exploits the fact that the integral of a function $f(x)$ in the region $x_1 < x < x_2$ can be expressed as the average of the integrand

$$I = \int_{x_1}^{x_2} dx f(x) = (x_2 - x_1)\langle f(x)\rangle \approx (x_2 - x_1)\frac{1}{N}\sum_{i=1}^{N} f(x_i) \tag{2.15}$$

where x_i are N points distributed randomly in the region $x_1 < x < x_2$ [48]. This method is governed by the Central Limit theorem with an error that scales as $\propto 1/\sqrt{N}$. The advantage of Monte Carlo integration over other numerical integration methods is that its convergence remains as $\propto 1/\sqrt{N}$ in extensions to higher dimensions d. This makes it faster than other methods for large d, for instance, the trapezium rule has an error that scales with $\propto 1/N^{2/d}$ so for $d > 4$ the Monte Carlo integration technique is more efficient. We use Monte Carlo integration for the normalisation of PDFs in the fitting routine. The normalisation term can be estimated using N Monte Carlo events as

$$\int |A(p)|^2 R_4(p) dp \approx \frac{V}{N}\sum_{i=1}^{N}\frac{|A^{fit}(p_i)|^2}{|A^{Gen}(p_i)|^2} \tag{2.16}$$

where V represents the volume of allowed phasespace, $A^{fit}(p_i)$ is the value of the amplitude at phasespace point p_i and $A^{Gen}(p_i)$ is the value of the amplitude that the MC event with phasespace point p_i was generated with. Consider now that the amplitudes in this analysis are of the form $A(p) = \sum_j a_j A_j(p)$, then the normalisation term is

$$\frac{V}{N}\sum_{i=1}^{N}\frac{1}{|A^{Gen}(p_i)|^2}|\sum_j a_j A_j(p_i)|^2 = \frac{V}{N}\sum_{i=1}^{N}\frac{1}{|A^{Gen}(p_i)|^2}\times\sum_j\sum_k\left[a_j^* a_k A_j^*(p_i)A_k(p_i)\right]$$
$$= \frac{V}{N}\sum_j\sum_k\left[a_j^* a_k \times \sum_{i=1}^{N}\frac{A_j^*(p_i)A_k(p_i)}{|A^{Gen}(p_i)|^2}\right]$$

The value of V is a constant which will affect only the scale of the likelihood distribution and not the shape. Therefore V is not required and instead we use *relative* rather than *absolute* PDF normalisations. To improve the efficiency of the normalisation, for amplitude pairs A_j and A_k the value of

$$\sum_{i=1}^{N}\frac{A_j^*(p_i)A_k(p_i)}{|A^{Gen}(p_i)|^2}$$

can be calculated on the first fit interaction and saved to be used in all subsequent fit iterations; only the complex coefficients a_i change each fit iteration.

The integration error can be reduced by sampling more phasespace points where the PDF is largest, a technique known as *importance sampling*. Considering again equation 2.15 it is clear that when $f(x)$ is a constant the approximation becomes an equality, the more constant the integrand over the integration domain the smaller the integration error for the same number of events N. More specifically suppose a function $g(x)$ such that $h(x) = f(x)/g(x)$ is approximately constant over the integration range. Then

$$\int f(x)dx = \int \frac{f(x)}{g(x)}g(x)dx = \int h(x)g(x)dx$$

and we can integrate $f(x)$ by sampling $h(x)$ using events drawn from a non-uniform distribution $g(x)$. The MC events we use are generated according to an approximate, preliminary amplitude model for $D^0 \to K^+K^-\pi^+\pi^-$ decays. Referring back to equation 2.16 this has the effect of flattening the integrand

$$f(x) = \frac{|A^{fit}(p_i)|^2}{|A^{Gen}(p_i)|^2}.$$

2.7.2 Monte Carlo Event generation

Due to the presence of peaking structures such as the narrow ϕ resonance and the effects of interference, the amplitude model for $D^0 \to K^+K^-\pi^+\pi^-$ has extreme values which deviate far from the average PDF value. Simple accept-reject methods whereby events are accepted or rejected based on whether random numbers generated between zero and the maximum PDF height are above or below the PDF curve are very inefficient for event generation. To overcome this, Monte Carlo events are generated for an approximate PDF based on the incoherent sum of simple Breit-Wigners. This approximates the peaking structure of the full coherent PDF. These events are weighted by the ratio of the full coherent amplitude model divided by the approximate incoherent amplitude model. Accept-reject methods can be used on these weighted events with far greater efficiency. This process is as follows.

It can be shown that the integral over n-body final state phasespace can be expressed in terms of integrals over two-body final state phasespaces such as $\Phi_2(M_A^2; m_B^2, m_C^2)$ which is the integral over the final state phasespace for the decay $A \to BC$ [1]. For cascade decays

$$\Phi_4 = \int \Phi_2(M_D^2; s_{234}, m_1^2)\Phi_2(s_{234}; s_{34}, m_2^2)\Phi_2(s_{34}; m_3^2, m_4^2) ds_{234} ds_{34}$$

and for all other decays

$$\Phi_4 = \int \Phi_2(M_D^2; s_{12}, s_{34})\Phi_2(s_{12}; m_1^2, m_2^2)\Phi_2(s_{34}; m_3^2, m_4^2) ds_{12} ds_{34}.$$

Therefore referring back to left-hand side of equation 2.16 we can write the probability for an event with invariant mass squared values between (s_{12}, s_{34}) and $(s_{12}+ds_{12}, s_{34}+ds_{34})$ as proportional to

$$|A(s_{12}, s_{34})|^2 ds_{12} ds_{34} \Phi_2(M_D^2; s_{12}, s_{34})\Phi_2(s_{12}; m_1^2, m_2^2)\Phi_2(s_{34}; m_3^2, m_4^2). \tag{2.17}$$

Consider the decay of a resonance with mass M and decay width Γ where the amplitude squared $|A|^2$ can be approximated by a Breit-Wigner PDF

$$BW(s)ds = \frac{k}{M^2\Gamma^2 + (s - M^2)^2} ds.$$

Using the co-ordinate transformation $s \to \rho$,

$$s = M\Gamma \tan \rho + M^2$$

which has the Jacobian

$$J = \left| \frac{\partial s}{\partial \rho} \right| = M\Gamma \mathrm{sec}^2 \rho$$

the Breit Wigner can be expressed in terms of the new co-ordinate ρ as

$$BW(s)ds \to \frac{kM\Gamma \mathrm{sec}^2 \rho}{M^2\Gamma^2 \tan^2 \rho + M^2\Gamma^2} d\rho = \frac{k}{M\Gamma} d\rho.$$

The probability 2.17 can now be expressed as

$$\frac{1}{M\Gamma} d\rho_{12} d\rho_{34} \Phi_2(M_D^2; s_{12}, s_{34}) \Phi_2(s_{12}; m_1^2, m_2^2) \Phi_2(s_{34}; m_3^2, m_4^2).$$

In order to generate events according to 2.17 then, ρ values ρ_{12} and $d\rho_{34}$ are randomly and uniformly selected from the region $-\pi/2 < \rho < \pi/2$, the corresponding distribution of s_{ij} values follow a Breit-Wigner distribution. These events are then multiplied by a factor $1/M\Gamma$ and by the product of 2-body phasespace terms $\Phi_2(M_D^2; s_{12}, s_{34}) \Phi_2(s_{12}; m_1^2, m_2^2) \Phi_2(s_{34}; m_3^2, m_4^2)$. The final state particles' momenta for each of the two-body decays in the chain can then be generated. This of course only accounts for one intermediate state, in fact we sum over the contributions from all resonances for each choice of ρ values and use this value to weight the event. The events are then reweighted by the value of the full coherent PDF divided by this approximate incoherent PDF value and the accept-reject method can be applied on these weights with far greater efficiency. A component that is flat in phasespace is also generated to ensure there are events present in all regions across the phasespace.

Chapter 3

Particle detectors

The analyses presented in this thesis use data collected by two different particle detectors; CLEO and LHCb. Particle detectors measure the kinematic properties of particles through their interaction with the detector material i.e. their energy loss in the material. Incident particles lose energy when traversing material via several mechanisms detailed below which particle detectors exploit. The lost energy must be measurable through either the production of photons or induced electrical signals.

3.1 Energy loss in particle detectors

Ionisation/excitation

Charged particles lose energy through electromagnetic interactions with the atomic electrons of the detector material, this results in either excitation or ionisation of the atoms. Energy losses per interaction are small with 90% less than 100 eV. The mean energy loss per unit length, $\langle dE/dx \rangle$, for heavy, charged particles of mass M[1] and $0.1 \lesssim \beta\gamma \lesssim 1000$, traversing materials with intermediate atomic number Z, is well-described by the Bethe-Bloch formula [23]

[1] $M \gg m_e$ where m_e is the mass of the electron

$$-\left\langle \frac{dE}{dx} \right\rangle = Kz^2 \frac{Z}{A} \frac{1}{\beta^2} \left(\frac{1}{2} \ln \frac{2m_e c^2 \beta^2 \gamma^2 T_{max}}{I^2} - \beta^2 - \frac{\delta(\beta\gamma)}{2} \right) \tag{3.1}$$

Parameter A is the atomic mass and I the mean excitation energy of the detector material, K is a constant related to electron properties and $\delta(\beta\gamma)$ is a density correction factor depending only on β. T_{max} is the maximum kinetic energy the traversing particle can transfer to a free electron in a single collision, it has a dependence on M that only becomes significant at very high energies. Figure 3.1 shows $-\langle dE/dx \rangle$ for positive muons traversing copper as a function of $\beta\gamma$ and the Bethe-Bloch region ($0.1 \lesssim \beta\gamma \lesssim 1000$) where the formula applies. The value of $\langle dE/dx \rangle$ is independent of the incident particle's mass in this region and depends only on the velocity v of the particle. This can be used for the identification of charged hadrons; a determination of v along with a momentum measurement allows the mass of the particle to be found from

$$M = p\sqrt{\frac{1}{v^2} - \frac{1}{c^2}}.$$

Pair production

Pair production is the dominant interaction of high energy photons in matter. In the presence of a nucleus (to conserve momentum) the energy of a high energy photon can convert to an electron-positron pair.

Strong interactions

Charged and neutral hadrons interact inelastically with the nuclei of the detector material via the strong interaction, producing showers of secondary particles through multiple interactions. These nuclear interactions can be used to identify hadrons.

Bremsstrahlung

The Bethe-Bloch equation (equation 3.1) does not describe the energy loss of electrons in matter, electrons lose significant energy due to bremsstrahlung (breaking radiation).

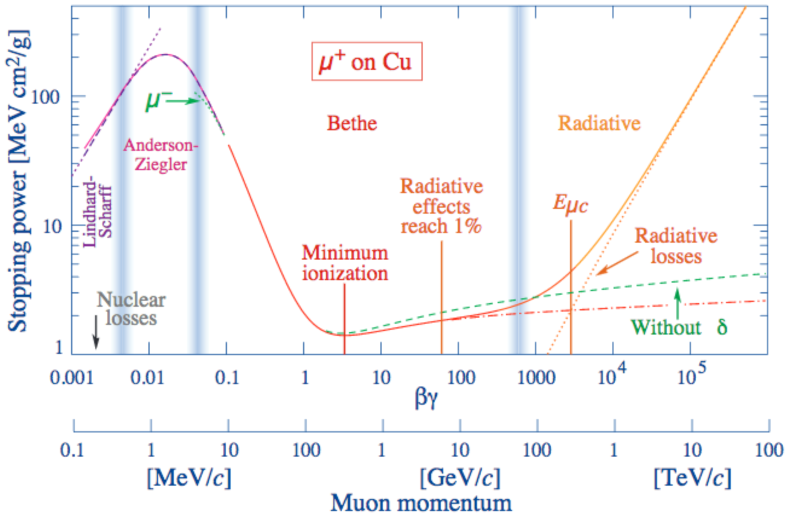

Figure 3.1: Mean energy loss per unit length, $-\langle dE/dx \rangle$, for positive muons in copper as a function of $\beta\gamma$. The Bethe-Bloch region is indicated. Taken from reference [23].

All high energy charged particles undergo bremsstrahlung; the radiation of photons due to deceleration in the electromagnetic field of a nucleus. The rate of energy loss depends on the atomic mass and number of the detector material and has a $1/M^4$ dependence meaning less massive incident particles such as electrons suffer Bremsstrahlung at a greater level.

Cherenkov radiation

Exploited by the RICH detectors of CLEO III, CLEO-c and LHCb for particle identification purposes is the effect of Cherenkov radiation. Charged particles traversing a medium of refractive index, n, with velocity $v > c/n$ emit a cone of photons centred around the particle's trajectory with opening angle θ_c. This angle is related to the particle's velocity (v) by

$$\cos(\theta_c) = \frac{c}{nv} \tag{3.2}$$

The associated energy loss is small and although the effect occurs in all materials, only some are transparent to the Cherenkov light produced.

Multiple Coulomb Scattering

Multiple Coulomb scattering is the many, small angle deflections/scatters of an incident charged particle by the electric field of nuclei in the detector material. Although the energy transfer is small due to the mass difference between the nuclei and the incident particle, each scatter adds a small deviation to the particle's trajectory, the cumulative effect being a smearing of the particle's momentum direction. This effect is larger for thicker materials and those of higher atomic number, Z. Multiple coulomb scattering ultimately limits the precision with which the momentum of a particle can be determined. Particle detectors therefore have to limit the material in the detector acceptance for tracking and particle identification (PID) purposes. The amount of material in the path of incident particles is known as the material budget and is quantified in units of radiation length and nuclear interaction length.

Radiation length and nuclear interaction length

Materials can be described by their ability to attenuate the energy of incident particles. The radiation length, X_0, is the length of a material required to reduce the mean energy of incident electrons to $1/e^{th}$ (37%) of its initial value through radiation losses. It is also equal to 7/9 of the mean free path for pair production by a high energy photon. The nuclear interaction length, λ_i, is the thickness of material at which a hadron has a $1/e^{th}$ probability of not having had a nuclear interaction and so is a measure of the probability that a hadron is absorbed by a material.

Calorimeters are designed to absorb all the energy of incident particles (full containment of particle showers) so a measurement of the incident particle's energy can be made. Electromagnetic calorimeters measure the energy of incident particles that interact primarily through electromagnetic interactions and so consist of many radiation lengths. Hadronic calorimeters measure the energy of incident particles that interact primarily via strong interactions and so consist of many nuclear interaction lengths. Prior to these subdetectors the amount of material, measured in both radiation lengths and nuclear interaction lengths, should be minimised.

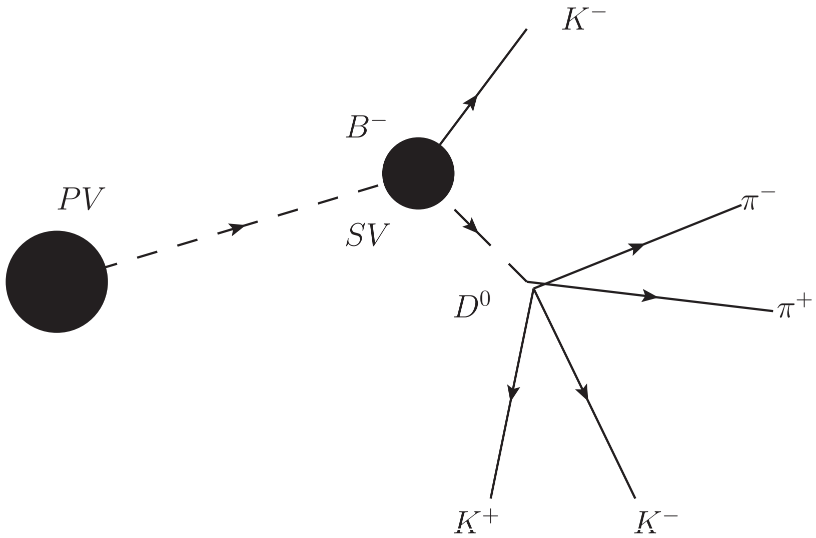

Figure 3.2: A schematic of the $B^\pm \to D(\to K^+K^-\pi^+\pi^-)K^\pm$ decay at LHCb showing the primary vertex (PV) of the $p-p$ collision, and the secondary vertices (SV) of the B and D decays.

3.2 Reconstructing D and B decays

Decays of D and B particles have distinctive features upon which one can select events. Precise reconstruction of decay vertices is essential. The primary vertex (PV) is the position of the particle collision. At LHCb reconstructed vertices of D and B candidates are significantly displaced from the PV [49] due to their long lifetime; they typically travel 1 cm in the detector before decaying and so their decay vertices are spatially displaced from the PV (known as a secondary vertices). A schematic of the $B^\pm \to D(\to K^+K^-\pi^+\pi^-)K^\pm$ decay at LHCb can be seen in figure 3.2 showing the primary vertex of the $p-p$ collision, and the secondary vertices (SV) of the B and D decays. It is useful to introduce some of the variables used to select B and D decays and although many of these are presented in regard to $B^\pm \to D(\to K^+K^-\pi^+\pi^-)K^\pm$ decays they are also relevant for selecting $D^0 \to K^+K^-\pi^+\pi^-$ decays.

Impact Parameter (IP)

The impact parameter (IP) of a track is found by extrapolating the track back towards the PV and determining the distance of closest approach of the track to the PV. This parameter is shown in figure 3.3. The χ^2_{IP} of a track is defined as the difference between

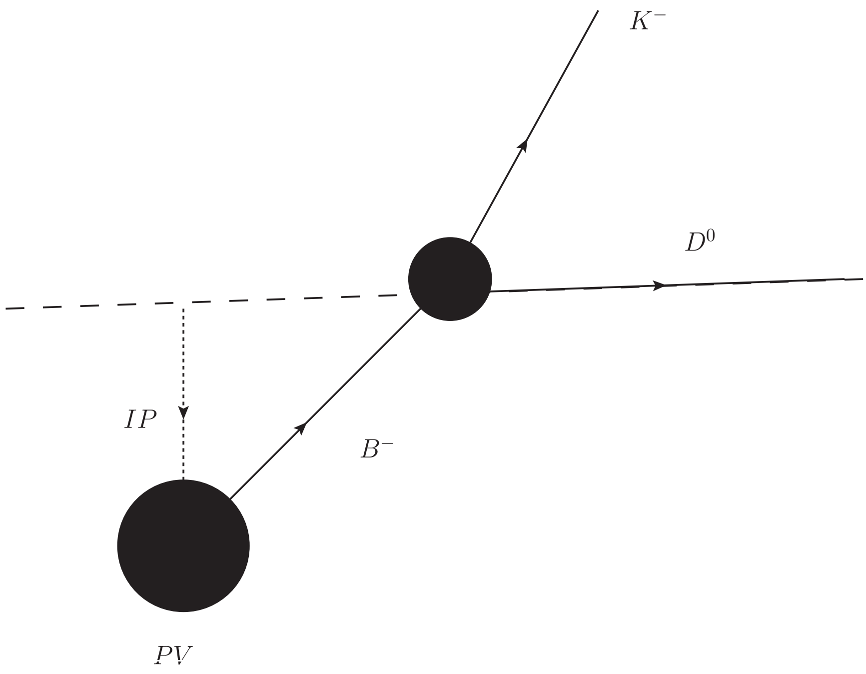

Figure 3.3: A schematic of the IP parameter for the D track in a $B^\pm \to D(\to K^+K^-\pi^+\pi^-)K^\pm$ decay.

the χ^2 goodness-of-fit measure for the PV reconstructed with and without the track of interest. A track with small IP and χ^2_{IP} values is likely to have originated from the PV and so these parameters can be used to select B decays and prompt D decays [50]. On the other hand, a large IP with respect to the associated PV for the D meson in $B^\pm \to D(\to K^+K^-\pi^+\pi^-)K^\pm$ is required in order to suppress prompt charm decays. Generally, the products of heavy flavour decays have a large impact parameter with respect to the PV so this parameter can also be used to select the daughter particles [51].

DIRA

DIRA is defined as the cosine of the angle, θ, between a particle's momentum vector (as defined by its decay products) and a vector from the primary vertex to the particle's origin vertex. This parameter is particularly useful to select particles with displaced vertices such as the B and D. Figure 3.4 shows the DIRA angle.

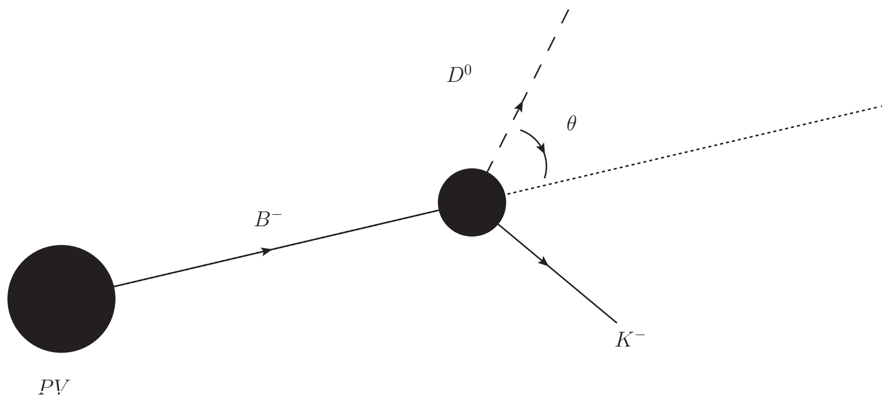

Figure 3.4: A schematic of the DIRA parameter for the D track in a $B^{\pm} \to D(\to K^+K^-\pi^+\pi^-)K^{\pm}$ decay.

Flight distance χ^2 and D flight distance significance

The flight distance, FD, of a particle is the distance between its production vertex and its decay vertex. The flight distance χ^2, χ^2_{FD}, is this distance squared divided by its uncertainty squared; the uncertainty arises from the determination of the positions of the vertices,

$$\chi^2_{FD} = \frac{FD^2}{\sigma^2_{FD}}.$$

Closely related to this but only applicable for the selection of $B^{\pm} \to D(\to K^+K^-\pi^+\pi^-)K^{\pm}$ decays is the D flight distance significance, FD_{sig}. This is defined as the difference between the z positions of the D vertex and the B vertex divided by the uncertainties on these positions added in quadrature

$$FD_{sig} = \frac{z^{\text{D vtx}} - z^{\text{B vtx}}}{\sqrt{\sigma^2_{\text{D vtx}} + \sigma^2_{\text{B vtx}}}}.$$

This parameter is used to suppress charmless background in the selection of $B^{\pm} \to D(\to K^+K^-\pi^+\pi^-)K^{\pm}$ decays. Charmless backgrounds have the same final state as the signal decay but do not decay via a D particle. A high value of FD_{sig} indicates that a decay is less likely to be charmless.

p_T asymmetry

The p_T asymmetry isolation variable, as its name suggests, considers how isolated a particle is within a cone of 1.5 radians constructed around its decay vertex. The difference divided by the sum of the p_T of the B candidate, Bp_T, and the vector sum of p_T values for charged tracks not involved in the signal decay, $\sum \mathbf{p}_T$ is found,

$$\frac{Bp_T - (\sum \mathbf{p}_T)}{Bp_T + (\sum \mathbf{p}_T)}.$$

The B p_T asymmetry isolation variable can select vertices with a higher chance of correct reconstruction. A value closer to 1 means less charged spectator tracks and so a vertex is less likely to be misreconstructed [52].

There are broadly three stages to the selection of B and D decays of interest, each more effective but crucially more time-consuming than the last. The crudest, but most importantly, fastest selection criteria for a B or D decay is the presence of tracks with a high transverse momentum. Particles resulting from a B or D decay tend to have higher transverse momentum than those resulting directly from the PV due to their large mass. Calorimeter information can be used to select particles with high transverse momentum and can be read out from the detector extremely quickly with a latency (the time between the particle collision and the readout) in the order of microseconds. The next selection criteria for B and D decays is the presence of tracks with significant IP with respect to the PV which is indicative of displaced vertices. For this the whole of the detector readout is required to reconstruct tracks through the detector. Finally the most complex form of selection is based on the full reconstruction of primary and secondary vertices. It will be explained how the LHCb trigger utilises these three stages of selection in section 3.4.2.

The rest of this section will describe the CLEO and LHCb detectors in more detail and the accelerators used for particle collisions.

3.3 The CLEO Detector

The amplitude analysis of $D^0 \to K^+K^-\pi^+\pi^-$ decays uses data collected by the CLEO detector. The CLEO detector was stationed at the Cornell Electron Storage Ring (CESR), a 768m circumference symmetric e^+ - e^- collider located at Cornell University, USA. CLEO collected data from these collisions between 1979 and 2008 at centre of mass energies ranging from 3.5–12.0 GeV [53]. The detector was originally designed for the study of the Υ (Upsilon) system (bound states of a b and $\bar{b}$ quark) and for precision measurements of B mesons, this required collision energies in the region of 10 GeV [54]. In its later stages (CLEO-c), focus turned to the study of charm mesons requiring lower collision energies at or slightly above the charm production threshold, 3.77 GeV, with a luminosity of 1–5$\times 10^{32}$ cm^{-2}s^{-1}. During this time the detector underwent several major upgrades. Relevant to this analysis are the CLEO II.V (1995), CLEO III (1999) and CLEO-c (2003) incarnations of the CLEO detector.

3.3.1 Cornell Electron Storage Ring (CESR)

The Cornell Electron Storage Ring (CESR) (which is still in commission) is based at the University of Cornell, USA, providing symmetric e^+ - e^- collisions. Electrons are produced by an electron gun - a heated cathode that creates an electron stream via thermionic emission. Upon production, electrons are formed into bunches and accelerated down a 30m long vacuum pipe by an electric field, this is know as the linear accelerator or Linac. At an intermediate point along the Linac, at energies of ≈140 MeV, some of these electrons are deflected to strike a tungsten plate, producing a shower of electrons, positrons and X-rays from which positrons can be extracted, focused and also accelerated down the Linac. The Linac produces electrons with energies up to 300 MeV and positrons with energies 150-200 MeV. Electron and positron bunches are then injected into the synchrotron which provides further acceleration via 4 superconducting radio frequency (RF) cavities to 5 GeV. Dipole magnets keep the particle bunches rotating around the synchrotron, clockwise for positrons, counter-clockwise for electrons. Once the desired collision energies are reached the bunches are deflected via transfer

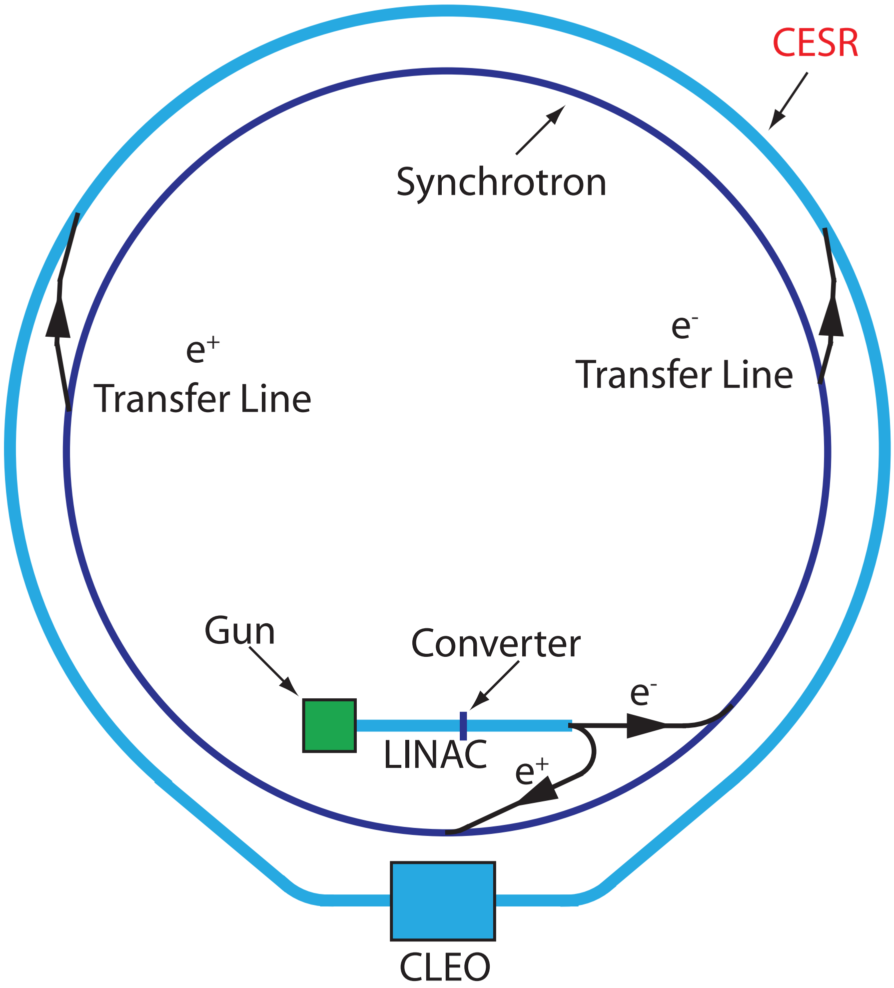

Figure 3.5: Cornell Electron Storage Ring (CESR) complex. Taken from reference [55].

lines into the storage ring (CESR) which encompasses the accelerators. This forms two counter rotating beams, one of electrons and one of positrons, which can be held in the storage ring for several hours. The energy lost via synchrotron radiation is restored by RF cavities and the beams are focused by quadrupole and sextuple magnets. These three main components can be seen in the diagram in figure 3.5.

3.3.2 CLEO

While the CLEO detector underwent several major upgrades, many systems are common to all incarnations. Closest to the interaction point is the tracking systems consisting of a silicon vertex locator (ZD detector) and drift chamber for CLEO II.V and CLEO III (CLEO-c). Following this is the particle identification system: a RICH detector (Time of Flight detector) used in conjunction with dE/dx information from the drift chambers for CLEO III onwards (CLEO II.V). Surrounding the tracking and PID systems is the superconducting solenoid magnet and finally, furthest away from the collision point, the muon chambers. These detector components are described further in the following, a schematic of the CLEO III detector can be see in figure 3.6.

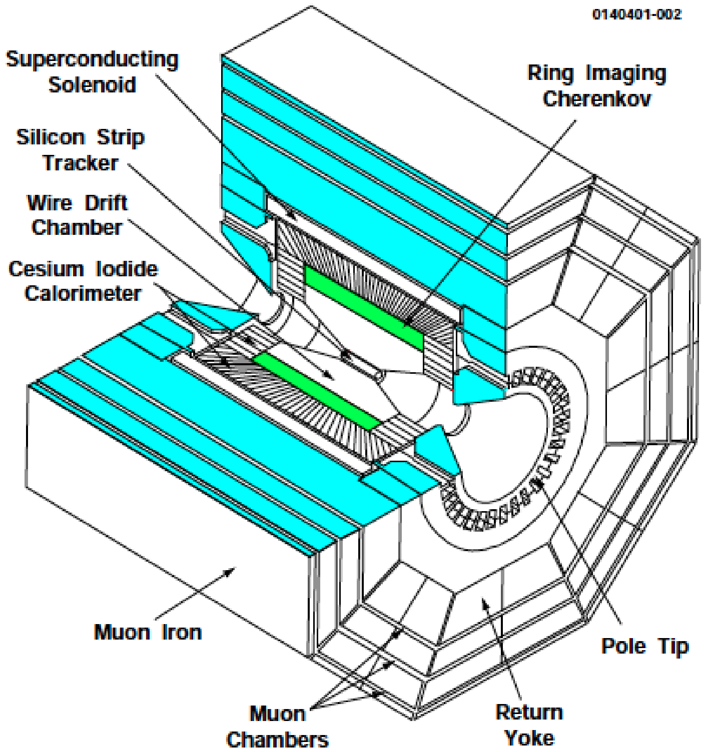

Figure 3.6: Schematic of the CLEO III detector. Taken from reference [53].

Superconducting coil

A 3.5 m superconducting coil provides a magnetic field that runs parallel to the beamline. The radius of curvature, r, of a charged particle track (charge z) caused by the bending power of the magnet, B, is related to its momentum, p, by

$$r[\mathrm{m}] = \frac{p[\mathrm{GeV/c}]\sin\theta}{0.3zB[\mathrm{T}]}$$

where θ is the angle between the particle's velocity vector and the beamline. Charged particle tracks where $\theta \neq 0$ are helical.

The magnetic field was 1.5 T for CLEO II.V and CLEO III. For CLEO-c, lower energy collisions result in particles with a lower average momentum which experience a higher degree of track bending. These particles may only traverse a small region of the drift chamber before curling back on themselves towards the interaction point. For low momentum particles to penetrate far enough into the drift chambers to allow reconstruction, and then escape the drift chambers for particle identification, the strength of the magnetic field was reduced to 1.0 T for CLEO-c.

Tracking System

The tracking system for CLEO II.V and CLEO III consists of the silicon vertex detector and the drift chamber.

The silicon vertex detector provides $r-\phi$ and z track position measurements for charged particles close to the interaction point, where r is the perpendicular distance from the beam line, ϕ is the azimuthal angle relative to the vertical and z is the distance along the beam line from the interaction point. It consists of concentric detection layers (three layers for CLEO II.V and four thereafter) centred around the beamline and made up of 5.0 cm$\times$ 2.5 cm$\times$300 μm double-sided silicon strip detectors, where the strips on one side are perpendicular to the strips on the other. Each double-sided silicon strip detector has strips every 50 μm along ϕ on one side (the side facing away from the centre) to measure $r - \phi$ and every 100 μm along z on the reverse to measure $r - z$. The layers occupy the region 25 mm to 110 mm radially from the collision point. As seen in figure 3.7 the layers have increasingly more silicon strip detectors in ϕ and z where, in the case of the CLEO III detector, the layer closest to the interaction point has 7 detectors in ϕ and 3 in z. It covers 93% of the solid angle [56] and is essential for vertex reconstruction. The resolution is < 11 μm in $r - \phi$ and < 24 μm in z.

The principle of all drift chambers is that, when traversing an enclosed gas, charged particles cause the ionisation of the gas atoms, liberating electrons. An electric field

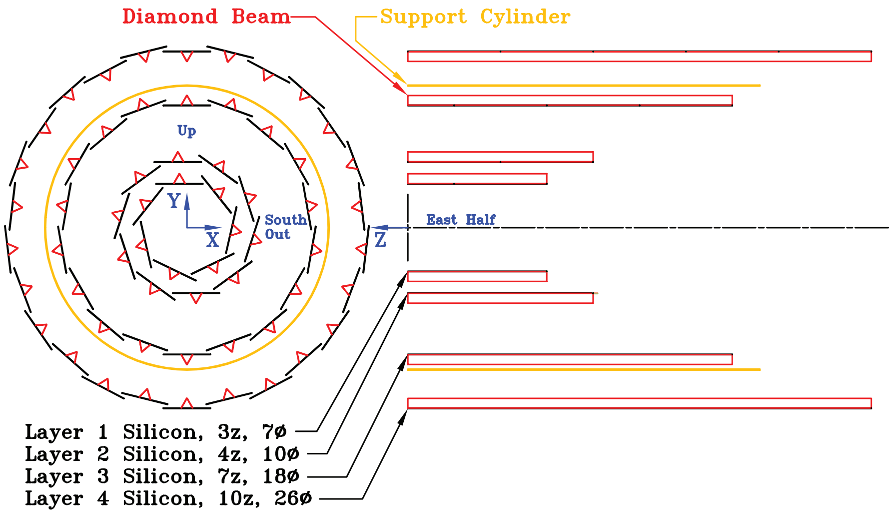

Figure 3.7: CLEO III silicon vertex detector, end-view and side-view. Taken from reference [57].

created by a potential difference between an anode and cathode attracts the electrons to the anode. Close to the anode the electric field is sufficiently strong that the electrons ionise more atoms, creating more free electrons, (an electron avalanche) causing a pulse of current in the anode. The timing of this pulse combined with the timing of a collision allows a measurement of the distance of closest approach of a charged particle to a particular anode. Current information from all anodes builds the trajectory of the charged particle through the drift chamber.

The drift chamber spans the radial region $132 < r < 790$ mm from the beamline, providing charged particle track measurements in $r - \phi$ and z essential for measurements of momentum. The drift chamber contains a 3:2 ratio of helium and propane gas selected for its long radiation length and is divided into 9796 cells. Each cell consists of a central gold-plated tungsten anode sense wire surrounded by 8 gold-plated aluminium field wires running parallel to the beam arranged in a square formation 14mm across. Between the sense wire and the field wires a 2.1kV potential difference is applied. There is an initial radial region comprising 16 layers of axial cells which runs exactly parallel to the beamline. This is followed by a region of 31 layers of stereo cells that provides information about the z position of tracks. Here, the ring of wires at one end of the drift chamber is twisted relative to the ring at the other end creating a small offset angle relative to the beamline. The offset is approximately 25mrad in ϕ and each 4 layers the offset alternates between clockwise/anti-clockwise. The outer wall of the drift chamber is lined with cathode strips such that a final position measurement can be made [58].The drift chamber of CLEO III has a position resolution of 85 μm and momentum resolution of 40 MeV for particles with p >5.3 GeV.

Pertinent to this analysis is the ability to measure the slow pion in the decay $D^{*+} \rightarrow D^0\pi_s^+$. The excellent spatial resolution of the silicon vertex detector allows for the $D^{*+} - D^0$ mass difference (a key selection parameter in the analysis to follow) to have a resolution of 0.19 MeV.

ZD detector

For CLEO-c the silicon vertex detector was replaced by a smaller inner drift chamber called the ZD detector to provide position information for charged particles close to the interaction point. The silicon vertex detector experienced an unexpected, non-uniform loss in efficiency, the upgrade to the ZD detector also allows a reduction in material within the detector. The silicon vertex detector contributes approximately 1.6% of a radiation length (X_0) between the beampipe and the drift chamber, while the ZD detector contributes approximately 1.2%. The replacing of the silicon vertex detector with the ZD provides almost equivalent momentum resolution due to a reduction in the material budget with $\Delta p/p = 0.6\%$ for charged particles at 1 GeV [59]. The ZD detector uses the same gas mixture as the drift chamber and is located in the radial region $41.0 < r < 117.0$mm from the beamline. It comprises six layers of a total of 300 anode wires surrounded by field wires with cells configured as described for the drift chamber. It should be noted that at the energies of CLEO-c D particles are produced almost at rest. The resulting flight distances are smaller than even silicon trackers are capable of measuring and so vertexing through very precise position resolution is not an important feature of the ZD detector.

Particle Identification

Particle identification is provided by the drift chamber as well as dedicated PID subsystems.

PID using tracking system

As explained in section 3.1, for particle energies of those seen in CLEO, dE/dx depends only on the value of β for the particle.

The drift chamber provides a measurement of dE/dx from the relative strength of the electrical signals from the sense wires along the particle's trajectory. Figure 3.8 shows a plot of momentum against dE/dx for pion, kaon and proton tracks measured in CLEO III. Particularly relevant to this analysis is the ability to distinguish pions from kaons. It can be seen that below 700MeV this is possible using information from only the tracking system. For each particle a metric is formed based on the number of standard deviations the dE/dx measurement lies from that expected from a pion or kaon, σ,

$$\Delta\chi^2_{dE/dx} = \sigma_K^2 - \sigma_\pi^2.$$

Particles with $\Delta\chi^2_{dE/dx} < 0$ are more likely to be kaons than pions and vice versa.

Ring Imaging CHerenkov (RICH) detector

For CLEO III a Ring Imaging CHerenkov (RICH) detector was installed for increased PID performance, particularly between kaons and pions, covering 83% of the solid angle. The velocity of a charged particle can be determined from the opening angle of the ring of Cherenkov photons it radiates and the mass (identity) of a particle can be inferred. A likelihood ($\mathcal{L}$) can be constructed for each particle hypothesis from the photons which lie within 5 standard deviations of the expected ring size for that hypothesis. For reliable identification it is also required that at least three photons lie within three standard

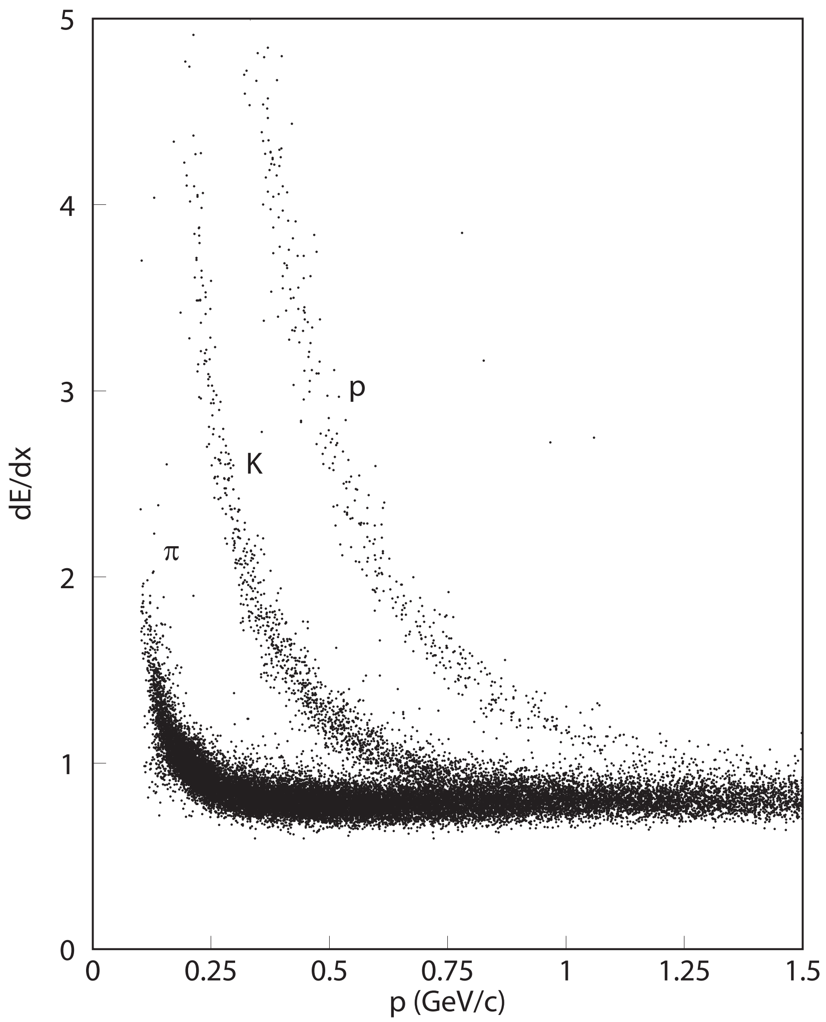

Figure 3.8: Values of dE/dx as a function of momentum for pions, kaons and protons in the CLEO III detector. Taken from reference [53].

deviations of the expected ring size. The likelihood difference is found

$$\Delta\chi^2_{RICH} = -2\ln(\mathcal{L}_K) - (-2\ln(\mathcal{L}_\pi))$$

such that kaons are expected to take negative $\Delta\chi^2_{RICH}$ values [60].

The subdetector is located between the drift chambers and the calorimeter; therefore the detector is restricted to being only 20 cm in radial thickness and 2.5m in length, as well as having a small material budget. The radiator chosen is a 17 mm thick layer of low density solid lithium fluoride crystals (LiF) (n=1.5), transparent to much of the Cherenkov light produced. The ring of Cherenkov photons then traverses a 16 cm thick volume of nitrogen gas, known as the expansion gap, within which the ring expands allowing for better resolution of opening angles. For particles with near normal track incidence, total internal reflection occurs at the boundary between the radiator and the expansion gap. For this reason a small region of the boundary around the interaction point (θ close to 90 degrees) has a sawtooth shape ensuring that the photons arrive at an angle to the interface. Beyond the expansion gap are multi-wire proportional chambers filled with a methane-triethylamine gas mixture. Cherenkov photons convert to electrons via the photo-electric effect. The signal is amplified by the avalanche mechanism described above and the position of the photon conversion is determined via the induced charge on an array of cathode pads. It is this array on which the image of the photon ring is built. The configuration, including the saw-tooth shape of the interface between the radiator and the expansion gap can be seen in figure 3.9

The momentum ranges for which the dE/dx and RICH PID systems are effective are complementary. Figure 3.10 shows the $\Delta\chi^2_{dE/dx}$ distributions from the tracking system and $\Delta\chi^2_{RICH}$ distributions from the RICH for simulated kaons as a function of momentum. This shows that dE/dx information performs at lower momentum values and the RICH at higher momentum values. Information from both systems can be combined into a single metric

$$\Delta\chi^2 = -2\ln(\mathcal{L}_K) - (-2\ln(\mathcal{L}_\pi)) + \sigma_K^2 - \sigma_\pi^2.$$

The RICH is capable of identifying kaons with a 92% success rate for tracks with momentum between 0.7 and 2.7 GeV. CLEO II.V has no RICH system and instead has a Time Of Flight (TOF) detector (using thick bars of Bicron scintillator) immediately after the drift chamber able to measure the time of flight to within 150ps. The particle identification capabilities of this system are significantly less than that of the RICH system.

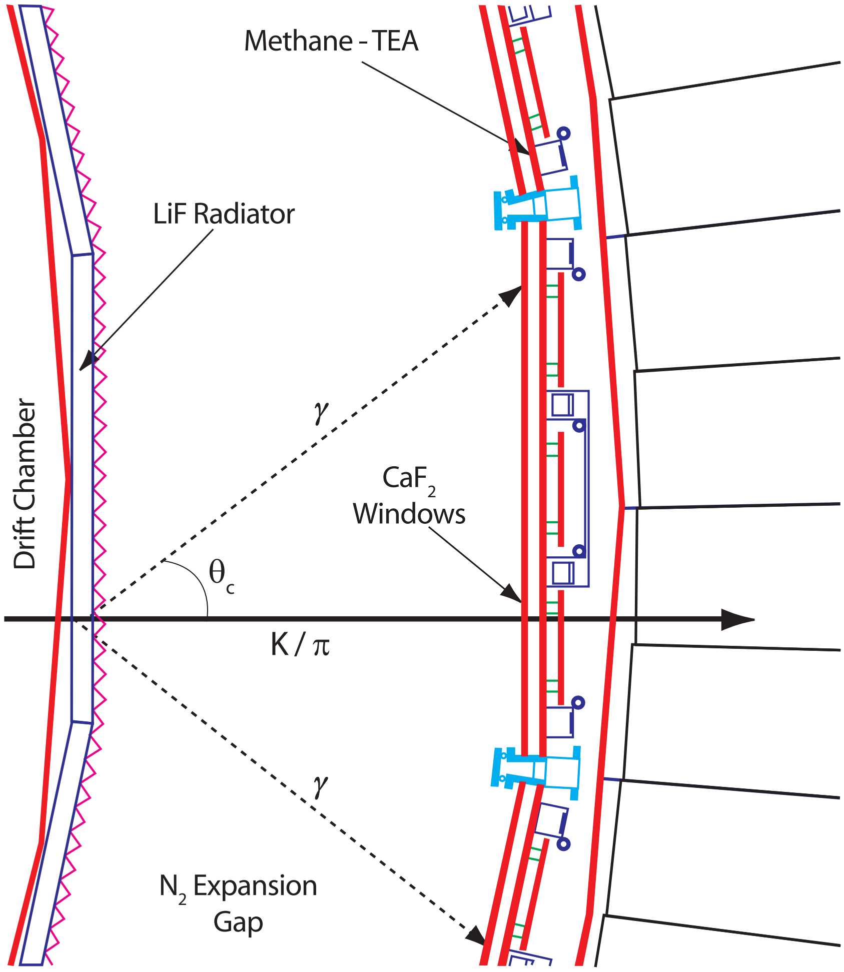

Figure 3.9: The RICH detector in CLEO III.Taken from reference [53].

Calorimeter

The CLEO calorimeter provides the primary identification for electrons and photons and is essential in the reconstruction of π^0 mesons. It covers 93% of the solid angle and is built from 7800 $5 \times 5 \times 30$ cm thallium-doped CsI scintillating crystals. Calorimeters convert the energy of incident particles into showers of particles with progressively reduced energies. The total energy of electrons and photons entering the calorimeter is absorbed and measured. High energy incident electrons mainly lose energy in the calorimeter via bremsstrahlung, producing secondary photons, and photons incident on the calorimeter produce secondary electrons and positrons via pair production. These secondary particles produce more (lower energy) particles by the same mechanisms until

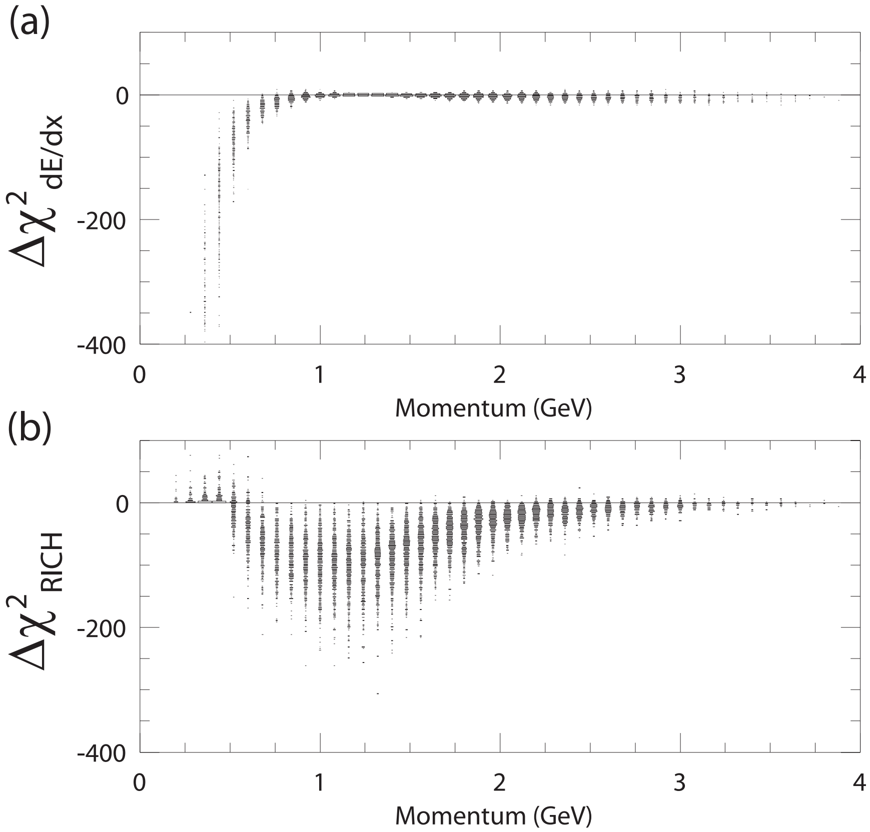

Figure 3.10: Particle identification $\Delta\chi^2_{dE/dx}$ distributions from the tracking system and $\Delta\chi^2_{RICH}$ distributions from the RICH for simulated kaons as a function of momentum. Taken from reference [57].

energies fall below a critical level. At this point the energy of the particles is absorbed by atomic electrons through ionisation and band promotion rather than particle generation. The subsequent de-excitation of atomic electrons between valance bands and conduction bands (scintillation) produces photons. In CLEO these photons are detected by silicon photo-diodes on the back of each crystal; the intensity of the signals is used to determine the total energy of the shower. Doping the CsI crystals introduces energy states between the valance and conduction bands, de-excitation via these extra energy states prevent the emitted photons being reabsorbed by atomic electrons. The calorimeter is capable of photon energy resolutions of σ_E/E=1.5% at 5 GeV, 4% at 1000 MeV and 7% at 30 MeV.

Muon tracking chambers

Muons experience minimal interaction with the detector material before the muon chambers. The muon chambers are located outside of the main detector body between layers of iron (which also act as the magnetic yoke) to stop any other type of particle from traversing the muon system. The muon detector is a straw-tube drift chamber. Similar to the drift chamber described above, it consists of three layers of anode wires each at the centre of a plastic tube (forming the cathode) filled with gas. The anode wires conduct electrical signals produced by the ionisation of the gas atoms by the incident muons. It has a 85% solid angle coverage.

Trigger, data recording and reconstruction for physics analysis

The Data AQuisition (DAQ) system writes event information from the detector to disk for analysis. Events occur at too high a rate to read out the full detector information and many events are not of interest for later analysis. The level 1 trigger is used to determine which events contain interesting physics and should be saved. Eight different trigger lines containing multiple selection requirements on tracks in the drift chamber and energy deposits in the calorimeter are used to select events of interest for different types of physics analysis without the need to fully reconstruct the event.

Events that have the full detector information saved to disk undergo full off-line reconstruction. From calibration constants determined at run time, particle tracks, PID information and short lived particles are reconstructed. From this point the data can be used for offline physics analysis.

Monte Carlo (MC) simulation data

Monte Carlo (MC) simulation data is used extensively in this analysis to determine the impact of efficiency effects, model backgrounds and establish fits to the signal data. The simulation data must describe both the particle decays and the interaction and response of the detector. The initial $e^+ - e^-$ collision and decays of subsequent particles are simulated using the EvtGen [61] (QQ [62] prior to CLEO-c) software for given beam conditions. The user is able to define the branching fractions of decays through a *decay file*.

The GEANT [63] package uses the resulting 4-momenta information to simulate the detector interactions and detector response using the same calibration information as for the real data taking. This produces data identical in format to that stored in the DAQ for real events and thus it can be run through the same reconstruction. The power of MC data is the access to the truth information for events which is stored from the output of EvtGen.

3.4 The LHC and LHCb detector

The second part of this thesis analyses data collected by the LHCb experiment from proton-proton collisions in the LHC, CERN. This section begins with a description of the LHC and then details the different components of the LHCb detector.

3.4.1 Large Hadron Collider (LHC)

The Large Hadron Collider (LHC) is a 27km circumference proton-proton collider located on the Swiss-French border approximately 100m underground. At four interaction points along the collider counter-rotating proton beams are crossed and focused for collisions, these are the locations of the four main detectors. ATLAS and CMS are the general purpose detectors that were responsible for the discovery of the Higgs boson in 2012, ALICE focuses on collisions of heavy-ions in the LHC and LHCb is designed for precision measurements of beauty and charm hadrons, which are produced in vast quantities in proton-proton collisions at the LHC.

The LHC is currently the world's most powerful particle accelerator designed to collide protons with a collision energy of $\sqrt{s} = 14$ TeV. The collider uses 1232 superconducting dipole magnets cooled using liquid helium to keep protons circulating in the LHC ring. The dipole magnets house two beampipes, subject to opposite magnetic fields creating the two counter-rotating beams of protons.

The acceleration process begins (as it does in CESR) in a linear accelerator known as LINAC2. Bunches of protons (hydrogen ions) are accelerated to 50 MeV where they enter a series of synchrotrons; the Proton Synchrotron Booster (PSB) where protons reach 1.4 GeV, the Proton Synchrotron (PS) where protons reach 25 GeV and the Super Proton Synchrotron which is the last accelerator before they enter the LHC at 450 GeV. Proton bunches are injected into the LHC's two beampipes and accelerated up to collision energy by eight radio frequency cavities. The bunches in the beampipes are focussed by superconducting quadrupole magnets and made to cross at the interaction points creating $p - p$ collisions. The design center-of-mass collision energy for the LHC is $\sqrt{s} = 14$ TeV, the data used in this analysis however was collected during the Run

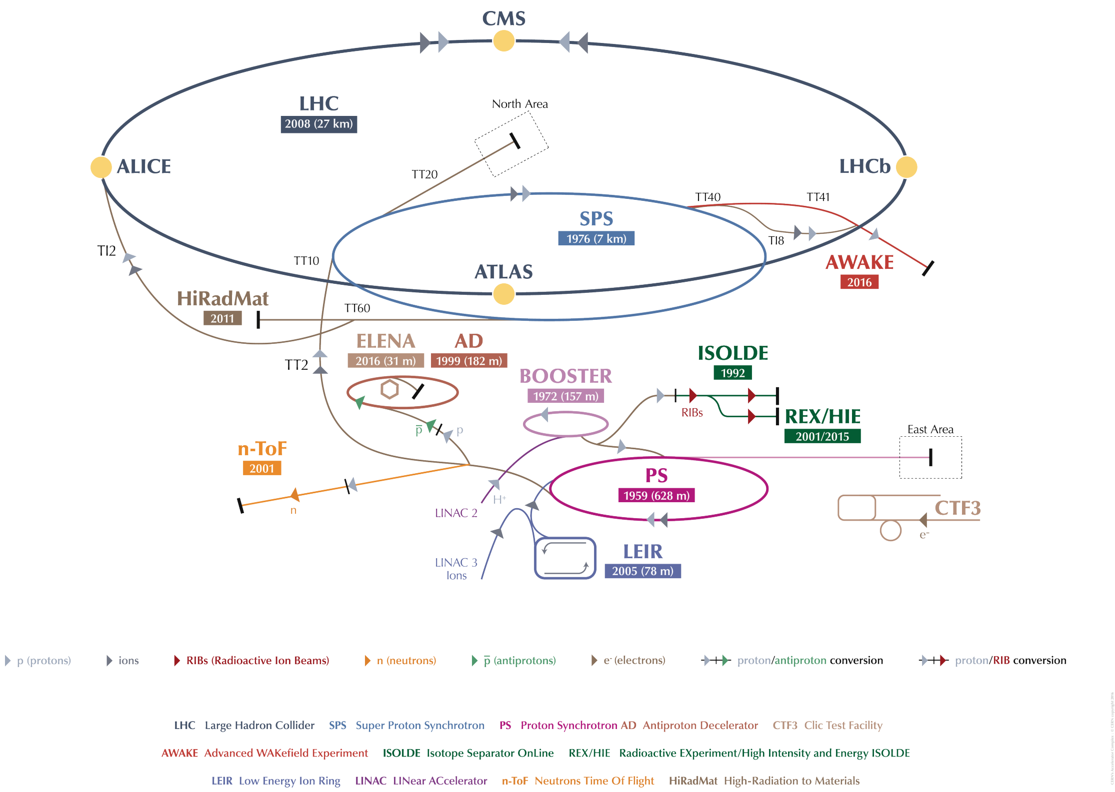

Figure 3.11: A schematic diagram of the LHC accelerator complex at CERN. Taken from reference [65].

1 phase where $\sqrt{s}$=7 TeV and $\sqrt{s}$ = 8 TeV [64]. Figure 3.11 shows a schematic of the accelerator complex for the LHC.

As well as the collision energy another important parameter for particle colliders is the number of collisions produced. The number of collisions produced per unit time and unit cross section is the luminosity, it is the proportionality factor between the cross-section and collision rate. The design luminosity of the LHC is 10^{34} cm^{-2}s^{-1} [66], in Run 1 a maximum luminosity of 7.7$\times$10^{33} cm^{-2}s^{-1} was achieved at the general purpose detectors with approximately 1.6x10^{11} protons per bunch and a bunch spacing of 50 ns. LHCb however does not collect data at the highest luminosity available, reaching a peak of only 4$\times$10^{32}cm^{-2}s^{-1} in Run 1. This is done to reduce pile-up (multiple $p-p$ collisions per bunch crossing) which make events more difficult to reconstruct. The luminosity is controlled and *levelled* by changing the lateral separation of the two proton beams, as the number of protons per bunch decreases over the course of a run the beams can be adjusted gradually to give a stable luminosity [67]. This also prolongs the

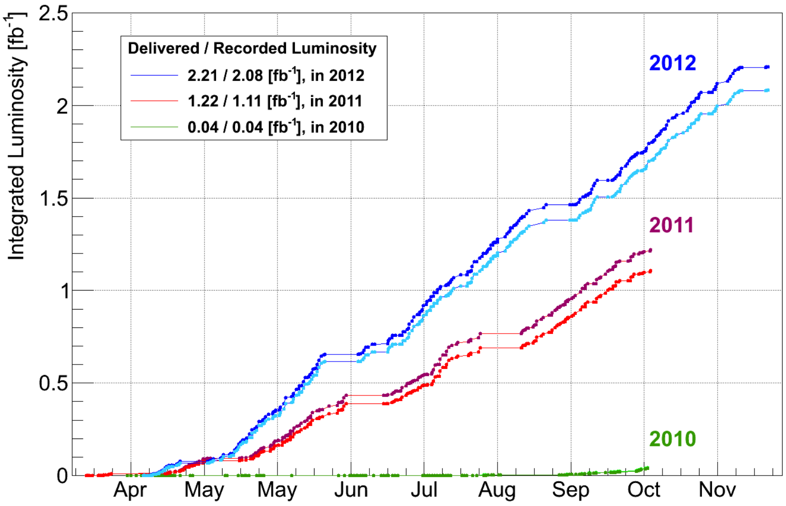

Figure 3.12: Integrated luminosity collected by the LHCb detector over the course of the Run 1 data taking period. The darker lines show the delivered values and the lighter lines the recorded values. Reference taken from [64].

lifetime of sensitive detector components by reducing radiation exposure. The luminosity integrated over time for LHCb over the course of Run 1 can be seen in figure 3.12.

3.4.2 LHCb

The LHCb detector is designed to search for evidence of new physics through precision measurements of beauty and charm hadron decays and through the study of *CP*-violation [68]. A key element of this is the precision measurement of the CKM phase γ. The LHCb detector takes a very different form to the CLEO detector. LHCb is a single-arm forward spectrometer with an acceptance of $15 < \theta < 300(250)$ mrad in the horizontal(vertical) plane where θ is the angle between the particle's trajectory and the beamline (z). The dominant production mechanism for b and $\bar{b}$ hadrons[2] is quark-antiquark pair production via gluon-gluon fusion where the b and $\bar{b}$ hadrons are produced in the same forward or backward cone around the beamline. Figure 3.13 shows the Feynman diagram for the dominant production mechanism of b and $\bar{b}$ hadrons and the θ distributions for b and $\bar{b}$ hadrons produced in $p-p$ collisions of $\sqrt{s}$=14 TeV simulated with Pythia[3].

[2]This also applies to $c\bar{c}$ pairs

[3]Another parameter used to describe the acceptance of LHCb is the pseudorapidity defined as $\eta = -\ln(\tan\frac{\theta}{2})$ for which LHCb has an acceptance range of $1.9 \leq \eta \leq 4.9$

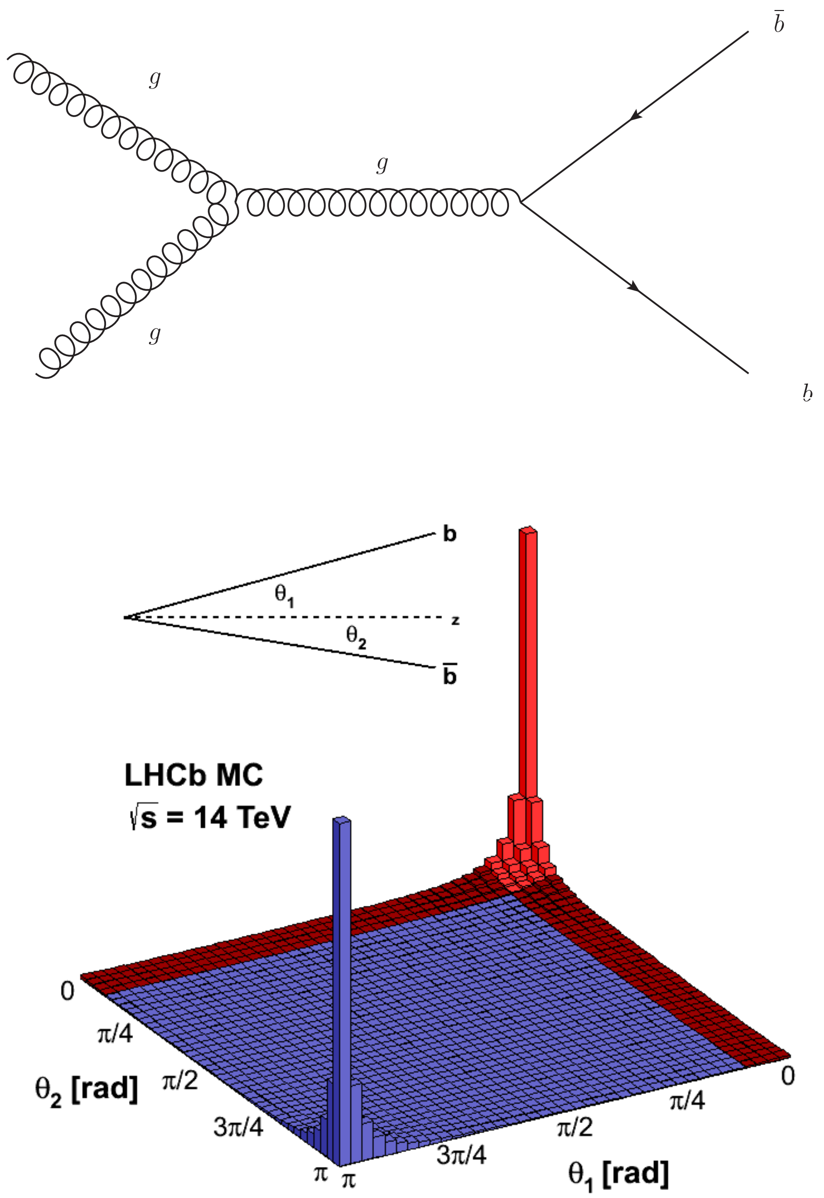

Figure 3.13: Feynman diagram for the dominant production mechanism of b and $\bar{b}$ hadrons from $p-p$ collisions (top) and distribution of θ for b and $\bar{b}$ hadrons produced in $p-p$ collisions of $\sqrt{s}$ =14 TeV simulated with Pythia where $\theta = 0$ corresponds to the beamline (bottom). Figure taken from reference [69].

Despite the difference in structural shape many of the detector subsystems of LHCb are similar to that of CLEO. Immediately surrounding the collision or interaction point is the VErtex LOcator (VELO); a silicon vertex detector vital for for the identification of primary and secondary vertices such as that of the B meson. The first of two Ring Imaging CHerenkov (RICH1) detectors follows for the identification of charged hadrons. The rest of the tracking system begins with the Tracker Turencis (TT) with the LHCb magnet separating this from three tracking stations (T1-T3). The total tracking system has a momentum resolution from $\Delta p/p = 0.4\%$ at 5GeV to $\Delta p/p = 0.6\%$ at 100 GeV. The second RICH detector (RICH2) for the identification of higher momentum hadrons precedes the Scintillator Pad Detector (SPD), Preshower (PS) and Electromagnetic Calorimeter for identification and energy measurements of electrons and photons. The Hadronic Calorimeter (HCAL) follows and finally the muon stations (M1-M5) are located at the far end of the detector for the identification/measurement of muons. Figure 3.14 shows a schematic diagram of the LHCb detector with the interaction point on the left. The beamline runs along the z axis, with y vertically upwards and x pointing towards the centre of the LHC. The $x - z$ plane is the bending plane; the plane within which charged particle tracks are curved due to the magnet. The $y - z$ plane is the non-bending plane. We also define downstream as the direction from the VELO to the muon stations. Within the LHCb cavern the beampipe is mainly made of Beryllium (Z=4) in order to minimise the multiple Coulomb scattering experienced by charged decay particles. In the main sections of the accelerator the beampipe is made from stainless steel.

VErtex LOcator (VELO)

Hadrons containing a b-quark fly a distance before decaying due to their relatively long lifetime. This creates secondary vertices displaced from the PV and is a key signature used to identify b-hadron decays. The VELO is a silicon vertex detector designed for precision measurements of particle tracks near the PV such that primary and secondary vertices can be reconstructed and parameters such as particle lifetime and impact parameter found [70]. The VELO has an impact parameter resolution of < 35 μm for

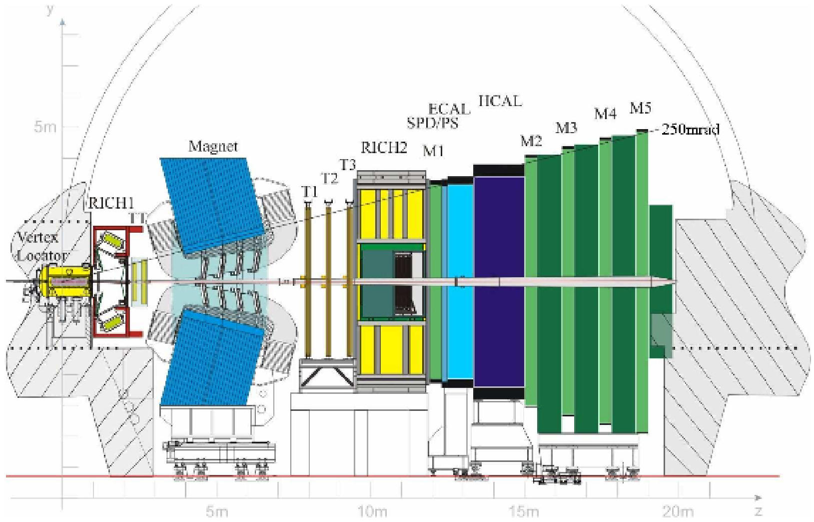

Figure 3.14: A schematic diagram of the LHCb detector. Taken from reference [68].

particles with $p_T > 1$ GeV [71]. Semi-circular, double-sided silicon stripped detector modules are paired and located at 21 stations along a 1 m section of the beampipe under vacuum. One side of the detector module has strips running in a semi-circular configuration and the other side has strips running radially to be sensitive to r and ϕ respectively. The spacing of the 21 stations provides z measurements.

The VELO detector is the closest of any at the LHC to the beam. To protect the sensitive electronics the semi-circular halves are retracted to a distance of 35 mm during beam injection and ramp up and then moved in to just 7 mm from the beam when the beam is stable for collisions. Figure 3.15 shows the VELO module stations and the modules in an open and closed configuration. The VELO covers the full $15 < \theta < 300$mrad acceptance, ensuring all tracks in this region cross 3 or more VELO stations.

Ring Imaging CHerenkov (RICH) detectors

Like for the CLEO detector, RICH detectors are fundamental to LHCb's particle identification abilities and are particularly relevant to the decay of interest in this thesis due to their capability to distinguish between hadronic multibody final states. LHCb has two RICH detectors that cover complementary momentum ranges ranging from 2-150 GeV using three (in Run 1) different radiators with different refractive indices, n. The

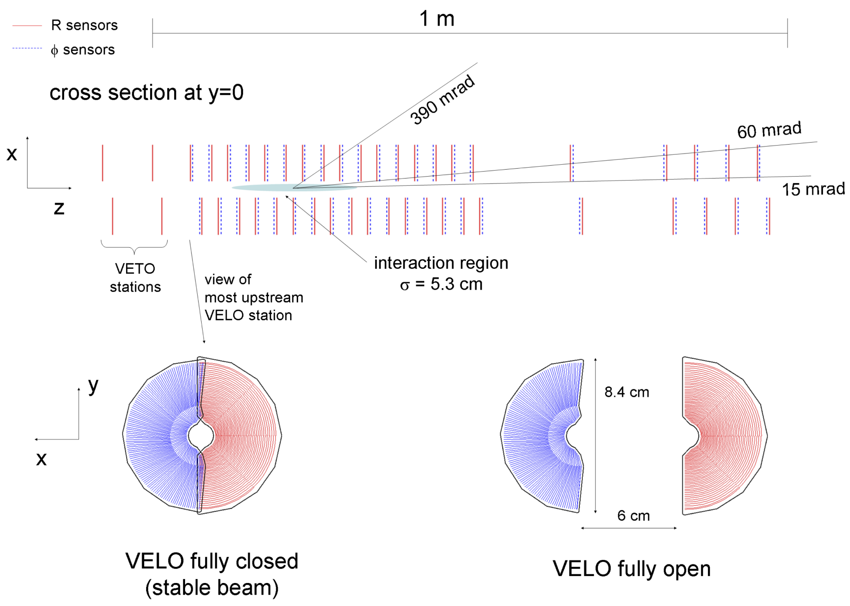

Figure 3.15: VELO stations along the beamline z and VELO silicon detectors in open and closed configuration shown in the $x-z$ plane. Taken from reference [70].

Cherenkov angle as a function of particle momentum for the radiators used in the RICH detectors is shown in figure 3.16. It can be seen that the RICH detectors are effective mainly for hadron identification. In order to minimise the amount of material in the LHCb acceptance and protect the photodetectors from the magnetic field, the photodetectors are housed outside of the acceptance in iron shield boxes. The material budget of RICH1 amounts to $\approx 8\%$ of a radiation length and RICH2 $\approx 15\%$ of a radiation length [72].

RICH1 is located upstream of the magnet and uses silica aerogel (n=1.03)[4] and C_4F_{10} gas (n=1.0014). It is used for the identification of particles in the momentum range 2-40GeV with an acceptance of 25-300 mrad (vertical) and 25-250mrad (horizontal), this is the full LHCb acceptance range with the lower limit being due to the size of the beampipe. RICH1 is located prior to the magnet as these low momentum tracks may be deflected out of the acceptance by the magnet. RICH1 uses tilted, spherical mirrors to focus the Cherenkov light out of the detector acceptance and then planar mirrors to reflect the image onto the photodetectors. The spherical mirrors of RICH1 are made

[4]This was removed at the beginning of Run 2 as it was found to be less effective at higher luminosities, the benefits from a decreased material budget upon its removal were greater than the small improvement in PID it provided

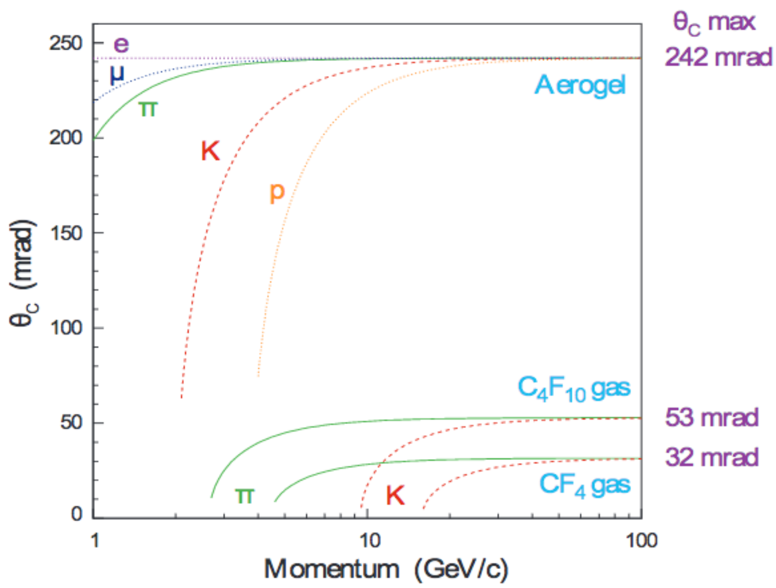

Figure 3.16: Cherenkov angle, θ_c, as a function of particle momentum for the three RICH radiators. The momentum thresholds, where particles begin to radiate Cherenkov photons can be seen for each radiator as well as the saturation angle. Taken from reference [73].

from Carbon Fibre Reinforced Polymer (CFRP) substrate whilst the planar mirrors that are outside of the acceptance are made from a glass substrate.

RICH2 is located downstream of the magnet (after tracking) and has a CF_4 (n=1.0005) gas radiator with a limited acceptance of 15-120mrad (horizontal) and 15-100 mrad (vertical). Higher momentum tracks have smaller polar angles as seen in figure 3.17 [74] which shows all tracks in simulated $B_d^0 \rightarrow \pi^+\pi^-$ events, therefore this limited acceptance is suitable for the identification of particles with a momentum from 15GeV to >100GeV. RICH2 uses tilted spherical mirrors and secondary flat mirrors to reflect the Cherenkov photons out of the acceptance onto the photodetectors in order to reduce the sub-detector length. All RICH2 mirrors are made from a glass substrate. Figure 3.18 shows RICH1 and RICH2.

The photodetectors used for both RICH detectors are cylindrical Pixel Hybrid Photon Detector (HPDs) tubes each with 1024 2.5×2.5mm pixels. They are hexagonally close packed in two detector planes each consisting of 98 HPDs for RICH1 and 144 HPDs for RICH2. A fit to photon rings allows the measurement of θ_c and determination of the velocity of a particle.

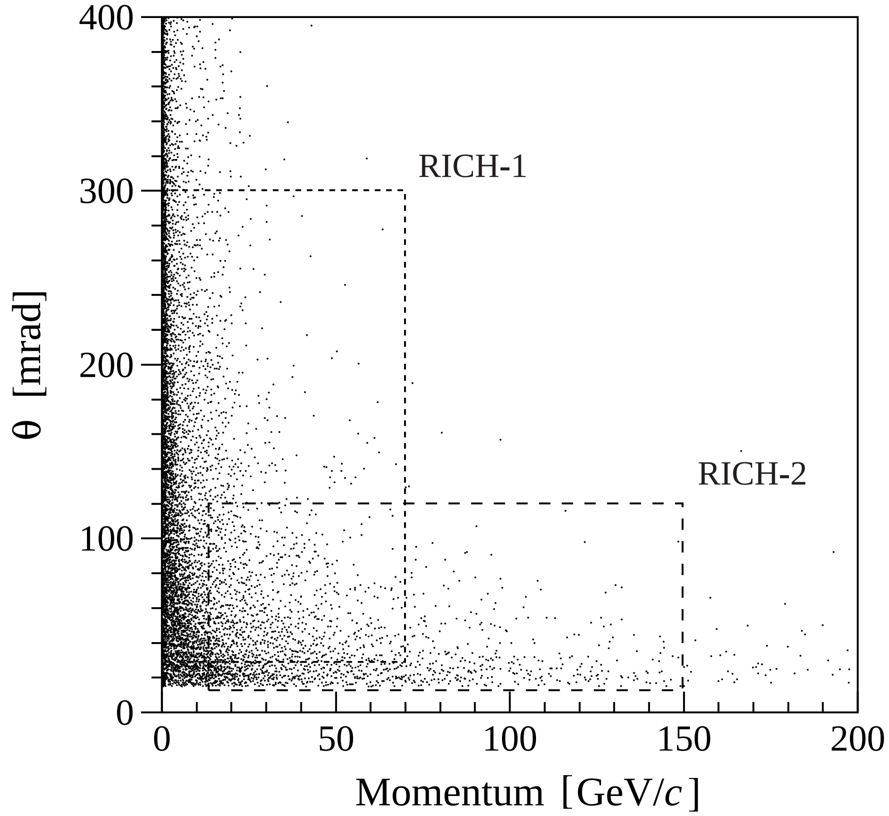

Figure 3.17: Polar angle θ with respect to the beam axis as a function of momentum for simulated tracks in $B_d^0 \rightarrow \pi^+\pi^-$ events. Acceptance regions for RICH1 and RICH 2 are shown. Taken from reference [74].

For each track the photon rings from RICH1 and RICH2 are compared to that expected for a pion, kaon, proton, electron or muon (X) to give a likelihood for each particle hypothesis. The particle is assigned the identity of the particle hypothesis giving the maximum likelihood. LHCb also uses a PID variable based on the likelihood for a particular particle hypothesis, known as the Difference in Log Likelihood, DLL. The difference in the likelihood of hypothesis X is taken with respect to the likelihood of the pion hypothesis (the most abundant particles in $p-p$ collisions)

$$\mathrm{DLL}_{X\pi} = \log\mathcal{L}_X - \log\mathcal{L}_\pi \tag{3.3}$$

Magnet

Unlike the magnet in the CLEO detector the LHCb magnet, used to measure the momentum of charged particles, is not superconducting. It is a dipole magnet that creates

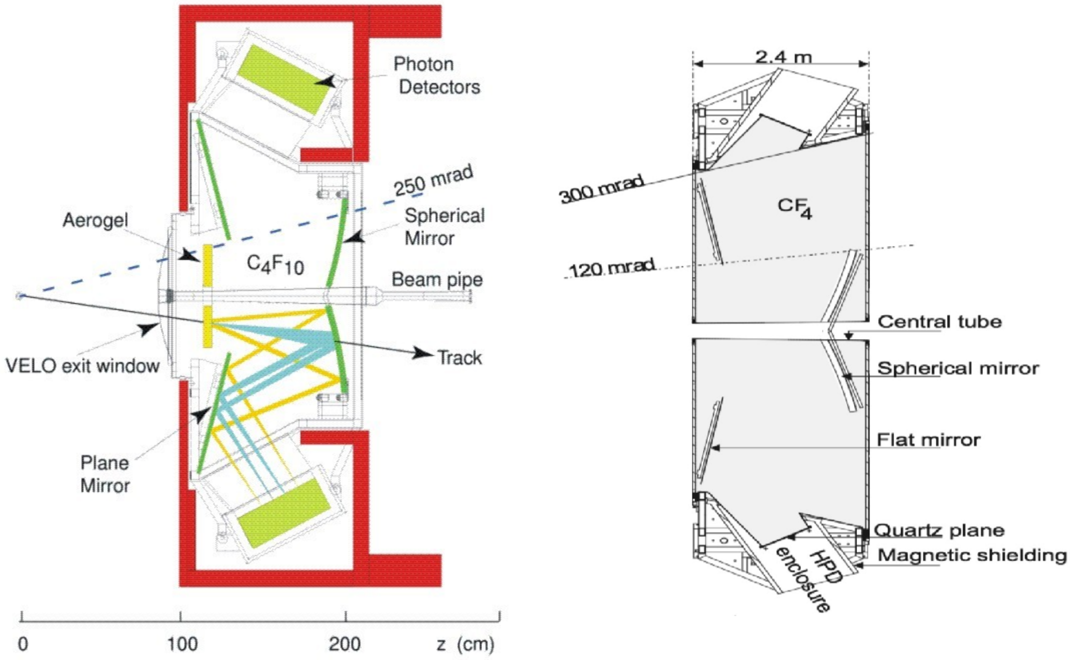

Figure 3.18: Schematic diagrams of the RICH1 (left) and RICH2 (right) detectors. Taken from reference [73].

a magnetic field perpendicular to the beamline. The magnet design allows regular reversals of the magnet polarity. By taking data where the magnetic field points upwards and where the magnetic field points downwards in equal proportions, any asymmetric acceptance effects that could affect measurements of *CP*-violating decays are removed. The magnet provides an integrated field of 4 Tm.

Tracking

As well as the VELO for charged particle tracking there is the Tracker Turencis (TT); a silicon microstrip detector, and three tracking stations, T1-T3.

The TT covers the full LHCb acceptance and is located upstream of the magnet. Downstream of the magnet low momentum particles are likely to have been bent out of the LHCb acceptance, the TT allows reconstruction of these tracks as well as the reconstruction of longer lived particles that decay outside of the VELO such as the K^0_S meson. The tracking stations T1-T3 consist of an inner and outer tracker. The inner tracker is a silicon detector and is a 120 cm wide and 40 cm high cross-shaped region surrounding the beampipe. The outer tracker is a larger straw-tube drift chamber covering the rest of the LHCb acceptance. Silicon detectors have far greater granularity than drift chambers and are therefore used where the particle flux is high ($\approx 5 \times 10^5$ cm^{-2}s^{-1} in the inner tracker region). However they are expensive and so cheaper straw-tube detectors cover the large areas of the tracking stations where the particle flux is lower.

The TT together with the inner tracker of T1-T3 is known as the Silicon Tracker (ST). Silicon strips are pitched at 200 μm and each of the four ST stations has four detection layers. The first and last layer have vertically aligned silicon strips measuring position in x, and the second and third layers are rotated -5^o and +5^o respectively improving the x measurement, while providing some sensitivity to y position. The ST has a hit resolution of $\approx$50μm.

Each outer tracker station comprises four layers in the same alignment configuration as the ST. Each layer has two sub-layers containing 4.9mm diameter straw tubes filled with a gas mixture of 7:3 argon:carbon dioxide, chosen for its fast drift time. The hit resolution for the outer tracker is 205 μm for tracks with $p > 10$ GeV. Figure 3.19 shows the configuration of the TT and the inner and outer trackers in the tracking stations T1-T3.

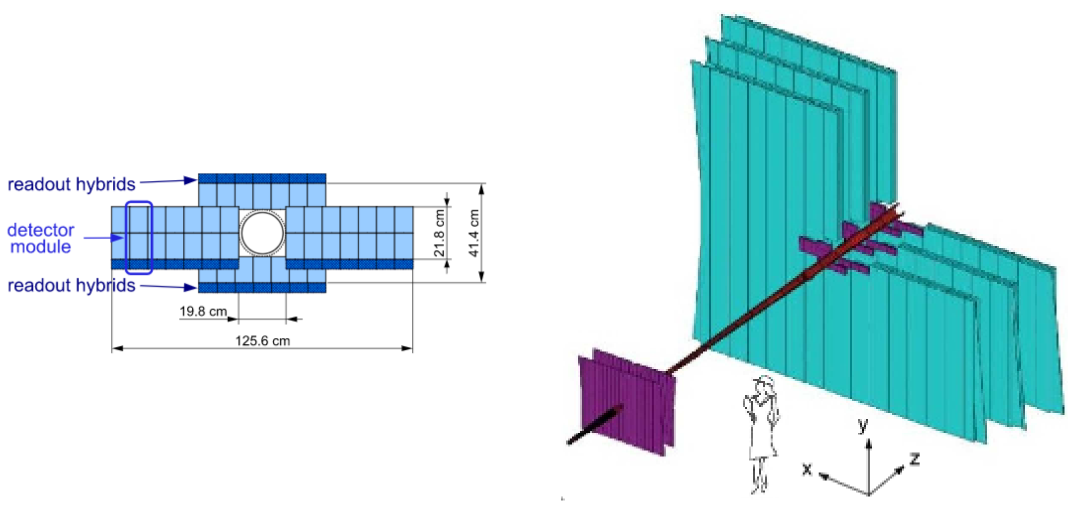

Figure 3.19: Cross shape of Inner Tracker (IT) sensors in the $x-y$ plane with beampipe in the center (left). Tracker Turencis (TT) closest to interaction point and T1-T3 stations consisting of IT and Outer tracker (OT) (right) Taken from reference [68].

Calorimeters

The Calorimeter system comprises several subdetectors; the Scintillating Pad Detector (SPD), the Pre Shower (PS), the Electromagnetic Calorimeter (ECAL) and finally the Hadronic Calorimeter (HCAL). This system measures the energy of neutral particles as well as providing PID information for electrons, photons and hadrons [75]. It is essential input for the Level 0 trigger which provides a decision as to whether to keep an event within 4 μs of the $p-p$ collision. It is the only subdetector sensitive to neutral photons and π^0 particles.

Both the SPD and PS use $\approx$ 6000 15 mm thick scintillating pads. In between the two lies a $2.5X_0$ lead converter. The SPD is designed to identify charged particles as only they will deposit energy here [76], both incident electrons and photons will shower in the lead converter and deposit energy in the PS and ECAL. The scintillation light is transmitted via wavelength shifting fibres to Photo-Multiplier Tubes (PMTs).

The ECAL thickness is $\approx 25X_0$ for full containment of the particle showers and consists of 66 layers of 2 mm thick lead absorber followed by a 4 mm scintillator pad interspersed with wavelength shifting fibres.

In the HCAL hadrons interact with the nuclei of the material creating hadronic showers, which consist mainly of pions. Like the ECAL, the HCAL uses layers of scintillating pads and absorber, in this case 1 cm thick iron. The HCAL has a thickness of $5.6\lambda_i$.

For all the subdetectors of the calorimeter system the granularity of the scintillator pads is higher close to the beampipe where the particle density is highest.

Muon chambers

There is a total of 5 muon stations (M1-M5) which, like the calorimeters, provide information for the Level-0 trigger. Each muon station is divided into four regions (R1-R4) around the beampipe with varying granularity dependent on the expected particle density. This results in an occupancy that is approximately constant over the detector plane. Figure 3.20 shows the muon stations M1-M5 and the regions R1-R4 on one of the stations. M1 is located prior to the calorimeter system and uses 274 chambers. The chambers in R1 are triple-GEM (Gas Electron Multiplier) chambers chosen for their radiation hardness as particle density in front of calorimeters is considerably higher than behind [77]. M2-M5 are multiwire proportional chambers and are downstream of the HCAL interspersed by 80cm iron planes. Only the minimally interacting muons reach the muon stations as the iron planes prevent any high energy hadrons penetrating all muon stations.

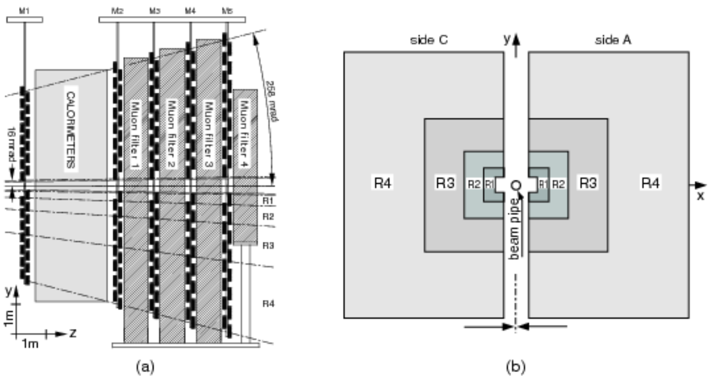

Figure 3.20: A side view of the muon subdetector (a) and the layout of regions R1-R4 on a muon station (b). Taken from reference [73].

Trigger systems

In the LHCb detector, visible interactions[5] occur at a rate of ≈ 13 MHz. It is not possible to readout the full detector at this rate. A two stage trigger uses the characteristics of B decays to decide which events to save for further processing.

[5]Visible interactions contain at least two charged particles with hits in the VELO and T1-T3 such that they are re-constructable

The trigger system consists of a hardware Level-0 trigger (L0) that runs synchronously with the bunch crossing frequency of the LHC and a software High Level Trigger (HLT) that runs asynchronously on a computing farm. The trigger lines relevant for this analysis are described in the following.

Level-0 trigger

The LHCb detector can be read out at a rate of 1 MHz, the L0 trigger reduces the event rate from the 40 MHz bunch crossing to this level. As it must run synchronously with the bunch crossings only a small component of the detector information is used. L0 trigger latency (the time between the $p-p$ collision and the L0 decision) is 4 μs, half of which is particle flight time and cable and front end electronics delays [78] .

Trigger lines either use information from the calorimeter or muon chambers, these sub-detectors have fast readout times. The L0 Calorimeter triggers use information from the whole calorimeter system to determine the transverse energy, E_T (energy in the $x-y$ plane), of candidate particles in an event, this forms the L0-hadron, L0-photon, L0-electron triggers. For the L0-hadron trigger a hadron candidate is associated to the highest E_T cluster in the HCAL. The hadron candidate's E_T value must be greater than 3.5(3.7)GeV for 2011(2012) running for the trigger to fire.

For the L0-photon trigger a photon candidate is associated with the highest E_T cluster in the ECAL which must have $E_T > 2.5(3.0)$GeV for 2011(2012) running and also requires hits in the PS. For the L0-electron trigger, electron candidates have the requirements of a photon but with the added requirement of hits in the SPD.

There are also L0-muon and L0-dimuon triggers that use hit information from the muon stations.

Together these L0 triggers are known as L0-global, should any of the above L0 triggers fire the event is kept by the L0-global trigger.

HLT trigger

To reduce the rate further so that events can be written to disk. The HLT uses a C++ application that runs on an Event Filter Farm (EFF) of 30,000 processing cores and has access to the full detector information. It consists of two stages; HLT1 and HLT2.

At HLT1 an event is assigned an alley based on the L0 trigger that fired for the event. HLT1 uses information from the tracking stations and VELO to confirm the L0 decision by fully reconstructing the triggering candidate track in the tracking system and cutting on parameters such as impact parameter and p_T. For this analysis the trigger line HLT1TrackAllL0Decision is used which is efficient for the selection of B decays. An event passes this line if it contains a track with $p_T > 1.7$GeV with impact parameter >0.1mm [79].

HLT2 runs a full reconstruction of events passing HLT1 allowing the reconstruction of tracks, vertices and PID information to which selection criteria can be applied. Exclusive HLT2 algorithms such as those requiring fully reconstructed final states like $J/\psi \to \mu^+\mu^-$ and inclusive algorithms requiring only partial reconstruction are used. This analysis uses the inclusive HLT2TopoNBodyBDTDecision topological triggers. If the distance of closest approach (DOCA) of two charged tracks with significant IP is less than 0.2mm they are combined into a 2-body object. If there is an additional track with a DOCA to the 2-body object less than 0.2mm a 3-body object is formed and so on. A multivariate classifier (BDT, discussed in section 5.2) which uses a corrected mass variable (accounting for decay products not included in the vertex) and kinematic variables such as χ^2_{IP} of the n-body vertex is then used to select events with 2, 3 or 4 body vertices of charged tracks displaced from the PV. This BDT was trained on reconstructable simulation data signal events and minimum-bias data background events.

A schematic of the LHCb trigger system is shown in figure 3.21.

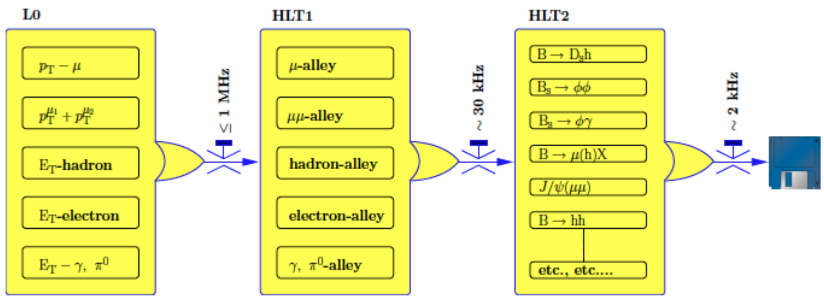

Figure 3.21: LHCb trigger flow sequence

LHCb software

Simulation

Simulation data is vital for physics analyses. The simulation of primary and secondary particle decays and detector geometry/interactions are implemented using the same software framework as in CLEO; EVTGEN [80] and GEANT [81], [82]. The $p-p$ collisions and subsequent creation of b-hadrons however is simulated using the PYTHIA [83] program tuned for LHCb with parton density functions described in [84]. This part of the simulation uses the LHCb GAUSS software [85].

The LHCb software package BOOLE simulates the LHCb sub-detector response to the simulated particles using observed performance information and also simulates the L0 trigger [86]. Upon digitisation the simulated data readout is in the same format as the real data readout with the addition of truth information. Henceforth both MC data and real data can be treated in the same manner. Access to the truth information throughout is invaluable for assessing detection/reconstruction and selection efficiencies.

Reconstruction

The HLT triggers are run using a software package called MOORE [87], online for real data and offline for the simulated data. BRUNEL performs a final reconstruction of raw hits into physics objects such as tracks, clusters and photon rings in the RICH, using detector conditions recorded at run time [88]. It is these objects that are saved for final analysis. The DAVINCI software package takes the output of BRUNEL and attempts to form user defined decay chains of particles upon which comprehensive offline selection can take place [89].

Chapter 4

Amplitude analysis of $D^0 \rightarrow K^+K^-\pi^+\pi^-$

This section presents the amplitude analysis of $D^0 \rightarrow K^+K^-\pi^+\pi^-$ decays. This work is a continuation of that presented in the paper *Amplitude Analysis of* $D^0 \rightarrow K^+K^-\pi^+\pi^-$ published by the CLEO collaboration in 2012 [1]. Part of the selection procedure including the data tagging was kept for this analysis and is detailed at the beginning of this section for completeness. All subsequent work reported from section 4.4 onwards was performed by the author.

4.1 Introduction

The decay $D^0 \rightarrow K^+K^-\pi^+\pi^-$ has a rich resonant structure, proceeding via many intermediate states. An amplitude analysis of this 4-body, self-conjugate final state decay is performed in order to disentangle these various contributions. The resulting model can make important contributions to the determination of the CP-violating phase γ using $B^\pm \rightarrow D(\rightarrow K^+K^-\pi^+\pi^-)K^\pm$ decays both in model-dependent and model-independent measurements. This analysis uses data collected by the CLEO experiment in symmetric electron-positron collisions at the Cornell Electron-positron Storage Ring (CESR) between 1995 and 2008.

4.1.1 Previous Results

Prior to CLEO only the FOCUS (E831) [90] and E791 [91] experiments at Fermilab had conducted a fully coherent amplitude analysis of $D^0 \to K^+K^-\pi^+\pi^-$ decays. The FOCUS amplitude analysis was based on a sample size of approximately 1300 events and included 10 amplitude components in the amplitude model. It was found that the dominant contributions were that of $(D \to AP)$[1] $D^0 \to K_1(1270)K^-$ and $D^0 \to K_1(1400)K^-$ decays as well as the $(D \to VV)$ $D^0 \to \phi\rho$ decay. A sizable contribution ($\approx 15\%$) also came from the $(D \to SPP)$ $D \to f_0(980)\pi\pi$ decay mode. No non-resonant term was included in this model. The E791 experiment published an amplitude analysis of $D^0 \to K^+K^-\pi^+\pi^-$ based on approximately 150 events and included 7 amplitude components in the amplitude model, including a non-resonant mode which was found to dominate. In both these analyses no separation was made between D^0 and $\bar{D}^0$ decays. This analysis benefits from the ability to cleanly distinguish between D^0 and $\bar{D}^0$ decays and also from significantly higher statistics. As mentioned, an amplitude analysis of $D^0 \to K^+K^-\pi^+\pi^-$ decays has already been performed using the CLEO and CLEO-c dataset [1], the analysis presented here however greatly benefits from improved formalism and amplitude analysis techniques.

4.2 CLEO Datasets

The dataset for the following analysis spans three configurations of the CLEO detector referred to as CLEO II.V, CLEO III and CLEO-c. The CLEO-c data has two distinct centre of mass energies for $e^+ - e^-$ collisions, namely CLEO-c 3770 and CLEO-c 4170. The relative amounts of each dataset are as follows:

1. approximately 9 fb^{-1} taken at $\sqrt{s} \approx 10$ GeV by CLEO II.V

2. 15.3 fb^{-1} taken by CLEO III at $\sqrt{s} = 7.0 - 11.2$ GeV

3. 818 pb^{-1} taken at the $\psi(3770)$ resonance energy by CLEO-c

[1]Here, A denotes an axial-vector particle, V a vector particle, S a scalar particle and P a pseudoscalar particle

4. 600 pb^{-1} taken by CLEO-c at $\sqrt{s} = 4170$ MeV.

Due to the different CLEO detector configurations and collision energies each data sample is treated separately as described in the following sections. Detailed first are the various D tagging methods used in the analysis followed by the basic selection criteria. This is followed by further, improved selection criteria specific to this analysis including specific decay vetoes and a re-determination of signal and background regions for the datasets. Signal fractions and background models are discussed in section 4.6 and the fit to the data from section 4.7 onwards.

4.2.1 Data tagging

Each event in the data sample must be tagged. This analysis uses both flavour tagged (FT) and CP tagged data.

Flavor-tagged data

Flavour tagging refers to the determination of the signal D decay to be either D^0 or $\bar{D}^0$. The amplitude of the decay can then be modelled as $A_{D^0}(p)$ or $A_{\bar{D}^0}(p)$ respectively. For the CLEO II.V and CLEO III datasets the flavour of the signal D meson is determined via the charge of the *slow pion*, π_s, in the decay $D^{*+} \to D^0\pi_s^+$[2]. The *slow pion* is named as such due to the low momentum available to it given the small mass difference between the D^{*+} and D^0 mesons. The two CLEO-c datasets are flavor tagged via the charge of the kaon associated with the decay of the other D meson in the event. Presuming Cabibbo favoured decays and by requiring only one possible tagging kaon in the event, a positive tagging kaon indicates the signal decay is that of a D^0 meson and a negative tagging kaon implies that the signal decay is that of a $\bar{D}^0$ meson. This is possible as $D^0 \to K^-X$ and $\bar{D}^0 \to K^+X$ (where X is the other decay products and does not contain a kaon) are Cabibbo favoured whereas the alternative decays are doubly Cabibbo suppressed. There is a mistag rate, w, associated with both of these methods of flavor tagging. The mistag rate is determined for each dataset separately through a data-driven method

[2] Charge conjugation implied

using $D^0 \to K^-\pi^+\pi^-\pi^+$ decays, where the flavour of the D meson can be inferred from the charge of the kaon it decays to. For CLEO-c the mistag rate is estimated at (3.4±0.4)% and (7.5±0.7)% for CLEO-c 3770 and CLEO-c 4170 respectively, the main cause of this being pions from the other D decay misidentified as kaons. For CLEO II.V and III the mistag rate is at the sub-percent level.

CP tagged data

CP-tagging refers to the determination of a signal D decay to be in a specific state of *CP*. The CLEO-c 3770 configuration produces D particles through the quantum correlated $e^+e^- \to \psi(3770) \to D^0\bar{D}^0$ process which is a *CP* eigenstate with eigenvalue -1 (a *CP* odd eigenstate). Therefore the D^0 and $\bar{D}^0$ must subsequently decay into states of opposite *CP*. This analysis uses the *CP* even and *CP* odd tagging decays shown in table 4.1. If the other D in the event is tagged as decaying to a *CP* odd state the signal D must necessarily decay to a *CP* even state and hence its amplitude is given by

$$A_{\text{even}} = \frac{1}{\sqrt{2}}(A_{D^0}(p) + A_{\bar{D}^0}(p)) \tag{4.1}$$

Table 4.1: CP tagging decays

CP even tags	CP odd tags
$\pi^+\pi^-$	$K_s^0\pi^0$
K^+K^-	$K_s^0\omega(\pi^+\pi^-\pi^0)$
$K_s^0\pi^0\pi^0$	$K_s^0\phi(K^+K^-)$
$K_L\pi^0$	$K_s^0\eta(\gamma\gamma)$
$K_L\omega(\pi^+\pi^-\pi^0)$	$K_s^0\eta(\pi^+\pi^-\pi^0)$
	$K_s^0\eta'(\pi^+\pi^-\eta)$

This expression is derived from the antisymmetric matrix element that describes the *CP* odd $D^0\bar{D}^0$ decay system [92].

$$A_{ij} \propto A_{D^0\to i}A_{\bar{D}^0\to j} - A_{D^0\to j}A_{\bar{D}^0\to i} \tag{4.2}$$

If $D^0 \to j$ is a *CP* odd tagging decay such that $A_{D^0\to j} = -A_{\bar{D}^0\to j}$ then the signal decay amplitude $D^0 \to i$ is described by 4.1. Alternatively if $D^0 \to j$ is CP even so that $A_{D^0\to j} = +A_{\bar{D}^0\to j}$, the signal decay amplitude is given by

$$A_{odd} = \frac{1}{\sqrt{2}}(A_{D^0}(p) - A_{\bar{D}^0}(p)) \tag{4.3}$$

As well as flavour specific states and *CP* odd and even states, two further types of D decay are utilised in this analysis for tagging purposes; $D \to K_s^0\pi^+\pi^-$ and $D \to K_L^0\pi^+\pi^-$. Again using 4.2, by reconstructing $D \to K_s^0\pi^+\pi^-$ or $D \to K_L^0\pi^+\pi^-$ as a tagging decay the rate of the signal D decay is expressed as

$$\Gamma = \Gamma_t|A_{\bar{s}}(p)|^2 + \Gamma_{\bar{t}}|A_s(p)|^2 - 2\sqrt{\Gamma_t\Gamma_{\bar{t}}}[\cos\theta_t\Re(A_s(p)A^*_{\bar{s}}(p)) + \sin\theta_t\Im(A^*_s(p)A_{\bar{s}}(p))] \tag{4.4}$$

The subscript t refers to the tagging $D \to K^0_{S,L}\pi^+\pi^-$ decay and subscript s refers to the signal decay. θ_t is the phase difference between $A_t(p)$ and $A_{\bar{t}}(p)$ (or equivalently the phase difference between the amplitudes $A_t(p)$ and $A_t(\bar{p})$ if we assume no *CP*-violation in charm decays). The CLEO collaboration have performed a binned analysis of the $D \to K_s^0\pi^+\pi^-$ and $D \to K_L^0\pi^+\pi^-$ decays obtaining the signal yield and average values $\langle\cos\theta_t\rangle = C_b$ and $\langle\sin\theta_t\rangle = S_b$ in each Dalitz plot bin, b [93]. The binning scheme used is shown in figure 4.1. Here, $m_+^2 = (p_{K^0_{S,L}} + p_{\pi^+})^2$ and $m_-^2 = (p_{K^0_{S,L}} + p_{\pi^-})^2$ and the bins are defined symmetrically along $m_+^2 = m_-^2$ such that the upper left half of the Dalitz plot contains bins 1 to 8 and the lower right half contains bins -1 to -8. For a point in phasepace p that falls in bin b, its *CP* transformed phasespace point $\bar{p}$ will fall in bin $-b$. For this binning scheme $S_{-b} = -S_b$, $C_{-b} = C_b$ and the number of $\bar{D} \to K^0_{S,L}\pi^-\pi^+$ events in bin b is equal to the number of $D \to K^0_{S,L}\pi^+\pi^-$ events in bin $-b$. We approximate equation 4.4 in a Dalitz plot bin b by

$$\Gamma \propto N_b|A_{\bar{s}}(p)|^2 + N_{-b}|A_s(p)|^2 - 2\sqrt{N_bN_{-b}}\Big[C_b\Re(A_sA^*_{\bar{s}}(p)) + S_b\Im(A^*_sA_{\bar{s}}(p))\Big]$$

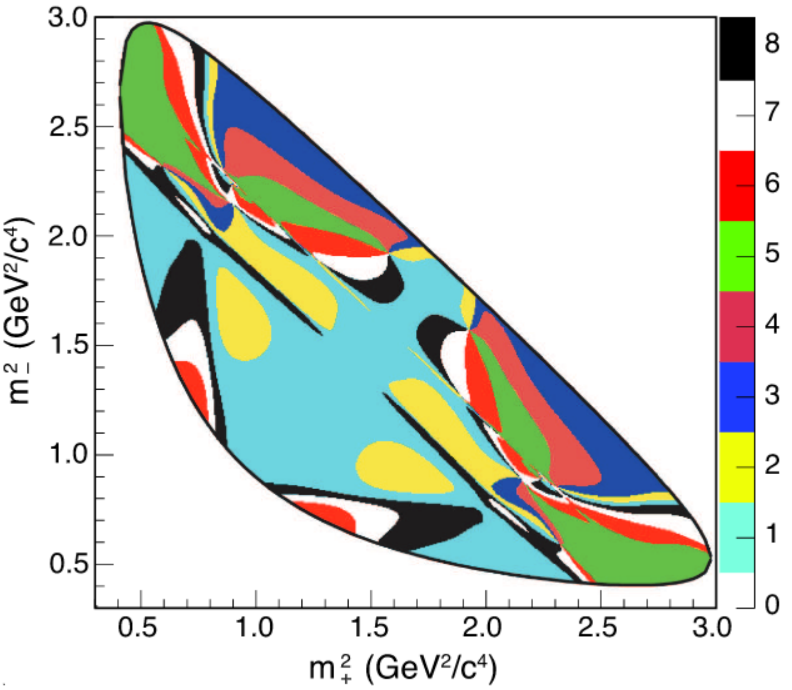

Figure 4.1: Dalitz plot binning scheme used for the binned analysis of the $D \to K_s^0\pi^+\pi^-$ and $D \to K_L^0\pi^+\pi^-$ decays performed by the CLEO collaboration. Taken from reference [93].

where N_b is the number of signal events in bin b divided by the bin area. Events that are tagged and modelled in this way are known in the following as admixture tagged events. Information about the final state of the tagging decay is required for these events, namely the Dalitz bin occupied.

The addition of *CP* tagged events to the flavour tagged data sample means we have extra sensitivity to the phase $\delta_D(p)$ of the amplitude model $A_{D^0}(p)$. Taking the amplitude squared of the *CP* odd and *CP* even tagged event amplitudes we obtain

$$|A|^{2\,\text{CP even}}_{\text{CP odd}} = |A_{D^0}(p)|^2 + |A_{\bar{D}^0}(p)|^2 \pm 2|A_{D^0}(p)||A_{\bar{D}^0}(p)|\cos(\delta_D(p) - \delta_{\bar{D}}(p)). \quad (4.5)$$

It can be seen by the expressions 4.4 and 4.5 that the cross-term gives access to the phase motion over the D decay phasespace, $\delta_D(p)$. This makes the *CP* tagged events a particularly valuable dataset.

4.3 Selection procedure

Events collected by the CLEO detector are extremely clean. Each dataset requires a separate selection procedure due to differences in detector configuration and collision energy. The background contamination in the datasets comes from two main sources; the flat, combinatorial background arising from random combinations of kaons and pions and the incoherent, peaking background $D^0 \to K^0_S(\pi^+\pi^-)K^+K^-$. Whilst this decay has the same final state as the signal decay, it does not interfere with other intermediate resonance states as the K^0_S lifetime is far greater than that of other resonances: it is an incoherent process. The branching fraction of $D^0 \to K^0_s K^+K^-$ is $4.5{\times}10^{-3}$ with $K^0_S \to \pi^+\pi^-$ occuring approximately 70% of the time [23]. The branching fraction of $D^0 \to K^+K^-\pi^+\pi^-$ is $2.4{\times}10^{-3}$ and as such $D^0 \to K^0_S(\pi^+\pi^-)K^+K^-$ is a significant background to the signal decay.

CLEO II.V and CLEO III

Due to the flavour tagging method for the CLEO II.V and CLEO III data, the selection procedure is optimised to select fully reconstructed $D^{*+} \to D^0\pi^+_s$ decays where $D^0 \to K^+K^-\pi^+\pi^-$ and its charged conjugate. A cut is placed on the slow pion momentum; $150 \leq p_{\pi_s} \leq 500$ MeV for the CLEO III dataset and $100 \leq p_{\pi_s} \leq 500$ MeV for the CLEO II.V dataset. The difference in lower limit is due to the lower collision energies for CLEO II.V. To favour events where charm mesons are produced in the primary interaction and remove those that are the result of a B decay for example, the D^{*+} momenta must be at least half of the maximum kinematically permitted. The final state particles of the signal decay are required to have momentum values between 250 and 5000 MeV for CLEO II.V and 200 and 5000 MeV for CLEO III.

Particle identification of kaons and pions is particularly important for multi-body, hadronic final states. For CLEO III, tracks with $p > 500$ MeV are classified as kaons rather than pions if they have 3 or more associated photons in the RICH detector and the fit to the photon hits shows that the kaon hypothesis is more likely than the pion hypothesis. For tracks with $p < 500$ MeV, tracks are classified as kaons if their dE/dX value is within

2.1 sigma of that expected of a kaon. Tracks are classified as pions if they have a dE/dX value within 3.2 sigma of that expected from a pion. There was no RICH detector installed for CLEO II.V, tracks are identified as kaons (pions) if their dE/dX value is within 2.1 (2.5) sigma of that expected for a true kaon (pion). If ToF information can be used candidates must also lie within 2.5 sigma of the values expected for the relevant hypothesis.

A veto is applied to remove $D^0 \to K^0_S(\pi^+\pi^-)K^+K^-$ decays. The K^0_S veto for CLEO II.V and CLEO III requires that if the two final state pions have an invariant mass consistent with that of the K^0_S then the event is rejected if either:

- The flight distance of the K^0_S candidate is greater than twice its uncertainty or
- Either of the two pions has an impact parameter greater than 1.5 mm.

Finally the selected events undergo a kinematic fit whereby the four daughter tracks of the D candidate and the D candidate and the π_s track are constrained to originate from common vertices.

CLEO-c 3770 and 4170

For the CLEO-c datasets the standard CLEO-c track classification and selection is employed as described in [94]. For CLEO-c running at the $\psi(3770)$ resonance, pairs of $D^0\bar{D}^0$ mesons are produced at the primary interaction point via a virtual photon. For CLEO-c data produced at a collision energy of 4170 MeV many higher energy charm pairs are produced. Decays of $D^{*+}\bar{D}^{*-}$ and $D^{*0}\bar{D}^{*0}$ where $D^{*+} \to D^0\pi^+$ and $D^{*0} \to D^0\gamma$ or $D^{*0} \to D^0\pi^0$ are selected as they have the highest rate and best signal to background ratio as illustrated by Monte Carlo studies in [95]. It should be noted that the bachelor pion or photon in these decays does not need to be reconstructed, these events can be selected based on their position in m_{bc} and ΔE phasespace (see figure 4.6).

As described in section 4.2.1 CLEO-c events are flavour tagged using the decay of the other D meson in the event to a kaon. Only events with a single tagging kaon candidate are considered. A lower momentum limit is put on the kaon used for tagging of 400 MeV for CLEO-c 3770 and 600 MeV for CLEO-c 4170 (a higher value is used for CLEO-c 4170 due to more background being present in this sample), this is found to both increase purity and suppress mistagged events.

The CLEO-c samples require a tighter K_S^0 veto than CLEO II.V/III as the flight distance of any potential K_S^0 will be smaller as the D meson is produced closer to threshold. Here the flight distance rejection criteria for a potential K_S^0 is reduced to greater than one uncertainty and the impact parameter of either pion reduced to 1 mm.

For further background suppression the momentum of the D candidate in the CLEO-c 4170 dataset must exceed 450 MeV.

CP tagged data

CP tagged data is obtained from CLEO-c 3770 where both the signal D decay and the other D decay in the event is fully reconstructed. Decays used for *CP* tagging that involve a K_L particle require use of the missing mass technique as the K_L particle has a significant lifetime and likely decays outside of the CLEO-c acceptance. The details of the selection procedure for the *CP* even and odd tagging decays can be found in reference [96] and for the $D \to K_s^0\pi^+\pi^-$ and $D \to K_L^0\pi^+\pi^-$ tagging decays in reference [93]. The signal side D decays are selected in the same way as for the flavour tagged CLEO-c 3770 data.

Finally for all flavour and *CP* tagged events a kinematic fit is performed where the daughters of the D candidate are constrained to originate from a common vertex and have invariant mass equal to that of the D meson. This improves the resolution of the 4-vectors for use in the amplitude fit.

4.4 Further Selection

Further selection to that in [1], as well as the re-determination of signal and background regions is performed.

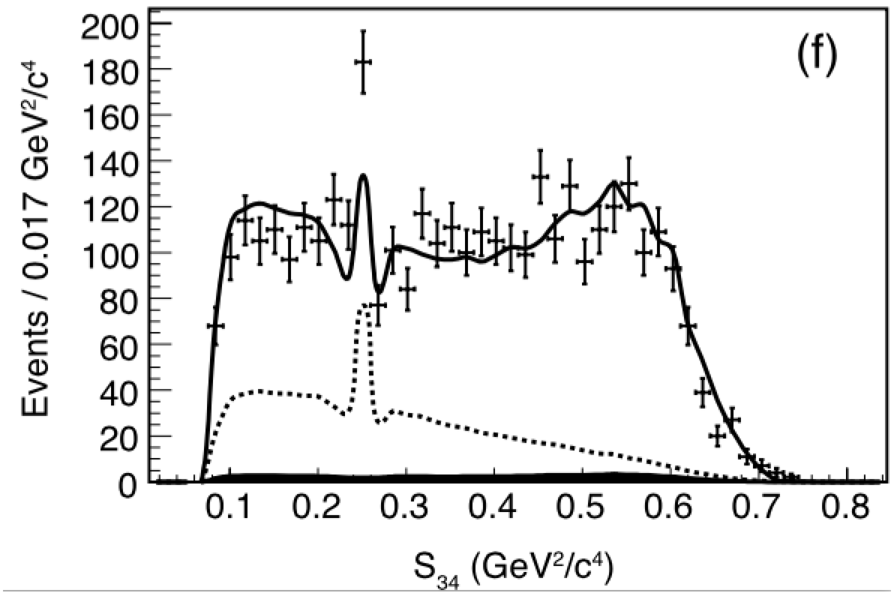

Figure 4.2: Invariant mass distribution of two pion system, $m_{\pi\pi}$, with fit overlaid for the previous amplitude analysis of $D^0 \to K^+K^-\pi^+\pi^-$ decays using this dataset. Taken from reference [1].

4.4.1 Further K_S^0 background removal

As explained above, a peaking background to the signal decay is $D^0 \to K_S^0(\pi^+\pi^-)K^+K^-$. The previous amplitude analysis of $D^0 \to K^+K^-\pi^+\pi^-$ decays using this dataset employed a flight-distance significance cut that partially removed this background. The remaining K_S^0 background could not be well described in the fit as shown in figure 4.2 taken from reference [1]. For this analysis the K_S^0 background is reduced to a negligible level by applying a veto on the invariant mass distribution of the two pion system, $m_{\pi\pi}$. This veto is taken into account as a region of zero efficiency in the fit. The size of the $m_{\pi\pi}$ window cut on is dependent on the different detector configurations' ability to resolve the K_S^0. To determine the window around the K_S^0 mass, m_{K_S}, to cut on for each dataset, the original K_S^0 veto is reversed (deliberately selecting a sample of K_S^0 events) and the $m_{\pi\pi} - m_{K_S}$ distribution fit with a Gaussian. For both CLEO-c 3770 and CLEO-c 4170 the fitted sigma value is found to be 3.0 MeV, figure 4.3 shows this process for the CLEO-c 3770 dataset.

In this amplitude analysis the normalisations of the Probability Density Functions (PDFs) are determined through a numerical MC integration technique using fully selected MC events to take into account efficiency effects across phasespace (explained

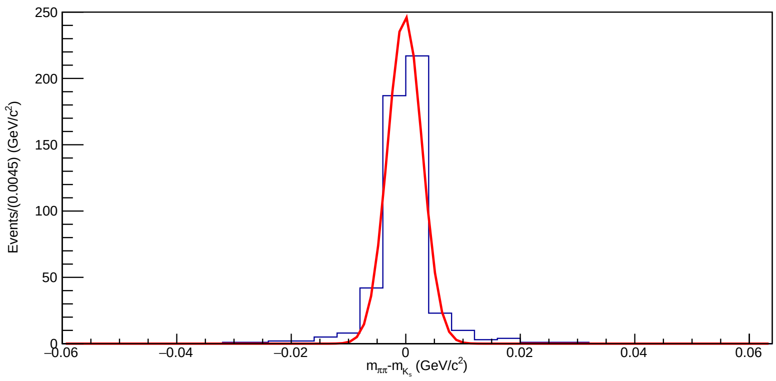

Figure 4.3: Distribution of $m_{\pi\pi} - m_{K_S}$ for CLEO-c 3770 events failing the original K^0_S veto. The distribution is fit with a Gaussian where σ=3 MeV.

further in section 4.5.1). It is imperative that the same cuts are used on the normalisation MC events as on the data events. The pre-mass/vertex-constraint kinematic variables are no longer available for these normalisation MC samples and therefore the $m_{\pi\pi}$ mass veto cut must be made on the post-mass/vertex-constraint variables in both data and MC. It is known that (since the K^0_S is long lived) the vertex constraint will smear the K^0_S events in $m_{\pi\pi}$. Therefore it is hypothesised that a 4 sigma cut on post-mass/vertex-constraint $m_{\pi\pi}$ removes all the events that a 3 sigma cut on unconstrained $m_{\pi\pi}$ would. This can be tested using the data samples for which both constrained and unconstrained $m_{\pi\pi}$ variables are available. For CLEO-c 4170 this is found to be true and for CLEO-c 3770 there is a possible contamination of 2 events. This is considered negligible and a 4 sigma (12 MeV) window in post-mass/vertex-constraint $m_{\pi\pi}$ is used in both data and MC. The *CP*-tagged data uses the same $m_{\pi\pi}$ cut as the CLEO-c 3770 flavour tagged data.

For CLEO III, figure 4.4 shows the $m_{\pi\pi} - m_{K_S}$ distribution for events failing the original K^0_S veto. Here the width of the Gaussian is much larger with a sigma value of 5.5 MeV indicating that the mass resolution of the CLEO III detector is poorer than that of CLEO-c. It is found that a 3 sigma cut around m_{K_S} made in post-mass/vertex-constraint $m_{\pi\pi}$ removes all but 4 of the events removed by the same cut on unconstrained $m_{\pi\pi}$ in the data. Given that four events can be considered negligible and that further increasing this window to remove these events significantly reduces the size of the dataset, a 3

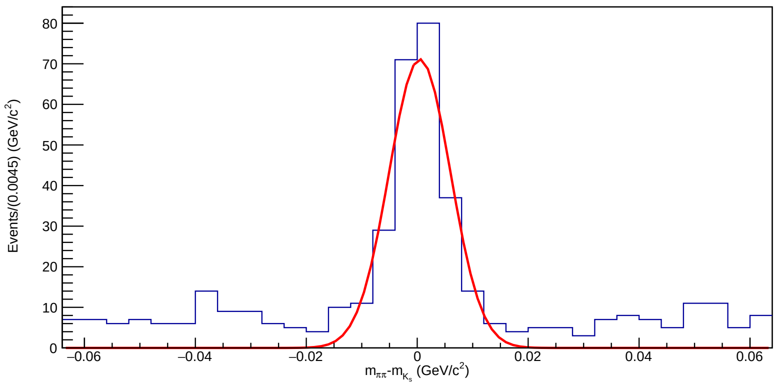

Figure 4.4: Distribution of $m_{\pi\pi} - m_{K_S}$ for CLEO III events failing the original K_S^0 veto. The distribution is fit with a Gaussian where σ=5.5 MeV.

sigma cut around m_{K_S} in post-mass/vertex-constraint $m_{\pi\pi}$ is used. It is assumed that the CLEO II.V resolution will be similar to that of CLEO III.

The efficiencies of these $m_{\pi\pi}$ mass vetoes on signal are estimated at $> 94\%$.

4.4.2 Determination of signal and background windows

Signal regions, as well as regions of background that accurately model the remaining background within the signal regions must be established. The background regions must exclusively select events where the D candidate mass is consistent with the actual D mass, m_D. If not the mass constraint applied to the D daughter particles as part of the selection results in events migrating into the allowed phasespace. This creates an excess of events at the edges of phasespace, which is not representative of the background in the signal region.

For CLEO-c we define the beam-constrained mass, m_{bc},

$$m_{bc} \equiv \sqrt{\frac{{E_{CM}}^2}{4} - {\mathbf{p}_D}^2}$$

and ΔE,

$$\Delta E \equiv E_D - \frac{E_{CM}}{2}$$

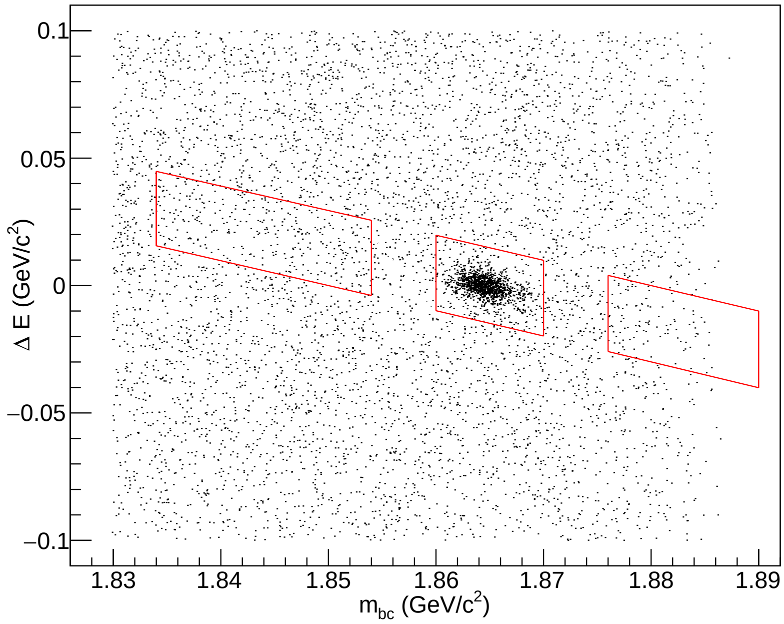

Figure 4.5: Signal (middle) and background (left and right) regions for CLEO-c 3770 in m_{bc} and ΔE space.

where E_{CM} is the centre-of-mass energy of the $e^+ - e^-$ collision, $\mathbf{p}_D$ is the reconstructed 3-momentum and E_D the total reconstructed energy of the D candidate. Signal and background regions are then selected in m_{bc} and ΔE space. The signal and background regions lie on a band where the mass of the D candidate is consistent with m_D to within some margin X MeV. The equation for this band is

$$\left|\sqrt{(\Delta E)^2 + (\Delta E)E_{CM} + {m_{bc}}^2} - m_D\right| < X\mathrm{MeV}. \tag{4.6}$$

In the case of CLEO-c 3770 the signal and background regions are defined within the band $X = 15$ MeV. The signal region is defined as $|m_{bc} - m_D| < 5$ MeV as with a collision energy of 3770 MeV the D particles are primarily produced at the interaction point and at threshold. Two background regions of $1.834 < m_{bc} < 1.854$ GeV and $1.876 < m_{bc} < 1.89$ GeV are defined. These regions are shown in figure 4.5. After full selection the signal region contains 1300 events and the background region contains 441 events.

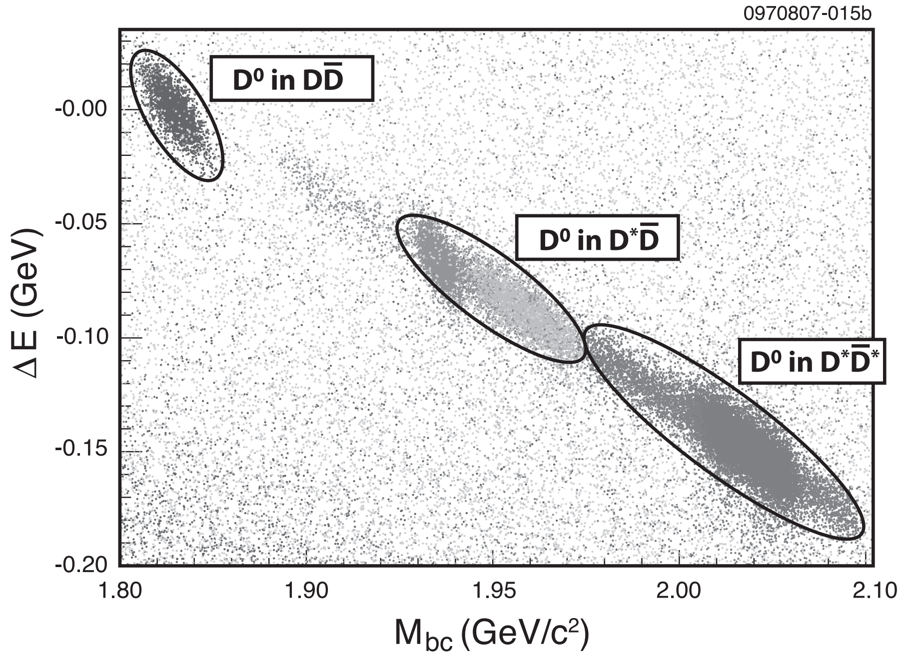

Figure 4.6: Distribution of events in m_{bc} and ΔE space for a Monte Carlo simulation of CLEO-c data at $\sqrt{s} = 4160$ MeV. Taken from reference [95]

In the case of CLEO-c 4170 the signal and background regions are governed by the use of $D^{*+}\bar{D}^{*-}$ and $D^{*0}\bar{D}^{*0}$ decay chains as described in section 4.3. Figure 4.6 shows charmed meson pair decays to D^0 in m_{bc} and ΔE space for a Monte Carlo simulation of CLEO-c data at a collision energy of 4160 MeV [95]. The signal region is defined using equation 4.6, where $X = 10$ MeV, and $2.005 < m_{bc} < 2.030$ GeV. (A tighter band is chosen here compared to CLEO-c 3770 due to the higher level of background present in this sample). The background region is chosen to lie within the same band but avoiding the other charmed meson pair decays, the m_{bc} range $1.880 < m_{bc} < 1.920$ GeV is chosen. Figure 4.7 shows these regions in m_{bc} and ΔE space. After full selection the signal region contains 598 events and the background region contains 180 events.

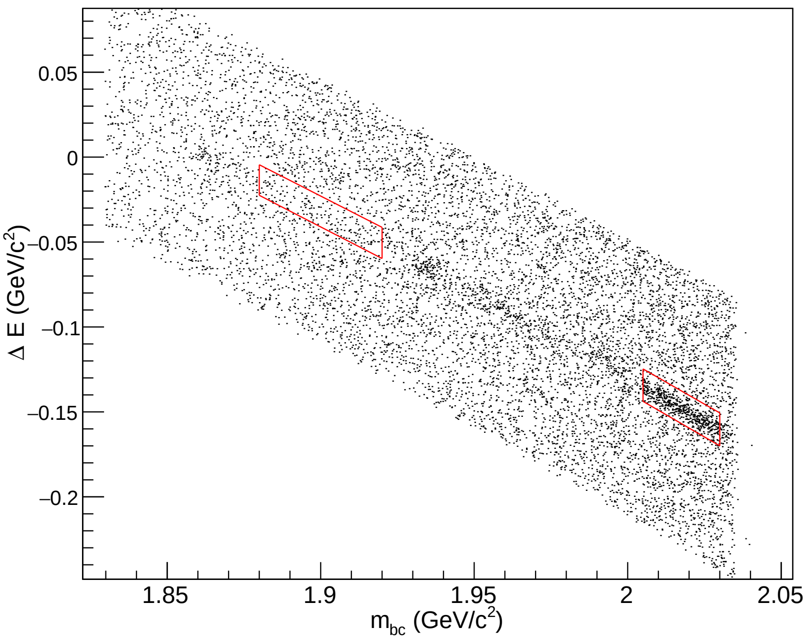

Figure 4.7: Signal (right) and background (left) regions for CLEO-c 4170 in m_{bc} and ΔE space.

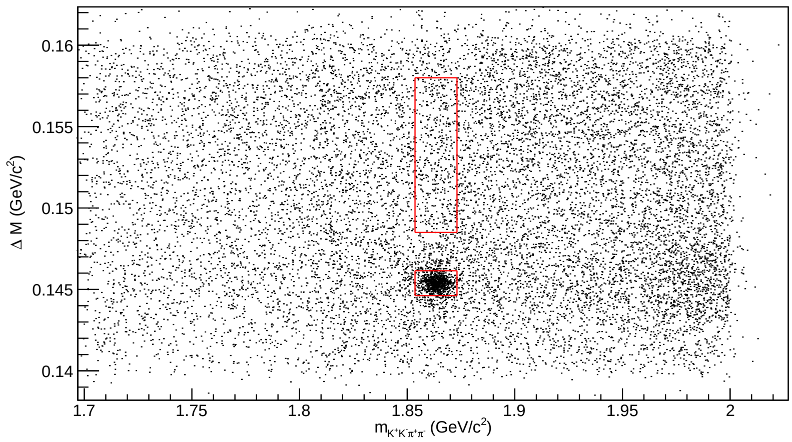

Figure 4.8: Signal (lower) and background (upper) regions for CLEO III in $m_{KK\pi\pi}$ and ΔM space.

For CLEO II.V and CLEO III, signal and background regions are defined in $m_{KK\pi\pi}$ and ΔM space where $m_{KK\pi\pi}$ is the invariant mass of the D candidate and

$$\Delta M = m_{D^*} - m_{KK\pi\pi}$$

is the mass difference between the reconstructed D^* and the reconstructed signal D candidate.

For the CLEO III signal region the mass of the D candidate is required to be within the range $^{+08.3}_{-11.2}$ MeV of the D mass and ΔM is required to be within $^{+0.72}_{-0.80}$ MeV of the accepted value. A background region is defined with the same D candidate mass requirement as the signal but with $0.1485 < \Delta M < 0.1600$ GeV. Figure 4.8 shows these signal and background regions within which there are 1163 signal events and 794 background events. For CLEO II.V a similar approach is taken where the signal window is defined as $|m_{KK\pi\pi} - m_D| < 5$ MeV and ΔM is required to be within 0.8 MeV of the accepted value. The background region is defined as $|m_{KK\pi\pi} - m_D| < 5$ MeV and $0.1485 < \Delta M < 0.1600$ GeV as shown in figure 4.9. A total of 237 signal events and 284 background events are selected.

For the CP-tagged data samples, there is not sufficient sideband data to define background regions. In this case background samples are taken from Monte Carlo data that simulates the background in the signal regions.

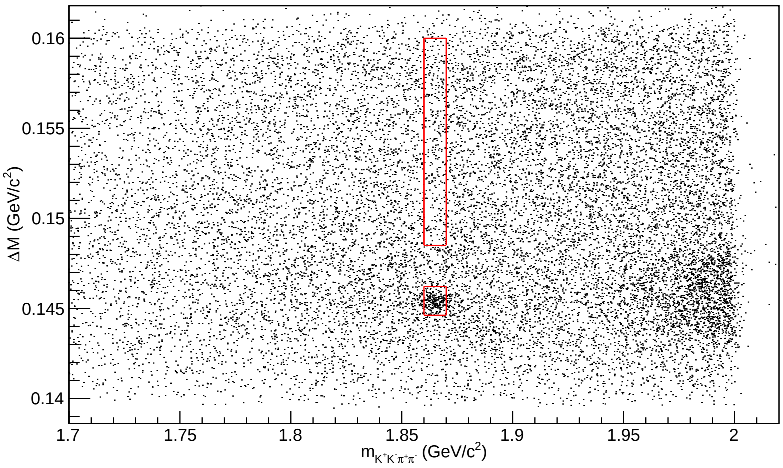

Figure 4.9: Signal (lower) and background (upper) regions for CLEO II.V in $m_{KK\pi\pi}$ and ΔM space.

4.5 Likelihood fit

The set, a, of complex coefficients for the amplitude components included in A_{D^0} are determined through a maximum likelihood fit. The Likelihood ($\mathcal{L}$) consists of signal Probability Density Functions (PDFs); $S_{D^0}(a,p)$ and $S_{\bar{D}^0}(\bar{a},p)$, for D^0 and $\bar{D}^0$ decays respectively, and background PDFs; $B(b,p)$ where b is the set of complex coefficients for the background model, these are determined prior to the fit for a. The log likelihood is given by

$$\begin{aligned}\log\mathcal{L} = &\sum^{\mathrm{N_{D0}}} \log[f_s[(1-w)S_{D^0}(a,p) + wS_{\bar{D}^0}(\bar{a},p)] + (1-f_s)B(b,p)] \\ &+ \sum^{\mathrm{N_{\bar{D}0}}} \log[f_s[(1-w)S_{\bar{D}^0}(\bar{a},p) + wS_{D^0}(a,p)] + (1-f_s)B(b,p)].\end{aligned} \tag{4.7}$$

Here, w is the mistag rate and f_s is the signal fraction. We assume no CP-violation in the D system such that $a = \bar{a}$ and perform a CP transformation on the final state particles of $\bar{D}^0$ decays. This leaves the expression

$$\log\mathcal{L} = \sum^{\mathrm{all}} \log[f_s[(1-w)S_{D^0}(a,p) + wS_{\bar{D}^0}(a,p)] + (1-f_s)B(b,p)]. \tag{4.8}$$

4.5.1 Efficiency effects

There are efficiency effects that vary over the D decay phasespace which can distort the signal and background amplitude models. These must be taken into account in the fit.

The signal PDF ($S_{D^0}(a, p)$) is described by the following

$$S_{D^0}(a,p) = \frac{\epsilon(p)|A_{D^0}(a,p)|^2 R_4(p)}{\int \epsilon(p)|A_{D^0}(a,p)|^2 R_4(p) dp}, \tag{4.9}$$

where $\epsilon(p)$ is the efficiency as a function of p and $R_4(p)$ is the phasespace density function for 4-body decays. The efficiency function, $\epsilon(p)$, and phasespace density function, $R_4(p)$, are only functions of p and not the fit parameters a. Therefore, within the numerator they have no effect on the minimisation of $S_{D^0}(a, p)$ with respect to a and can be ignored. The terms $\epsilon(p)$ and $R_4(p)$ then appear only in the normalisation. Finding a parameterisation for the efficiency function, $\epsilon(p)$, is non-trivial. Efficiency effects can instead be accounted for by using Monte Carlo (MC) events that have been through the full detector simulation and offline selection procedure that is applied to the data to perform the normalisation of the signal and background PDFs. Monte Carlo events are generated according to an approximate, preliminary signal model with amplitude component coefficients a^{gen},

$$|A_{D^0}(a^{gen}, p)|^2 R_4(p)$$

This is to ensure the phasespace is populated in regions where we expect high event density, a technique known as importance sampling which is fully described in section 2.7. The events are then passed through the GEANT-based CLEO detector response simulation and the full offline selection procedure that is applied to the data. This gives a distribution according to

$$\epsilon(p)|A_{D^0}(a^{gen}, p)|^2 R_4(p).$$

With this the normalisation term can be approximated by

$$\int \epsilon(p)|A_{D^0}(a,p)|^2 R_4(p) dp \approx \frac{1}{N_{sel}} \sum_i^{N_{sel}} \frac{|A_{D^0}(a,p_i)|^2}{|A_{D^0}(a^{gen},p_i)|^2}$$

where N_{sel} is the set of fully selected MC events.

To allow $\epsilon(p)$ to factor out of both the signal and background terms of equation 4.8, the background models are fit relative to the signal efficiency by using fully selected MC events to normalise the PDF when establishing the set of amplitude coefficients. The background models used in the likelihood are then

$$B_\epsilon(b_\epsilon, p) = \frac{B(b,p)}{\epsilon(p)}$$

where b_ϵ is the set of amplitude coefficients when the model is fit relative to $\epsilon(p)$. The background PDF given in 4.8 transforms as

$$\frac{B(b,p)R_4(p)}{\int B(b,p)R_4(p)dp} \to \frac{\epsilon(p)B_\epsilon(b_\epsilon,p)R_4(p)}{\int \epsilon(p)B_\epsilon(b_\epsilon,p)R_4(p)dp}$$

allowing $\epsilon(p)$ to factor out of the PDF.

A initial sample of 1 million MC events is used for the CLEO III and the CLEO-c datasets which are then subject to the detector response and full selection procedure relevant to that detector configuration, including the K^0_S background mass veto. CLEO II.V uses a re-weighted CLEO III sample due to the similarity between the configurations. After full selection the the MC samples for each configuration are in the order of 900,000 events.

The following sections will show the determination of signal and background models, $S(a,p)$ and $B_\epsilon(b_\epsilon, p)$ and signal fractions f_s. The mistag rate w was discussed in section 4.2.1.

4.6 CLEO Background Sources

For the background that remains within the signal regions of the datasets, both the background level and an amplitude model describing it must be found.

4.6.1 Flavour tagged data background determination

After the $m_{\pi\pi}$ mass veto to remove the $D^0 \to K^0_S(\pi^+\pi^-)K^+K^-$ peaking background only the combinatorial background source remains for the flavour tagged data.

Signal fractions

In order to establish the signal fraction within the signal region of the CLEO III data, fits to the $m_{KK\pi\pi}$ and ΔM distributions are performed. By integrating fitted signal and background PDFs within the signal regions of these variables the signal fraction can be determined. Figure 4.10a shows the fit to the $m_{KK\pi\pi}$ distribution after the signal cut on ΔM has been applied. A bifurcated Gaussian (a Gaussian with different width values on either side of the peak) is used as the signal PDF along with an exponential function for the background. Figure 4.10b shows the fit to the ΔM distribution after the signal $m_{KK\pi\pi}$ cut has been performed. The signal PDF used here is the sum of two bifurcated Gaussians with a common mean parameter. The background is modelled with the *RooDstD0BG* empirical function which was designed to model the background shape of $m_{D^*} - m_{D^0}$ distributions [97]. It is defined as

$$\begin{cases} (1 - \exp(-\frac{x-x_0}{c}))(\frac{x}{x_0})^A + B(\frac{x}{x_0} - 1) & : x > x_0 \\ 0 & : \text{otherwise,} \end{cases} \tag{4.10}$$

where the mass threshold, x_0, is fixed to the pion mass and the shape parameters, A, B and C, are fit parameters to be determined. The fit to $m_{KK\pi\pi}$ yields a purity of (89.7±0.5)% and the fit to ΔM a purity of (89.9±0.4)%. As these are consistent an average of the two values is taken. Similar fits for CLEO II.V are shown in figure 4.11. These too yield consistent signal fractions and the value taken for CLEO II.V is (75.9±1.9)%.

For CLEO-c 3770 and CLEO-c 4170 a *cut and count* method is used to determine the level of combinatorial background in the signal region. Within a region of phasespace containing only combinatorial background events, the number of events present is scaled to the relative area of the signal region compared to this *counting* region. It is obviously

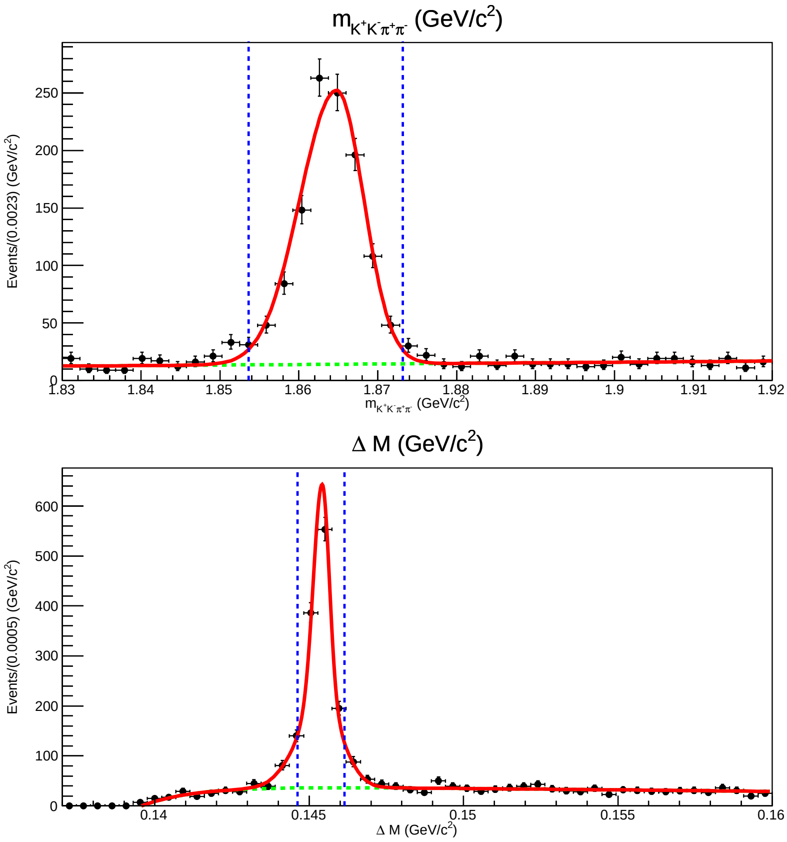

Figure 4.10: Fits to a) $m_{KK\pi\pi}$ (top) and b) ΔM (bottom) in CLEO III data after the signal requirement on the other variable has been applied. The dashed green line shows the background function, the solid red line shows the combined signal and background PDFs and the blue dashed lines indicate the signal region.

important that the level of combinatorial background is consistent between the signal and the *counting* region.

For CLEO-c 3770 data, figure 4.12 shows that for data lying within the selection band (given in equation 4.6) the background level across m_{bc} is flat up to approximately 1.878 GeV where there is a shoulder due to the kinematic limit. It is therefore possible to use the background region of $1.834 < m_{bc} < 1.854$ GeV, shown in 4.5, for the cut and count method. The signal fraction is determined to be $(87.1 \pm 0.5)\%$.

For CLEO-c 4170 the situation in more complicated. It can be clearly seen from figure 4.7 that the event density in m_{bc} and ΔE space grows with m_{bc}. Therefore when using the cut and count method, regions with the same m_{bc} range as the signal must be used.

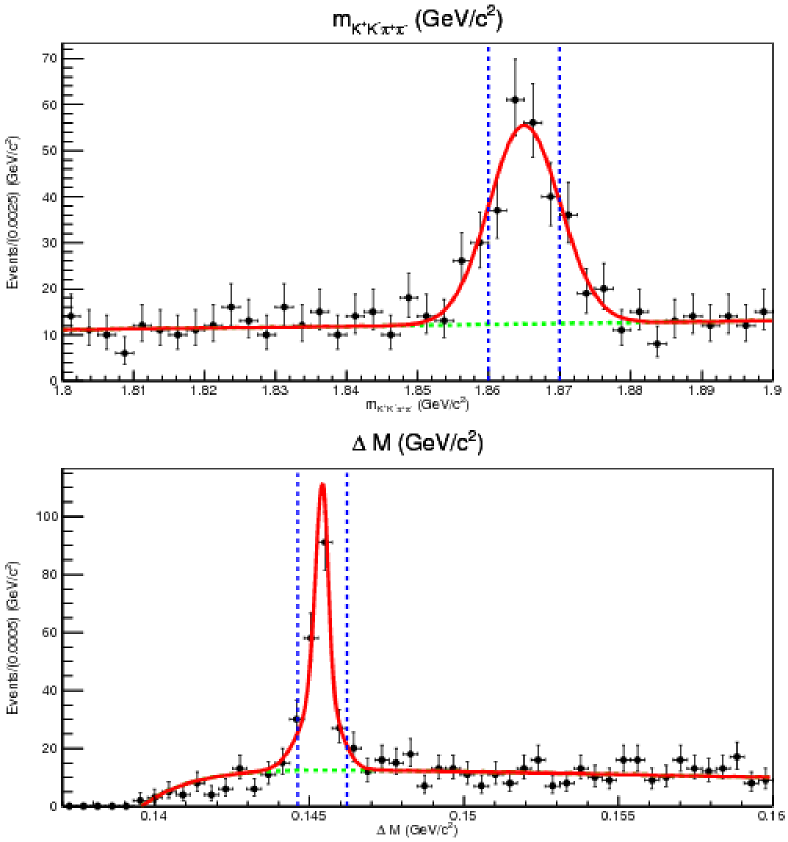

Figure 4.11: Fit to a) $m_{KK\pi\pi}$ (top) and b) ΔM (bottom) in CLEO II.V data after the signal requirement on the other variable has been applied. The dashed green line shows the background function, the solid red line shows the combined signal and background PDFs and the blue dashed lines indicate the signal region.

Bands that lie above and below the signal region are chosen, more specifically

$$\left| \sqrt{(\Delta E)^2 + (\Delta E)E_{CM} + m_{bc}^2} - m_D \right| \pm 30\text{MeV} < 10\text{MeV}$$

with $2.005 < m_{bc} < 2.030$ MeV as for the signal region. The average number of events in these two bands is 183 events. This gives a signal purity in the signal region of $(69.4 \pm 1.0)\%$.

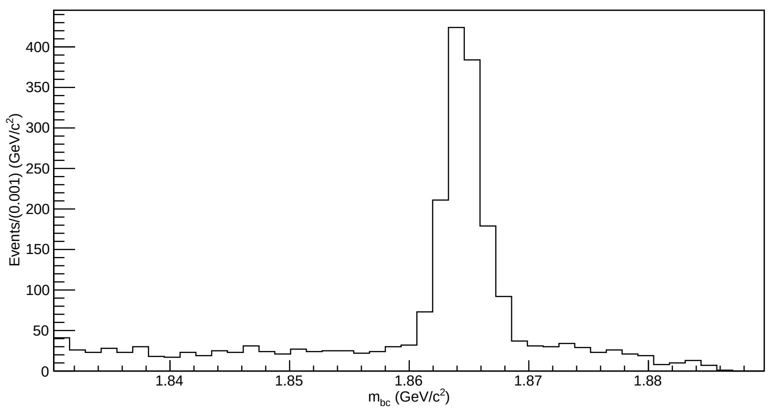

Figure 4.12: Distribution of m_{bc} for CLEO-c 3770 events lying on the band defined in equation 4.6 where $X = 15$ MeV.

Background Model determination for flavour tagged samples

Amplitude models describing the combinatorial background are determined through fits to the events in the chosen background regions detailed in section 4.4. These events are not expected to feature a real $D \to K^+K^-\pi^+\pi^-$ decay but rather random combinations of kaons, pions and sometimes resonances that happen to pass all selection criteria. Because of this, the amplitude components are added incoherently as there should be no interference between the intermediate states. Also, the angular distribution terms are omitted as the final state particles are not expected to have originated from the same D and therefore no conservation of angular momentum needs to be enforced. This leaves only the lineshapes. The background amplitude models are determined relative to efficiency corrected phasespace using fully selected Monte Carlo events for the normalisation of the PDFs. A base set of 15 amplitude components are included in the initial fit to the background samples, these amplitude components are shown in table 4.2. The component that is least significant relative to its uncertainty is removed and the fit repeated, this process continues until all remaining components have a significance greater than 2 sigma.

In the case of CLEO-c 4170, the background region lying on the signal band (bkg sample 1) (see figure 4.7) is likely to have a small contamination from real $D \to K^+K^-\pi^+\pi^-$ events due to other charm meson pair decays. The background regions used for the *cut and count* method (bkg sample 2) do not have the same $m_{KK\pi\pi}$ range as the signal events. In the absence of a single suitable region to describe the combinatorial background in the signal region, both these regions are fit. The final amplitude fit is performed using both amplitude models to describe this background and the difference between the fit results is taken as a systematic.

Table 4.3 shows the fit fractions of the amplitude components in the background models for the flavour tagged data. Large non-resonant components are seen as expected. Figures 4.13, 4.14, 4.15 and 4.16 show these fits in the 5 independent invariant mass squared projections; s_{12}, s_{23}, s_{34}, s_{123} and s_{234}. In this thesis fits to the D decay phasespace are plotted using the same Monte Carlo events that are used to normalise the PDFs during the fit routine. Plots of the fit are not smooth due to limited statistics.

Table 4.2: Base set of amplitudes for background models. If a decay is not self-conjugate the conjugate decay is also included. The notation $D^0[X] \to$ indicates that the subsequent two-body systems are in a relative X wave. For two particles that do not originate from a resonance but are in a relative partial wave state, the particles are enclosed in brackets and the partial wave given as a subscript.

Amplitude component
$D^0 \to K^- \,[K_1(1270)^+ \to \pi^+ \, K^{*0}(1430)]$
$D^0 \to K^- \,[K_1(1270)^+ \to \pi^+ \, K^{*0}(892)]$
$D^0 \to K^- \,[K_1(1270)^+ \to K^+ \, \rho^0(770)]$
$D^0 \to K^- \,[K_1(1400)^+ \to \pi^+ \, K^{*0}(892)]$
$D^0[S] \to K^{*0}(892) \, \bar{K}^{*0}(892)$
$D^0[S] \to \phi(1020) \, \rho^0(770)$
$D^0 \to K^{*0} \, (K^-\pi^+)_S$
$D^0 \to \phi(1020) \, (\pi^+\pi^-)_S$
$D^0 \to \rho^0(770) \, (\pi^+\pi^-)_S$
$D^0 \to (K^+K^-)_S \, (\pi^+\pi^-)_S$

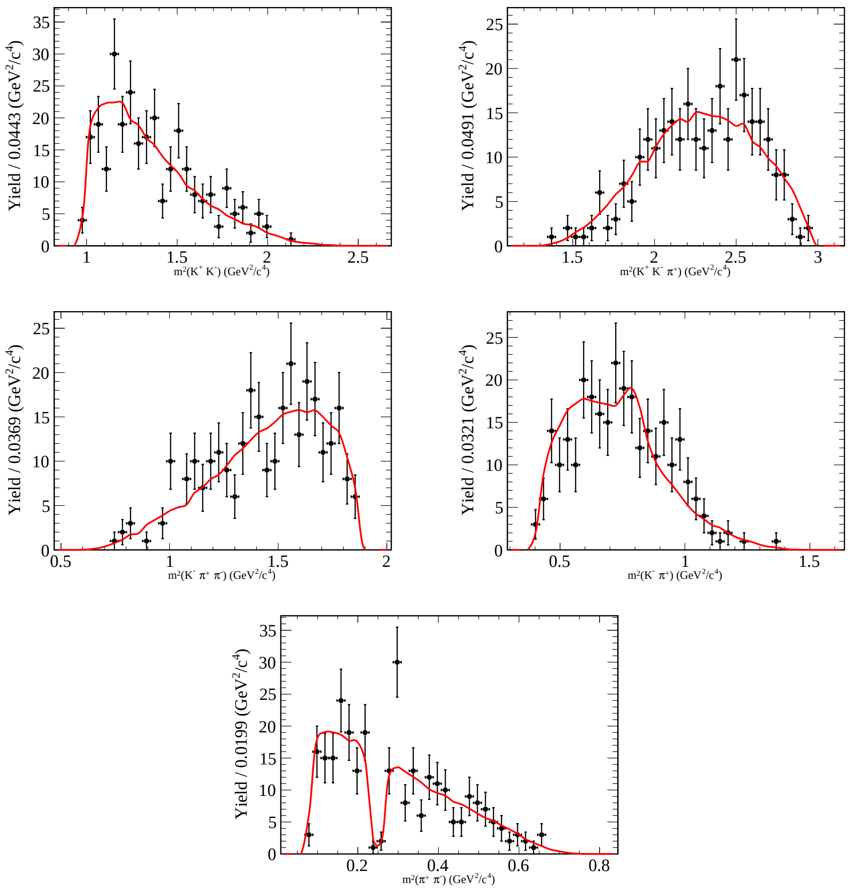

Figure 4.13: CLEO II.V background sample with fit projections overlaid.

Table 4.3: Fit fractions (%) of amplitude components used in flavour tagged background models.

Amplitude component	CLEO II.V	CLEO III	CLEO-c 3770	CLEO-c 4170 bkg sample 1 (2)
$D^0 \to K^- [K_1(1400)^+ \to \pi^+ K^{*0}(892)]$	-	-	-	$12.16 \pm 5.13(4.83 \pm 2.87)$
$D^0 \to \phi(1020)\,(\pi^+\pi^-)_S$	1.64 ± 1.42	9.55 ± 1.39	12.98 ± 1.92	$8.67 \pm 2.74(11.27 \pm 2.07)$
$D^0 \to K^{*0}\,(K^-\pi^+)_S$	6.97 ± 4.54	11.32 ± 2.85	9.94 ± 3.64	-
$D^0 \to \bar{K}^{*0}\,(K^+\pi^-)_S$	9.06 ± 4.84	13.21 ± 2.91	15.96 ± 3.73	$24.37 \pm 6.18(8.69 \pm 03.72)$
$D^0 \to \phi(1020)\,(\pi^+\pi^-)_S$	11.91 ± 6.09	13.43 ± 3.56	13.81 ± 5.06	-
$D^0 \to (K^+K^-)_S\,(\pi^+\pi^-)_S$	70.43 ± 8.05	52.50 ± 4.63	47.31 ± 6.38	$54.80 \pm 6.85(75.20 \pm 4.70)$

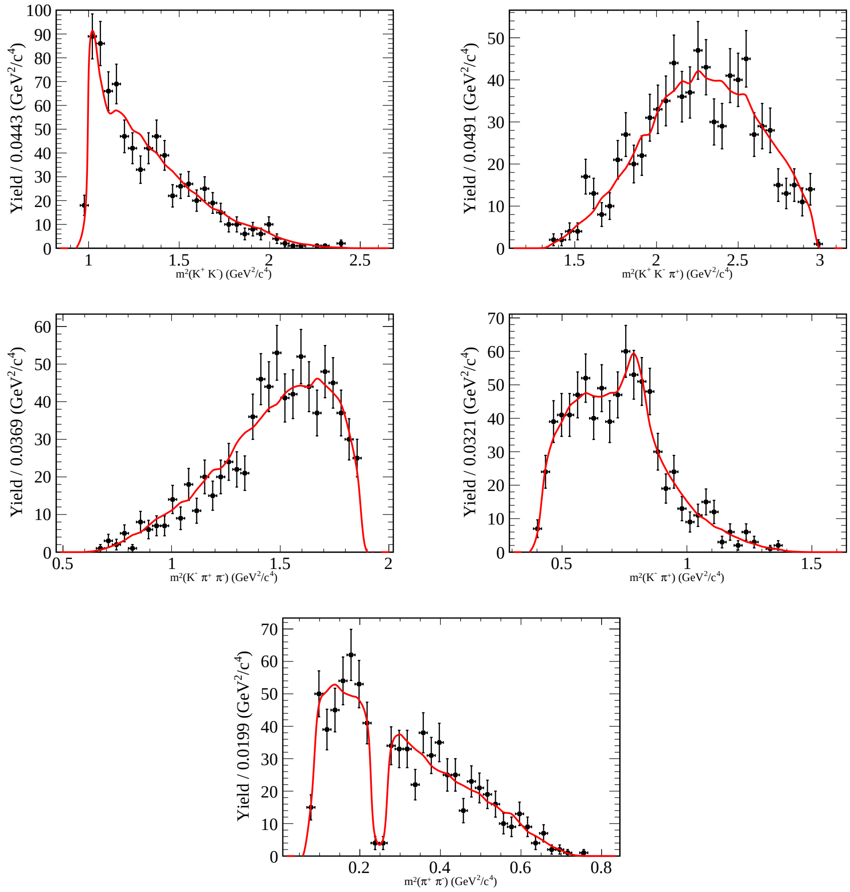

Figure 4.14: CLEO III background sample with fit projections overlaid.

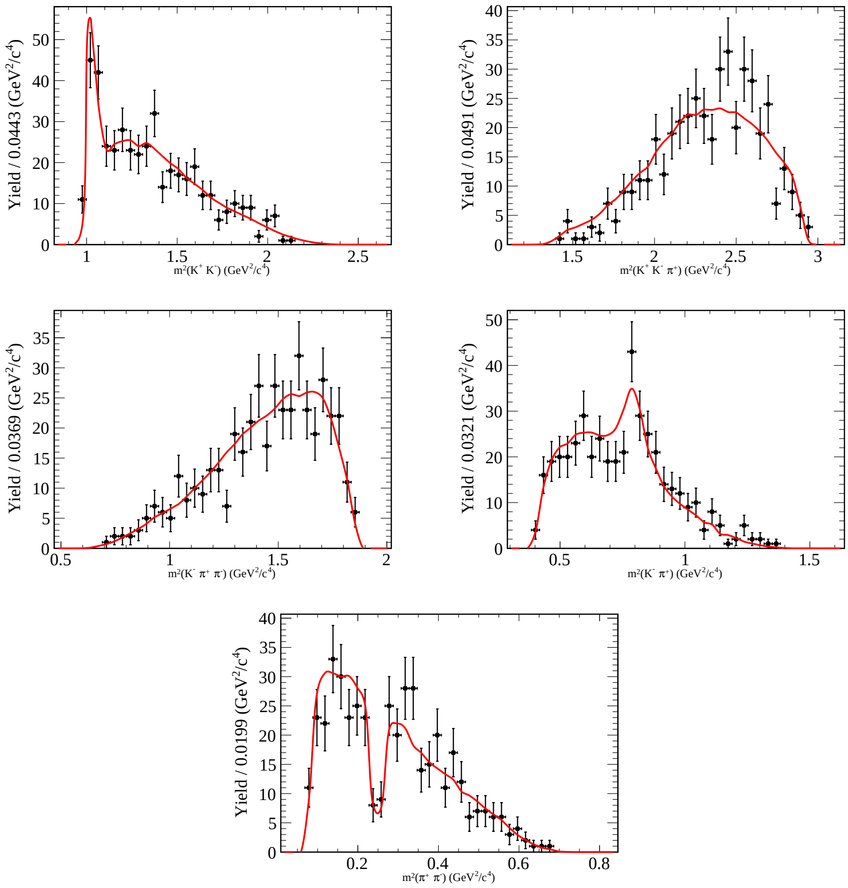

Figure 4.15: CLEO-c 3770 background sample with fit projections overlaid.

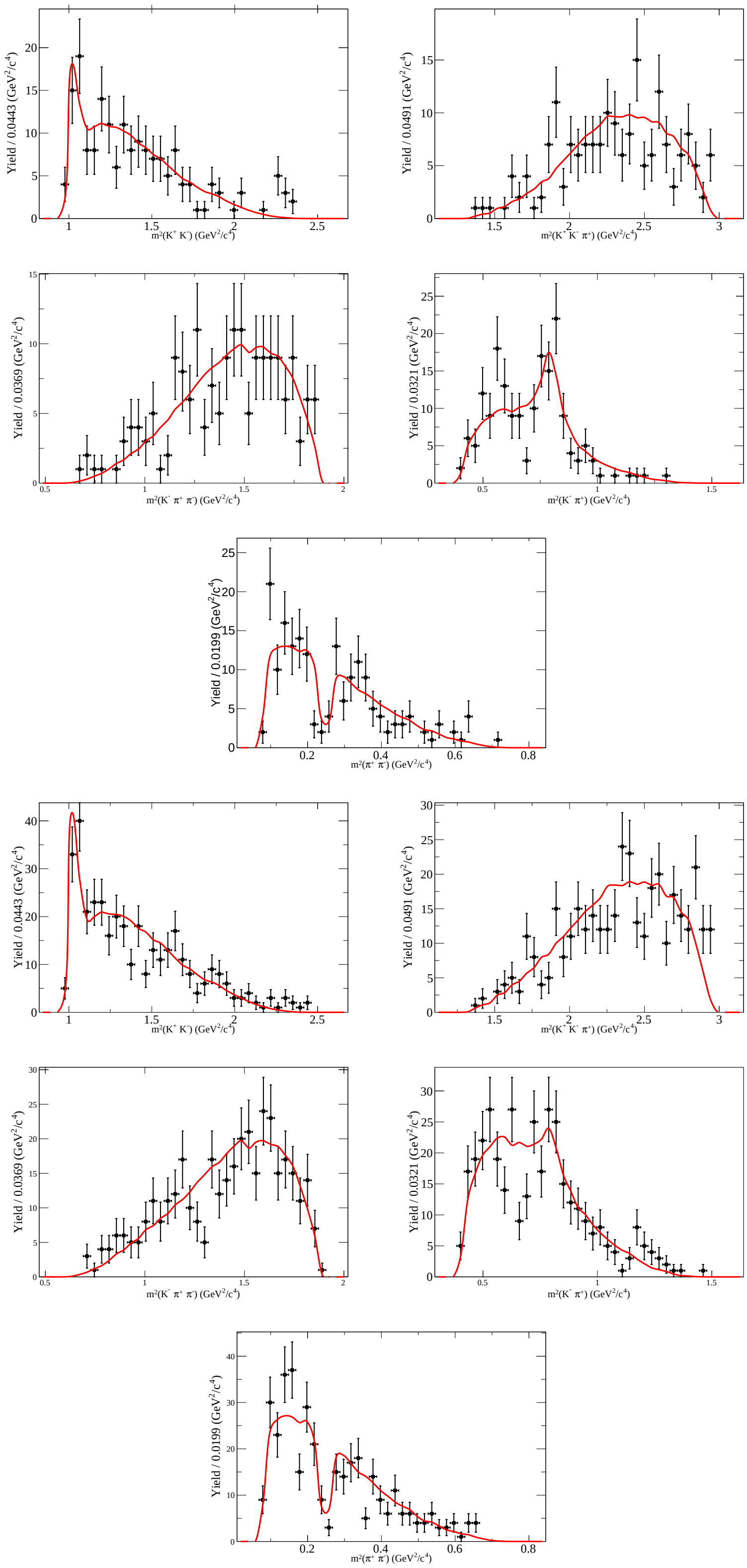

Figure 4.16: CLEO-c 4170 background samples 1 and 2 with fit projections overlaid.

4.6.2 CP tagged data background determination

The background is more complicated in the case of *CP* tagged data. Background does not only arise from the signal side D decay but also from the reconstruction of the tagging decay. In total 6 backgrounds are initially considered:

- Continuum background - this background arises from decays that are not via a $\psi(3770)$ resonance
- Flat signal side background - this is similar to the flat, combinatorial background in flavour tagged data. It was determined from MC studies to be negligible in [1]
- Peaking signal side background - this is composed of specific decays that appear in the signal region of the signal D decay. MC studies in [1] show this background is solely $D^0 \to K^0_S(\pi^+\pi^-)K^+K^-$ decays which have now been removed from the dataset
- Flat tag-side background - this is a combinatorial background of the tagging decay but the event does contain a real $D \to K^+K^-\pi^+\pi^-$ signal decay
- Peaking tag-side background - this arises due to specific decays appearing in the signal region of the tagging decay but the event does contain a real $D \to K^+K^-\pi^+\pi^-$ signal decay
- D^+D^- background - this background is from D^+D^- decays that are reconstructed as $D^0\bar{D}^0$

As the two types of tag-side background contain real $D \to K^+K^-\pi^+\pi^-$ signal decays they are modelled in the same way and can be treated together. This leaves three background types to consider; continuum, tag-side and D^+D^- background.

Signal fractions

The efficiency of the K^0_S mass veto on the signal and on the different backgrounds in *CP* tagged data is determined to be approximately constant. Because of this background levels are taken from [1] where the background levels were determined from large MC samples. These levels are corrected to account for the different treatment of the background categories in this analysis and are given in table 4.4 for each of the *CP* tagged datasets.

Table 4.4: *CP* tagged data background fractions

Dataset	D^+D^-	Continuum	Tag-side backgrounds	Total
CP-even	0.048±0.003	0.136±0.011	0.050±0.005	0.234±0.012
CP-odd	0.002±0.001	0.008±0.002	0.034±0.006	0.044±0.006
$K_s\pi^+\pi^-$				
bin 1	0.014±0.005	0.062±0.021	0.011±0.009	0.087±0.023
bin 2	0.009±0.003	0.041±0.015	0.0 ±0.0	0.05 ±0.015
bin 3	0.004±0.004	0.018±0.017	0.004±0.004	0.026±0.018
bin 4	0.006±0.004	0.026±0.019	0.015±0.015	0.047±0.025
bin 5	0.004±0.002	0.017±0.007	0.005±0.006	0.026±0.01
bin 6	0.001±0.001	0.003±0.003	0.0 ±0.0	0.004±0.003
bin 7	0.001±0.001	0.004±0.004	0.015±0.015	0.02 ±0.016
bin 8	0.005±0.002	0.024±0.008	0.009±0.009	0.038±0.012
bin -1	0.014±0.003	0.065±0.016	0.015±0.015	0.094±0.022
bin -2	0.013±0.006	0.061±0.029	0.0 ±0.0	0.074±0.030
bin -3	0.003±0.002	0.015±0.01	0.0 ±0.0	0.018±0.010
bin -4	0.0 ±0.0	0.0±0.0	0.044±0.025	0.044±0.025
bin -5	0.003±0.001	0.015±0.005	0.0 ±0.0	0.018±0.005
bin -6	0.019±0.007	0.085±0.03	0.0 ±0.0	0.104±0.031
bin -7	0.009±0.005	0.04 ±0.023	0.044±0.024	0.093±0.034
bin -8	0.006±0.002	0.027±0.01	0.0 ±0.0	0.033±0.010
$K_L\pi^+\pi^-$				
bin 1	0.035±0.005	0.017±0.003	0.059±0.009	0.111±0.011
bin 2	0.028±0.009	0.013±0.004	0.047±0.014	0.088±0.017
bin 3	0.011±0.004	0.005±0.002	0.019±0.007	0.035±0.008
bin 4	0.023±0.008	0.011±0.004	0.038±0.013	0.072±0.016
bin 5	0.038±0.009	0.018±0.004	0.064±0.015	0.120±0.018
bin 6	0.025±0.007	0.012±0.003	0.042±0.011	0.079±0.013
bin 7	0.028±0.008	0.013±0.004	0.047±0.014	0.088±0.017
bin 8	0.055±0.009	0.026±0.004	0.092±0.015	0.173±0.018
bin -1	0.028±0.004	0.013±0.002	0.046±0.007	0.087±0.008
bin -2	0.030±0.009	0.014±0.004	0.051±0.015	0.068±0.018
bin -3	0.045±0.016	0.022±0.007	0.076±0.026	0.143±0.031
bin -4	0.000±0.000	0.000±0.000	0.000±0.000	0.000±0.000
bin -5	0.056±0.017	0.026±0.028	0.093±0.028	0.175±0.043
bin -6	0.018±0.006	0.009±0.010	0.031±0.010	0.058±0.015
bin -7	0.050±0.013	0.024±0.022	0.085±0.022	0.159±0.034
bin -8	0.026±0.007	0.012±0.012	0.044±0.012	0.082±0.018

Background model determination for *CP* tagged samples

The continuum background can be treated like the combinatorial background of the flavour tagged data. It is modelled by an incoherent sum of amplitude components that are determined in a fit to a representative sample of the background from simulation. The amplitudes considered are as shown in table 4.2 and the fit procedure the same as that for flavour tagged background samples. The fit can be seen in figure 4.17.

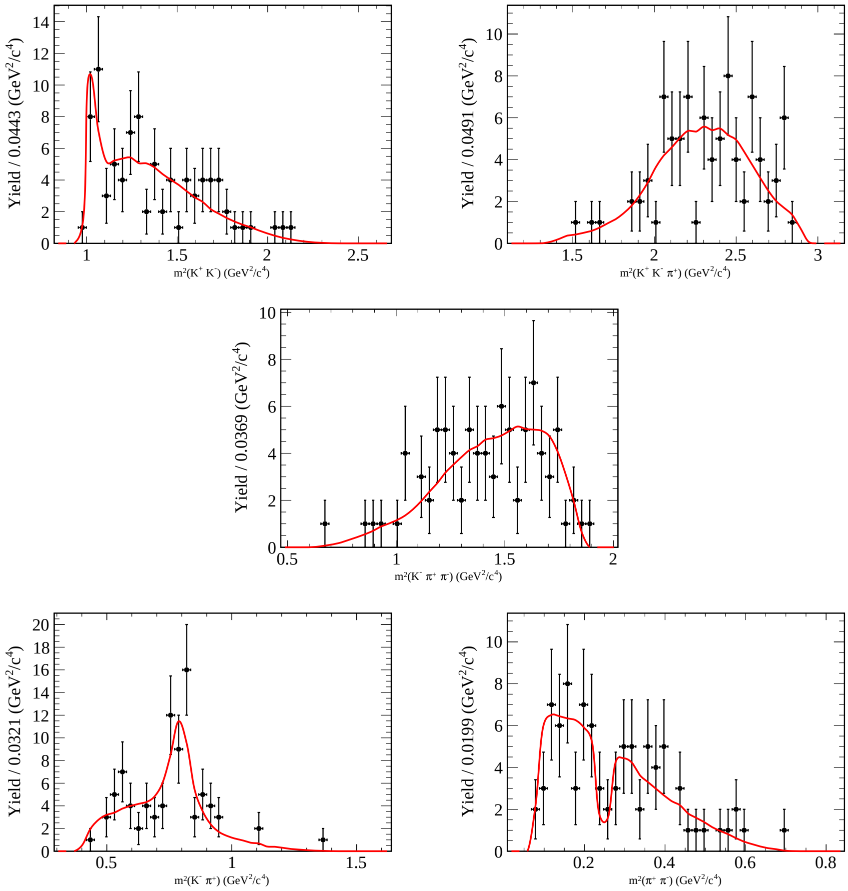

Figure 4.17: *CP* tagged continuum background sample with fit overlaid.

In the case of the tag-side backgrounds the event contains a real $D \to K^+K^-\pi^+\pi^-$ signal decay, however the *CP* state of the signal decay cannot be inferred as the tag decay was not a definite *CP* state. The signal decay is therefore equally likely to be a D^0 or $\bar{D}^0$ decay and can be described by

$$\frac{1}{2}(|A_{D^0}(p)|^2 + |A_{\bar{D}^0}(p)|^2) \tag{4.11}$$

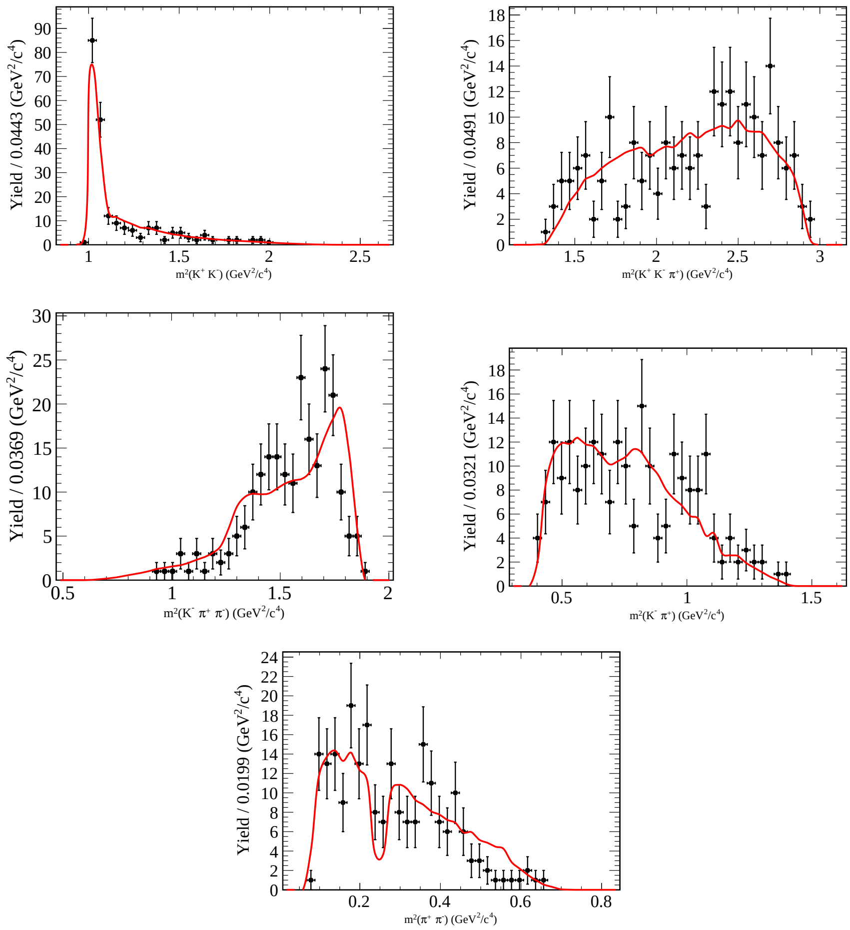

Figure 4.18: *CP* tagged D^+D^- background sample with fit overlaid.

where $A_{D^0}(p)$ is a coherent amplitude for the signal decay based on a preliminary fit to flavour tagged data only (the amplitude model used is that obtained in the first stage of the LASSO method reported in section 4.8).

The D^+D^- background is assumed to take the same mathematical form as $D^0\bar{D}^0$ decays. The coherent model for $A_{D^0}(p)$ is determined through a fit to a representative sample of these background events taken from simulation. Figure 4.18 shows this fit. Table 4.5 gives the fit fractions for the amplitude components in the background models of the *CP* tagged datasets.

Table 4.5: Fit fractions (%) of amplitude components used in the background models for *CP* tagged data

Amplitude component	Continuum	Tag-side bkg	D^+D^- bkg
$D^0 \to K^- [K_1(1270)^+ \to \pi^+ K^{*0}(1430)]$	-	6.75±1.37	-
$D^0 \to K^- [K_1(1270)^+ \to \pi^+ K^{*0}(892)]$	-	8.99±1.89	-
$D^0 \to K^+ [K_1(1270)^- \to \pi^- \bar{K}^{*0}(892)]$	-	1.40±0.66	10.24±3.28
$D^0 \to K^- [K_1(1270)^+ \to K^+ \rho^0(770)]$	-	10.24±1.81	-
$D^0 \to K^+ [K_1(1270)^- \to K^- \rho^0(770)]$	-	5.05±0.70	-
$D^0 \to K^- [K_1(1270)^+ \to K^+ \omega^0(782)]$	-	0.49±0.24	-
$D^0 \to K^- [K_1(1400)^+ \to \pi^+ K^{*0}(892)]$	-	14.27±2.06	-
$D^0 \to K^+ [K_1(1400)^- \to \pi^- \bar{K}^{*0}(892)]$	-	2.59±0.86	-
$D^0 \to K^- [K^*(1680)^+ \to \pi^+ K^{*0}(892)]$	-	2.98±0.89	-
$D^0 \to K^+ [K^*(1680)^- \to \pi^- \bar{K}^{*0}(892)]]$	-	0.66±0.41	-
$D^0[S] \to K^{*0}(892)\, \bar{K}^{*0}(892)$	39.26±9.69	12.04±1.28	-
$D^0[P] \to K^{*0}(892)\, \bar{K}^{*0}(892)$	-	3.60±0.88	-
$D^0[D] \to K^{*0}(892)\, \bar{K}^{*0}(892)$	-	4.02±0.66	-
$D^0[S] \to \phi(1020)\, \rho^0(770)$	-	26.46±1.36	11.42±3.36
$D^0[P] \to \phi(1020)\, \rho^0(770)$	-	1.79±0.42	-
$D^0[D] \to \phi(1020)\, \rho^0(770)$	-	6.43±1.07	-
$D^0 \to K^{*0}\, (K^-\pi^+)_S$	19.49±10.69	-	-
$D^0 \to \phi(1020)\, (\pi^+\pi^-)_S$	11.40±4.27	-	34.49±4.25
$D^0 \to \rho^0(770)\, (\pi^+\pi^-)_S$	-	-	17.63±3.93
$D^0 \to (K^+K^-)_S\, (\pi^+\pi^-)_S$	29.85±8.58	10.08±1.25	27.76±4.56

4.7 Fit to data

Table 4.6 summarises the final data samples used in this analysis.

Table 4.6: Selected data samples

Sample	Yield	Purity (%)
Flavor tagged		
CLEO II.V	237	75.9±1.9
CLEO III	1163	89.8±0.4
CLEO-c 3770	1300	87.1±0.5
CLEO-c 4170	598	69.4±1.0
CP tagged		
CP odd	42	96.0±1.2
CP even	29	77.0±0.6
$K_s\pi^+\pi^-$	50	95.2±1.8 (bin average)
$K_L\pi^+\pi^-$	72	90.3±1.8 (bin average)

4.7.1 LASSO method

The presence of some resonant states in the $D^0 \to K^+K^-\pi^+\pi^-$ decay is clear from the projections of the D decay phasespace (see figure 4.20 and 4.21), for instance the $\phi(1020)$ resonance in the s_{12} projection. However any further structure cannot be inferred due to the many overlapping and interfering amplitude components. This amplitude analysis employs the LASSO method [98]. Traditionally, to select amplitude components to include in an amplitude model, a stepwise approach is used. An initial, basic model has additional amplitudes added one at a time and the additional component is rejected if the χ^2 of the fit does not improve by a pre-defined amount. This method is suboptimal for amplitude analyses due to the interference effects between components. This method risks never considering two interfering amplitudes together in the same model and so an amplitudes' contribution may never be observed, leading to an over simplified model. The Least Absolute Shrinkage and Selection Operator (LASSO) method is a data-driven method used to determine which amplitude components to include in the model; it is a regularisation method which allows control over the model complexity. All amplitude components are considered together in a fit giving them opportunity to contribute to the model through their interference with one another. A term is added to the minimisation quantity $-2\log\mathcal{L}$ that penalises the fit for including too many amplitude components

$$-2\log\mathcal{L} \to -2\log\mathcal{L} + \lambda\left[\sum_i \sqrt{\int |a_i A_i(p)|^2 dp}\right]. \tag{4.12}$$

The λ parameter is known as the LASSO regularisation parameter and controls the complexity of the model by weighting the regularisation term. As $\lambda \to 0$ there is no penalty for including more and more amplitude components and the result is an over complex and over-fit model. Conversely as $\lambda \to \infty$ the penalty term for even a small number of amplitude components is large and the model is over simplified with only a few non-zero amplitude coefficients. The LASSO method therefore determines the best model for a given, fixed level of complexity. To determine the optimal level of complexity, this analysis uses the Bayesian Information Criteria (BIC)

$$\mathrm{BIC}(\lambda) = -2\log\mathcal{L} + r\log n \tag{4.13}$$

where r is the number of amplitude components with fit fractions above 0.5% and n is the number of events in the data sample. By scanning over λ values and minimising the BIC metric, a balance between improvement in the fit quality and complexity of the model is found. The full LASSO method involves the following steps:

- Begin with a large set of possible amplitude components
- Scan over λ values, minimising equation 4.12 for each λ
- Determine the value of λ that minimises BIC(λ). The collection of amplitude components selected for this particular model (those with fit fractions $> 0.5\%$) is the LASSO model
- Re-run the fit without the penalty term in the likelihood using only the amplitude components in the LASSO model. This ensures correct errors on the fit parameters.

Prior to the LASSO procedure the complex coefficients, a_i, for each amplitude component included in the fit are normalised so that the integral of $|a_i A_i(p)|^2$ over phasespace is unity.

4.8 Results of Amplitude Analysis

The LASSO method is used to determine which amplitude components should contribute to the $D^0 \to K^+K^-\pi^+\pi^-$ decay model. In total 58 amplitude components are considered, these can be seen in table 4.7. Due to the vast number of potential amplitude components and limits on computational resources arising when handling multiple datasets, a staged LASSO method, initially considering only the flavour tagged data, is used. At each stage, a degree of judgement is applied to the model selection.

Table 4.7: Decays considered in $D^0 \to K^+K^-\pi^+\pi^-$ LASSO model building. For non self -conjugate decay modes the CP conjugate decay is also considered.

Decay channel
Cascade
$D^0 \to K^- \, [K^*(1410)^+ \to \pi^+ \, K^{*0}(892)]$
$D^0 \to K^- \, [K_1(1270)^+[S,D] \to \pi^+ \, K^{*0}(892)]$
$D^0 \to K^- \, [K_1(1270)^+[S,D] \to \pi^+ \, K^{*0}(1430)]$
$D^0 \to K^- \, [K_1(1270)^+[S,D] \to K^+ \, \rho^0(770)]$
$D^0 \to K^- \, [K_1(1270)^+[S,D] \to K^+ \, \omega^0(782)]$
$D^0 \to K^- \, [K_1(1400)^+[S,D] \to \pi^+ \, K^{*0}(892)]$
$D^0 \to K^- \, [K_2^*(1430)^+ \to \pi^+ \, K^{*0}(892)]$
$D^0 \to K^- \, [K_2^*(1430)^+ \to K^+ \, \rho^0(770)]$
$D^0 \to K^- \, [K^*(1680)^+ \to \pi^+ \, K^{*0}(892)]$
$D^0 \to K^- \, [K^*(1680)^+ \to K^+ \, \rho^0(770)]$
Quasi-2-body
$D^0[S,P,D] \to K^{*0}(892) \, \bar{K}^{*0}(892)$
$D^0[S,P,D] \to \phi(1020) \, \rho^0(770)$
$D^0 \to \phi(1020) \, \omega^0(782)$
$D^0[P,D] \to f_2(1270)^0 \, \phi(1020)$
Single-resonant
$D^0 \to \rho^0(770) \, (K^+K^-)_S$
$D^0[S,P,D] \to \rho^0(770) \, (K^+K^-)_P$
$D^0 \to K^{*0} \, (K^-\pi^+)_S$
$D^0[S,P,D] \to K^{*0} \, (K^-\pi^+)_P$
$D^0 \to \phi(1020) \, (\pi^+\pi^-)_S$
$D^0[S,P,D] \to \phi(1020) \, (\pi^+\pi^-)_P$
$D^0 \to f_0(980) \, (\pi^+\pi^-)_S$
$D^0 \to f_0(980) \, (K^+K^-)_S$
Non-resonant
$D^0 \to (K^+K^-)_S \, (\pi^+\pi^-)_S$

The staged LASSO method is based on the assumption that the $D^0 \to K^+K^-\pi^+\pi^-$ decay is primarily modelled by doubly resonant decays i.e. cascade and quasi-2-body decays, rather than those with non-resonant components. It should be noted that in the case of decays that are not self-conjugate, if LASSO picks an amplitude component but not its CP conjugate decay, the conjugate decay is also considered in the next stage. In stage 1 we LASSO only the doubly resonant decays along with the simplest non-resonant

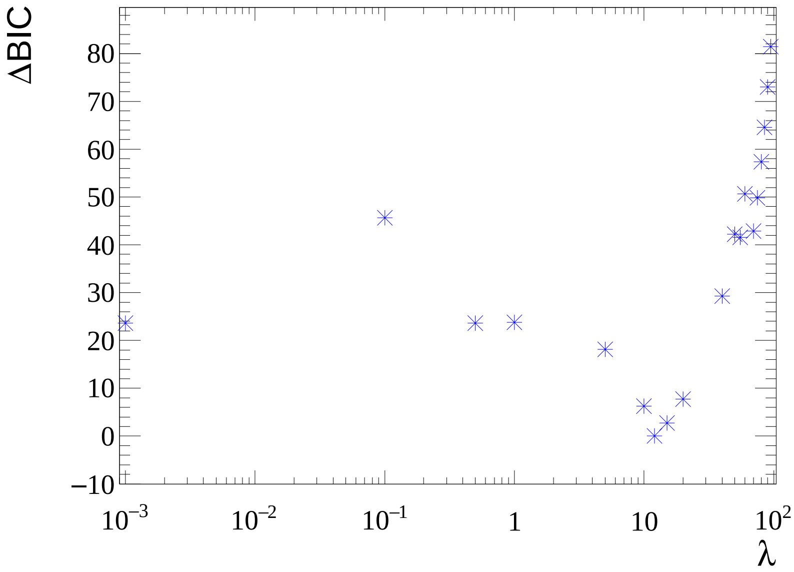

Figure 4.19: Stage 1 LASSO - regularisation factor λ against BIC(λ) value.

component $D^0 \to (K^+K^-)_S\,(\pi^+\pi^-)_S$. Figure 4.19 shows a plot of the regularisation factor, λ, against the resulting BIC(λ) values. A clear minimum is observed and table 4.8 shows the amplitude components selected by stage 1 of the LASSO method. The fit fractions quoted in this table are from a repeat of the fit where only the chosen 17 amplitude components are considered with no penalty term, because only then are the errors unbiased.

In stage 2 the components selected in stage 1 are re-LASSO-ed with the single-resonant components shown in table 4.7. The components $D^0 \to f_0(980)\,(\pi^+\pi^-)_S$ and $D^0 \to f_0(980)\,(K^+K^-)_S$ have the same $D \to SS$ angular distribution as the simple non-resonant amplitude component. This leads to artificially large interference effects and so the $D^0 \to f_0(980)\,(\pi^+\pi^-)_S$ and $D^0 \to f_0(980)\,(K^+K^-)_S$ components are considered as a replacement for the simple non-resonant amplitude component in an alternative model. LASSO stages 1 and 2 pick the same top 7 amplitude components, supporting our initial assumption of the amplitude model consisting primarily of doubly resonant decays. With the exception of $D^0[P] \to \phi(1020)\,(\pi^+\pi^-)_P$, only components of the form $D^0 \to V\,(hh)_S$[3] are selected from the pool of single resonant components. The selection of $D^0[P] \to \phi(1020)\,(\pi^+\pi^-)_P$ is accompanied by the de-selection of

[3]Where h is a π or K

Table 4.8: Amplitude components with fit fractions (%) chosen by stage 1 of LASSO method

Amplitude component	Fit fraction
$D^0 \to K^- [K_1(1270)^+ \to \pi^+ K^{*0}(892)]$	8.99 ± 1.89
$D^0 \to K^+ [K_1(1270)^- \to \pi^- \bar{K}^{*0}(892)]$	1.40 ± 0.66
$D^0 \to K^- [K_1(1270)^+ \to \pi^+ K^{*0}(1430)]$	6.75 ± 1.37
$D^0 \to K^- [K_1(1270)^+ \to K^+ \rho^0(770)]$	10.24 ±1.81
$D^0 \to K^+ [K_1(1270)^- \to K^- \rho^0(770)]$	5.05 ± 0.70
$D^0 \to K^- [K_1(1270)^+ \to K^+ \omega^0(782)]$	0.49 ± 0.24
$D^0 \to K^- [K_1(1400)^+ \to \pi^+ K^{*0}(892)]$	14.27 ± 2.06
$D^0 \to K^+ [K_1(1400)^- \to \pi^- \bar{K}^{*0}(892)]$	2.59 ± 0.86
$D^0 \to K^- [K^*(1680)^+ \to \pi^+ K^{*0}(892)]$	2.98 ± 0.89
$D^0 \to K^+ [K^*(1680)^- \to \pi^- \bar{K}^{*0}(892)]$	0.66 ± 0.41
$D^0[S] \to K^{*0}(892)\, \bar{K^{*0}}(892)$	12.04 ± 1.28
$D^0[P] \to K^{*0}(892)\, \bar{K^{*0}}(892)$	3.60 ± 0.88
$D^0[D] \to K^{*0}(892)\, \bar{K^{*0}}(892)$	4.02 ± 0.66
$D^0[S] \to \phi(1020)\, \rho^0(770)$	26.46 ± 1.36
$D^0[P] \to \phi(1020)\, \rho^0(770)$	1.79 ± 0.42
$D^0[D] \to \phi(1020)\, \rho^0(770)$	6.43 ± 1.07
$D^0 \to (K^+K^-)_S\, (\pi^+\pi^-)_S$	10.08 ± 1.25
Sum	117.82 ± 4.20

$D^0[P] \to \phi(1020)\, \rho^0(770)$ by LASSO stage 2, given that these components share the same angular structure this suggests that the two components are interchangeable. In line with our initial assumption, and also because the presence of the S wave and the D wave components suggest the presence of the P wave component, $D^0[P] \to \phi(1020)\, \rho^0(770)$ is chosen going forward.

Studying the LASSO models resulting from λ values close to that which is optimal, the components chosen are found to be very consistent. It is seen however that the fit cannot distinguish between $K^*(1680)^+ \to \pi^+ K^{*0}(892)$ and $K_1(1410)^+ \to \pi^+ K^{*0}(892)$, both of which peak outside of the kinematically allowed phasespace of the D decay, leaving only the resonance's tail in the fitted region. For this reason an alternative model is considered where $K_1(1410)^+$ replaces $K^*(1680)^+$ in the final model.

The final fit is a hybrid of LASSO stage 1 and 2 where the components chosen in stage 1 and the single-resonant $D^0 \to V\, (hh)_S$ components chosen in stage 2 are fit together. Of these components 6 are considered insignificant relative to their uncertainty and removed from the fit with no significant impact on the χ^2. Table 4.9 shows the fitted parameter values and fit fractions for the final model fit (known as *the* LASSO model going forward) where the CP tagged data is now included in the fit. The uncertainties on the fit fractions are found from the RMS of 10,000 pseudo-experiments where the real and imaginary parts of the complex amplitude coefficients are varied within their uncertainties taking into account the full covariance matrix. Also quoted here is the model-dependent error which is derived from the RMS of the fit fractions found using the alternative models given in table 4.12. The interference fractions between amplitude components can be seen in appendix A.2.

The χ^2 goodness-of-fit metric is determined by binning the phasespace into N bins and evaluating

$$\chi^2 = \sum_{b=1}^{N_{\text{bins}}} \frac{(N_b - N_b^{\text{exp}})^2}{N_b^{\text{exp}}}$$

where N_b is the number of data events that fall in bin b and N_b^{exp} is the number of events predicted by the PDF fit to the data to fall in bin b. The bins are constructed in the phasespace such that at least 25 data points fall in each bin allowing for a reliable χ^2 value. The effective number of degrees of freedom for this fit is determined using 100 pseudo-experiments (as explained further in section 4.9) as the relatively small dataset used in this analysis results in negative degrees of freedom when using the traditional $ndof = (N_{bins} - 1) - N_{par}$ value. The χ^2 per effective degree of freedom ($\chi^2/ndof$) for the final LASSO model is 1.494 with $ndof = 116$ showing a good fit quality for an amplitude fit of this complexity. Figures 4.20 and 4.21 show the invariant 2 and 3-body mass distributions with fit projections, a reasonable agreement between data and the fit model can be seen. As mentioned in section 2, invariant mass combinations cannot fully describe the angular distribution of the decay. To show the description of the angular structure of the decay we use the transversity basis. This basis consists of:

- Acoplanarity angle χ - the angle between the two decay planes formed by the K^+K^- combination and the $\pi^+\pi^-$ combination in the rest frame of the D
- Helicity variable $\cos\theta_{K^+}$ - the cosine of the angle, θ_{K^+}, between the K^+ momentum and the D flight direction in the rest frame of the two-body K^+K^- system

- Helicity variable $\cos\theta_{\pi^+}$ - the cosine of the angle, θ_{π^+}, between the π^+ momentum and the D flight direction in the rest frame of the two-body $\pi^+\pi^-$ system.

The fits to flavour tagged data for this basis are shown in figure 4.22.

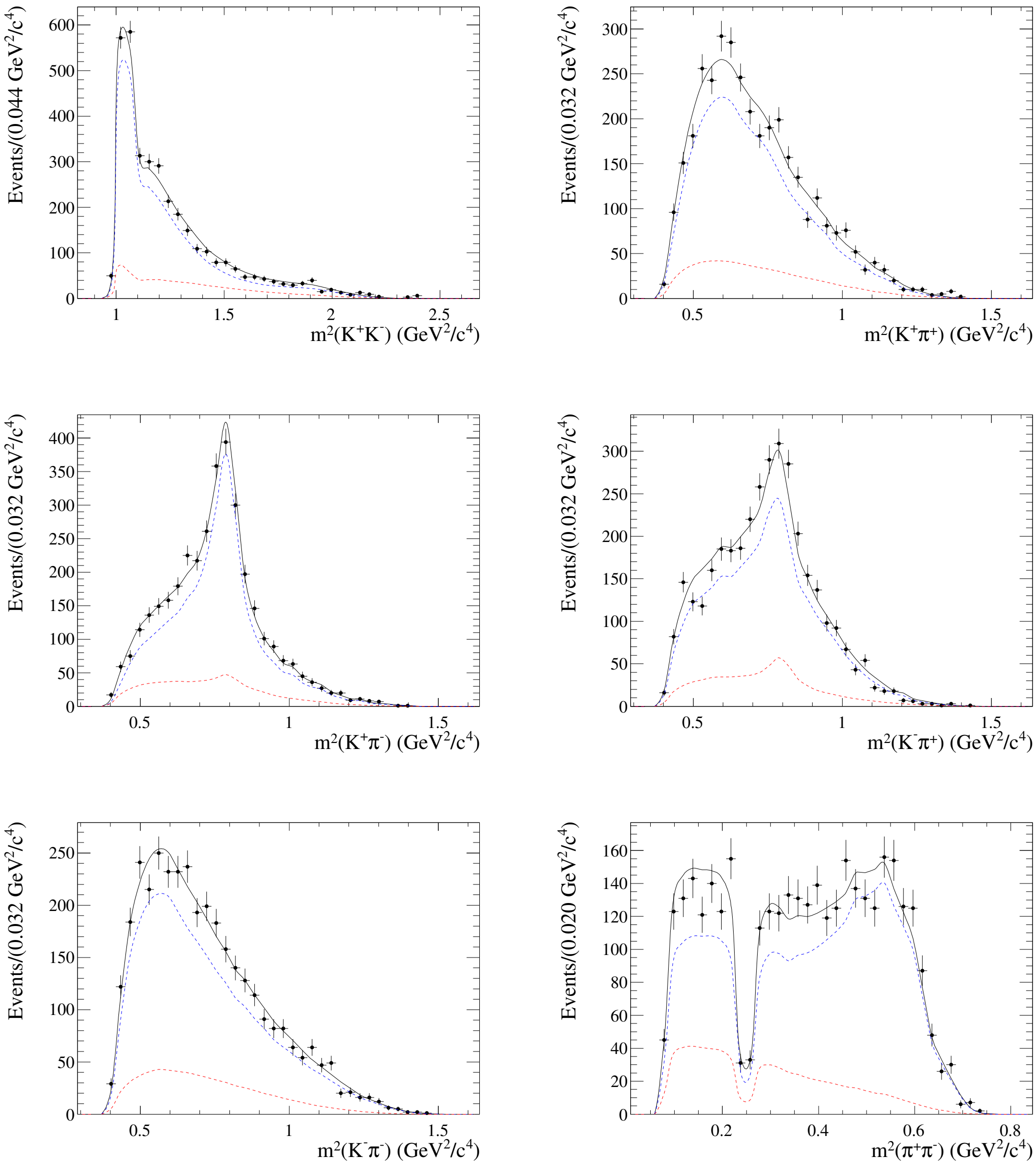

Figure 4.20: Invariant 2-body mass distributions with fit projection. The solid black line shows the combined fit projection, the dashed red line shows the background fit and the dashed blue line the signal fit.

Table 4.9: Real and imaginary part of the complex amplitude coefficients and the fit fractions of each component of the LASSO model. The first uncertainty is statistical and the second systematic. The third uncertainty for the fit fractions arise from the alternative models.

Decay channel	$\Re(a_i)$	$\Im(a_i)$	$F_i(\%)$
$D^0 \to K^- [K_1(1270)^+ \to \pi^+ K^*(892)^0]$	6.36 ± 1.24 ± 3.41	-6.86 ± 1.37 ± 3.38	5.5 ± 1.4 ± 2.7 ± 2.0
$D^0 \to K^- [K_1(1270)^+ \to \pi^+ K^*(1430)^0]$	34.93 ± 3.74 ± 8.39	5.66 ± 4.50 ± 6.92	6.1 ± 1.2 ± 1.3 ± 1.3
$D^0 \to K^- [K_1(1270)^+ \to K^+ \rho(770)^0]$	-17.63 ± 2.44 ± 5.26	-11.51 ± 2.27 ± 3.38	9.1 ± 1.5 ± 1.9 ± 0.1
$D^0 \to K^+ [\bar{K}_1(1270)^- \to K^- \rho(770)^0]$	9.87 ± 1.75 ± 2.61	-12.91 ± 1.49 ± 3.82	5.4 ± 0.7 ± 1.1 ± 0.7
$D^0 \to K^- [K_1(1270)^+ \to K^+ \omega(782)]$	3.78 ± 3.34 ± 3.81	-9.36 ± 2.35 ± 5.87	0.6 ± 0.3 ± 0.4 ± 0.2
$D^0 \to K^- [K_1(1400)^+ \to \pi^+ K^*(892)^0]$	-8.08 ± 5.11 ± 8.93	-36.92 ± 4.35 ± 10.98	12.4 ± 2.6 ± 3.9 ± 5.0
$D^0 \to K^- [K^*(1680)^+ \to \pi^+ K^*(892)^0]$	132.69 ± 15.81 ± 27.13	-35.45 ± 19.13 ± 29.21	3.6 ± 0.8 ± 1.0 ± 0.3
$D^0[S] \to K^*(892)^0 \bar{K}^*(892)^0$	822.04 ± 81.84 ± 126.47	-350.52 ± 105.58 ± 234.41	4.5 ± 0.8 ± 1.1 ± 1.7
$D^0[P] \to K^*(892)^0 \bar{K}^*(892)^0$	-975.58 ± 115.30 ± 241.90	-476.35 ± 148.15 ± 162.11	3.6 ± 0.7 ± 1.4 ± 0.5
$D^0[D] \to K^*(892)^0 \bar{K}^*(892)^0$	-4786.72 ± 408.23 ± 503.72	985.18 ± 533.86 ± 941.34	4.0 ± 0.6 ± 0.7 ± 0.2
$D^0[S] \to \phi(1020)\, \rho(770)^0$	5158.65 (fixed)	0.00 (fixed)	28.1 ± 1.3 ± 1.7 ± 0.3
$D^0[P] \to \phi(1020)\, \rho(770)^0$	-1552.19 ± 203.06 ± 271.29	-354.72 ± 432.81 ± 531.39	1.6 ± 0.3 ± 0.6 ± 0.3
$D^0[D] \to \phi(1020)\, \rho(770)^0$	5208.02 ± 685.26 ± 840.57	791.86 ± 954.63 ± 689.75	1.7 ± 0.4 ± 0.4 ± 0.2
$D^0 \to K^*(892)^0 (K^-\pi^+)_S$	43.52 ± 4.59 ± 9.73	-1.20 ± 5.20 ± 5.27	5.8 ± 1.2 ± 2.1 ± 0.0
$D^0 \to \phi(1020) (\pi^+\pi^-)_S$	29.62 ± 7.39 ± 12.19	-54.93 ± 5.65 ± 11.92	4.0 ± 0.6 ± 1.3 ± 1.7
$D^0 \to (K^+K^-)_S (\pi^+\pi^-)_S$	0.42 ± 0.05 ± 0.10	0.49 ± 0.05 ± 0.09	11.1 ± 1.2 ± 2.1 ± 0.7
Sum			106.9 ± 4.5 ± 6.9 ± 6.1

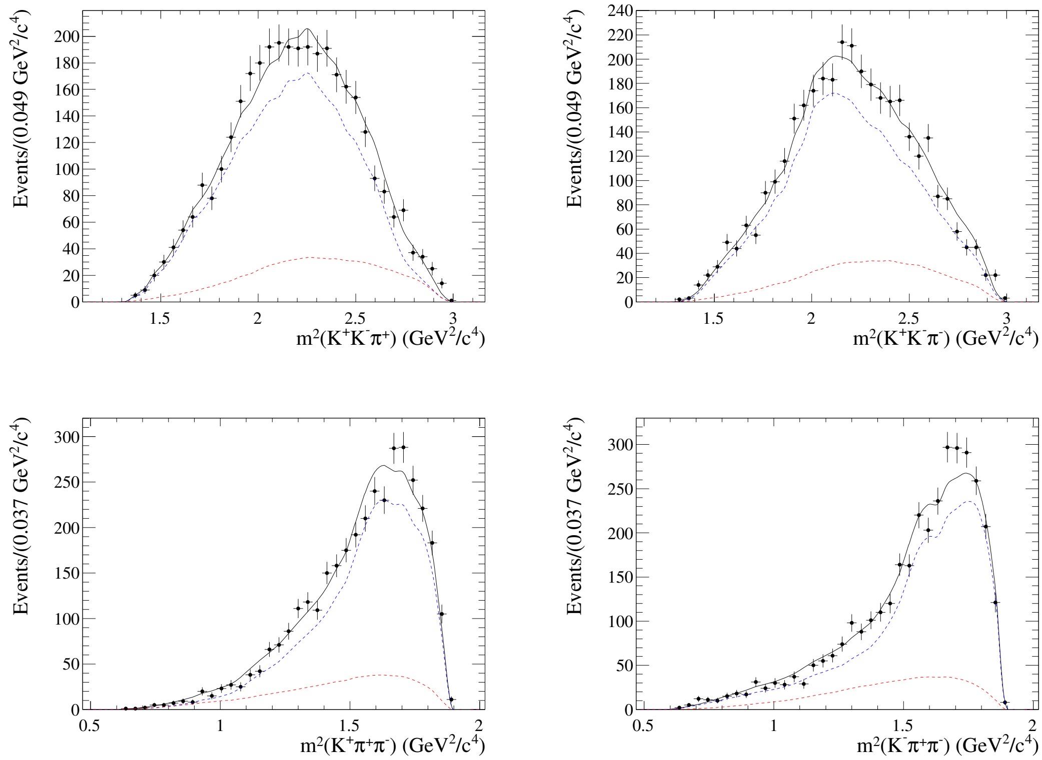

Figure 4.21: Invariant 3-body mass distributions with fit projection. The solid black line shows the combined fit projection, the dashed red line shows the background fit and the dashed blue line the signal fit.

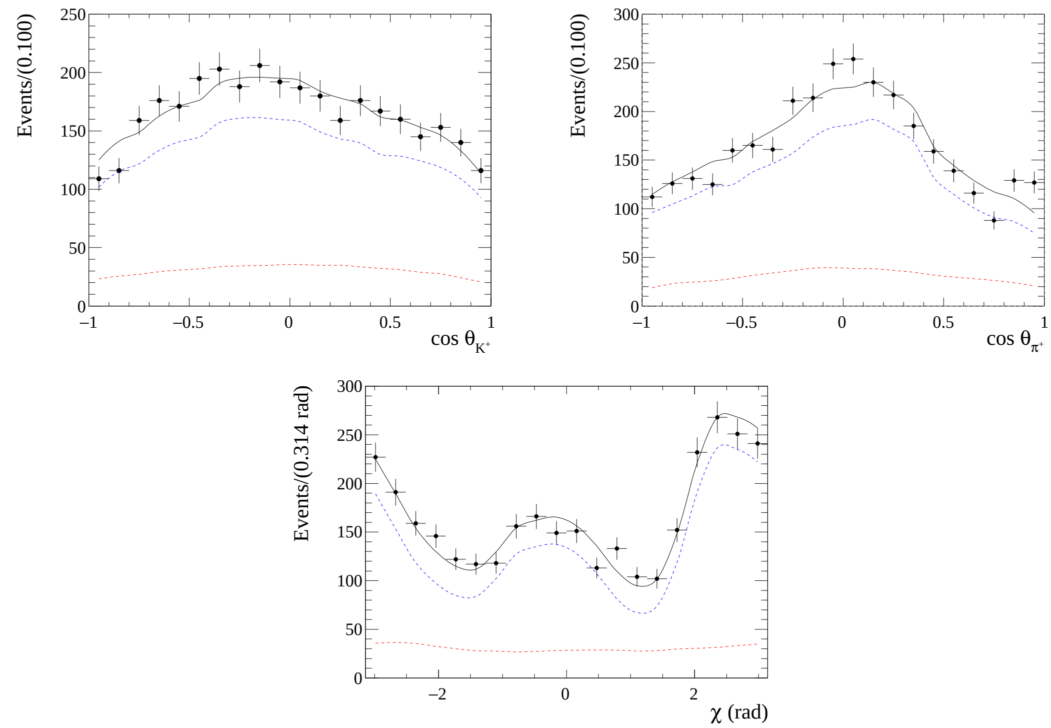

Figure 4.22: Angular distribution projections in the transversity basis, to the flavor-tagged data sample. The total contribution is shown in solid black, the signal component is shown in blue (dashed) and the background component in red (dashed).

4.8.0.1 Addition of *CP* tagged data

The *CP* tagged data represents less than 10% of the statistics for this analysis. However the *CP* tagged events are sensitive to the phase motion over the D decay phasespace as explained in section 4.2.1. The effect of the *CP* tagged data on the fitted amplitude component parameters can be seen in table 4.10 where we compare a fit with and without the *CP* tagged data.

Table 4.10: Real and imaginary part of the complex amplitude coefficients for fits with and without the contribution of *CP* tagged data

Decay channel	With CP tagged data		Without CP tagged data	
	$\Re(a_i)$	$\Im(a_i)$	$\Re(a_i)$	$\Im(a_i)$
$D^0 \to K^- [K_1(1270)^+ \to \pi^+ K^{*0}(892)]$	6.36±1.23	-6.86±1.37	6.59±1.28	-6.99±1.37
$D^0 \to K^- [K_1(1270)^+ \to \pi^+ K^{*0}(1430)]$	34.93±3.75	5.66±4.50	32.87±3.85	5.54±4.42
$D^0 \to K^- [K_1(1270)^+ \to K^+ \rho^0(770)]$	-17.63±2.44	-11.51±2.27	-16.06±2.55	-11.07±2.19
$D^0 \to K^+ [\bar{K_1}(1270)^- \to K^- \rho^0(770)]$	9.87±1.75	-12.91±1.49	8.28±1.89	-13.36±1.44
$D^0 \to K^- [K_1(1270)^+ \to K^+ \omega^0(782)]$	3.78±3.34	-9.36±2.35	2.54±3.31	-10.36±2.41
$D^0 \to K^- [K_1(1400)^+ \to \pi^+ K^{*0}(892)]$	-8.08±5.11	-36.92±4.36	-9.59±5.16	-37.34±4.37
$D^0 \to K^- [K^*(1680)^+ \to \pi^+ K^{*0}(892)]$	132.69±15.81	-35.45±19.13	131.74±16.08	-38.20±19.60
$D^0[S] \to K^{*0}(892)\, \bar{K^{*0}}(892)$	822.04±81.84	-350.52±105.58	830.07±83.43	-362.64±106.77
$D^0[P] \to K^{*0}(892)\, \bar{K^{*0}}(892)$	-975.58±115.30	-476.35±148.15	-1022.49±115.23	-432.07±154.06
$D^0[D] \to K^{*0}(892)\, \bar{K^{*0}}(892)$	-4786.72±408.23	985.18±533.86	-4809.61±414.99	993.86±541.07
$D^0[S] \to \phi(1020)\, \rho^0(770)$	5158.64 (fixed)	0.0 (fixed)	5158.64 (fixed)	0.0 (fixed)
$D^0[P] \to \phi(1020)\, \rho^0(770)$	-1552.19±203.06	-354.72±432.81	-1552.52±209.07	-543.81±443.46
$D^0[D] \to \phi(1020)\, \rho^0(770)$	5208.02±685.26	791.86±954.63	5228.63±710.94	924.93±993.01
$D^0 \to K^{*0}\, (K^-\pi^+)_S$	43.52±4.59	-1.20±5.20	43.40±4.73	-3.14±5.29
$D^0 \to \phi(1020)\, (\pi^+\pi^-)_S$	29.62±7.39	-54.93±5.65	32.73±7.42	-49.50±5.99
$D^0 \to (K^+K^-)_S\, (\pi^+\pi^-)_S$	0.42±0.05	0.49±0.05	0.41±0.05	0.46±0.05

4.8.0.2 *CP*-violation in the D^0 system

Up to this point this analysis assumes no *CP*-violation in the D^0 system. As a search for new physics effects the LASSO model is fit to the flavour tagged samples such that the fit parameters a_i are allowed to take different values for D^0 and $\bar{D}^0$ events. The PDF used to fit the D^0 flavour tagged events is shown in equation 4.14 where (w) is the mistag rate and ε_{D^0} is the efficiency of tagging a D^0 signal decay. The PDF used to fit the $\bar{D}^0$ flavour tagged events is shown in 4.15. These fits happen simultaneously.

$$\mathrm{PDF}_{\mathrm{D^0}} = \frac{(1-w)\times\varepsilon_{D^0}\times|A_{D^0}(a,p)|^2 + w\times\varepsilon_{\bar{D}^0}\times|A_{\bar{D}^0}(\bar{a},p)|^2}{\frac{1}{2}(\varepsilon_{D^0}\times\int|A_{D^0}(a,p)|^2dp + \varepsilon_{\bar{D}^0}\times\int|A_{\bar{D}^0}(\bar{a},p)|^2dp)} \tag{4.14}$$

$$\mathrm{PDF}_{\mathrm{\bar{D}^0}} = \frac{(1-w)\times\varepsilon_{\bar{D}^0}\times|A_{\bar{D}^0}(\bar{a},p)|^2 + w\times\varepsilon_{D^0}\times|A_{D^0}(a,p)|^2}{\frac{1}{2}(\varepsilon_{D^0}\times\int|A_{D^0}(a,p)|^2dp + \varepsilon_{\bar{D}^0}\times\int|A_{\bar{D}^0}(\bar{a},p)|^2dp)} \tag{4.15}$$

The direct *CP* asymmetry for each amplitude component can be determined from the fit fractions F_i and $\bar{F}_i$ determined from the fit to D^0 and $\bar{D}^0$ events respectively by

$$\mathcal{A}^i_{CP} \equiv \frac{F_i - \bar{F}_i}{F_i + \bar{F}_i}.$$

These A_{CP} values along with their significance are displayed in table 4.11. The four cascade $D^0 \to K^- K_1(1270)^+$ components are combined in a weighted average as *CP*-violation can only occur in the initial weak part of the decay and not the subsequent strong decays. Also combined in a weighted average are the [S, P, D] wave components of $D \to VV$ decays, the Feynman diagrams for these [S, P, D] decay modes are the same and so they share the same weak decay properties.

A global direct *CP* asymmetry can also be determined from the integrated decay rates

$$\mathcal{A}_{CP} \equiv \frac{\Gamma(D^0\to K^+K^-\pi^+\pi^-) - \Gamma(\overline{D}^0\to K^+K^-\pi^+\pi^-)}{\Gamma(D^0\to K^+K^-\pi^+\pi^-) + \Gamma(\overline{D}^0\to K^+K^-\pi^+\pi^-)} = \frac{\varepsilon_{D^0}N_{D^0} - \varepsilon_{\bar{D}^0}N_{\bar{D}^0}}{\varepsilon_{D^0}N_{D^0} + \varepsilon_{\bar{D}^0}N_{\bar{D}^0}}, \tag{4.16}$$

where N_{D^0} ($N_{\bar{D}^0}$) is the number of D^0 ($\overline{D}^0$) signal decays and ε_{D^0} ($\varepsilon_{\bar{D}^0}$) is the efficiency of tagging a D^0 ($\overline{D}^0$) signal decay. For CLEO-c data, the ratio of the signal $\overline{D}^0$ and D^0

Table 4.11: Direct CP asymmetry for each component of the LASSO model along with significance. The first uncertainty given is statistical, the second is a systematic uncertainty and the third the result from alternative models.

Decay channel	$\mathcal{A}^i_{CP}$ (%)	Significance (σ)
$D^0 \to K^- \, K_1(1270)^+$	$+25.3 \pm 9.7 \pm 9.2 \pm 8.81$	1.58
$D^0 \to K^+ \, \bar{K}_1(1270)^-$	$-50.4 \pm 12.0 \pm 15.9 \pm 2.39$	2.51
$D^0 \to K^- \, K_1(1400)^+$	$+9.2 \pm 15.1 \pm 20.3 \pm 1.12$	0.36
$D^0 \to K^- \, K^*(1680)^+$	$-17.1 \pm 21.8 \pm 18.0 \pm 4.15$	0.59
$D^0 \to K^{*0}(892)\bar{K^{*0}}(892)$	$-4.6 \pm 9.0 \pm 9.84 \pm 5.69$	0.31
$D^0 \to \phi(1020)\, \rho^0(770)$	$+1.5 \pm 4.6 \pm 8.0 \pm 0.51$	0.14
$D^0 \to K^{*0}\, (K^-\pi^+)_S$	$-13.1 \pm 17.9 \pm 29.7 \pm 9.38$	0.36
$D^0 \to \phi(1020)\, (\pi^+\pi^-)_S$	$-4.0 \pm 18.0 \pm 44.6 \pm 1.16$	0.08
$D^0 \to (K^+K^-)_S\, (\pi^+\pi^-)_S$	$+8.2 \pm 10.9 \pm 16.9 \pm 2.68$	0.40

tagging efficiencies is

$$\frac{\varepsilon_{\bar{D}^0}}{\varepsilon_{D^0}} = 0.9899 \pm 0.0015$$

as taken from [99]. No asymmetry is found for the reconstruction of the slow pion in CLEO II.V and CLEO III data samples so the efficiency ratio here is set to (1.0±0.015)% [100]. The global direct CP asymmetry is then

$$\mathcal{A}_{CP} = [+1.84 \pm 1.74\,(\text{stat}) \pm 0.30\,(\text{syst})]\%. \tag{4.17}$$

CP asymmetry measurements at both the global and amplitude component level indicate no evidence of CP-violation in the D system.

4.8.0.3 Alternative models

Several alternative amplitude models are reported. These are:

- A: LASSO model where for those decays that are not self-conjugate the conjugate decay is included
- B: LASSO model where $D^0 \to K^-\,[K^*(1680)^+]$ is replaced with $D^0 \to K^-\,[K_1(1410)^+]$
- C: LASSO model where the non-resonant component is replaced with the $D^0 \to f_0(980)\,(\pi^+\pi^-)_S$ and $D^0 \to f_0(980)\,(K^+K^-)_S$ components

- D: The model reported in the previous amplitude analysis of this decay channel using this dataset [1].

Table 4.12 shows the fit fractions of the components included in each of these alternative models as well as their χ^2 per effective degree of freedom ($\chi^2/ndof$) values.

Table 4.12: Fit fractions for alternative models. Model A: LASSO model with all conjugate decays, model B: LASSO model with replacement of $K^*(1680)$ resonance with $K^*(1410)$ resonance, model C: LASSO model with replacement of flat, non-resonant component with $D^0 \to f_0(980)\,(\pi^+\pi^-)_S$ and $D^0 \to f_0(980)\,(K^+K^-)_S$ and model D: $D \to KK\pi\pi$ model reported in [1]

Decay Mode	Model A	Model B	Model C	Model D
$D^0 \to K^-\,[K_1(1270)^+ \to \pi^+\,K^{*0}(892)]$	5.76 ± 1.65	6.06 ± 1.45	8.23 ± 1.29	9.38 ± 0.98
$D^0 \to K^+\,[[\bar{K}_1(1270)^- \to \pi^-\,\bar{K}^{*0}(892)]$	1.12 ± 0.76	-	-	0.50 ± 0.28
$D^0 \to K^-\,[K_1(1270)^+ \to \pi^+\,K^{*0}(1430)]$	5.78 ± 1.63	6.31 ± 1.20	9.51 ± 1.64	-
$D^0 \to K^+\,[[\bar{K}_1(1270)^- \to \pi^-\,\bar{K}^{*0}(1430)]$	0.69 ± 0.60	-	-	-
$D^0 \to K^-\,[K_1(1270)^+ \to K^+\,\omega^0(782)]$	0.78 ± 0.41	0.58 ± 0.26	0.94 ± 0.34	-
$D^0 \to K^+\,[[\bar{K}_1(1270)^- \to K^-\,\omega^0(782)]$	0.39 0.37	-	-	-
$D^0 \to K^-\,[K_1(1270)^+ \to K^+\,\rho^0(770)]$	9.06 ± 1.85	9.43 ± 1.56	10.45 ± 1.79	7.58 ± 0.95
$D^0 \to K^+\,[\bar{K}_1(1270)^- \to K^-\,\rho^0(770)]$	1.42 ± 0.76	4.84 ± 0.73	5.05 ± 0.83	6.10 ± 0.83
$D^0 \to K^-\,[K_1(1400)^+ \to \pi^+\,K^{*0}(892)]$	14.05 ± 3.13	14.51 ± 2.82	22.28 ± 3.52	-
$D^0 \to K^+\,[\bar{K}_1(1400)^+ \to \pi^-\,\bar{K}^{*0}(892)]$	1.17 ± 1.00	-	-	-
$D^0 \to K^-\,[K^*(1680)^+ \to \pi^+\,K^{*0}(892)]$	2.97 ± 0.95	-	4.60 ± 0.92	-
$D^0 \to K^+\,[\bar{K}^*(1680)^+ \to \pi^-\,\bar{K}^{*0}(892)]$	0.68 ± 0.43	-	-	-
$D^0[S] \to K^{*0}(892)\,\bar{K}^{*0}(892)$	4.60 ± 1.19	4.54 ± 0.77	4.84±0.81	9.14 ± 1.29
$D^0[P] \to K^{*0}(892)\,\bar{K}^{*0}(892)$	3.06 ± 1.10	3.91 ± 0.70	5.14 ± 0.78	-
$D^0[D] \to K^{*0}(892)\,\bar{K}^{*0}(892)$	3.55 ± 0.75	3.83 ± 0.63	5.08 ± 0.76	-
$D^0[S] \to \phi(1020)\,\rho^0(770)$	27.13 ± 1.59	27.47 ± 1.32	27.66± 1.35	31.08 ± 1.38
$D^0[P] \to \phi(1020)\,\rho^0(770)$	1.91 ± 0.47	1.80 ± 0.39	1.70 ± 0.37	-
$D^0[D] \to \phi(1020)\,\rho^0(770)$	1.58 ± 0.46	1.47 ± 0.42	1.70 ± 0.45	2.60 ± 0.61
$D^0 \to K^{*0}\,(K^-\pi^+)_S$	5.33±1.40	5.75 ± 1.21	6.20 ± 1.34	-
$D^0 \to \bar{K}^{*0}\,(K^+\pi^-)_S$	1.26 ± 0.83	-	-	-
$D^0 \to \phi(1020)\,(\pi^+\pi^-)_S$	4.35 ± 0.85	4.47 ± 0.69	5.40 ± 0.76	7.86 ± 0.88
$D^0 \to K^-\,[K_1(1410)^+ \to \pi^+\,K^{*0}(892)]$	-	3.35 ± 0.78	-	3.23 ± 0.69
$D^0 \to K^+\,[\bar{K}_1(1410)^+ \to \pi^-\,\bar{K}^{*0}(892)]$	-	-	-	5.55 ± 0.77
$D^0 \to (K^+K^-)_S\,(\pi^+\pi^-)_S$	10.14 ± 1.41	10.82 ± 1.22	-	-
$D^0 \to f_0(980)\,(\pi^+\pi^-)_S$	-	-	1.32 ± 0.76	-
$D^0 \to f_0(980)\,(K^+K^-)_S$	-	-	1.01 ± 0.64	-
$\{K^-\pi^+\}_P\,\{K^+\pi^-\}_S$	-	-	-	10.69 ± 1.10
Sum	106.76 ± 5.83	109.13 ± 4.70	121.11± 5.38	93.72± 3.10
$\chi^2/ndof$	1.490	1.503	1.707	1.754

4.9 Systematic uncertainties

The systematic uncertainties in this analysis are divided into two sources; model-dependent uncertainties that arise from fixed parameters in the amplitude model fit and experimental uncertainties. The process for determining systematic uncertainties is in general the same. The fit to the data is repeated with a single parameter (or set of parameters) that accounts for a certain systematic effect changed. The difference in the value of each fit parameter between this refit and the LASSO model is assigned as a systematic uncertainty. The systematic uncertainties from all effects are added in quadrature. Often quoted in the following is the difference in the fit parameter value divided by the statistical error on the fit parameter, this gives a more informative *relative shift* value for each parameter.

Fitter bias

In order to test for potential biases in the amplitude fitter, a toy Monte Carlo study is performed. An ensemble of one hundred toy MC data samples (including both flavour tagged and *CP* tagged data) are generated using the signal and background PDFs of the LASSO model. The yields in each event category are Poisson distributed around their values in data and as such these MC data samples reflect the real data samples except for efficiency and resolution effects. A pull study is performed using phasespace events to normalise the PDFs in the fitting routines. The pull for a fit parameter X, which has generation value X_{gen} and new fit value X_{fit} with error X_{error}, is defined as

$$X_{\text{pull}} = \frac{X_{\text{fit}} - X_{\text{gen}}}{X_{\text{error}}}.$$

The mean pull value for each of the fit parameters is multiplied by the statistical error for that fit parameter in the LASSO model and taken as a systematic uncertainty. The results of the pull study are shown in table 4.13, it can be seen that the width of the pulls are compatible with unity.

This study is not only used to test for potential fitter bias but also to determine the effective number of degrees of freedom ($ndof$) required in the goodness-of-fit metric,

Table 4.13: Pull study for imaginary and real parts of amplitude coefficients, a_i, using 100 toy MC fits to test for fitter bias.

Component	Pull mean	Pull width
$D^0 \to K^- \, [K_1(1270)^+ \to \pi^+ \, K^{*0}(892)] \; \Re(a_i)$	-0.090±0.095	0.944±0.067
$D^0 \to K^- \, [K_1(1270)^+ \to \pi^+ \, K^{*0}(892)] \; \Im(a_i)$	0.040±0.109	1.08±0.076
$D^0 \to K^- \, [K_1(1270)^+ \to \pi^+ \, K^{*0}(1430)] \; \Re(a_i)$	-0.274±0.102	1.017±0.072
$D^0 \to K^- \, [K_1(1270)^+ \to \pi^+ \, K^{*0}(1430)] \; \Im(a_i)$	0.190±0.101	1.008±0.071
$D^0 \to K^- \, [K_1(1270)^+ \to K^+ \, \rho^0(770)] \; \Re(a_i)$	0.292±0.109	1.082±0.077
$D^0 \to K^- \, [K_1(1270)^+ \to K^+ \, \rho^0(770)] \; \Im(a_i)$	-0.042±0.101	1.001±0.071
$D^0 \to K^+ \, [\bar{K_1}(1270)^- \to K^- \, \rho^0(770)] \; \Re(a_i)$	-0.100±0.104	1.033±0.073
$D^0 \to K^+ \, [\bar{K_1}(1270)^- \to K^- \, \rho^0(770)] \; \Im(a_i)$	-0.306±0.103	1.028±0.073
$D^0 \to K^- \, [K_1(1270)^+ \to K^+ \, \omega^0(782)] \; \Re(a_i)$	0.157±0.107	1.061±0.075
$D^0 \to K^- \, [K_1(1270)^+ \to K^+ \, \omega^0(782)] \; \Im(a_i)$	-0.178±0.098	0.973±0.069
$D^0 \to K^- \, [K_1(1400)^+ \to \pi^+ \, K^{*0}(892)] \; \Re(a_i)$	-0.057±0.111	1.102±0.078
$D^0 \to K^- \, [K_1(1400)^+ \to \pi^+ \, K^{*0}(892)] \; \Im(a_i)$	0.312±0.100	0.991±0.070
$D^0 \to K^- \, [K^*(1680)^+ \to \pi^+ \, K^{*0}(892)] \; \Re(a_i)$	0.010±0.118	1.176±0.083
$D^0 \to K^- \, [K^*(1680)^+ \to \pi^+ \, K^{*0}(892)] \; \Im(a_i)$	0.043±0.092	0.918±0.065
$D^0[S] \to K^{*0}(892) \, \bar{K^{*0}}(892) \; \Re(a_i)$	-0.357±0.096	0.958±0.068
$D^0[S] \to K^{*0}(892) \, \bar{K^{*0}}(892) \; \Im(a_i)$	-0.091±0.108	1.075±0.076
$D^0[P] \to K^{*0}(892) \, \bar{K^{*0}}(892) \; \Re(a_i)$	0.015±0.104	1.035±0.073
$D^0[P] \to K^{*0}(892) \, \bar{K^{*0}}(892) \; \Im(a_i)$	0.226±0.089	0.884±0.063
$D^0[D] \to K^{*0}(892) \, \bar{K^{*0}}(892) \; \Re(a_i)$	0.069±0.100	0.991±0.070
$D^0[D] \to K^{*0}(892) \, \bar{K^{*0}}(892) \; \Im(a_i)$	0.013±0.105	1.042±0.074
$D^0[S] \to \phi(1020) \, \rho^0(770) \; \Re(a_i)$	0.0±0.0	0.0±0.0
$D^0[S] \to \phi(1020) \, \rho^0(770) \; \Im(a_i)$	0.0±0.0	0.0±0.0
$D^0[P] \to \phi(1020) \, \rho^0(770) \; \Re(a_i)$	-0.128±0.106	1.052±0.074
$D^0[P] \to \phi(1020) \, \rho^0(770) \; \Im(a_i)$	-0.112±0.117	1.169±0.083
$D^0[D] \to \phi(1020) \, \rho^0(770) \; \Re(a_i)$	0.009±0.101	1.005±0.071
$D^0[D] \to \phi(1020) \, \rho^0(770) \; \Im(a_i)$	0.152±0.106	1.052±0.074
$D^0 \to K^{*0} \, (K^-\pi^+)_S \; \Re(a_i)$	-0.309±0.096	0.953±0.067
$D^0 \to K^{*0} \, (K^-\pi^+)_S \; \Im(a_i)$	0.228±0.102	1.014±0.072
$D^0 \to \phi(1020) \, (\pi^+\pi^-)_S \; \Re(a_i)$	-0.446±0.099	0.990±0.070
$D^0 \to \phi(1020) \, (\pi^+\pi^-)_S \; \Im(a_i)$	0.292±0.109	1.087±0.077
$D^0 \to (K^+K^-)_S \, (\pi^+\pi^-)_S \; \Re(a_i)$	-0.044±0.084	0.840±0.059
$D^0 \to (K^+K^-)_S \, (\pi^+\pi^-)_S \; \Im(a_i)$	-0.020±0.097	0.969±0.069

Table 4.14: Mass and width parameters of resonant particles used in the fit [22].

Particle	Mass (MeV)	Width (MeV)
$K^*(1680)$	1717±27	322±110
$K^{*0}(1430)$	1425±50	270±80
$K_1(1410)$	1414±15	232±21
$K_1(1400)$	1403±7	174±13
$K_1(1270)$	1272±7	90±20
$\phi(1020)$	1019.46±0.02	4.27±0.03
$f_0(980)$	990±20	40±100
$K^{*0}(892)$	895.81 ±0.19	47.4±0.6
$\omega^0(782)$	782.65±0.12	8.49±0.08
$\rho^0(770)$	775.26±0.25	149.1±0.8

$\chi^2/ndof$. To obtain this value, for each toy fit, the χ^2 values for the CLEO-c 4170, CLEO-c 3770 and CLEO III datasets are summed and divided by increasing $ndof$ values until the mean of the p-values for the 100 toy fits reaches ≈ 0.5. (The CLEO II.V and CP tagged data samples have too few statistics to calculate a reliable χ^2). This value of $ndof$ is used for the determination of $\chi^2/ndof$ for the final LASSO fit and the process is repeated for the $\chi^2/ndof$ values of the alternative models.

Masses/widths of resonant particles

The mass and width parameters for the resonant particles are taken from the Particle Data Group (PDG)[23] and are fixed in the fit to the data. Table 4.14 shows the values of these parameters used in the fit and their associated uncertainties. To assess the effect of the uncertainty on these parameters, they are, in turn, varied up and down by their uncertainty and the fit repeated, resulting in a total of 32 additional fits. The shift occurring in each fit parameter from varying a mass or width value up and down is averaged, then for each fit parameter these averages are added in quadrature and this value assigned as a systematic uncertainty. Poor knowledge of prominent $K_1(1270)$ mass and width parameters make this the dominant systematic as shown in table 4.15.

Table 4.15: Systematic shifts due to uncertainty in mass/widths of resonant particles. All shifts are quoted relative to the LASSO model and in units of the statistical uncertainty.

Component	$K_1(1270)$	$K_1(1400)$	$K^{*0}(1430)$	$K^*(1680)$	$K^{*0}(892)$	$\omega^0(782)$	$\phi(1020)$	$\rho^0(770)$	Total
$D^0 \to K^-\,[K_1(1270)^+ \to \pi^+\,K^{*0}(892)]\ \Re(a_i)$	1.929	0.587	0.321	0.322	0.367	0.321	0.314	0.315	2.126
$D^0 \to K^-\,[K_1(1270)^+ \to \pi^+\,K^{*0}(892)]\ \Im(a_i)$	1.888	1.373	0.221	0.211	0.391	0.211	0.210	0.213	2.396
$D^0 \to K^-\,[K_1(1270)^+ \to \pi^+\,K^{*0}(1430)]\ \Re(a_i)$	1.540	0.089	1.348	0.037	0.053	0.037	0.038	0.040	2.050
$D^0 \to K^-\,[K_1(1270)^+ \to \pi^+\,K^{*0}(1430)]\ \Im(a_i)$	0.730	0.189	0.823	0.047	0.125	0.047	0.053	0.047	1.125
$D^0 \to K^-\,[K_1(1270)^+ \to K^+\,\rho^0(770)]\ \Re(a_i)$	2.001	0.145	0.051	0.073	0.075	0.073	0.075	0.066	2.011
$D^0 \to K^-\,[K_1(1270)^+ \to K^+\,\rho^0(770)]\ \Im(a_i)$	1.095	0.192	0.104	0.045	0.133	0.045	0.051	0.049	1.127
$D^0 \to K^+\,[\bar{K}_1(1270)^- \to K^-\,\rho^0(770)]\ \Re(a_i)$	0.955	0.168	0.048	0.015	0.040	0.015	0.017	0.021	0.972
$D^0 \to K^+\,[\bar{K}_1(1270)^- \to K^-\,\rho^0(770)]\ \Im(a_i)$	2.108	0.259	0.039	0.031	0.043	0.031	0.021	0.030	2.125
$D^0 \to K^-\,[K_1(1270)^+ \to K^+\,\omega^0(782)]\ \Re(a_i)$	0.707	0.033	0.035	0.040	0.035	0.057	0.037	0.043	0.713
$D^0 \to K^-\,[K_1(1270)^+ \to K^+\,\omega^0(782)]\ \Im(a_i)$	1.486	0.091	0.113	0.108	0.129	0.108	0.102	0.111	1.506
$D^0 \to K^-\,[K_1(1400)^+ \to \pi^+\,K^{*0}(892)]\ \Re(a_i)$	0.470	1.453	0.184	0.179	0.297	0.178	0.174	0.183	1.587
$D^0 \to K^-\,[K_1(1400)^+ \to \pi^+\,K^{*0}(892)]\ \Im(a_i)$	1.288	1.365	0.071	0.069	0.039	0.069	0.069	0.076	1.880
$D^0 \to K^-\,[K^*(1680)^+ \to \pi^+\,K^{*0}(892)]\ \Re(a_i)$	0.097	0.081	0.025	0.706	0.143	0.020	0.018	0.028	0.732
$D^0 \to K^-\,[K^*(1680)^+ \to \pi^+\,K^{*0}(892)]\ \Im(a_i)$	0.519	0.169	0.053	0.421	0.177	0.055	0.057	0.050	0.716
$D^0[S] \to K^{*0}(892)\,\bar{K}^{*0}(892)\ \Re(a_i)$	0.221	0.356	0.080	0.084	0.322	0.085	0.091	0.076	0.547
$D^0[S] \to K^{*0}(892)\,\bar{K}^{*0}(892)\ \Im(a_i)$	0.723	0.876	0.022	0.031	0.182	0.031	0.030	0.027	1.151
$D^0[P] \to K^{*0}(892)\,\bar{K}^{*0}(892)\ \Re(a_i)$	0.212	0.038	0.042	0.046	0.372	0.047	0.046	0.050	0.437
$D^0[P] \to K^{*0}(892)\,\bar{K}^{*0}(892)\ \Im(a_i)$	0.440	0.152	0.015	0.021	0.116	0.014	0.017	0.016	0.480
$D^0[D] \to K^{*0}(892)\,\bar{K}^{*0}(892)\ \Re(a_i)$	0.130	0.196	0.012	0.006	0.091	0.007	0.023	0.019	0.252
$D^0[D] \to K^{*0}(892)\,\bar{K}^{*0}(892)\ \Im(a_i)$	0.576	0.067	0.033	0.034	0.122	0.034	0.032	0.028	0.595
$D^0[S] \to \phi(1020)\,\rho^0(770)\ \Re(a_i)$	0.000	0.000	0.000	0.000	0.000	0.000	0.000	0.000	0.000
$D^0[S] \to \phi(1020)\,\rho^0(770)\ \Im(a_i)$	0.000	0.000	0.000	0.000	0.000	0.000	0.000	0.000	0.000
$D^0[P] \to \phi(1020)\,\rho^0(770)\ \Re(a_i)$	0.134	0.034	0.043	0.046	0.029	0.045	0.039	0.046	0.161
$D^0[P] \to \phi(1020)\,\rho^0(770)\ \Im(a_i)$	0.241	0.047	0.051	0.054	0.124	0.053	0.048	0.055	0.289
$D^0[D] \to \phi(1020)\,\rho^0(770)\ \Re(a_i)$	0.040	0.088	0.004	0.004	0.025	0.004	0.004	0.011	0.100
$D^0[D] \to \phi(1020)\,\rho^0(770)\ \Im(a_i)$	0.214	0.030	0.018	0.025	0.060	0.024	0.022	0.026	0.227
$D^0 \to K^{*0}\,(K^-\pi^+)_S\ \Re(a_i)$	0.111	1.138	0.106	0.110	0.075	0.110	0.111	0.116	1.161
$D^0 \to K^{*0}\,(K^-\pi^+)_S\ \Im(a_i)$	0.299	0.057	0.040	0.037	0.176	0.038	0.036	0.044	0.358
$D^0 \to \phi(1020)\,(\pi^+\pi^-)_S\ \Re(a_i)$	0.203	0.019	0.024	0.025	0.015	0.025	0.019	0.019	0.209
$D^0 \to \phi(1020)\,(\pi^+\pi^-)_S\ \Im(a_i)$	0.048	0.112	0.081	0.076	0.068	0.076	0.074	0.082	0.194
$D^0 \to (K^+K^-)_S\,(\pi^+\pi^-)_S\ \Re(a_i)$	0.456	0.125	0.087	0.079	0.161	0.079	0.080	0.078	0.519
$D^0 \to (K^+K^-)_S\,(\pi^+\pi^-)_S\ \Im(a_i)$	0.485	0.061	0.047	0.016	0.185	0.016	0.017	0.020	0.525

Running width model

The energy-dependent width used in the Breit-Wigner term for cascade decays, as described in 2.3, is calculated using knowledge of the branching fractions of the various possible decay channels of the resonance. To assess the potential effect our knowledge of these branching fractions has on the fit, the energy-dependent widths are re-calculated assuming a flat phasespace distribution. The shifts in the fit parameters are assigned as a systematic uncertainty.

Blatt-Weisskopf factors

In the formalism used in this analysis Blatt-Weisskopf barrier factors are used to describe the form factors of decaying resonances. A fit is performed where the form factors are set to unity and the shifts in the fit parameters are set as a systematic uncertainty.

Background level/model uncertainties

The signal fractions for the flavour tagged data are allowed to float under Gaussian constraints and the differences in the fitted amplitude parameters are assigned as a systematic. The same procedure is repeated for the mistag rates. For the flavour tagged data each background model is replaced, one at a time, by a flat, non-resonant model and the fit rerun, the resulting shifts are added in quadrature to give a systematic error due to the knowledge of the background shapes. As explained in section 4.6 for CLEO-c 4170 two background fits are established, the difference in the fit parameters given by the use of each is included in this systematic.

In the case of *CP* tagged data, one by one fits are run where the background contribution from each sample (*CP* even, *CP* odd, admixture) is ignored in the fit. The 4 resulting shifts are added in quadrature to obtain a systematic uncertainty.

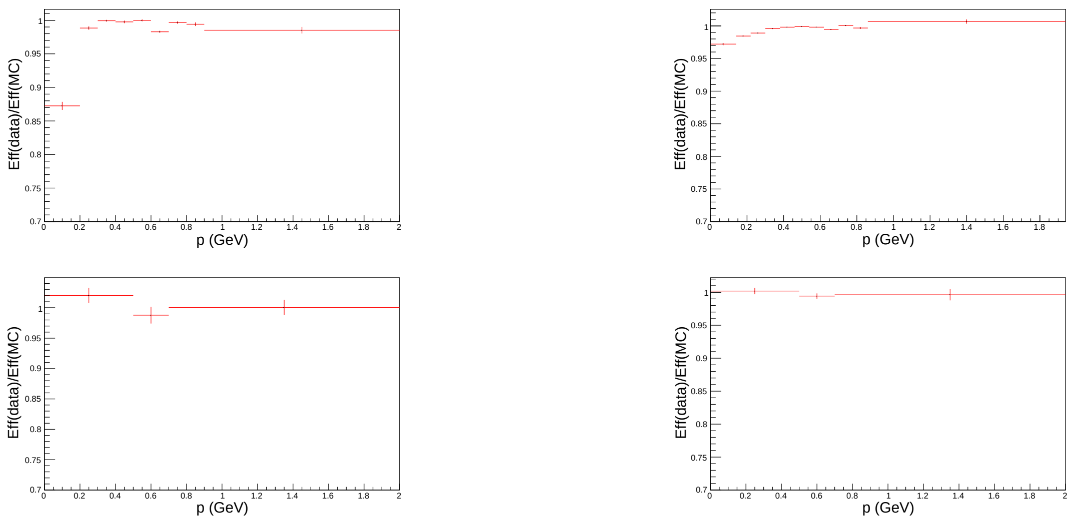

Figure 4.23: Plots of data/MC differences in PID and tracking efficiencies for CLEO-c; kaon PID (top left), pion PID (top right), kaon tracking (bottom left) pion tracking (bottom right).

Efficiency effects

In this analysis the variation in the efficiency of selecting signal decays across phasespace is accounted for with the use of fully selected MC events which are used to normalise the PDFs during the fit routine. The MC events are re-weighted according to data/MC differences in the PID and tracking efficiencies as a function of the track momentum, p, of the daughter particles. The fit is then rerun using these weighted MC events. The corrections to the MC events for PID and tracking are applied separately allowing for the separation of the two effects, table 4.16 shows the shifts on each of the fit parameters. It is assumed here that the data/MC differences are consistent between CLEO III and CLEO II.V and between CLEO-c 3770 and CLEO-c 4170. There is no tracking efficiency correction for CLEO III MC events as this efficiency is found to be consistent between data and MC. Figure 4.23 and 4.24 shows the look up histograms as a function of daughter track momentum p used for these corrections.

The shifts in the fit parameters arising from applying PID and tracking efficiency corrections to the MC are added in quadrature to give a final systematic uncertainty. It can be seen that the effect of PID efficiency differences between data and MC are dominant over tracking efficiency differences.

Table 4.16: Systematic shifts given in units of statistical uncertainty due to data/MC differences in PID and tracking efficiency

Component	PID efficiency	Tracking efficiency
$D^0 \to K^-\,[K_1(1270)^+ \to \pi^+\,K^{*0}(892)]\ \Re(a_i)$	-0.347	-0.145
$D^0 \to K^-\,[K_1(1270)^+ \to \pi^+\,K^{*0}(892)]\ \Im(a_i)$	0.257	0.155
$D^0 \to K^-\,[K_1(1270)^+ \to \pi^+\,K^{*0}(1430)]\ \Re(a_i)$	-0.090	-0.001
$D^0 \to K^-\,[K_1(1270)^+ \to \pi^+\,K^{*0}(1430)]\ \Im(a_i)$	-0.060	0.004
$D^0 \to K^-\,[K_1(1270)^+ \to K^+\,\rho^0(770)]\ \Re(a_i)$	-0.048	-0.041
$D^0 \to K^-\,[K_1(1270)^+ \to K^+\,\rho^0(770)]\ \Im(a_i)$	0.213	0.029
$D^0 \to K^+\,[\bar{K}_1(1270)^- \to K^-\,\rho^0(770)]\ \Re(a_i)$	-0.136	-0.025
$D^0 \to K^+\,[\bar{K}_1(1270)^- \to K^-\,\rho^0(770)]\ \Im(a_i)$	0.213	-0.036
$D^0 \to K^-\,[K_1(1270)^+ \to K^+\,\omega^0(782)]\ \Re(a_i)$	-0.025	-0.004
$D^0 \to K^-\,[K_1(1270)^+ \to K^+\,\omega^0(782)]\ \Im(a_i)$	-0.266	-0.066
$D^0 \to K^-\,[K_1(1400)^+ \to \pi^+\,K^{*0}(892)]\ \Re(a_i)$	0.138	0.115
$D^0 \to K^-\,[K_1(1400)^+ \to \pi^+\,K^{*0}(892)]\ \Im(a_i)$	0.129	-0.078
$D^0 \to K^-\,[K^*(1680)^+ \to \pi^+\,K^{*0}(892)]\ \Re(a_i)$	-0.246	-0.003
$D^0 \to K^-\,[K^*(1680)^+ \to \pi^+\,K^{*0}(892)]\ \Im(a_i)$	-0.053	-0.029
$D^0[S] \to K^{*0}(892)\,\bar{K}^{*0}(892)\ \Re(a_i)$	-0.221	-0.003
$D^0[S] \to K^{*0}(892)\,\bar{K}^{*0}(892)\ \Im(a_i)$	-0.006	-0.027
$D^0[P] \to K^{*0}(892)\,\bar{K}^{*0}(892)\ \Re(a_i)$	0.198	-0.010
$D^0[P] \to K^{*0}(892)\,\bar{K}^{*0}(892)\ \Im(a_i)$	0.154	0.004
$D^0[D] \to K^{*0}(892)\,\bar{K}^{*0}(892)\ \Re(a_i)$	0.131	-0.051
$D^0[D] \to K^{*0}(892)\,\bar{K}^{*0}(892)\ \Im(a_i)$	0.137	0.070
$D^0[S] \to \phi(1020)\,\rho^0(770)\ \Re(a_i)$	0.0	0.0
$D^0[S] \to \phi(1020)\,\rho^0(770)\ \Im(a_i)$	0.0	0.0
$D^0[P] \to \phi(1020)\,\rho^0(770)\ \Re(a_i)$	-0.002	-0.023
$D^0[P] \to \phi(1020)\,\rho^0(770)\ \Im(a_i)$	0.094	0.033
$D^0[D] \to \phi(1020)\,\rho^0(770)\ \Re(a_i)$	-0.185	-0.012
$D^0[D] \to \phi(1020)\,\rho^0(770)\ \Im(a_i)$	-0.003	0.023
$D^0 \to K^{*0}\,(K^-\pi^+)_S\ \Re(a_i)$	0.128	0.038
$D^0 \to K^{*0}\,(K^-\pi^+)_S\ \Im(a_i)$	-0.046	0.094
$D^0 \to \phi(1020)\,(\pi^+\pi^-)_S\ \Re(a_i)$	-0.106	-0.016
$D^0 \to \phi(1020)\,(\pi^+\pi^-)_S\ \Im(a_i)$	-0.009	-0.057
$D^0 \to (K^+K^-)_S\,(\pi^+\pi^-)_S\ \Re(a_i)$	-0.112	0.127
$D^0 \to (K^+K^-)_S\,(\pi^+\pi^-)_S\ \Im(a_i)$	-0.287	0.047

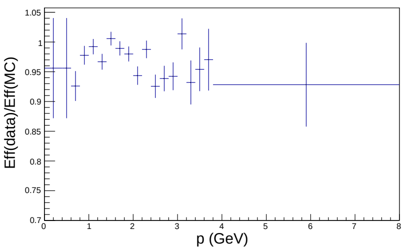

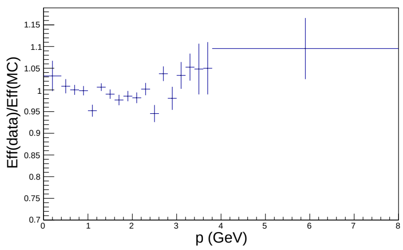

Figure 4.24: Plots of data/MC differences in PID efficiencies for CLEO III; kaon PID (left), pion PID (right).

Detector resolution effects

For most resonances in the LASSO model the detector resolution can be ignored. The narrow width of the $\phi(1020)$ at 4.27 MeV however is similar to the momentum resolution capabilities expected from the CLEO detector and this may lead to a bias. One hundred subsamples are drawn randomly from the efficiency corrected MC events. The relative amount of events drawn for each of the detector configurations is fluctuated according to a Poisson distribution around the values seen in data. These events are then weighted by

$$\frac{|A(a^{LASSO}, p_i)|^2}{|A(a^{gen}, p_i)|^2}$$

where a_i^{LASSO} are the parameters of the LASSO model and a_i^{gen} are the parameters of the model that the MC events were generated with. This simply leaves the detector/selection effects applied to the LASSO model distribution. The weighted data is then fit with the LASSO signal PDF using the remaining normalisation events. Table 4.17 shows the results of this pull study using 100 fits. The mean of the pull for each fitted parameter is multiplied by the statistical error and taken as a systematic uncertainty. The resolution systematic will also contain the effects of fitter bias, however a conservative approach is taken and they are considered uncorrelated.

Quantum correlations

It is assumed that for the flavour tagged samples from CLEO-c data, D^0 and $\bar{D}^0$ decays can be described by A_{D^0} and $A_{\bar{D}^0}$ respectively. However, in the case of CLEO-c 3770, $D^0\bar{D}^0$ pairs are produced through the $e^+e^- \to \psi(3770) \to D^0\bar{D}^0$ decay process which has a definite *CP* odd state and so there exists quantum correlations between the decay of the D^0 and $\bar{D}^0$. For a quantum correlated $D^0 \to i$ and $\bar{D}^0 \to j$ decay the *CP*-odd decay rate follows the antisymmetric amplitude squared [92]

$$\Gamma_{D^0\bar{D}^0}(i,j) \propto \mathcal{M}_{ij}^2 = |A_i\bar{A}_j - \bar{A}_iA_j|^2 \tag{4.18}$$

Table 4.17: Pull study for imaginary and real parts of amplitude coefficients, a_i, using 100 toy MC fits to test for bias introduced by resolution effects.

Component	Pull mean	Pull width
$D^0 \to K^- [K_1(1270)^+ \to \pi^+ K^{*0}(892)]$ $\Re(a_i)$	-0.211±0.073	0.728±0.051
$D^0 \to K^- [K_1(1270)^+ \to \pi^+ K^{*0}(892)]$ $\Im(a_i)$	0.233±0.081	0.81±0.057
$D^0 \to K^- [K_1(1270)^+ \to \pi^+ K^{*0}(1430)]$ $\Re(a_i)$	-0.434±0.085	0.851±0.060
$D^0 \to K^- [K_1(1270)^+ \to \pi^+ K^{*0}(1430)]$ $\Im(a_i)$	0.085±0.090	0.903±0.064
$D^0 \to K^- [K_1(1270)^+ \to K^+ \rho^0(770)]$ $\Re(a_i)$	0.283±0.099	0.988±0.070
$D^0 \to K^- [K_1(1270)^+ \to K^+ \rho^0(770)]$ $\Im(a_i)$	0.021±0.089	0.89±0.063
$D^0 \to K^+ [\bar{K_1}(1270)^- \to K^- \rho^0(770)]$ $\Re(a_i)$	-0.226±0.104	1.037±0.073
$D^0 \to K^+ [\bar{K_1}(1270)^- \to K^- \rho^0(770)]$ $\Im(a_i)$	0.178±0.109	1.092±0.073
$D^0 \to K^- [K_1(1270)^+ \to K^+ \omega^0(782)]$ $\Re(a_i)$	-0.087±0.124	1.235±0.087
$D^0 \to K^- [K_1(1270)^+ \to K^+ \omega^0(782)]$ $\Im(a_i)$	0.387±0.0125	1.252±0.089
$D^0 \to K^- [K_1(1400)^+ \to \pi^+ K^{*0}(892)]$ $\Re(a_i)$	0.169±0.089	0.886±0.063
$D^0 \to K^- [K_1(1400)^+ \to \pi^+ K^{*0}(892)]$ $\Im(a_i)$	0.082±0.062	0.618±0.044
$D^0 \to K^- [K^*(1680)^+ \to \pi^+ K^{*0}(892)]$ $\Re(a_i)$	-0.567±0.094	0.945±0.067
$D^0 \to K^- [K^*(1680)^+ \to \pi^+ K^{*0}(892)]$ $\Im(a_i)$	0.301±0.096	0.962±0.068
$D^0[S] \to K^{*0}(892)\, \bar{K^{*0}}(892)$ $\Re(a_i)$	-0.146±0.076	0.763±0.054
$D^0[S] \to K^{*0}(892)\, \bar{K^{*0}}(892)$ $\Im(a_i)$	-0.019±0.080	0.801±0.057
$D^0[P] \to K^{*0}(892)\, \bar{K^{*0}}(892)$ $\Re(a_i)$	0.236±0.102	1.019±0.072
$D^0[P] \to K^{*0}(892)\, \bar{K^{*0}}(892)$ $\Im(a_i)$	-0.020±0.096	0.957±0.068
$D^0[D] \to K^{*0}(892)\, \bar{K^{*0}}(892)$ $\Re(a_i)$	0.430±0.098	0.983±0.070
$D^0[D] \to K^{*0}(892)\, \bar{K^{*0}}(892)$ $\Im(a_i)$	-0.162±0.081	0.805±0.057
$D^0[S] \to \phi(1020)\, \rho^0(770)$ $\Re(a_i)$	0.0±0.0	0.0±0.0
$D^0[S] \to \phi(1020)\, \rho^0(770)$ $\Im(a_i)$	0.0±0.0	0.0±0.0
$D^0[P] \to \phi(1020)\, \rho^0(770)$ $\Re(a_i)$	0.132±0.112	1.122±0.079
$D^0[P] \to \phi(1020)\, \rho^0(770)$ $\Im(a_i)$	0.322±0.109	1.094±0.077
$D^0[D] \to \phi(1020)\, \rho^0(770)$ $\Re(a_i)$	-0.399±0.094	0.941±0.067
$D^0[D] \to \phi(1020)\, \rho^0(770)$ $\Im(a_i)$	-0.107±0.113	1.125±0.080
$D^0 \to K^{*0}\, (K^-\pi^+)_S$ $\Re(a_i)$	-0.233±0.070	0.702±0.050
$D^0 \to K^{*0}\, (K^-\pi^+)_S$ $\Im(a_i)$	0.194±0.085	0.849±0.060
$D^0 \to \phi(1020)\, (\pi^+\pi^-)_S$ $\Re(a_i)$	-0.657±0.094	0.943±0.067
$D^0 \to \phi(1020)\, (\pi^+\pi^-)_S$ $\Im(a_i)$	0.402±0.116	1.162±0.082
$D^0 \to (K^+K^-)_S\, (\pi^+\pi^-)_S$ $\Re(a_i)$	-0.087±0.099	0.987±0.070
$D^0 \to (K^+K^-)_S\, (\pi^+\pi^-)_S$ $\Im(a_i)$	-0.038±0.086	0.859±0.061

where

$$A_i \equiv \langle i|D^0\rangle \text{ and } \bar{A}_i \equiv \langle i|\bar{D}^0\rangle.$$

Referring back to section 4.2.1, if i is the signal decay and j is the corresponding flavour tagging decay then

$$A_i = A(D^0 \to K^+K^-\pi^+\pi^-) = A_{D^0} \text{ and } \bar{A}_i = A(\bar{D}^0 \to K^+K^-\pi^+\pi^-) = A_{\bar{D}^0}$$

and

$$\bar{A}_j = A(\bar{D}^0 \to K^+X) = K_t \text{ and } A_j = A(D^0 \to K^+X) = K_t k_t e^{i\delta t}$$

where k_t is an amplitude suppression factor between the two tagging (t) decays and δ_t is a relative phase. Using 4.18 the decay rate for this correlated pair of decays can be expressed as

$$\Gamma \propto K_t^2\left[|A_{D^0}|^2 + |A_{\bar{D}^0}|^2 k_t^2 - 2k_t[\Re(A_{D^0}A^*_{\bar{D}^0})\cos(\delta_t) + \Im(A_{\bar{D}^0}A^*_{D^0})\sin(\delta_t)]\right] \tag{4.19}$$

There are multiple tagging decays that are used, all of which have different amplitude suppression factors, k_t and phases δ_t. The value of k_t for all tagging decays is small due to Cabibbo suppression and estimated at an average of $1/\sqrt{300}$ [23], therefore the term $|A_{\bar{D}^0}|^2 k_t^2$ can be ignored as can the factor K_t^2 in the minimisation. The fit to data is repeated where the signal PDF for CLEO-c 3770 is replaced by equation 4.19 with values of δ chosen such that $k_t\cos(\delta_t)$ and $k_t\sin(\delta_t)$ take maximal values around a circle of radius $1/\sqrt{300}$. The values of $k_t\cos(\delta_t)$ and $k_t\sin(\delta_t)$ causing the largest shift in the fit parameters from their LASSO values are $1/\sqrt{300}$ and 0 respectively. These shifts are taken as a systematic uncertainty. Quantum correlations also can occur in the CLEO-c 4170 dataset, however to a lesser degree as the $D^0/\bar{D}$ are not generally produced directly but via higher energy charm meson decays. Given that the CLEO-c 4170 sample is also much smaller than the CLEO-c 3770 the effect of quantum correlations in the CLEO-c 4170 is neglected.

Summary of systematic uncertainties

Table 4.18 shows a summary of the systematic uncertainties in this analysis. There are two overall systematic errors; the model systematic error which includes contributions from Blatt-Weisskopf barrier factors, uncertainties in masses/widths of resonances and the implementation of the energy-dependent width in the Breit-Wigner term; and the experimental systematic that includes all other contributions. The dominant systematic uncertainty arises from the uncertainty on the masses and widths of the resonances. In particular those amplitude components involving a $K_1(1270)$ particle, which has a large width uncertainty, have far larger model systematic uncertainties than those components involving the ϕ or ρ resonances that have very small mass/width uncertainties.

Table 4.18: Summary of the systematic uncertainties given in units of the statistical error separated into model and experimental (exp.) contributions. 1) Blatt-Weisskopf barrier factors, 2) Masses/width of resonances, 3) CP tagged backgrounds, 4) Flavour tagged backgrounds, 5) Flavour tagged background levels, 6) Mistag rates, 7) Quantum correlations, 8) Efficiency, 9) Fitter bias, 10) Detector resolution, 11) Energy-dependent widths

Component	1	2	3	4	5	6	7	8	9	10	11	Model	Exp.	fit value±stat±model syst±other syst
$D^0 \to K^-\ [K_1(1270)^+ \to \pi^+\ K^{*0}(892)]\ \Re(a_i)$	0.732	2.126	0.190	0.199	0.019	0.001	0.101	0.376	0.090	0.211	1.505	2.706	0.530	6.357±1.238±3.351±0.656
$D^0 \to K^-\ [K_1(1270)^+ \to \pi^+\ K^{*0}(892)]\ \Im(a_i)$	0.331	2.396	0.207	0.147	0.087	0.001	0.064	0.300	0.040	0.233	0.054	2.419	0.472	-6.858±1.371±3.317±0.646
$D^0 \to K^-\ [K_1(1270)^+ \to \pi^+\ K^{*0}(1430)]\ \Re(a_i)$	0.493	2.050	0.244	0.277	0.005	0.001	0.212	0.090	0.274	0.434	0.344	2.136	0.673	34.926±3.745±8.000±2.520
$D^0 \to K^-\ [K_1(1270)^+ \to \pi^+\ K^{*0}(1430)]\ \Im(a_i)$	0.295	1.125	0.196	0.147	0.024	0.002	0.842	0.060	0.190	0.085	0.445	1.245	0.903	5.657±4.500±5.605±4.064
$D^0 \to K^-\ [K_1(1270)^+ \to K^+\ \rho^0(770)]\ \Re(a_i)$	0.470	2.011	0.199	0.154	0.009	0.002	0.207	0.063	0.292	0.283	0.332	2.092	0.525	-17.632±2.438±5.099±1.280
$D^0 \to K^-\ [K_1(1270)^+ \to K^+\ \rho^0(770)]\ \Im(a_i)$	0.014	1.127	0.165	0.181	0.027	0.001	0.466	0.215	0.042	0.021	0.780	1.371	0.571	-11.513±2.274±3.118±1.299
$D^0 \to K^+\ [\bar{K}_1(1270)^- \to K^-\ \rho^0(770)]\ \Re(a_i)$	0.560	0.972	0.160	0.169	0.172	0.001	0.512	0.139	0.100	0.226	0.746	1.347	0.653	9.873±1.745±2.351±1.139
$D^0 \to K^+\ [\bar{K}_1(1270)^- \to K^-\ \rho^0(770)]\ \Im(a_i)$	1.008	2.125	0.213	0.298	0.123	0.000	0.346	0.216	0.306	0.178	0.773	2.476	0.664	-12.907±1.489±3.687±0.989
$D^0 \to K^-\ [K_1(1270)^+ \to K^+\ \omega^0(782)]\ \Re(a_i)$	0.549	0.713	0.149	0.216	0.024	0.001	0.165	0.025	0.157	0.087	0.605	1.084	0.360	3.784±3.335±3.616±1.200
$D^0 \to K^-\ [K_1(1270)^+ \to K^+\ \omega^0(782)]\ \Im(a_i)$	0.030	1.506	0.097	0.033	0.032	0.000	0.714	0.274	0.178	0.387	1.785	2.336	0.882	-9.363±2.352±5.494±2.075
$D^0 \to K^-\ [K_1(1400)^+ \to \pi^+\ K^{*0}(892)]\ \Re(a_i)$	0.228	1.587	0.292	0.176	0.132	0.000	0.221	0.180	0.057	0.169	0.489	1.676	0.496	-8.083±5.109±8.564±2.535
$D^0 \to K^-\ [K_1(1400)^+ \to \pi^+\ K^{*0}(892)]\ \Im(a_i)$	0.090	1.880	0.101	0.146	0.047	0.001	0.821	0.151	0.312	0.082	1.409	2.351	0.914	-36.923±4.355±10.238±3.978
$D^0 \to K^-\ [K^*(1680)^+ \to \pi^+\ K^{*0}(892)]\ \Re(a_i)$	0.636	0.732	0.639	0.095	0.106	0.000	0.989	0.246	0.010	0.567	0.467	1.076	1.337	132.692±15.810±17.012±21.140
$D^0 \to K^-\ [K^*(1680)^+ \to \pi^+\ K^{*0}(892)]\ \Im(a_i)$	0.423	0.716	0.254	0.136	0.066	0.003	0.051	0.060	0.043	0.301	1.206	1.465	0.431	-35.448±19.131±28.024±8.248
$D^0[S] \to K^{*0}(892)\ \bar{K}^{*0}(892)\ \Re(a_i)$	0.044	0.547	0.218	0.177	0.054	0.002	1.006	0.221	0.357	0.146	0.892	1.047	1.137	822.042±81.835±85.687±93.015
$D^0[S] \to K^{*0}(892)\ \bar{K}^{*0}(892)\ \Im(a_i)$	0.536	1.151	0.169	0.135	0.026	0.001	0.237	0.028	0.091	0.019	1.790	2.195	0.336	-350.520±105.579±231.700±35.510
$D^0[P] \to K^{*0}(892)\ \bar{K}^{*0}(892)\ \Re(a_i)$	0.575	0.437	0.171	0.261	0.016	0.001	1.909	0.198	0.015	0.236	0.213	0.753	1.958	-975.583±115.302±86.783±225.799
$D^0[P] \to K^{*0}(892)\ \bar{K}^{*0}(892)\ \Im(a_i)$	0.518	0.480	0.412	0.205	0.011	0.001	0.401	0.154	0.226	0.020	0.501	0.866	0.669	-476.349±148.151±128.259±99.151
$D^0[D] \to K^{*0}(892)\ \bar{K}^{*0}(892)\ \Re(a_i)$	0.863	0.252	0.636	0.273	0.068	0.000	0.055	0.141	0.069	0.430	0.132	0.909	0.835	-4786.723±408.232±371.042±340.684
$D^0[D] \to K^{*0}(892)\ \bar{K}^{*0}(892)\ \Im(a_i)$	0.445	0.595	0.162	0.228	0.085	0.002	0.453	0.154	0.013	0.162	1.489	1.664	0.584	985.176±533.858±888.230±311.711
$D^0[S] \to \phi(1020)\ \rho^0(770)\ \Re(a_i)$	0.000	0.000	0.000	0.000	0.000	0.000	0.000	0.000	0.000	0.000	0.000	0.000	0.000	1.000 ±0.000±0.000±0.000
$D^0[S] \to \phi(1020)\ \rho^0(770)\ \Im(a_i)$	0.000	0.000	0.000	0.000	0.000	0.000	0.000	0.000	0.000	0.000	0.000	0.000	0.000	0.000 ±0.000±0.000±0.000
$D^0[P] \to \phi(1020)\ \rho^0(770)\ \Re(a_i)$	0.695	0.161	0.145	0.435	0.009	0.003	1.006	0.023	0.128	0.132	0.139	0.727	1.121	-1552.191±203.056±147.666±227.586
$D^0[P] \to \phi(1020)\ \rho^0(770)\ \Im(a_i)$	0.243	0.289	0.209	0.793	0.014	0.000	0.085	0.099	0.112	0.322	0.747	0.837	0.898	-354.717±432.814±362.355±388.686
$D^0[D] \to \phi(1020)\ \rho^0(770)\ \Re(a_i)$	0.709	0.100	0.750	0.179	0.013	0.001	0.040	0.185	0.009	0.399	0.449	0.845	0.889	5208.024±685.263±579.206±609.162
$D^0[D] \to \phi(1020)\ \rho^0(770)\ \Im(a_i)$	0.064	0.227	0.524	0.349	0.002	0.001	0.053	0.023	0.152	0.107	0.178	0.296	0.659	791.856±954.634±282.158±629.397
$D^0 \to K^{*0}\ (K^-\pi^+)_S\ \Re(a_i)$	0.762	1.161	0.464	0.114	0.146	0.002	1.357	0.134	0.309	0.233	0.548	1.493	1.503	43.519±4.593±6.858±6.904
$D^0 \to K^{*0}\ (K^-\pi^+)_S\ \Im(a_i)$	0.693	0.358	0.162	0.145	0.118	0.001	0.070	0.105	0.228	0.194	0.502	0.928	0.408	-1.201±5.195±4.819±2.121
$D^0 \to \phi(1020)\ (\pi^+\pi^-)_S\ \Re(a_i)$	0.132	0.209	0.210	0.247	0.013	0.001	0.670	0.107	0.446	0.657	1.208	1.233	1.094	29.618±7.394±9.114±8.089
$D^0 \to \phi(1020)\ (\pi^+\pi^-)_S\ \Im(a_i)$	0.685	0.194	0.302	0.755	0.087	0.001	1.720	0.057	0.292	0.402	0.266	0.760	1.969	-54.929±5.646±4.289±11.118
$D^0 \to (K^+K^-)_S\ (\pi^+\pi^-)_S\ \Re(a_i)$	1.163	0.519	0.201	0.499	0.049	0.001	0.255	0.169	0.044	0.087	1.301	1.821	0.629	0.421±0.052±0.094±0.033
$D^0 \to (K^+K^-)_S\ (\pi^+\pi^-)_S\ \Im(a_i)$	0.999	0.525	0.202	0.606	0.319	0.001	1.223	0.291	0.020	0.038	0.531	1.247	1.446	0.486±0.048±0.060±0.069

4.10 Interpretation of Results

The results of the amplitude model for the decay $D^0 \to K^+K^-\pi^+\pi^-$ can be seen in table 4.9. As indicated in section 4 an amplitude analysis of the decay $D^0 \to K^+K^-\pi^+\pi^-$ has been performed previously by other experiments including FOCUS at Fermilab.

The largest single component of the model is the $D \to VV$ mode $D^0[S] \to \phi(1020)\,\rho(770)^0$ with a fit fraction of 28.1% which is consistent with the level seen in the FOCUS model (29.0%). This channel dominates over the other $D \to VV$ mode $D^0[S] \to K^{*0}(892)\,\bar{K^{*0}}(892)$ (4.5%) due to the production processes involved in the decays. $D^0[S] \to \phi(1020)\,\rho(770)^0$ can proceed through internal W radiation at tree level, whereas $D^0[S] \to K^{*0}(892)\,\bar{K^{*0}}(892)$ has two tree-level amplitudes that are suppressed through GIM cancellation. The Feynman diagrams for these processes are shown in figure 4.25. The next largest component is the $D \to AP$ mode $D^0 \to K^-\,[K_1(1400)^+ \to \pi^+\,K^*(892)^0]$ (12.4%) which also appears in the FOCUS model albeit at a higher level. Both models share these top two components that contribute a total of 40.4% and 51.0% to the LASSO model and the FOCUS model respectively. Both models also see contributions from $D^0 \to K^-\,[K_1(1270)^+ \to \pi^+\,K^*(1430)^0]$, a resonance that like $K_1(1400)^+$ peaks outside of the kinematically allowed region. Here the description of the lineshapes for cascade decays that implements the energy-dependent widths as explained in section 2.4.1 is particularly important.

An important component in the model is $D^0 \to K^-\,[K_1(1270)^+ \to K^+\,\rho^0(770)]$ (9.1%) which can be seen to dominate over the $D^0 \to K^+\,[K_1(1270)^- \to K^-\,\rho^0(770)]$ (5.4%). The dominance of $D^0 \to K^-K^{**+}$ modes over $D^0 \to K^+K^{**-}$ modes where K^{**} is an excited kaon is observed in alternative model A (LASSO model plus all conjugate decays) in all cases. This is consistent with other analyses, where it is observed that the virtual W couples to a vector or axial-vector meson with larger branching fractions compared to cases where the W couples to a pseudoscalar meson [101]. It appears favourable for the bachelor meson to be a product of the spectator quark rather than be a product of the weak vertex as seen in the Feynman diagrams in figure 4.26. The FOCUS analysis does not distinguish between D^0 and $\bar{D^0}$ decays. They quote $D^0 \to K^{\pm}\,K_1(1270)^{\mp}$

components as their dominant contribution. Summing all the $D^0 \to K^\pm K_1(1270)^\mp$ channels together in the LASSO model gives a contribution of 26.7% and therefore $D^0[S] \to \phi(1020)\,\rho(770)^0$ still dominates for the LASSO model. Even so the importance of this 3-body resonance is clear.

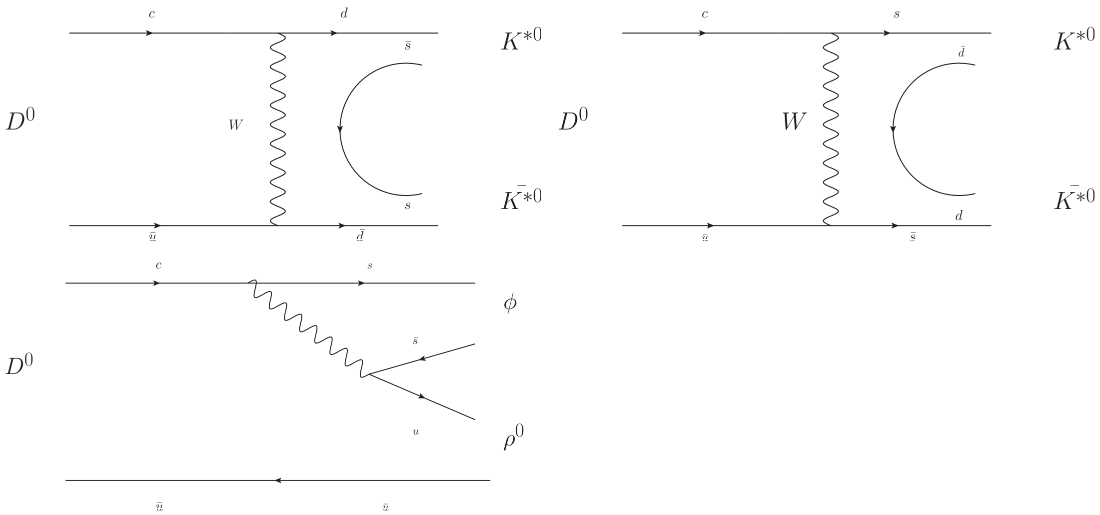

Figure 4.25: Feynman diagrams for the two tree-level amplitudes contributing to the GIM suppressed $D^0[S] \to K^{*0}(892)\,\bar{K}^{*0}(892)$ decay and the Feynman diagram for the tree-level $D^0[S] \to \phi(1020)\,\rho(770)^0$ decay.

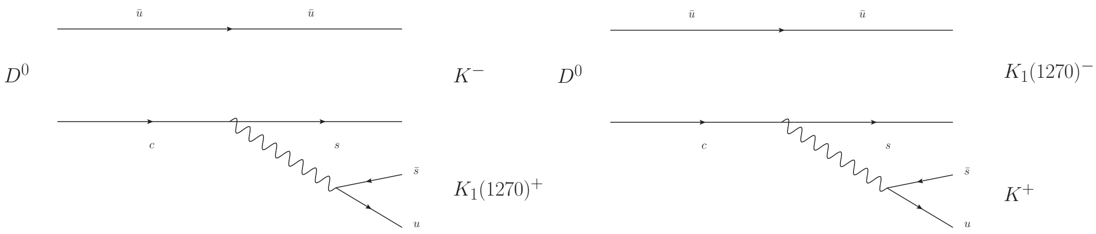

Figure 4.26: Feynman diagrams for the decays $D^0 \to K^-K_1(1270)^+$ (left) and $D^0 \to K^+K_1(1270)^-$ (right). Dominance of the modes $D^0 \to K^-K_1(1270)^+$ is seen.

The alternative models (shown in table 4.12) are largely in agreement with each other, $D^0[S] \to \phi(1020)\,\rho(770)^0$ contributes most significantly and (where applicable) $D^0 \to K^-\,[K_1(1400)^+ \to \pi^+\,K^*(892)^0]$ is the next largest contributor. For alternative model B the $D^0 \to K^-\,K^*(1680)^+$ is exchanged for the $D^0 \to K^-\,K_1(1410)^+$ as they are seen to be interchangeable in the building of the LASSO model. The fractional contributions of these components within their respective models are consistent.

The FOCUS model does not include the the flat, non-resonant component, achieving a good description of the data without it. The FOCUS model does however include $D^0 \to f_0(980)\,(\pi^+\pi^-)_S$ with a sum of fit fractions of 119% indicating higher destructive interference than seen in the LASSO model presented here. Alternative model C features the $D^0 \to f_0(980)\,(\pi^+\pi^-)_S$ and $D^0 \to f_0(980)\,(K^+K^-)_S$ components in place of the flat, non-resonant component. Interestingly, whilst in the LASSO model the non-resonant component constitutes a significant contribution (11.1%), the two replacement components in alternative model C only have contributions of 1.3% and 1.0% respectively. As with the FOCUS model however, alternative model C indicates significant destructive interference (the sum of the fit fractions is 121.1%) amongst components compared to the LASSO model. This alternative model also has a poorer fit quality indicating the need for the flat, non-resonant component.

For $D^0 \to K^*(892)^0\,\bar{K}^*(892)^0$ and $D^0 \to \phi(1020)\,\rho(770)^0$ the relative S wave contributions can be seen to be larger than the P and D wave contributions as expected. It is interesting to note that in stage 2 of the LASSO method only amplitude components of the form $D^0 \to V\,(hh)_S$ are selected from the pool of single resonant components. The two single resonant components appearing in the LASSO model also appear in the FOCUS model. Components of the form $D^0 \to V\,(hh)_P$ and $D^0 \to V\,(hh)_D$ are not required in the fit and would be expected to be suppressed compared to their $D^0 \to V\,(hh)_S$ counterparts.

The FOCUS analysis considered far fewer potential amplitude components. Due to greater statistics this analysis could also consider the P and D wave modes of $D \to VV$ components and contributions such as $D^0 \to K^-\,[K^*(1680)^+ \to \pi^+\,K^{*0}(892)]$ and $D^0 \to K^-\,[K_1(1270)^+ \to K^+\,\omega^0(782)]$ which were found to contribute at the level of 3.6% and 0.6% respectively.

Comparing the LASSO model to the model obtained in the previous analysis of this dataset [1], most apparent is the number of amplitude components used; eleven in [1] compared to sixteen for the LASSO model. Whereas in this analysis we use the LASSO method to obtain an amplitude model, the previous analysis used the traditional step-wise approach, a method where it is harder to consider a large number of amplitude components at the same time. The model presented here includes P-wave components for the $D \to VV$ decays whereas [1] does not, despite including both S-wave and D-wave $D^0 \to \phi(1020)\,\rho(770)^0$ components. It should be noted that alternative model 6 in [1] has a $D^0[P] \to K^{*0}\,(K^-\pi^+)_P$ component of similar size to the $D^0[P] \to K^{*0}(892)\,\bar{K}^{*0}(892)$ component in this analysis. Unlike the LASSO model, the dominance of $D^0 \to K^-K^{**+}$ modes over $D^0 \to K^+K^{**-}$ modes in [1] is only observed for the $D^0 \to K^-\,[K_1(1270)^+ \to \pi^+\,K^{*0}(892)]$ mode. Differences between cascade decays in the models are expected due to the improved lineshapes of resonance decays to 3-body final states. The improved lineshapes also give a better description of decays that peak outside of the kinematically allowed region, hence in this analysis we see $D^0 \to K^-\,[K_1(1400)^+ \to \pi^+\,K^*(892)^0]$ and $D^0 \to K^-\,[K_1(1270)^+ \to \pi^+\,K^*(1430)^0]$, unlike in [1].

Chapter 5

Model-dependent measurement of the CKM phase γ at the LHCb experiment

This section presents the work towards a model-dependent measurement of the CKM phase γ from $B^{\pm} \to D(\to K^{+}K^{-}\pi^{+}\pi^{-})K^{\pm}$ decays using the amplitude model for $D^{0} \to K^{+}K^{-}\pi^{+}\pi^{-}$ developed in section 4. Section 5.2 describes the selection of $B^{\pm} \to D(\to K^{+}K^{-}\pi^{+}\pi^{-})K^{\pm}$ decays as well as $B^{\pm} \to D(\to K^{+}K^{-}\pi^{+}\pi^{-})\pi^{\pm}$ decays that act as a control channel for this analysis. Mass fits to these two datasets are performed in section 5.3 to extract event-by-event signal and background weights. In section 5.4 a *CP*-violation measurement is performed using the $B^{\pm} \to D(\to K^{+}K^{-}\pi^{+}\pi^{-})\pi^{\pm}$ control channel data to investigate potential biases in the future extraction of γ from $B^{\pm} \to D(\to K^{+}K^{-}\pi^{+}\pi^{-})K^{\pm}$.

5.1 Datasets

This analysis uses the full LHCb 2011 ($\sqrt{s}$ =7 TeV) and 2012 ($\sqrt{s}$ =8 TeV) dataset taken during the Run 1 phase which corresponds to 3 fb^{-1} of integrated luminosity. Both the signal $B^{\pm} \to D(\to K^{+}K^{-}\pi^{+}\pi^{-})K^{\pm}$ decays and a control channel of $B^{\pm} \to$

$D(\rightarrow K^+K^-\pi^+\pi^-)\pi^\pm$ decays are selected from this dataset as described in the following. The control channel has a branching fraction of order 10 greater than the signal channel making it a useful high statistics channel upon which we can optimise selection cuts and establish mass fits. The control mode can also be used to perform a null test of the method to extract γ. While we expect r_B^{DK} for $B^\pm \rightarrow D(\rightarrow K^+K^-\pi^+\pi^-)K^\pm$ decays to be $r_B^{DK} \approx 0.102$, for the control channel we expect $r_B^{D\pi} \approx 0.027$ [102]. With the statistics available for this analysis we therefore expect no *CP*-violation to be observed in this control channel.

Event candidates for this analysis are required to have passed trigger requirements at L0 (hardware) and HLT[1, 2] (software) levels. The trigger decisions are either:

- Trigger On Signal (TOS) where particles associated with the signal decay chain inform the trigger decision
- Trigger Independent of Signal (TIS) where particles not associated with the signal decay chain inform the trigger decision

The required trigger decisions for signal candidates are detailed in table 5.1 and the requirements for each trigger to fire can be seen in section 3.4.2. L0 Global TIS requires that any one of the L0 triggers fire on a track not associated with the signal decay.

Table 5.1: Trigger Requirements

Trigger Level	Requirement
L0	L0 Hadron TOS OR L0 Global TIS
HLT1	HLT1 Track TOS
HLT2	HLT2 Topological 2-body TOS OR HLT2 Topological 3-body TOS OR HLT2 Topological 4-body TOS

The dataset also undergoes a central offline selection process known as stripping, each decay type analysed at LHCb has a designated stripping line. Stripping lines attempt to form specific decay chains by reconstructing composite particles. The stripping line used for the signal decay in this analysis attempts to first reconstruct a decay $D \to K^+K^-\pi^+\pi^-$ and then, using the D formed from the $K^+K^-\pi^+\pi^-$ tracks, attempts to reconstruct $B^\pm \to D(\to K^+K^-\pi^+\pi^-)K^\pm$. An established set of loose selection criteria is then applied to the particle tracks within the selected decay chains in order to keep only the events of interest for further analysis. As well as cuts to ensure the quality of decay vertices and particle tracks, the kinematic cuts (with definitions given in section 3.2) made by this stripping line are:

- For the D^0 daughter tracks:
  - $p_T > 100$MeV, $p > 1000$MeV, IP$>$ 2 standard deviations from any PV
- For the D^0 candidate:
  - $|m_{KK\pi\pi} - m_D| < 100$MeV, $p_T > 500$MeV, $p > 5000$MeV, vertex of the D candidate > 6 standard deviations from PV
- For the bachelor track:
  - $p_T > 500$MeV, $p > 5000$MeV
- For the B candidate:
  - $\tau_B > 0.2$ps, $\chi^2_{IP} < 25$, DIRA$>$ 0.999, $4750 < m_{DK} < 7000$MeV, $p_T > 1700$MeV, $p > 10000$MeV

Monte Carlo (MC) samples are produced for both the signal and control channel decays following the procedure described in section 3.4.2. As for the amplitude analysis, the samples are produced using a preliminary model for the $D^0 \to K^+K^-\pi^+\pi^-$ decay to ensure that for regions of phasespace that we expect to be highly populated, there are sufficient MC events present. Only the dominant D decay amplitude is generated depending on the charge of the B; for B^- events we generate $B^- \to D^0(\to K^+K^-\pi^+\pi^-)h^-$ and for B^+ events we generate $B^+ \to \bar{D}^0(\to K^+K^-\pi^+\pi^-)h^+$. Table 5.2 shows the MC samples produced for this analysis. For the purpose of investigating $B^\pm \to D(\to K^+K^-\pi^+\pi^-)\pi^\pm$ cross-feed background in the signal data, the control channel MC is also reconstructed as signal whereby the bachelor pion is given a kaon mass hypothesis, in the following indicated as $\pi_{\to K}$. The MC samples contain an even split of magnet up and magnet down configurations. The simulated data are run through the same offline reconstruction and selection procedure, which is described in the following, as the real data.

Table 5.2: Monte Carlo samples generated for $B \to Dh$ decays.

Decay	Sample size
$B^{\pm} \to D(\to K^+K^-\pi^+\pi^-)K^{\pm}$	2011 conditions: 1M
	2012 conditions: 2M
$B^{\pm} \to D(\to K^+K^-\pi^+\pi^-)\pi^{\pm}$	2011 conditions: 1M
	2012 conditions: 2M

5.1.1 Corrections for data/simulation differences

For this analysis we use the same technique as described in section 4.5.1 to take into account efficiency effects across the D decay phasespace; we use MC data that has been through detector simulation and the full selection procedure that is applied to the data to normalise the PDFs in the amplitude fit. Whilst we can determine the efficiency of most cuts from MC, the efficiency of PID cuts are found using a data-driven method. Corrections are also made to the MC data in order to correct for MC/data differences in tracking.

PID

The two RICH detectors, muon system and calorimeters are responsible for providing PID information on particles traversing the LHCb detector. Simulating the response of these detectors is non-trivial due to dependence on particle kinematics, detector occupancy which is event dependent and the conditions of the detector which can vary from run to run. Because of this the efficiency of selection cuts involving PID information are calculated using a data-driven method. For this the LHCb package *PIDCalib* is used [103].

Golden decay modes for the purpose of PID calibration are those that can be reconstructed without the need for PID information. These can provide pure calibration samples of pions and kaons without the use of PID cuts. For pions, channels such as $K_S^0 \to \pi^+\pi^-$ are used and for kaons, channels such as $\phi(1020) \to K^+K^-$ [104]. A *tag and probe* method is used on these two-prong decay vertices where one kaon/pion is used to tag the decay and the efficiency of a PID cut can be found by applying the cut to the other track of the vertex. Real data samples containing many of these *calibration* tracks of known particle type can be used to find the efficiency of a PID cut applied to a data sample used for analysis; this data sample is referred to as the *reference* sample and in our case, is the MC data used for the normalisation of PDFs in the fitting routine. The output of a PID variable is assumed to be fully parameterised by a set of kinematic and event variables. Most commonly used are the track momentum p and pseudorapidity η which are well modelled in MC data (often the number of tracks in the event N_{track} is also used but the distribution of this variable is known not to be well modelled in MC and so for analyses using MC reference samples this variable is not used). The calibration sample is binned in these variables; enough bins are used such that the efficiency of a PID cut is effectively constant within each bin. The efficiency of a PID cut on a track in the reference sample is found by finding the efficiency of the cut in the calibration bin i to which the track belongs,

$$\epsilon_i = \frac{N_i'}{N_i}$$

where N_i and N_i' are the number of tracks in the ith bin of the calibration sample before and after the PID cut is applied. When PID cuts are applied to multiple tracks in an event the total PID efficiency for that event is the product of the individual efficiencies

$$\epsilon_{PIDtotal} = \prod_i \epsilon_i.$$

The PIDCalib package creates histograms of the efficiency of a PID requirement as a function of track p and η for a given particle type for data taken in a specific data taking year (using data from all available runs) with a specific magnet polarity. These histograms are then used on the reference sample to find the efficiency of each PID cut on a track-by-track basis and calculate an overall PID efficiency for each event known as a PID weight.

Figure 5.1 shows the efficiency of the bachelor PID cut applied to the control channel data (see section 5.2) in bins of η and track momentum p for 2012 data where the magnet polarity is down. The efficiency appears fairly uniform apart from at the extremes of p and η.

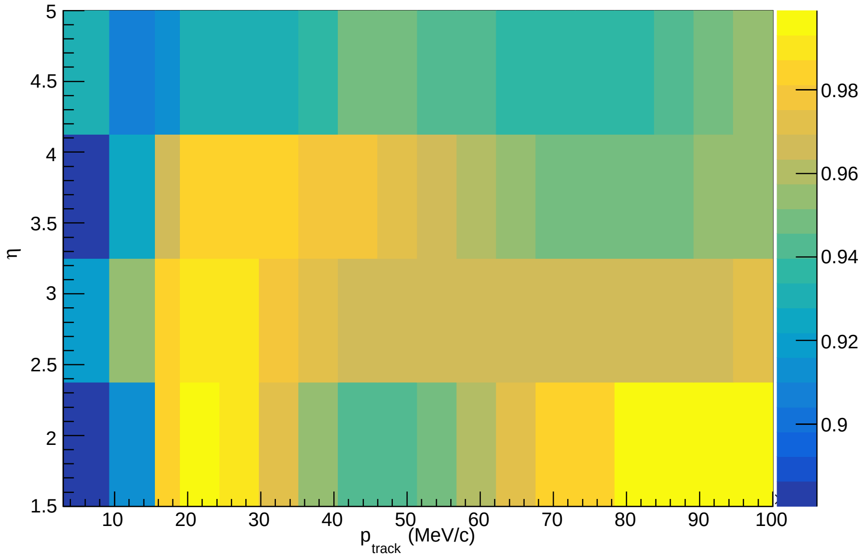

Figure 5.1: Efficiency of the bachelor PID cut applied to the control channel data in bins of pseudorapidity η and track momentum p for 2012, magnet down data. Created using the PIDCalib package [103].

Tracking

The track reconstruction efficiency is nominally taken from MC simulation, however the potential bias from data/MC differences must be accounted for. Corrections to be applied to simulated data to account for data/MC differences in the tracking efficiency are provided by the LHCb tracking group [105]. These corrections are found using a data-driven method that uses muons in $J/\psi \to \mu^+\mu^-$ decays. As for PID efficiency determination a tag and probe method is used where one of the muon tracks is fully reconstructed and the efficiency of the track reconstruction is found using the other track of the decay vertex. The ratio of track reconstruction efficiencies between data and simulation

$$\epsilon_{ratio} = \frac{\epsilon_{data}}{\epsilon_{sim}},$$

is found for different data taking periods and is used to correct the track reconstruction efficiency in simulated events.

The track reconstruction efficiency depends most on the on track momentum p, pseudorapidity η and the track multiplicity N_{track} of the event. Track reconstruction efficiency dependence in N_{track} is reasonably well described in simulation and so the simulated events are weighted to be in agreement with the N_{track} distribution of the data; ϵ_{ratio} is then determined in bins of p and η. The binning is chosen to keep the statistical uncertainty in each bin small. Figure 5.2 shows ϵ_{ratio} against p for 2011 and 2012 data split into two η regions where the simulated events are weighted in N_{track}. The average values of ϵ_{ratio} are compatible with unity where $\langle\epsilon^{2011}_{ratio}\rangle = 0.9983 \pm 0.0009$ and $\langle\epsilon^{2012}_{ratio}\rangle = 1.0053 \pm 0.0008$ with assigned systematic uncertainties of 0.4% [106].

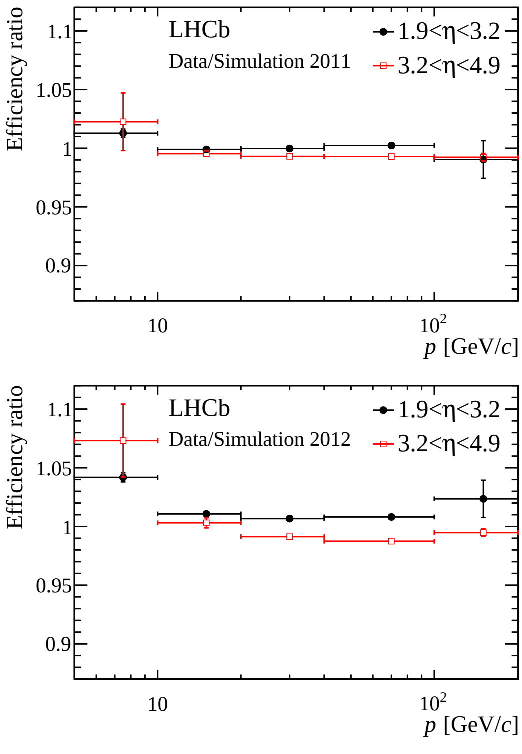

Figure 5.2: Ratio of track reconstruction efficiencies between data and simulation for 2011 (top) and 2012 (bottom) data as a function of track momentum p. This is further split into two pseudorapidity, η, regions and the simulated events are weighted in N_{track} to match the data distributions. These figures are taken from reference [106].

The results presented here are for muons that are not sensitive to hadronic interactions within the detector material. Due to uncertainty on the material budget of LHCb and hence on the level of hadronic interactions within the detector material, the track reconstruction efficiency of hadrons in simulated data has an uncertainty that is not yet accounted for. A further systematic of 1.4% is added to ϵ_{ratio} values for hadron tracks due to hadronic interactions [106].

5.2 Selection

The candidates that pass the trigger requirements and the stripping processing stage are subject to further offline selection.

5.2.1 Decay Tree Fitter

To improve the resolution of the 4-momenta of the final state particles, the DecayTreeFitter [107] (DTF) tool is applied to the events. DTF finds the best fit values for the 4-momentum of all particles in the decay chain with constraints applied to the masses of intermediate particles and to vertices. The quality of this refit is reported as a χ^2 value. Those events where this fit does not converge are removed from the dataset. In the refit for this analysis the mass of the D^0 meson is constrained to its nominal value (ensuring that events fall inside the kinematically allowed phasespace) and the B candidate is constrained such that its momentum vector points back to the PV. The refitted values of the 4-momenta are used in the amplitude fit to the D decay phasespace distribution to extract γ.

5.2.2 Multivariate Classifiers - boosted decision trees

Further classification of events into signal and background is achieved using a multivariate analysis technique known as a Boosted Decision Tree (BDT) which combines multiple (d) discriminating variables into one single discriminant $R^d \to R$. This is far more powerful than traditional, one-dimensional cut based methods [108].

Decision trees consist of a series of nodes. For each node (starting with the *root node*) a data splitting condition is established; a variable to be cut on and the cut value. The

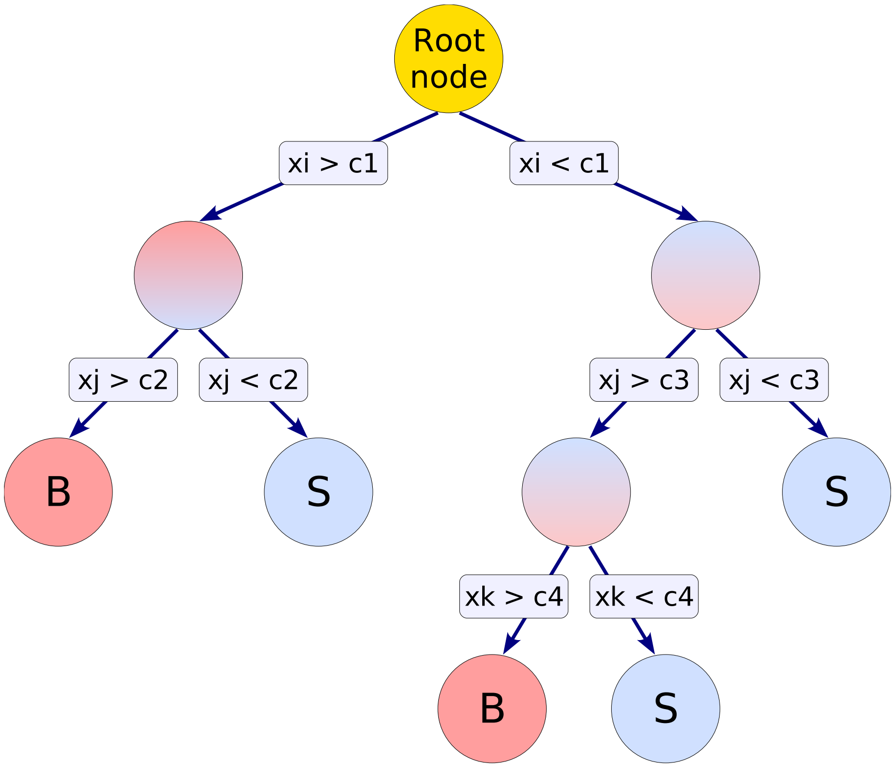

Figure 5.3: Illustration of a decision tree. Figure is taken from reference [108].

gain of a node can be found from the number of signal (s) and number of background (b) events or purity ($p = s/(s+b)$) of the events reaching the node

$$\text{gain} = 2p(1-p) = \frac{2s \times b}{(s+b)^2}.$$

The maximum value of gain is therefore 0.5 for a mixed sample with equal signal and background and the minimum value zero for a pure sample. The data splitting condition is found by maximising the difference in the gain between the node and the sum of its daughter nodes weighted by the relative fraction of events reaching them. This process is illustrated in figure 5.3 which is taken from reference [108]. A Decision Tree must be trained on events for which the classification (signal or background) of each event is known, this is an example of supervised machine learning. After a specified number of nodes, the d-dimensional phasespace is split into n regions known as *leaves* which are classified as either signal or background based on the classification of the majority of training events that reach them.

The power of a decision tree can be increased by *boosting* the decision tree. Boosted decision trees use the result of one decision tree in the creation of further decision trees. Misclassified training events in a decision tree are given a higher, common weight (or are boosted) in the training sample used to train subsequent decision trees. This creates a *forest* of decision trees. The final BDT response for N decision trees is a single value between -1 and +1 which is the combined weighted average of the output of all decision trees. For an event with a vector of input variables $\mathbf{x}$,

$$\text{BDT response}(\mathbf{x}) = \frac{1}{N}\sum_{i}^{N} \ln(\alpha_i)h_i(\mathbf{x}),$$

where $h_i(\mathbf{x})$ is the result of an individual decision tree i and takes discrete values -1 or +1; -1 if the event is classified as background or +1 if the event is classified as signal. The term α_i is given by $\alpha_i = (1 - \text{err}_i)/\text{err}_i$ where err_i is the proportion of misclassified training events in the decision tree i. In this way poorly performing decision trees contribute little to the overall BDT response for an event.

Decision tree classifiers have the advantage of being immune to the curse of dimensionality; a one-dimensional only optimisation is required at each node, achieved by scanning over 20 cut values in the chosen variable range. The particular collection of input variables available to the classifier is also less important which is advantageous as the discriminating power of a variable is not necessarily known a priori. While it is important to give the classifier access to the variables with the highest discriminating power, any input variables with a poor discriminating power will simply be ignored by the decision trees during the training process. Decision trees however can easily suffer from over-training, learning statistical fluctuations within the training samples rather than general trends in the data. Over-training is reduced by the process of boosting the tree. The individual decision trees in this analysis have a depth of only 2 nodes making them weak classifiers that are far less prone to over-training. The effect of any statistical fluctuations in the training data is reduced by using the weighted average of many individual weakly classifying trees. As a test for over-training a separate testing sample is created, the BDT response to the testing sample should match the BDT response to the training sample.

5.2.2.1 A BDT for $B^{\pm} \to D(\to K^{+}K^{-}\pi^{+}\pi^{-})K^{\pm}$ decays

A BDT using 1000 decision trees is built to remove combinatorial background from the data samples. Using the package TMVA (Toolkit for MultiVariate Analysis) [108] a BDT is built using variables that are predicted to discriminate most strongly between signal and combinatorial background. To train the BDT representative samples of signal and combinatorial background are provided to TMVA. Half is used for training the decision trees and half for testing for over-training. As a representative sample of signal decays $B^{\pm} \to D(\to K^{+}K^{-}\pi^{+}\pi^{-})K^{\pm}$ MC simulation data is used and for a representative combinatorial background sample $B^{\pm} \to D(\to K^{+}K^{-}\pi^{+}\pi^{-})K^{\pm}$ high-mass sideband data is used. The high-mass sideband consists of events in the region $5800 < m_{DK} < 7000$ MeV where we expect no specific decays to be present. The samples provided to TMVA are run through a basic pre-selection before training (which is also applied to the data samples to be used in the analysis) consisting of:

- DTF refit converges
- D candidate mass falls within 25 MeV of PDG value
- Bachelor track has momentum less than 100 GeV
- D flight distance significance (FD_{sig}) greater than zero i.e. the vertex of the D must be downstream from the B vertex.

The last of these requirements removes some of the charmless background events - decays where a $B^{\pm}$ particle decays to the same final state as the signal decay but not via a D meson. For these background decays the $B^{\pm}$ and fake D vertex will be concurrent, however due to the reconstruction the fake D vertex will be very slightly displaced in the positive or negative z direction relative to the $B^{\pm}$ vertex. This cut will remove all charmless backgrounds where the fake D has been reconstructed in the upstream direction relative to the $B^{\pm}$ vertex meaning approximately 50% of this background is removed.

The BDT method is implemented using the variables shown in table 5.3 with definitions given in section 3.2, by taking the logarithm of some of these variables their discriminating power is increased. Also shown are the variable's importance ranking i.e. how often the variable is chosen by the decision tree nodes.

Table 5.3: BDT input variables.

Variable	Ranking
D^0 momentum	1
log(Bachelor χ^2_{IP})	2
B momentum	3
log(B χ^2_{FD})	4
log(D^0 χ^2_{IP})	5
B p_t asymmetry	6
B χ^2_{IP}	7
log(D daughter[1, 2, 3, 4] χ^2_{IP})	8, 9, 10, 11

As explained above, once the BDT has been established each event can be given a BDT response value in the continuous range [-1, +1] where -1 is indicates the event is background and +1 indicates the event is signal. Figure 5.4 shows the values of the BDT response for the signal and background training and testing samples, where it can be seen how background events peak at -1 and signal events at +1. This plot also shows whether the BDT has been over-trained on the training sample which would be indicated by a poor match to the testing sample. No evidence of over-training is seen as the BDT response distributions for the training and testing samples are compatible.

In this analysis the BDT cut is left loose; events with a BDT response less than -0.9 are rejected. The motivation for this loose cut is the reduction of systematic uncertainties arising from unaccounted for MC/data differences in the BDT variables. The lack of any PID information in the discriminating variables chosen (motivated by the fact that the signal MC data does not reproduce the PID response well) means that this BDT can also be used to select the control channel decays.

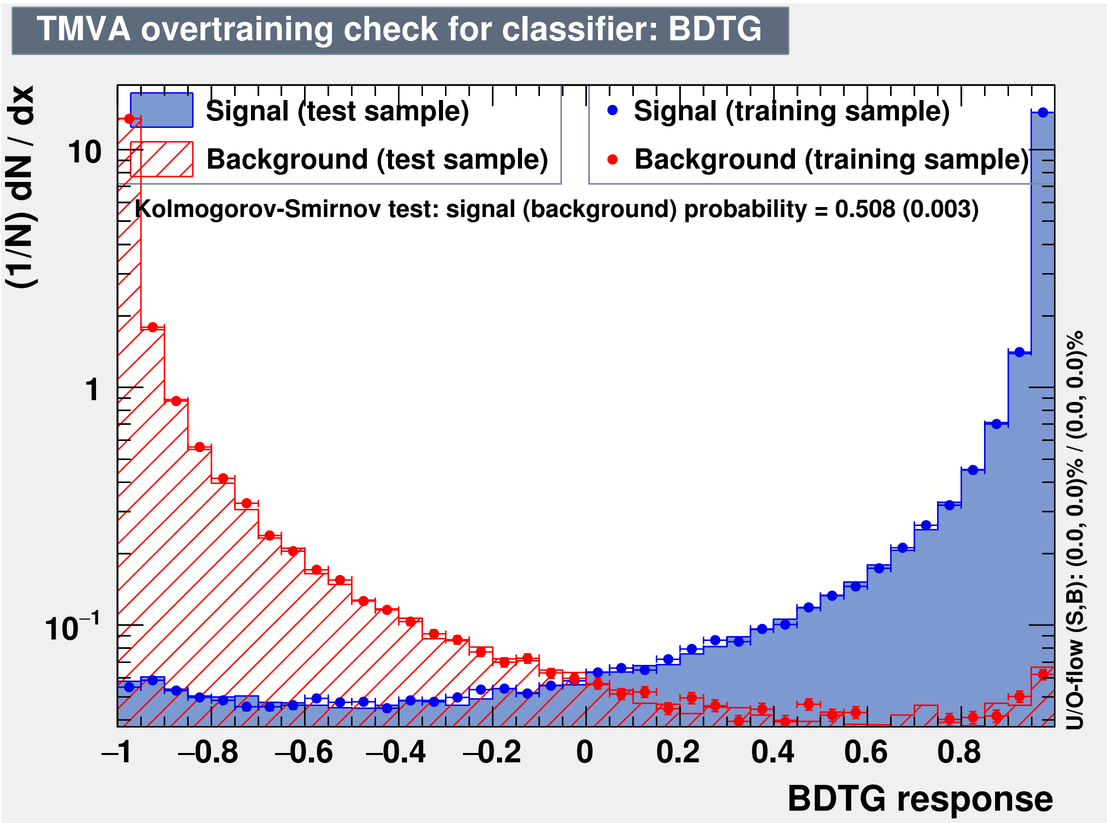

Figure 5.4: BDT response for representative signal and background samples used to train and test BDT.

5.2.3 Further cuts

After the BDT further vertex and kinematic cuts are made:

- DIRA of the D relative to the primary vertex greater than 0.99
- DIRA of the $B^{\pm}$ relative to the primary vertex greater than 0.9999
- D daughters momentum less than 100 GeV
- D flight distance significance > 2.0
- Kaon bachelor track DLL$(k - \pi) > 4$
- Pion bachelor track DLL$(k - \pi) < 4$

A cut on the DIRA variable of the D and $B^{\pm}$ particles further reduces combinatorial background and the flight distance significance of the D is tightened to remove any remaining charmless backgrounds. Up until this point in the analysis there has been no distinction made between the signal and control channels; a PID cut is applied to the bachelor particle to separate these decay modes.

The D daughter PID cuts are optimised using the control channel. The $m_{D\pi}$ distribution of $B^{\pm} \rightarrow D(\rightarrow K^{+}K^{-}\pi^{+}\pi^{-})\pi^{\pm}$ candidates after all other selection criteria has been applied is fitted with varying PID cuts applied to the D daughter particles. The level of signal and background retained is determined by integrating the signal and background PDFs in the $m_{D\pi}$ signal region. The fit for the optimal cut value is shown in figure 5.5 and is determined to be DLL$(k - \pi) > 6$ for D daughter kaons and DLL$(k - \pi) < 6$ for D daughter pions. Consistent with the amplitude analysis a selection cut is made to remove $B^{\pm} \rightarrow D(\rightarrow K_s(\pi^{+}\pi^{-})K^{+}K^{-})h^{\pm}$ background decays. To be conservative the same cut is applied to the $m_{\pi\pi}$ invariant mass distribution as is used for the CLEO II.V and CLEO III datasets.

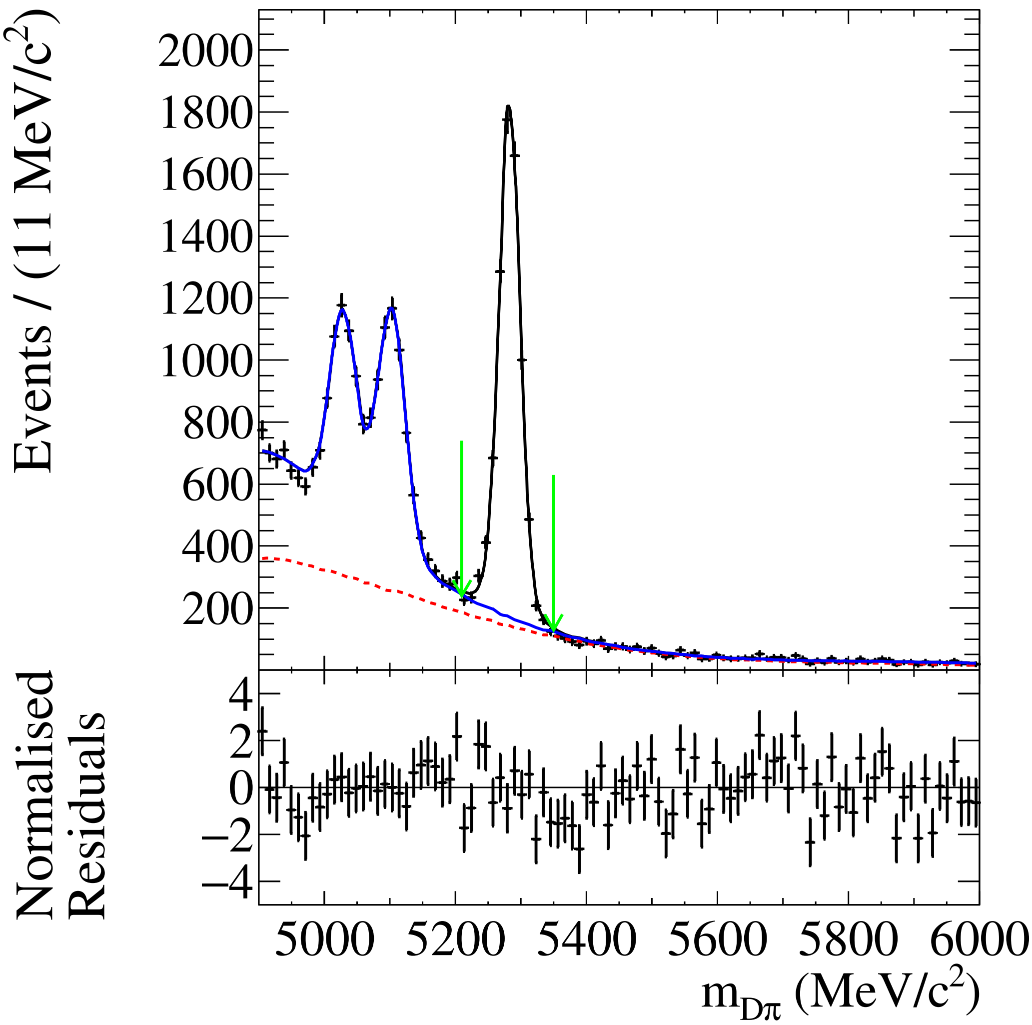

Figure 5.5: Fit to $B^{\pm} \to D(\to K^{+}K^{-}\pi^{+}\pi^{-})\pi^{\pm}$ $m_{D\pi}$ mass distribution with optimal D daughter PID cuts applied. The green arrows indicate the $m_{D\pi}$ signal region.

5.3 Mass fits

For events that pass the selection a fit to the $B^{\pm}$ candidate mass distribution, m_{Dh}, is performed. The mass fits are performed in the region $4900 < m_{Dh} < 6000$ MeV and provide the event-by-event signal and background weightings that are used in the likelihood fit (described fully in section 5.4). Events are grouped into 4 signal and background categories based on their description within the D decay phasespace:

- $B^{\pm} \to D(\to K^{+}K^{-}\pi^{+}\pi^{-})K^{\pm}$ signal
- $B^{\pm} \to D(\to K^{+}K^{-}\pi^{+}\pi^{-})\pi^{\pm}$ cross-feed background
- *Wrong D background* defined as events that are combinatorial in the reconstruction of the D candidate
- *Right D background* defined as partially reconstructed events or events that are combinatorial in the reconstruction of the $B^{\pm}$ candidate but contain a correctly reconstructed $D^{0} \to K^{+}K^{-}\pi^{+}\pi^{-}$ decay.

5.3.1 Control channel $B^{\pm}$ candidate mass fit

The control channel serves as a null test of the method used to extract γ. In this channel there is no cross-feed background from $B^{\pm} \to D(\to K^{+}K^{-}\pi^{+}\pi^{-})K^{\pm}$ decays due to the much lower branching fraction.

Signal shape

The signal shape in m_{DK} is taken from truth-matched MC events. The MC sample is fitted with a quadruple Gaussian whereby the mean and width of the second Gaussian is defined relative to the first Gaussian, the third Gaussian relative to the second Gaussian and so on. This results in one main Gaussian contributing approximately 85% of the total PDF and three much wider Gaussians that are required to fit the tails of this high statistics sample ($> 600,000$ events). This fit can be seen in figure 5.6 along with the residuals of the fit.

In the full fit to $m_{D\pi}$ for the control channel data, common control factors (cf) are applied to the mean and width of these Gaussians and are allowed to float in the fit to take into account any differences between data and MC.

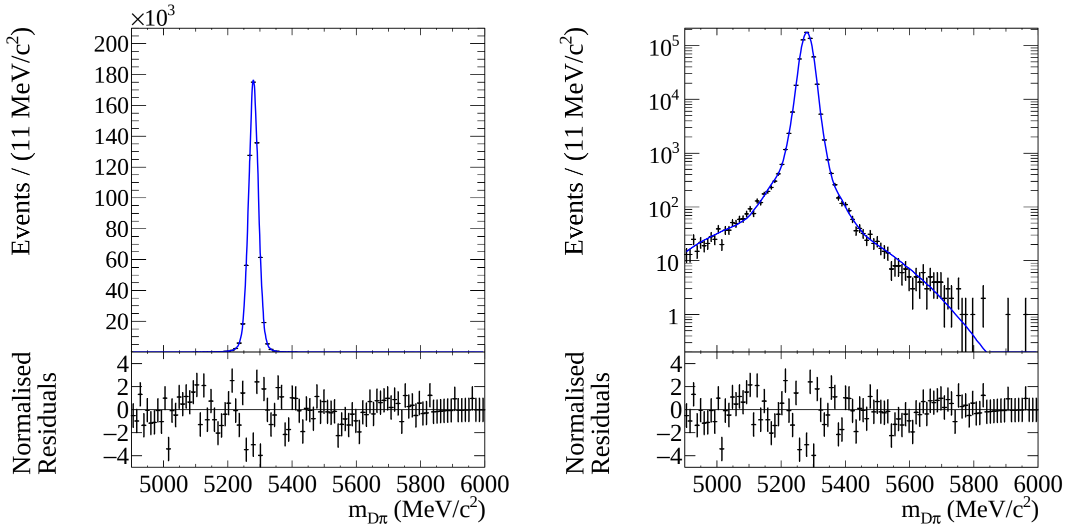

Figure 5.6: Fit to $m_{D\pi}$ for truth-matched $B^{\pm} \to D(\to K^+K^-\pi^+\pi^-)\pi^{\pm}$ MC data using a quadruple Gaussian on linear (left) and logarithmic (right) scales.

Wrong D background

Both the level of the wrong D background as well as a PDF in $m_{D\pi}$ to describe it must be found. Figure 5.7 shows the sidebands in $m_{KK\pi\pi}$ for the $B^{\pm} \to D(\to K^+K^-\pi^+\pi^-)\pi^{\pm}$ data after full selection; the lower sideband is defined as $1770 < m_{KK\pi\pi} < 1840$ MeV and the upper sideband as $1890 < m_{KK\pi\pi} < 1920$ MeV. These events are combinatorial in the reconstruction of the D candidate. To estimate the number of wrong D background events within the $m_{KK\pi\pi}$ signal region ($1840 < m_{KK\pi\pi} < 1890$ MeV) the sidebands in shown in 5.7 have been fitted in with a first order polynomial. This fit is extrapolated into the $m_{KK\pi\pi}$ signal region. By finding the integral of the polynomial in the signal region relative to that in the sidebands the number of wrong D background events in the signal region can estimated. The estimated number is 6070±58.

To establish a description of the wrong D background events in $m_{D\pi}$, these sideband events are fit with a 5th order Chebyshev polynomial. The fit to the $m_{D\pi}$ distribution

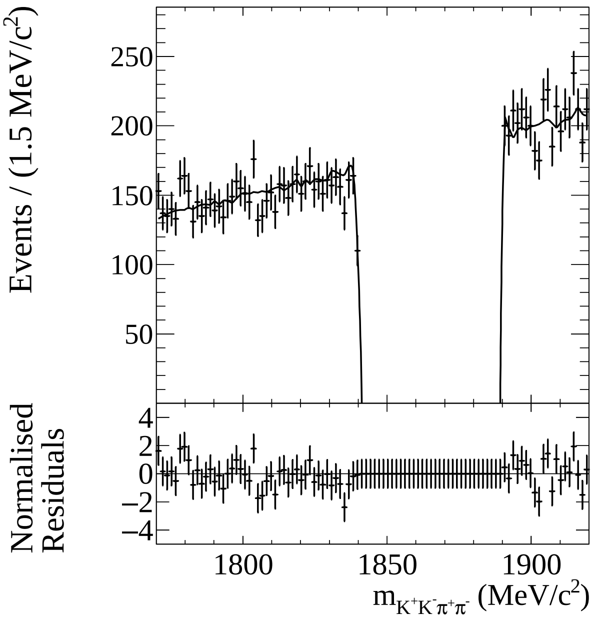

Figure 5.7: Fit to $m_{KK\pi\pi}$ distribution for $B^{\pm} \to D(\to K^+K^-\pi^+\pi^-)\pi^{\pm}$ events in the $m_{KK\pi\pi}$ sidebands.

can be seen in figure 5.8. Both the shape and yield of this background are fixed in the full fit to $m_{D\pi}$ for $B^{\pm} \to D(\to K^+K^-\pi^+\pi^-)\pi^{\pm}$ decays.

Right D background

Partially reconstructed background decays occur at low $m_{D\pi}$ values. These events are the result of decays that include all of the required particles of the signal decay chain (and so contain a real $D \to K^+K^-\pi^+\pi^-$ decay) but also have further particles in the decay chain that are not reconstructed. An example is $B^{\pm} \to D^{*0}(\to D^0\pi^0)\pi^{\pm}$ where the π^0 particle is not reconstructed. We model the low mass background by 2 overlapping Gaussians with a common width plus a wider Gaussian function. Also present are events that are combinatorial in the reconstruction of the $B^{\pm}$ candidate (rather than in the D candidate), this background is modelled by a first order polynomial. The parameters of these background shapes are allowed to float in the full fit to $m_{D\pi}$.

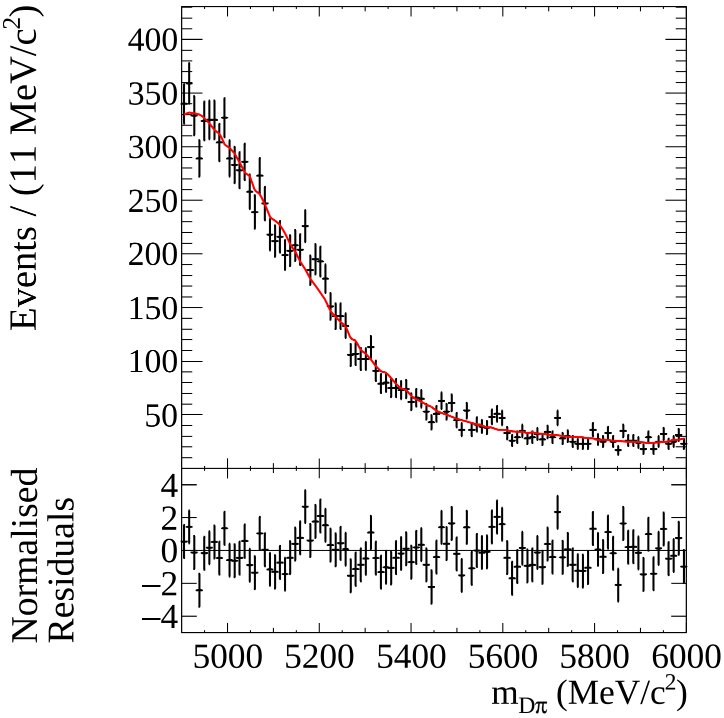

Figure 5.8: Fit to $m_{D\pi}$ distribution of $B^{\pm} \to D(\to K^{+}K^{-}\pi^{+}\pi^{-})\pi^{\pm}$ events in the $m_{KK\pi\pi}$ sidebands.

Full fit to $B^{\pm}$ candidate mass distribution for control channel events

A fit to $m_{D\pi}$ for $B^{\pm} \to D(\to K^{+}K^{-}\pi^{+}\pi^{-})\pi^{\pm}$ events is performed where the signal PDF and the wrong D background PDF and yield are fixed. Control factors applied to the signal PDF to account for data/MC differences are however allowed to float. The parameters of the shapes involved in the right D background PDF are also allowed to float in the fit. The result of this fit is shown in figure 5.9 with fitted parameter values shown in appendix A.3. The $\chi^2/ndof$ value for the fit is 1.32 where the value of $ndof$ has been found from $ndof = (N_{bins}-1)-N_{par}$, with the number of bins $N_{bins} = 100$ and the number of free parameters $N_{par} = 13$. The final yield of $B^{\pm} \to D(\to K^{+}K^{-}\pi^{+}\pi^{-})\pi^{\pm}$ signal events is 4700±82.

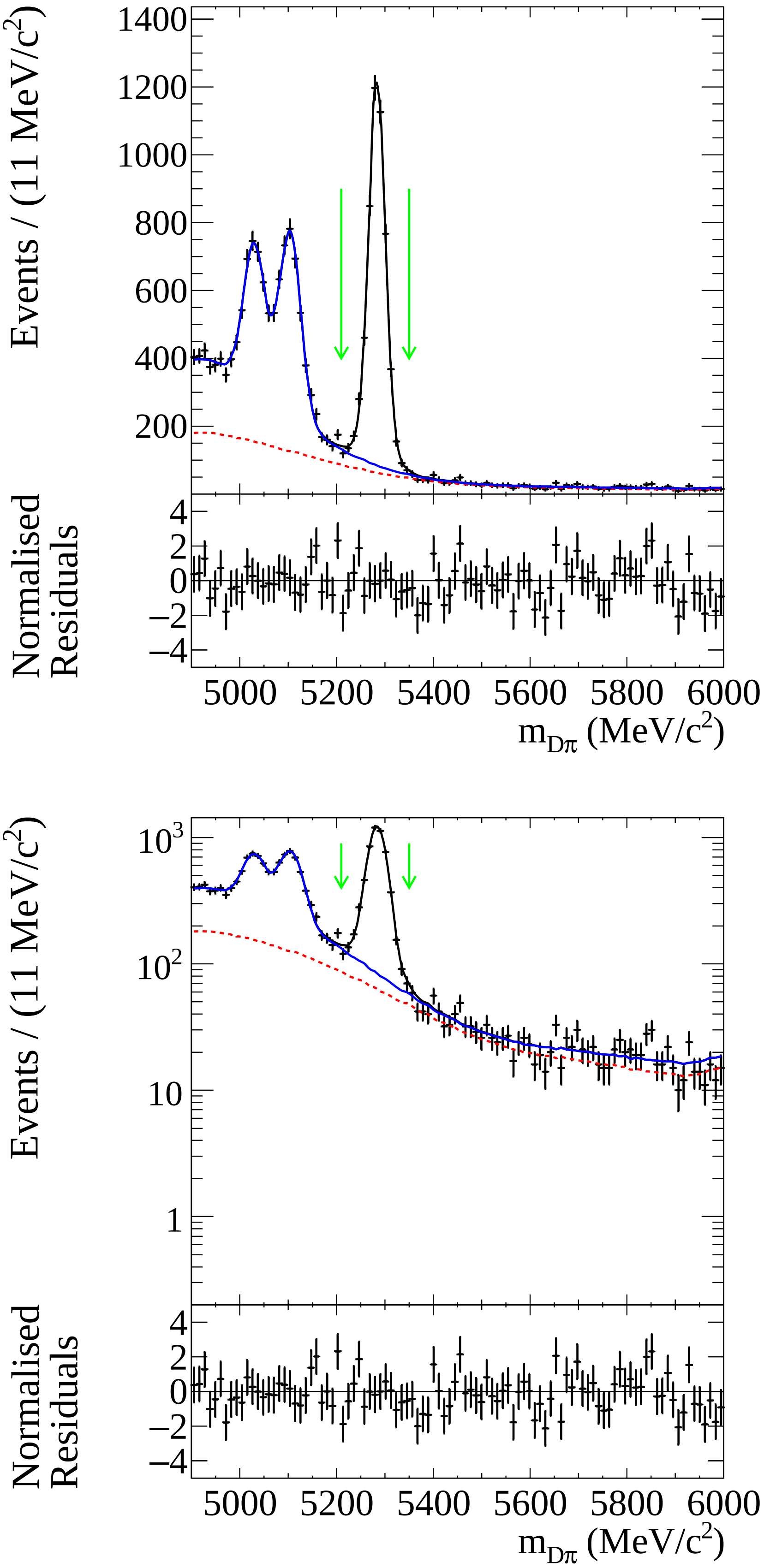

Figure 5.9: Fit to $m_{D\pi}$ for $B^{\pm} \rightarrow D(\rightarrow K^{+}K^{-}\pi^{+}\pi^{-})\pi^{\pm}$ control channel events on linear (top) and logarithmic (bottom) scales. The blue line represents the right D background, the red dashed line the wrong D background and total PDF is represented by the solid black line. The green arrows indicate the $m_{D\pi}$ signal region.

5.3.2 Signal channel $B^{\pm}$ candidate mass fit

Parameterisations of the signal and background components in $m_{D\pi}$ established from the high statistics control channel can be used in the fit to $B^{\pm} \to D(\to K^{+}K^{-}\pi^{+}\pi^{-})K^{\pm}$ data.

Signal shape

Truth-matched $B^{\pm} \to D(\to K^{+}K^{-}\pi^{+}\pi^{-})K^{\pm}$ MC data is fit with a quadruple Gaussian to obtain a signal shape in m_{DK}. Figure 5.10 shows this fit. As for the control channel, in the full fit to m_{DK}, floating control factors, cf, are applied to the means and widths of these Gaussians.

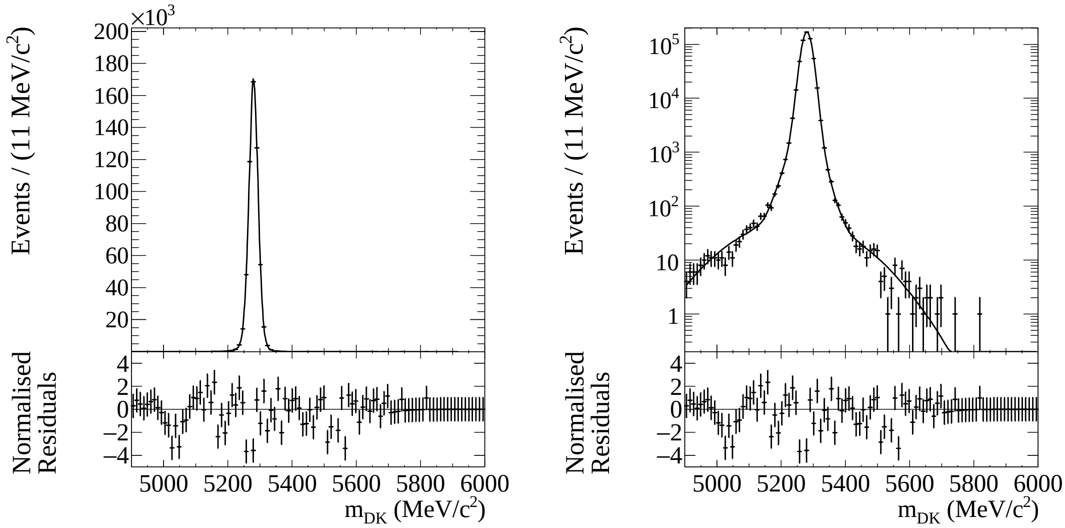

Figure 5.10: Fit to m_{DK} for truth-matched $B^{\pm} \to D(\to K^{+}K^{-}\pi^{+}\pi^{-})K^{\pm}$ MC data using a quadruple Gaussian on linear (left) and logarithmic (right) scales.

$B^{\pm} \to D(\to K^{+}K^{-}\pi^{+}\pi^{-})\pi^{\pm}$ cross-feed background

Unlike for the control channel there is the $B^{\pm} \to D(\to K^{+}K^{-}\pi^{+}\pi^{-})\pi^{\pm}$ cross-feed background to consider. $B^{\pm} \to D(\to K^{+}K^{-}\pi^{+}\pi^{-})\pi^{\pm}$ MC events are reconstructed as $B^{\pm} \to D(\to K^{+}K^{-}\pi^{+}\pi^{-})K^{\pm}$ events and the resulting $m_{D\pi\to K}$ distribution fit with a Crystal Ball[109] plus a triple Gaussian function. A Crystal-Ball function is a Gaussian with a width σ and power law tail at $\alpha \times \sigma$ from the mean. The sign of α determines if the power law tail is on the left or the right of the peak and a parameter n defines the slope of the exponential. Figure 5.11 shows this fit. In the full fit to m_{DK} the same control factors that are applied to the signal PDF are applied to the cross-feed background PDF.

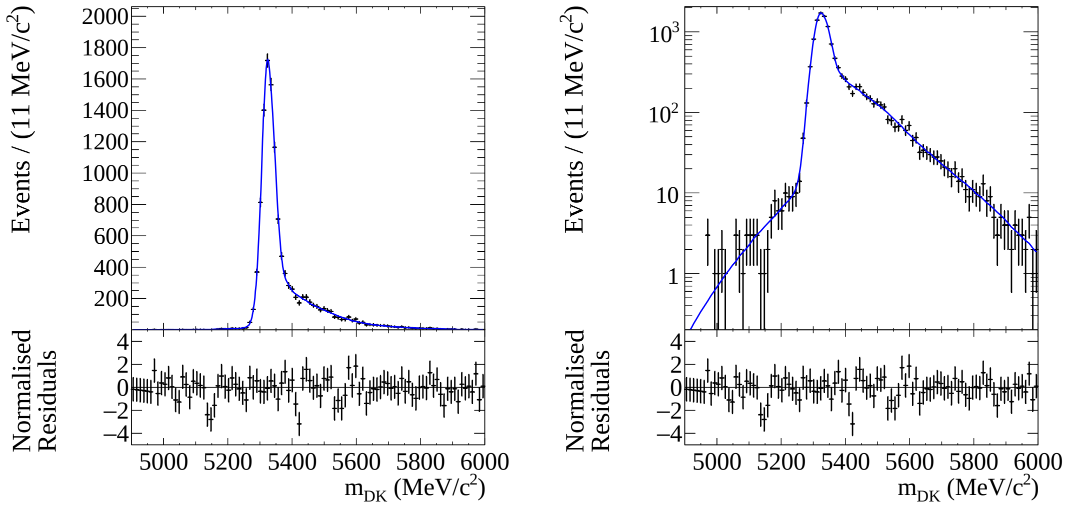

Figure 5.11: Fit to m_{DK} for $B^{\pm} \to D(\to K^+K^-\pi^+\pi^-)\pi^{\pm}$ MC events reconstructed as $B^{\pm} \to D(\to K^+K^-\pi^+\pi^-)K^{\pm}$ events.

Wrong D background

As for the control channel, the $m_{KK\pi\pi}$ distribution for events falling in the D mass sidebands are fit with a first order polynomial to determine the number of wrong D background events expected in the $m_{KK\pi\pi}$ signal region. Figure 5.12 shows the fit to the $m_{KK\pi\pi}$ sideband events. It is estimated that there are 1160 ± 25 wrong D background events in the signal region. Figure 5.13 shows the fit to m_{DK} for these events, again a 5th order Chebyshev polynomial is used.

Right D background

The form of the PDF used to describe the right D background is taken from the control channel fit, however, now there is a third, smaller Gaussian to be added to account for partially reconstructed $B^{\pm} \to D(\to K^+K^-\pi^+\pi^-)\pi^{\pm}$ cross-feed background events. The

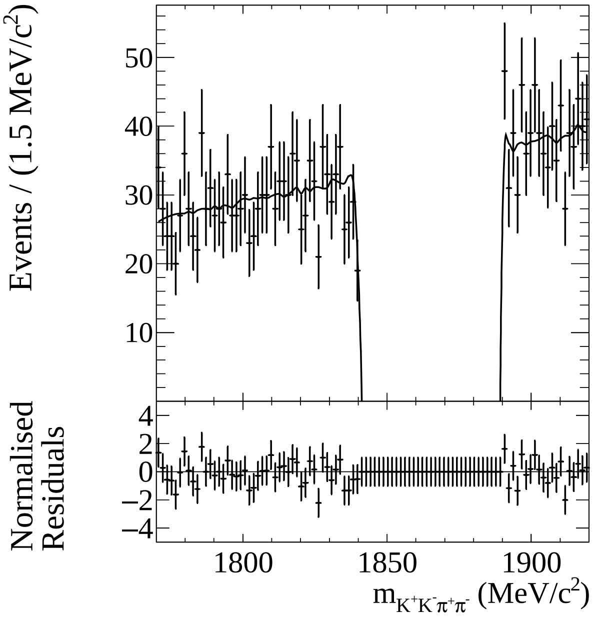

Figure 5.12: Fit to $m_{KK\pi\pi}$ for $B^{\pm} \rightarrow D(\rightarrow K^{+}K^{-}\pi^{+}\pi^{-})K^{\pm}$ events falling in the $m_{KK\pi\pi}$ sidebands.

additional Gaussian as well as the relative fractions of the different components involved in the right D background PDF are allowed to float in the full fit to m_{DK}.

Full fit to $B^{\pm}$ candidate mass distribution for signal channel events

In summary the signal and cross-feed background PDFs in m_{DK} are taken from MC and fixed with common control factors, cf, that are allowed to float in the fit to account for data/MC differences. The wrong D background yield and PDF are fixed. The right D background PDF is taken from the control channel fit where there is an additional Gaussian to account for partially reconstructed cross-feed background decays; the relative amounts of each component in the right D background PDF are allowed to float. The final mass fit to $B^{\pm} \rightarrow D(\rightarrow K^{+}K^{-}\pi^{+}\pi^{-})K^{\pm}$ events is shown in figure 5.14 and the fitted parameter values can be seen in appendix A.3. The $\chi^2/ndof$ value for the fit is 1.08 with the number of bins $N_{bins} = 100$ and the number of free parameters $N_{par} = 11$. The final yield of $B^{\pm} \rightarrow D(\rightarrow K^{+}K^{-}\pi^{+}\pi^{-})K^{\pm}$ signal events is 360±28.

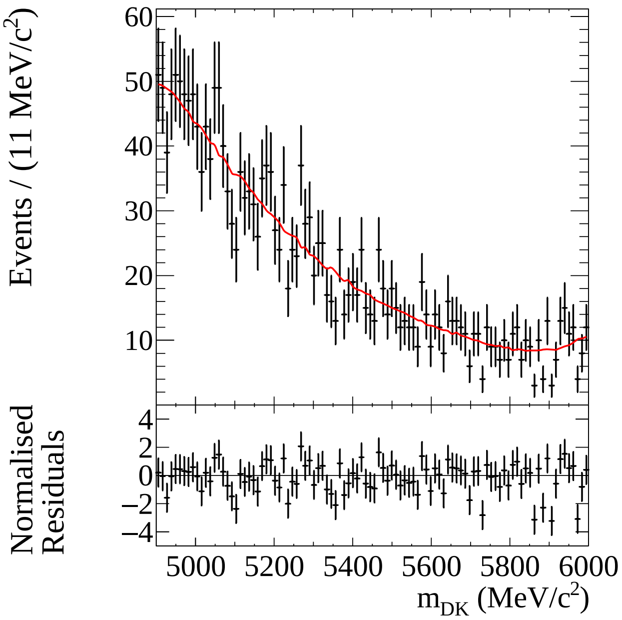

Figure 5.13: Fit to m_{DK} for $B^{\pm} \to D(\to K^+K^-\pi^+\pi^-)K^{\pm}$ events falling in the $m_{KK\pi\pi}$ sidebands.

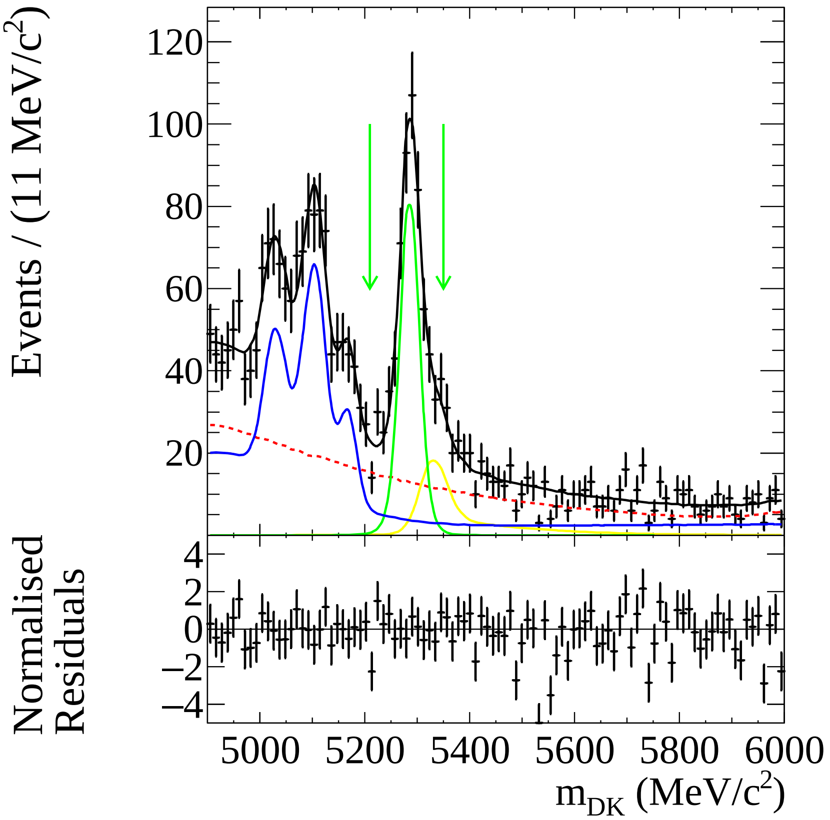

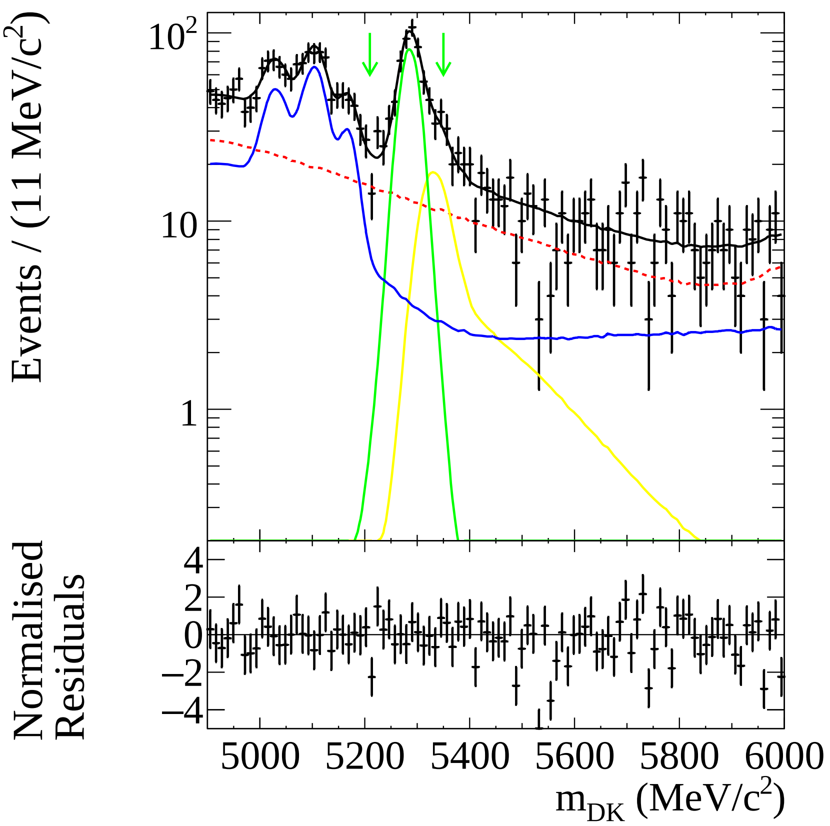

Figure 5.14: Fit to m_{DK} for $B^{\pm} \to D(\to K^{+}K^{-}\pi^{+}\pi^{-})K^{\pm}$ events on linear (top) and logarithmic (bottom) scales. The green line represents the signal shape, the yellow the cross-feed background, the blue the right D background and the red dashed line the wrong D background.The total PDF is represented by the solid black line and the green arrows indicate the m_{DK} signal region.

5.3.3 Signal and background probability weights

Using the mass PDFs, $P(m_{Dh})$, established above, the probability for each event to be either signal, cross-feed background, wrong D background or right D background can be calculated based on their position in m_{Dh}. These probabilities weight the events in the likelihood fit. The signal probability of an event, $W^{sig}(m_{Dh})$, is defined as

$$W^{sig}(m_{Dh}) = \frac{P_{\text{sig}}(m_{Dh})}{P_{\text{sig}}(m_{Dh}) + P_{\text{cross-feed bkg}}(m_{Dh}) + P_{\text{Right } D \text{ bkg}}(m_{Dh}) + P_{\text{Wrong } D \text{ bkg}}(m_{Dh})}$$

with analogous expressions for the cross-feed background, right D and wrong D background probabilities. It should be noted that for the control channel the probability for an event to be cross-feed background is zero. Figure 5.15 and figure 5.16 show the distributions of the signal and background probabilities against m_{Dh} for $B^{\pm} \to D(\to K^+K^-\pi^+\pi^-)\pi^{\pm}$ data and $B^{\pm} \to D(\to K^+K^-\pi^+\pi^-)K^{\pm}$ data respectively.

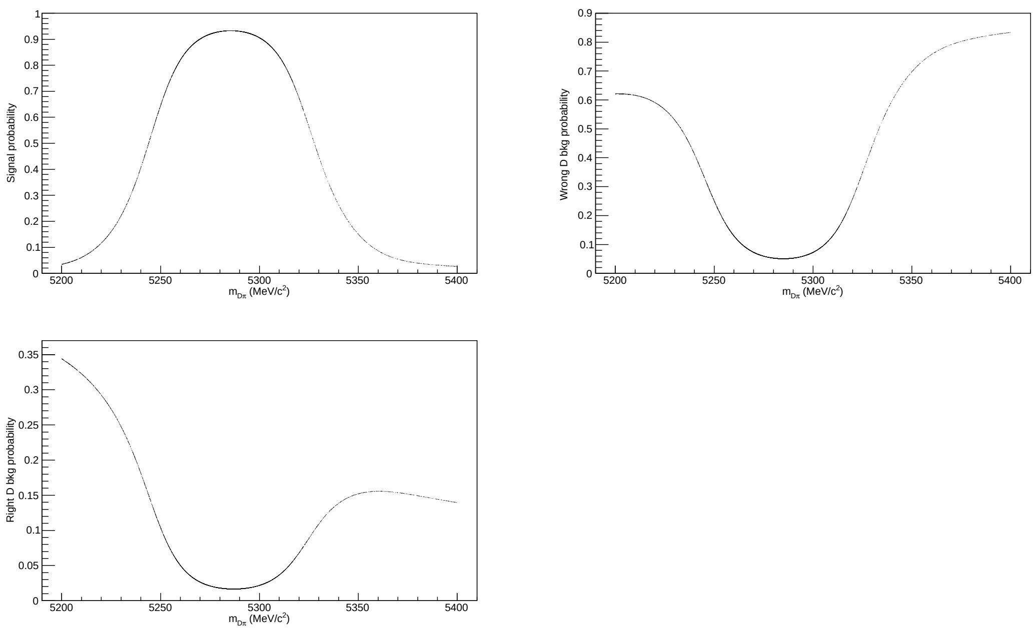

Figure 5.15: Signal and background probabilities against $m_{D\pi}$ for $B^{\pm} \to D(\to K^+K^-\pi^+\pi^-)\pi^{\pm}$ events.

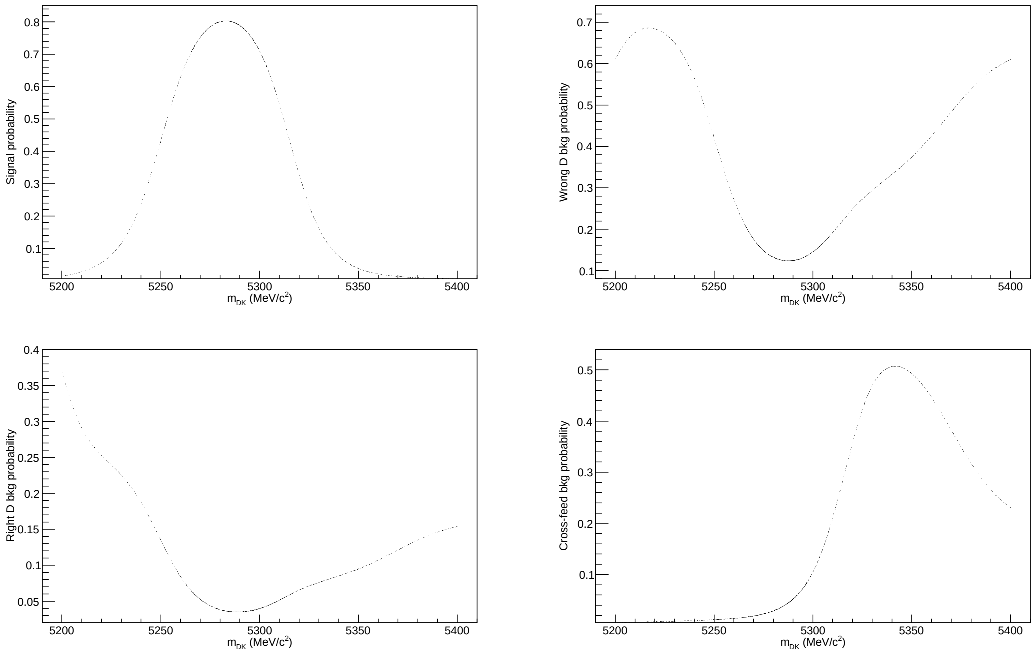

Figure 5.16: Signal and background probabilities against m_{DK} for $B^{\pm} \to D(\to K^{+}K^{-}\pi^{+}\pi^{-})K^{\pm}$ events.

5.4 Likelihood fit to extract γ

This section will describe the fit to the D decay phasespace used to extract γ, including how each of the signal and background components are modelled and the full likelihood function that we maximise.

In the likelihood fits the use of Cartesian coordinates is favoured over the use of polar coordinates where

$$x_\pm = r_B^{Dh}\cos(\delta_B^{Dh} \pm \gamma)$$

$$y_\pm = r_B^{Dh}\sin(\delta_B^{Dh} \pm \gamma)$$

as polar coordinates are cyclic. To obtain values for the parameters $x_\pm, y_\pm$ from which we extract γ, an unbinned maximum likelihood fit is performed to the selected events falling in the m_{Dh} signal range $5200 < m_{Dh} < 5400$ MeV. The reduced mass range retains 99% of signal decays as determined from the $B^\pm$ candidate mass fits. In total we have 3103 B^+ candidates and 3209 B^- candidates for the control channel and 378 B^+ candidates and 417 B^- candidates for the signal channel. The log likelihood function is

$$\begin{aligned}\log\mathcal{L} = &\sum_{B^+\text{cand }i}\left[\log\left(\sum_c W_i^c(m_{Dh}) \times P_c^{\text{D decay}}(x_+, y_+; p_i)\right)\right] \\ &+ \sum_{B^-\text{cand }j}\left[\log\left(\sum_c W_j^c(m_{Dh}) \times P_c^{\text{D decay}}(x_-, y_-; p_j)\right)\right]\end{aligned} \tag{5.1}$$

where c runs over the four signal and background components, p_i is the 4-momenta of the final state particles in event i, $W_i^c(m_{Dh})$ are the signal and background weights for the event and $P_c^{\text{D decay}}(x_\pm, y_\pm; p_i)$ are the PDFs describing the signal and background components in the phasespace of the D decay as a function of the fit variables $x_\pm$, $y_\pm$. These are described in the following.

5.4.1 Signal model

The PDF used to describe $B^\pm \to D(\to K^+K^-\pi^+\pi^-)h^\pm$ decays is defined using the LASSO amplitude model, $A_{D^0}(p)$, for $D^0 \to K^+K^-\pi^+\pi^-$ decays found in section 4.8. The PDF for B^+ signal decays is given by

$$P_{\text{sig}}^{\text{D decay}}(x_+, y_+; p_j) = \frac{\epsilon(p_j)|A_{\bar{D}^0}(p_j) + (x_+ + iy_+)A_{D^0}(p_j)|^2 R_4(p)}{\int \epsilon(p)|A_{\bar{D}^0}(p) + (x_+ + iy_+)A_{D^0}(p)|^2 R_4(p)\mathrm{d}p} \tag{5.2}$$

where $\epsilon(p)$ is the efficiency function across the D decay phasespace. A similar expression exists for B^- decays using the variables x_-, y_-. As described in section 4.5.1 the efficiency function in the numerator can be ignored as it does not depend on the fit parameters $x_\pm$, $y_\pm$, its only contribution is in the normalisation term of the PDF. Using the same technique as for the amplitude analysis, we use the MC simulation events to normalise the PDFs in the likelihood fit. Generally, the MC models the efficiencies for the real data well and corrections are applied as described in section 5.1.1 for known discrepancies. It is informative to see the variation in efficiency effects over the D decay phasespace. To do this we plot the B^+ and B^- MC simulation events weighted by the inverse of their generation values, $|A_{\bar{D}}^{\text{gen}}(p_j)|^2$ and $|A_{D}^{\text{gen}}(p_j)|^2$ respectively. This should leave the efficiency effects applied to a phasespace distribution. If the efficiency is uniform over the D decay phasespace these distributions will simply look like phasespace. These plots are shown in figure 5.17 and 5.18 where the phasespace distribution has also been plotted for comparison. As can be seen the efficiency effects over the D decay phasespace (that are visible in the ten possible invariant mass projections) are relatively uniform apart from the clearly visible K_S mass veto in $m_{\pi\pi}$. This is a good indicator of a uniform efficiency.

5.4.2 Background PDF description

Wrong D background decays

A description for the wrong D background must be found from a fit to a representative sample of these events. Due to the far greater statistics available and the fact that this background should not depend on the bachelor track the control channel data is used for this. Modelling this background using $m_{KK\pi\pi}$ sideband events is subject to the same issue as for the CLEO combinatorial background; the use of decay tree fitter with a constrained D candidate mass causes edge effects at the extremes of phasespace. A sample is required that uses the same D candidate mass range as the signal. This can

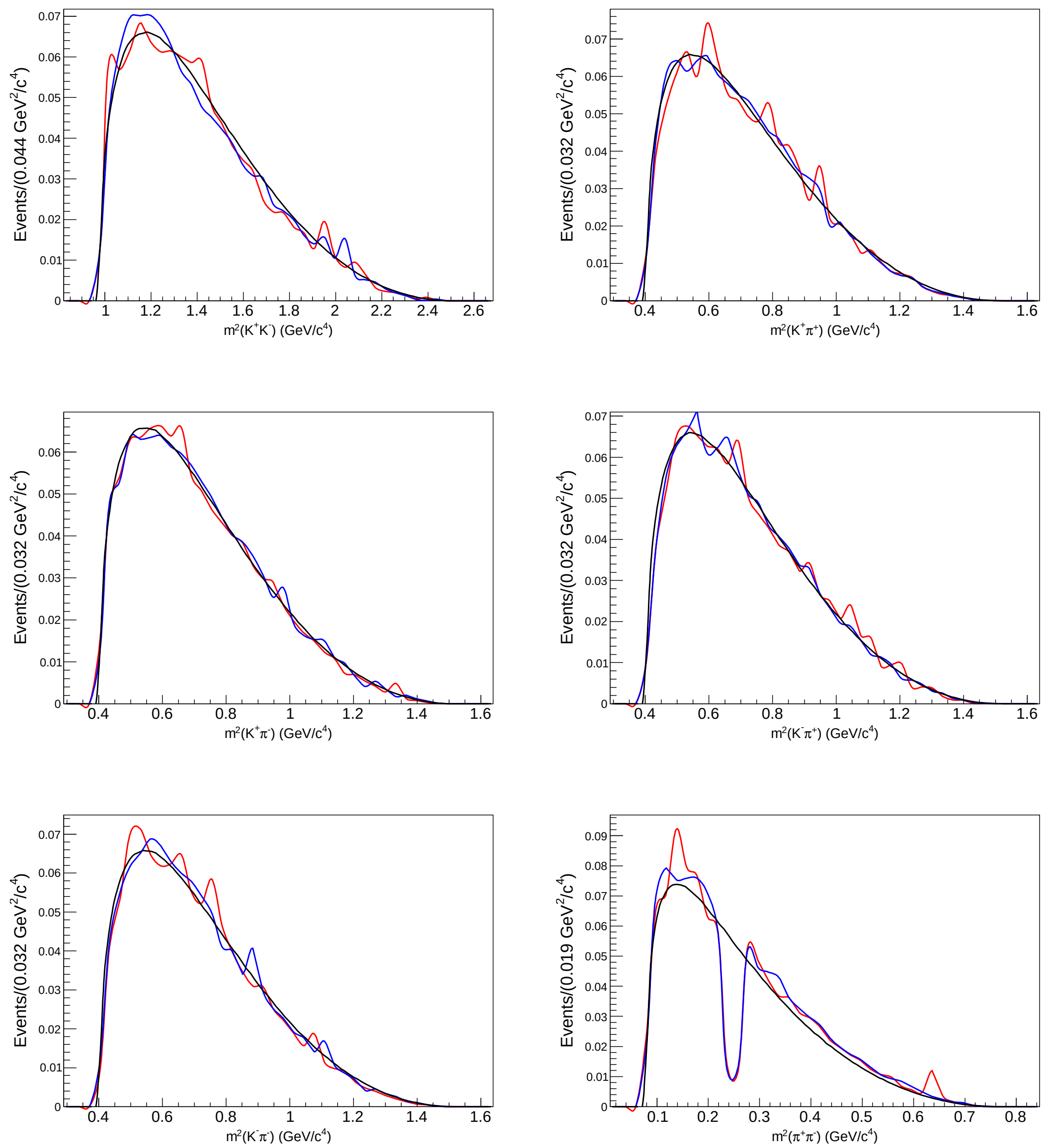

Figure 5.17: Invariant 2-body mass distributions of MC simulation events weighted by the inverse of their generation values. The red line represents B^- events, the blue line B^+ events and the black line is a phasespace distribution.

be obtained from the high $m_{D\pi}$ region $5500 < m_{D\pi} < 7000$ MeV. Figure 5.19 shows the $m_{KK\pi\pi}$ and $m_{D\pi}$ distribution for $B^{\pm} \to D(\to K^+K^-\pi^+\pi^-)\pi^{\pm}$ events where the signal region and the high $m_{D\pi}$ region have been highlighted. The high $m_{D\pi}$ region has contamination from events that have a real $D \to K^+K^-\pi^+\pi^-$ decay which is seen by a clear peak in the $m_{KK\pi\pi}$ distribution of these events. By reversing the D flight distance significance cut these events are removed from the sample leaving 852 events representative of wrong D background.

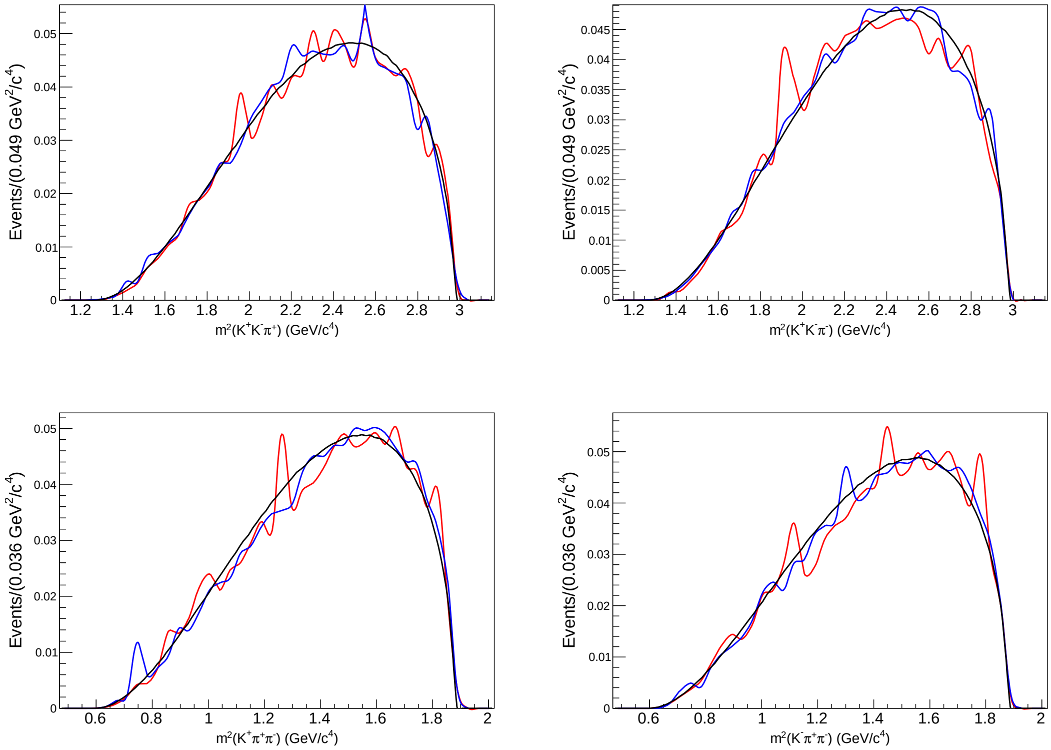

Figure 5.18: Invariant 3-body mass distributions of MC simulation events weighted by the inverse of their generation values. The red line represents B^- events, the blue line B^+ events and the black line is a phasespace distribution.

Table 5.4: Fit fractions (%) of amplitude components used in the wrong D background model.

Decay channel	Fit fraction (%)
$D^0 \to \phi(1020)\,(\pi^+\pi^-)_S$	9.13 ± 1.29
$D^0 \to K^{*0}\,(K^-\pi^+)_S$	3.36 ± 2.44
$D^0 \to \bar{K}^{*0}\,(K^+\pi^-)_S$	2.00 ± 2.36
$D^0 \to (K^+K^-)_S\,(\pi^+\pi^-)_S$	85.51 ± 3.26

An incoherent amplitude model is fit to these events following the same procedure as described in section 4.6. Figure 5.20 shows the invariant mass projections of this fit and table 5.4 the fit fractions of the amplitude components included.

Right D decays

The right D background events contain a correctly reconstructed $D \to K^+K^-\pi^+\pi^-$ decay and as such can still be described using the LASSO amplitude model found in section 4.8. It is assumed that the event is equally likely to contain a D^0 or $\bar{D}^0$ decay

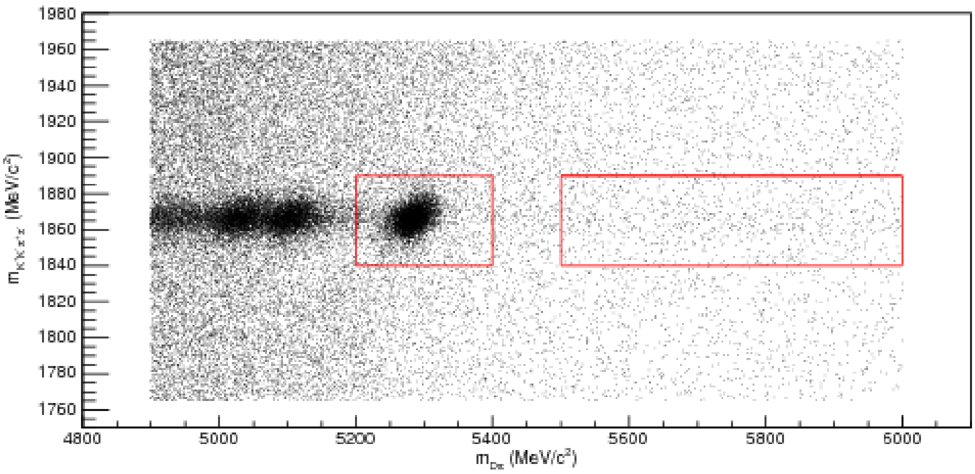

Figure 5.19: Distribution of $B^{\pm} \to D(\to K^{+}K^{-}\pi^{+}\pi^{-})\pi^{\pm}$ control channel events in $m_{KK\pi\pi}$ and $m_{D\pi}$ space. The signal box (left) and the high $m_{D\pi}$ mass region (right) are indicated.

and as such can be described by

$$\frac{1}{2}(|A_{D^0}(p)|^2 + |A_{\bar{D}^0}(p)|^2)$$

in the D decay phasespace.

Cross-feed background

For the signal channel there is the $B^{\pm} \to D(\to K^{+}K^{-}\pi^{+}\pi^{-})\pi^{\pm}$ cross-feed background to consider. The parameter $r_B^{D\pi}$ is an order of magnitude smaller than r_B^{DK} and so the interference term in $B^{\pm} \to D(\to K^{+}K^{-}\pi^{+}\pi^{-})\pi^{\pm}$ decays can be ignored at the level of precision attainable in this analysis. The cross-feed events are modelled in the same way as the signal events, using equation 5.2, but with $x_{\pm}$ and $y_{\pm}$ fixed to zero.

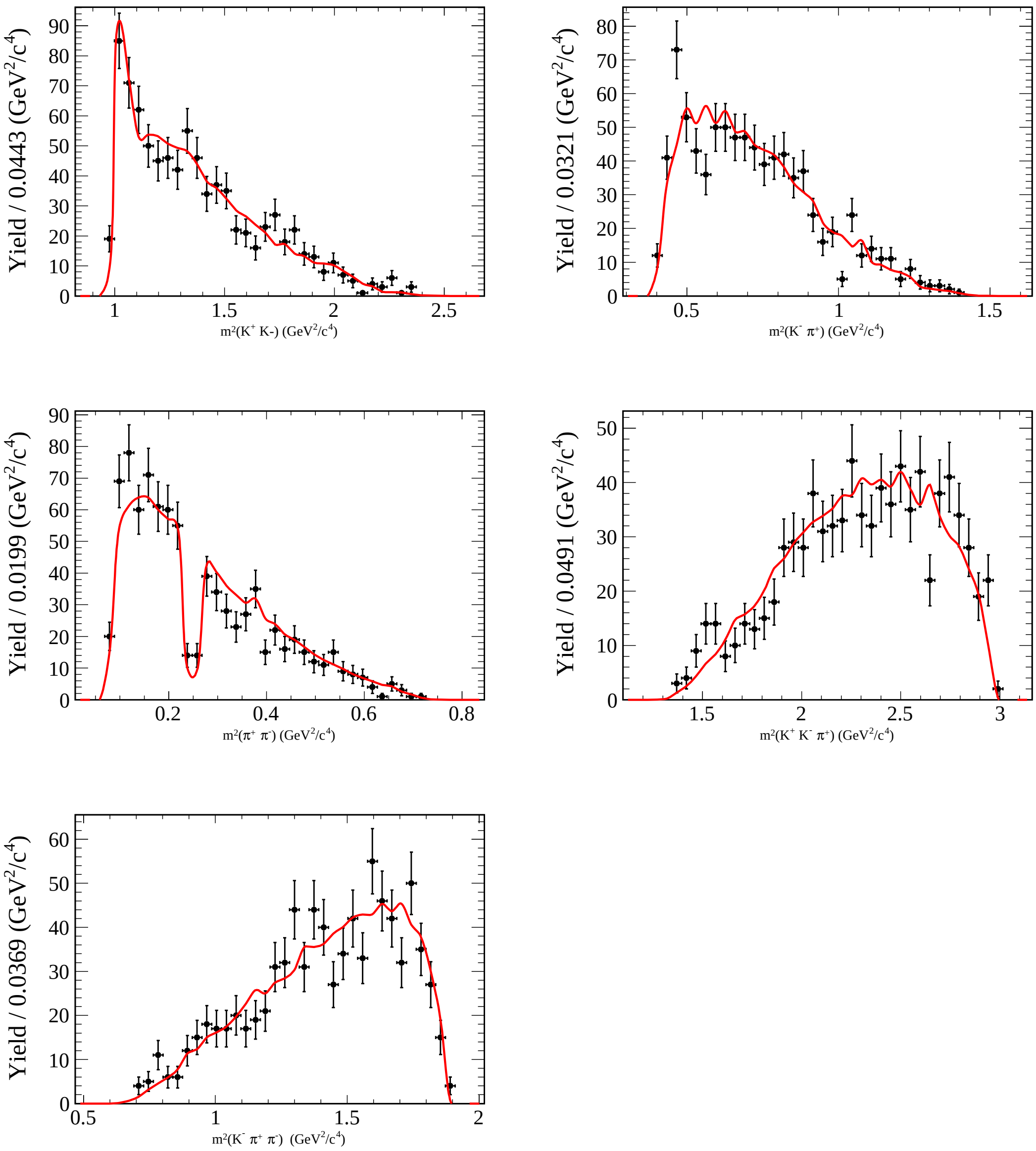

Figure 5.20: Invariant mass projections for the fit to $B^{\pm} \to D(\to K^+K^-\pi^+\pi^-)\pi^{\pm}$ wrong D background events

5.5 Fitter Validation

Pull studies using simulated data are performed to confirm whether we can recover $x_\pm$ and $y_\pm$ values in a fit to the D decay phasespace using the LASSO $A_{D^0}(p)$ model found in section 4.8.

5.5.1 Basic toy Monte Carlo pull study

A high statistics toy MC study is performed using approximately ten times the number of events expected in data. Events are produced in MINT according to the distribution

$$|A_{\bar{D}^0}(p_j) + (x_+ + iy_+)A_{D^0}(p_j)|^2$$

and

$$|A_{D^0}(p_j) + (x_- + iy_-)A_{\bar{D}^0}(p_j)|^2$$

for B^+ and B^- events respectively using the generation values shown in table 5.5. The samples are then fit using the PDF shown in 5.1 where background weights are set to zero. Approximately 300 such experiments are run using different random seeds for event generation and a pull study performed. The results of this study are shown in table 5.6 and are illustrated in figure 5.21. The pull study shows no bias over 2 sigma and confirms the viability of the measurement of $x_\pm$ and $y_\pm$ using the amplitude fitter. The pull study is repeated using the statistics available for the signal decay. The results for this lower statistics pull study can be seen in table 5.7 and are illustrated in figure 5.22. It can be seen that for the lower statistics pull study biases up to 2 sigma begin to appear, albeit only a small bias of 13% of the statistical uncertainty. To be conservative a systematic uncertainty could be assigned to the final $x_\pm$ and $y_\pm$ values.

Table 5.5: MC generation values. Angles given in radians

Parameter	Generation value
r_B	0.089
γ	1.27
δ	1.95
x_+	-0.089
y_+	-0.007
x_-	0.069
y_-	0.056

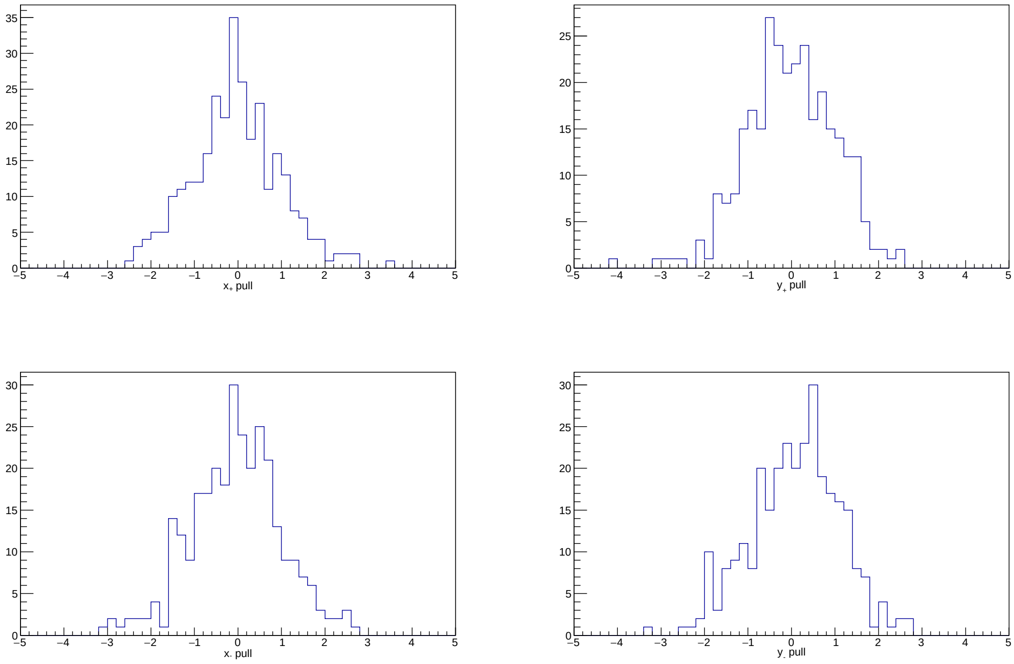

Figure 5.21: Distribution of pulls for high statistics toy MC pull study

Table 5.6: Results of high statistics pull study

Parameter	Pull mean	Pull width
x_+	-0.034±0.059	1.013±0.042
y_+	-0.020±0.059	1.019±0.042
x_-	-0.045±0.060	1.031±0.042
y_-	0.091±0.059	1.022±0.042

Table 5.7: Results of low statistics pull study

Parameter	Pull mean	Pull width
x_+	-0.032±0.063	1.086±0.045
y_+	-0.129±0.058	1.005±0.041
x_-	-0.075±0.060	1.036±0.043
y_-	-0.027±0.058	0.995±0.041

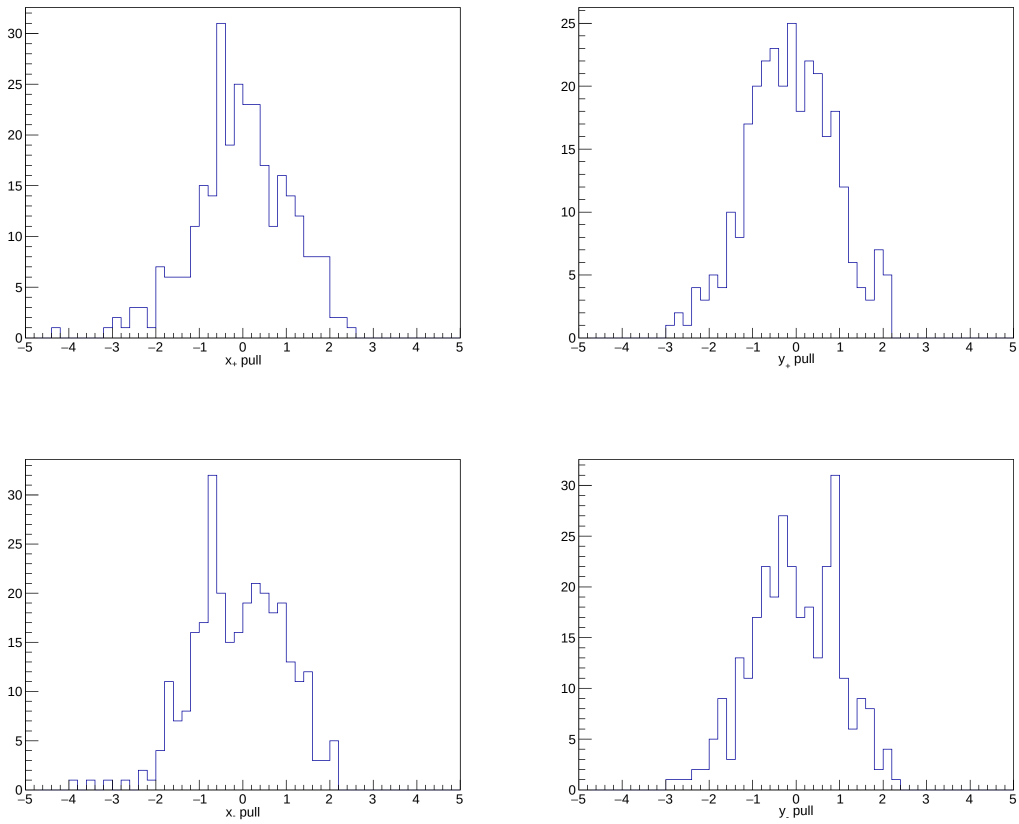

Figure 5.22: Distribution of pulls for low statistics toy MC pull study

5.5.2 Validation of method using control channel data

The control channel data serves as an excellent test of our method to extract γ; we expect the fit parameters $x_\pm, y_\pm$ to be consistent with zero. As an initial sanity check we plot the invariant mass projections of the B^+ and B^- events on top of one another where the invariant mass projection plotted for B^+ events is the conjugate of that plotted for B^- events i.e. the s_{123} distribution of B^+ events is plotted on top of the s_{124} distribution for B^- events. For control channel events these distributions should be in agreement with each other. These plots can be seen in figure 5.23 and 5.24.

We fit the control channel data using the likelihood function given in 5.1. The $A_{D^0}(p)$ amplitude component parameters, a_i, are Gaussian constrained to their values in the LASSO model (described in section 4.8) taking into account the full covariance matrix. The results of $x_\pm$ and $y_\pm$ for such a fit are given in table 5.8 and the modified amplitude component parameters, a_i and fit fractions are given in table 5.9. Figures 5.25 and 5.26 show the fit in the 2- and 3-body invariant mass projections for B^+ events and figures 5.27 and 5.28 for the B^- events. It can be seen that although the x parameters are consistent with zero the y parameters are inconsistent with zero at the level of 5 and 6 sigma. Reassuringly however, the x and y parameters between the B^+ and B^- events are in somewhat reasonable agreement with no observation for *CP*-violation in the control channel decay. For $B^\pm \to D(\to K^+K^-\pi^+\pi^-)\pi^\pm$ decays the x and y parameters are related to the CKM phase γ by

$$x_\pm = r_B^{D\pi} \cos(\delta_B^{D\pi} \pm \gamma)$$

$$y_\pm = r_B^{D\pi} \sin(\delta_B^{D\pi} \pm \gamma).$$

Given that we expect $r_B^{D\pi} \approx 0.027$ [102] the fitted value of $r_B^{D\pi}$ is too large.

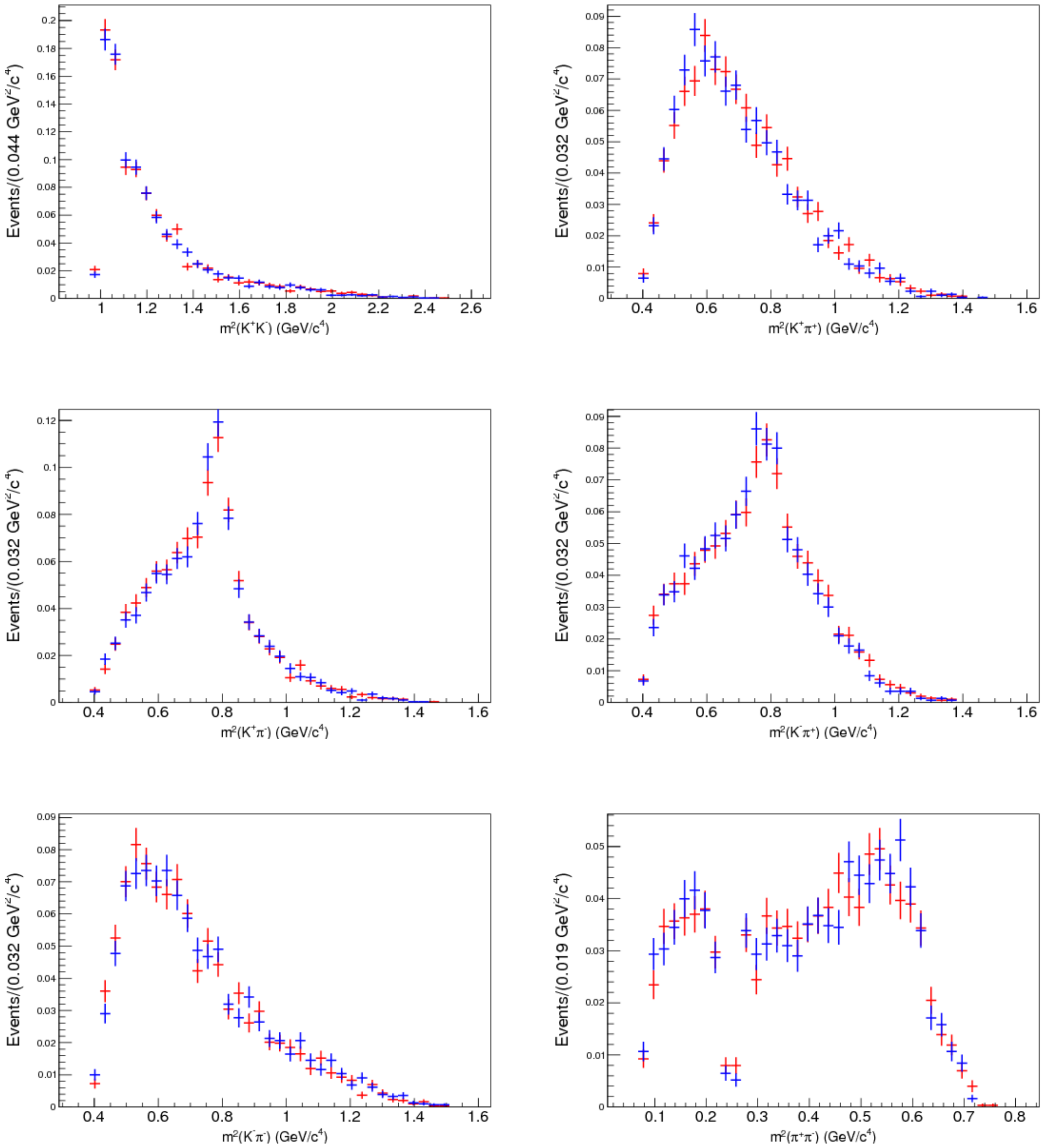

Figure 5.23: Invariant 2-body mass distributions of B^+ and B^- control channel events. The blue represents B^+ events and the red B^- events. The invariant mass distribution is defined as for the B^- events, the conjugate invariant mass distribution of B^+ events is overlaid.

Table 5.8: Results of $x_\pm$ and $y_\pm$ for a fit to control channel data using Gaussian constraints on the $A_{D^0}(p)$ parameters from the LASSO model.

Parameter	Fit value
x_+	0.012±0.021
y_+	-0.132±0.026
x_-	0.020±0.023
y_-	-0.198±0.031

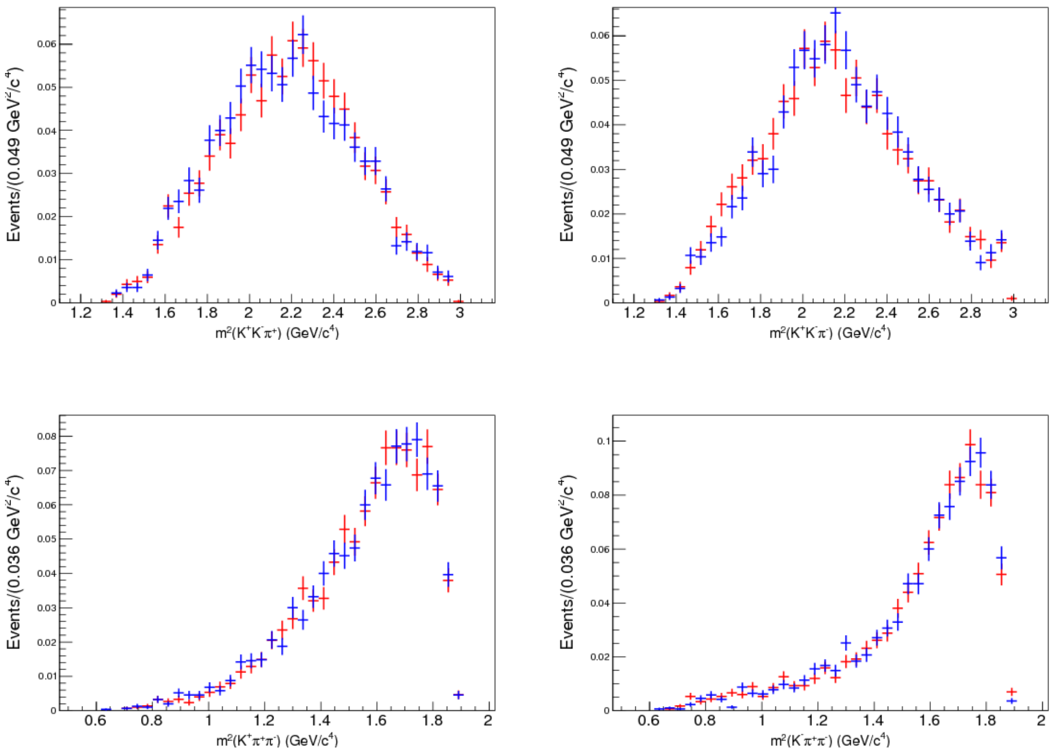

Figure 5.24: Invariant 3-body mass distributions of B^+ and B^- control channel events. The blue represents B^+ events and the red B^- events. The invariant mass distribution is defined as for the B^- events, the conjugate invariant mass distribution of B^+ events is overlaid.

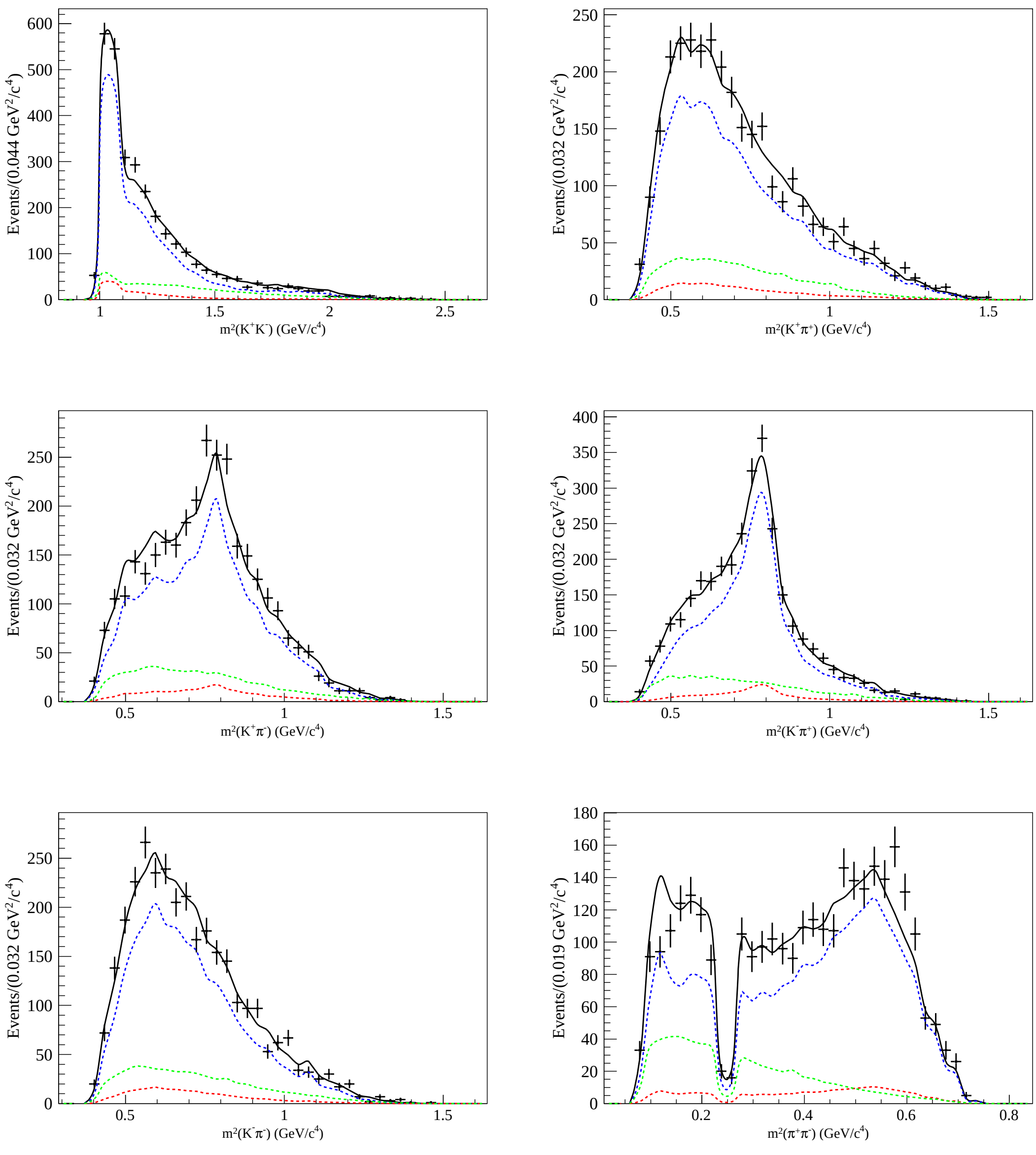

Figure 5.25: Invariant 2-body mass distributions of control channel B^+ events with fit projections. The blue dashed line represents the signal the red dashed line the right D background and the green dashed line the wrong D background. The total PDF is shown as a black solid line.

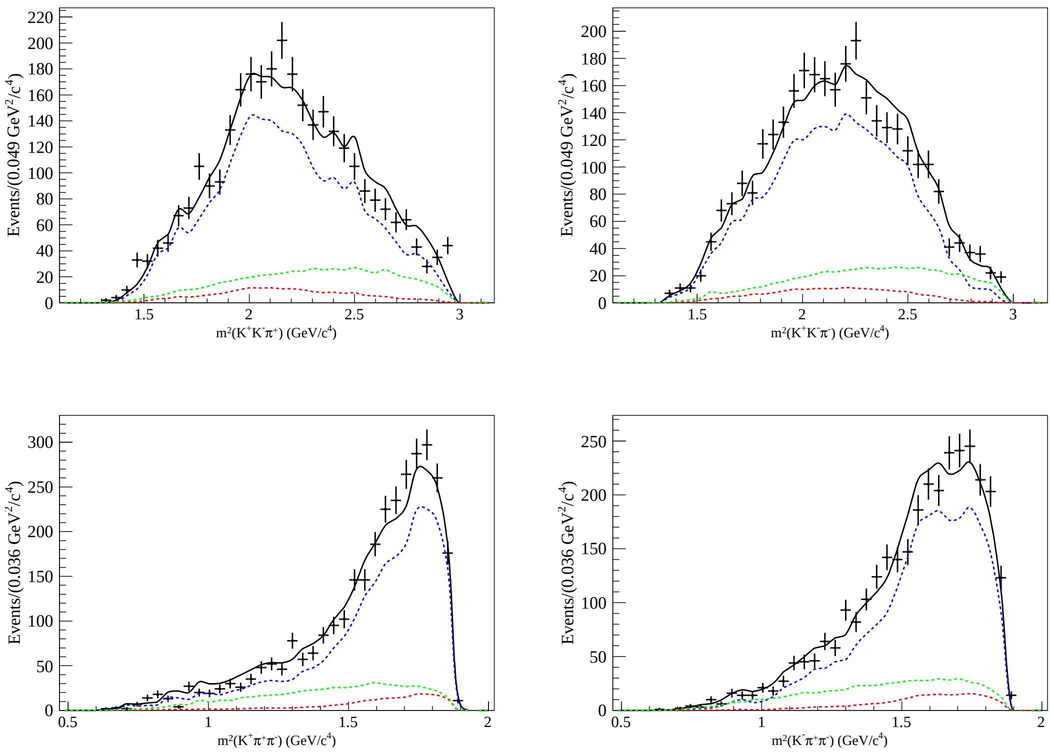

Figure 5.26: Invariant 3-body mass distributions of control channel B^+ events with fit projections. The blue dashed line represents the signal the red dashed line the right D background and the green dashed line the wrong D background. The total PDF is shown as a black solid line.

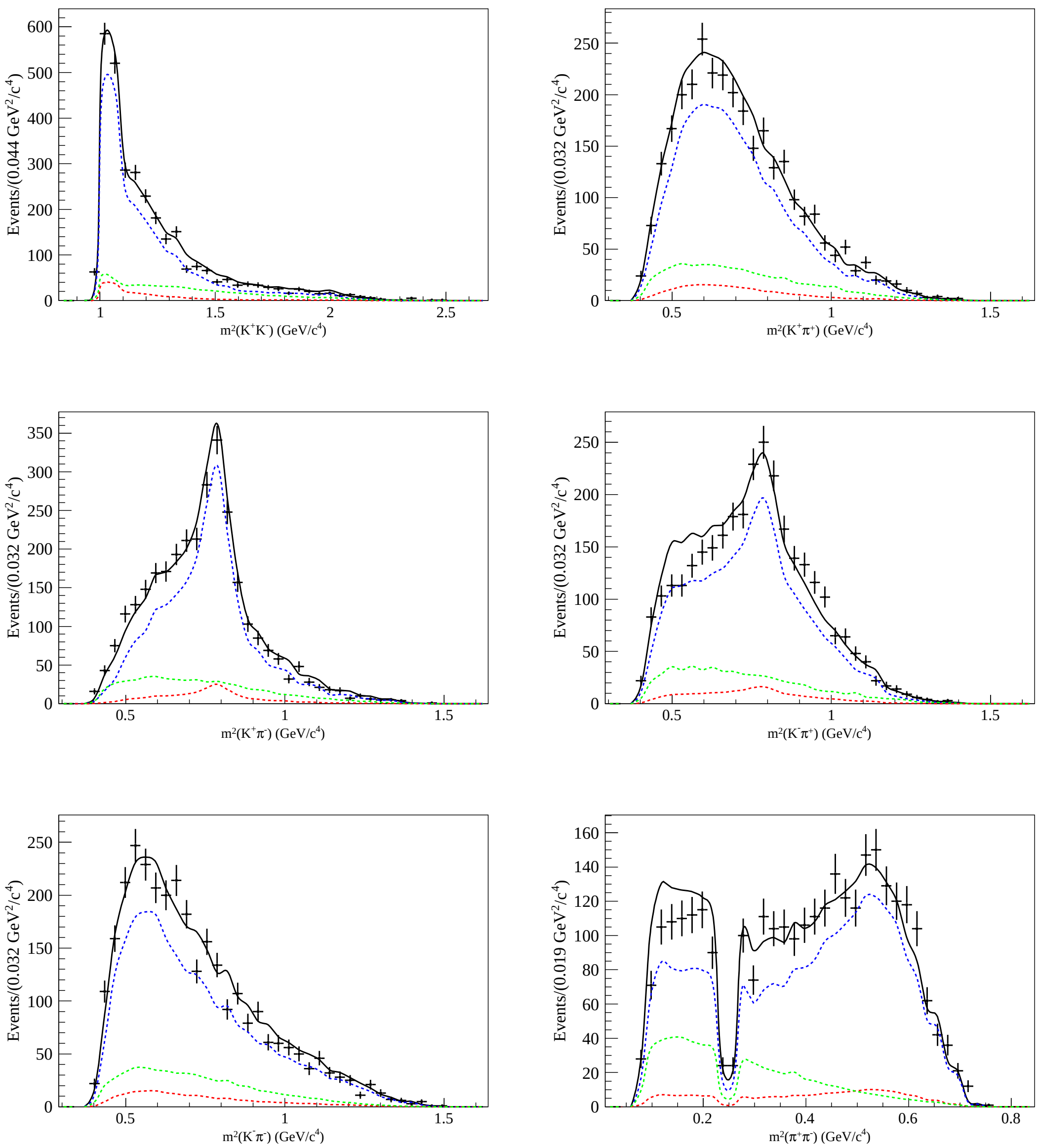

Figure 5.27: Invariant 2-body mass distributions of control channel B^- events with fit projections. The blue dashed line represents the signal the red dashed line the right D background and the green dashed line the wrong D background. The total PDF is shown as a black solid line.

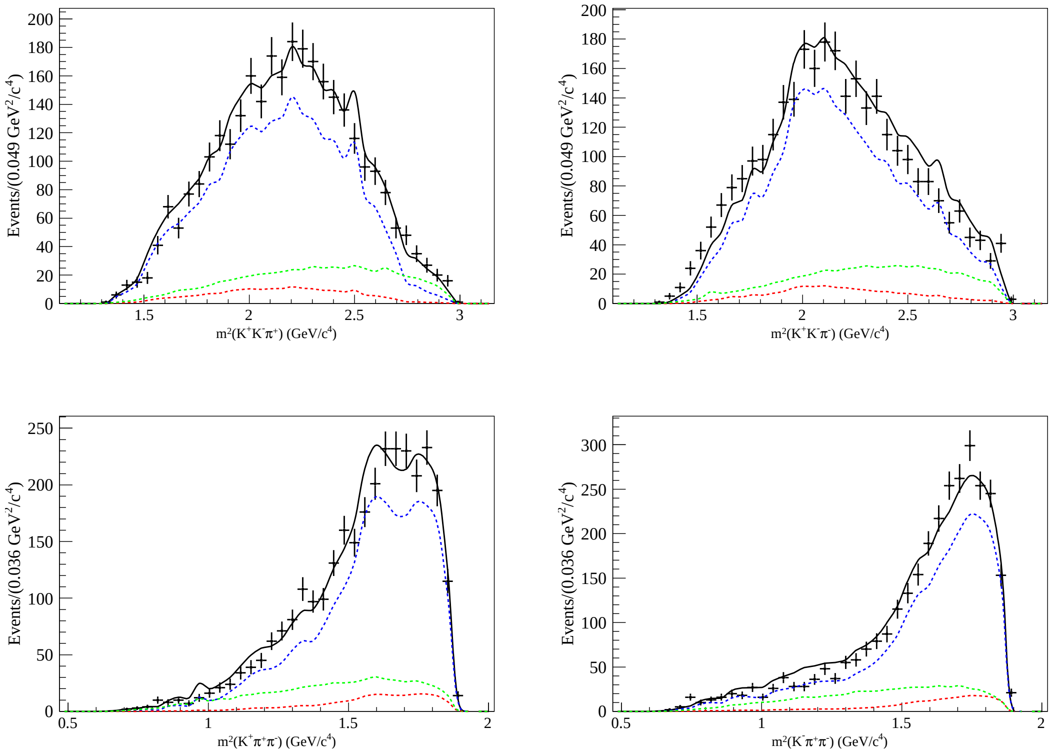

Figure 5.28: Invariant 3-body mass distributions of control channel B^- events with fit projections. The blue dashed line represents the signal the red dashed line the right D background and the green dashed line the wrong D background. The total PDF is shown as a black solid line.

Table 5.9: Real and imaginary part of the complex amplitude coefficients, a_i and the fit fractions of each component in the amplitude model resulting from fitting control channel dataset where the values of a_i are Gaussian constrained to their values in the LASSO model. The uncertainties are statistical.

Decay channel	$\Re(a_i)$	$\Im(a_i)$	$F_i(\%)$
$D^0 \to K^- \,[K_1(1270)^+ \to \pi^+ \, K^*(892)^0]$	9.27±0.73	-5.27±0.83	6.84±1.0
$D^0 \to K^- \,[K_1(1270)^+ \to \pi^+ \, K^*(1430)^0]$	30.91±1.87	16.96±2.51	6.1±0.7
$D^0 \to K^- \,[K_1(1270)^+ \to K^+ \, \rho(770)^0]$	-10.67±1.40	-20.19±1.24	10.2±1.1
$D^0 \to K^+ \,[\bar{K}_1(1270)^- \to K^- \, \rho(770)^0]$	11.74±0.96	-8.72±0.81	4.2±0.5
$D^0 \to K^- \,[K_1(1270)^+ \to K^+ \, \omega(782)]$	0.69±1.70	-7.58±1.29	0.3±0.1
$D^0 \to K^- \,[K_1(1400)^+ \to \pi^+ \, K^*(892)^0]$	-3.11±3.32	-44.64±2.57	16.6±1.7
$D^0 \to K^- \,[K^*(1680)^+ \to \pi^+ \, K^*(892)^0]$	106.85±8.96	18.26±9.71	2.1±0.3
$D^0[S] \to K^*(892)^0 \, \bar{K}^*(892)^0$	934.26± 50.79	-193.19±59.02	4.9±0.5
$D^0[P] \to K^*(892)^0 \, \bar{K}^*(892)^0$	-1071.16±84.64	-915.78±91.90	5.9±0.7
$D^0[D] \to K^*(892)^0 \, \bar{K}^*(892)^0$	-4999.10±238.31	939.71±300.91	4.3±0.4
$D^0[S] \to \phi(1020) \, \rho(770)^0$	5158.64 (fixed)	0.00 (fixed)	26.3±0.9
$D^0[P] \to \phi(1020) \, \rho(770)^0$	-1643.34±106.47	-293.30±178.38	1.7±0.2
$D^0[D] \to \phi(1020) \, \rho(770)^0$	6280.10±344.21	2951.02±500.86	2.7±0.3
$D^0 \to K^*(892)^0 \, (K^-\pi^+)_S$	47.91±2.49	3.01±3.23	6.7±0.7
$D^0 \to \phi(1020) \, (\pi^+\pi^-)_S$	39.73±3.56	-45.76±3.84	3.6±0.4
$D^0 \to (K^+K^-)_S \, (\pi^+\pi^-)_S$	0.28±0.03	0.61±0.02	11.9±0.9
Sum			114.1±3.1

To investigate what may be causing a large $r_B^{D\pi}$ fit value various other fits have been performed to the control channel data. First a fit to all control channel events is performed with the LASSO model for $A_{D^0}(p)$ fixed in the likelihood. Figure 5.29 shows the 1-4 sigma contours for the 2-dimensional log-likelihood scans for the B^+ and B^- events, a single defined minima is seen in each case. Then only the events falling in the ϕ region are fit with the fixed LASSO model; the ϕ region is defined as a two sigma window around the ϕ mass in the invariant mass of the two kaon system, m_{KK}. This region is where we expect the LASSO model to behave best, the region is dominated by the ϕ resonance with little contribution from other resonances and from background. To complement this, a fit is run using only the events that do not fall in the ϕ region. The results of these fits are shown in table 5.10.

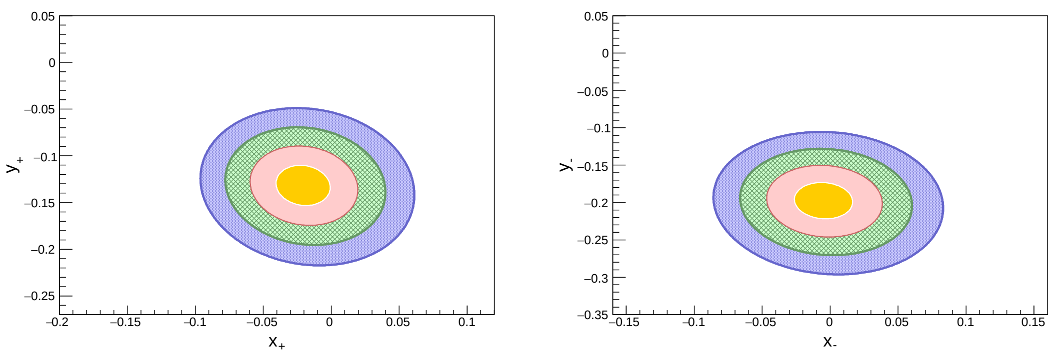

Figure 5.29: Contours representing 1-4 sigma in the two dimensional likelihood scans for B^+ (left) and B^- (right) control channel data. The amplitude component parameters of the A_{D^0} LASSO model are fixed.

Table 5.10: Fits to control channel data where a) LASSO model fixed b) only events in the ϕ region are fit with the fixed LASSO model c) all events not in the ϕ region are fit with the fixed LASSO model.

	a	b	c
x_+	-0.020±0.020	-0.038±0.034	-0.010±0.026
y_+	-0.132±0.021	-0.136±0.050	-0.161±0.024
x_-	-0.006±0.021	-0.089±0.036	-0.002±0.026
y_-	-0.194±0.024	-0.283±0.050	-0.132±0.027

Given the difference in statistics between the dataset used to obtain the A_{D^0} LASSO model at CLEO and the $B^\pm \to D(\to K^+K^-\pi^+\pi^-)\pi^\pm$ control channel dataset at LHCb, another test splits the control channel dataset into two. The first half of the data is used to establish a new model for A_{D^0} based on the LASSO model with $x_\pm$ and $y_\pm$ fixed to zero. This modified A_{D^0} model is then used in the likelihood 5.1 to fit for $x_\pm$ and $y_\pm$ using the other half of the dataset. In the first test of this type, A_{D^0} is refit to control channel events where the amplitude component parameters, a_i, are Gaussian constrained to their values in the LASSO model; the Gaussian constraints use an uncertainty simply equal to the statistical uncertainty and the full covariance matrix is taken into account. The second test takes the same approach but the uncertainties used for the Gaussian constraints are the statistical plus experimental systematic uncertainties (the model systematic uncertainties are not included as we expect similar model effects between CLEO and LHCb analyses). Finally this test is also repeated with no constraints on the amplitude component parameters; we fit a totally new model using the same amplitude components as the LASSO model. The amplitude component parameters, a_i, and fit fractions for the resulting A_{D^0} models can be seen in tables 5.12, 5.13 and 5.14, along with $\chi^2/ndof$ values which all indicate a good fit quality. The values for $x_\pm$ and $y_\pm$ obtained from using these three models in the likelihood fit given in 5.1 can be seen in table 5.11.

Table 5.11: Fits to control channel data where half of the dataset is used to fit an amplitude model, A_{D^0}, based on the LASSO model with $x_\pm$ and $y_\pm$ fixed to zero and the other half is used to test the model by fitting for $x_\pm$ and $y_\pm$ using the likelihood in 5.1. The results of $x_\pm$ and $y_\pm$ for amplitude models built with the following constraints on the LASSO model parameters are shown; a) Gaussian constraints applied to LASSO model parameters where uncertainties are statistical b) Gaussian constraints applied to LASSO model parameters where uncertainties are statistical plus experimental systematic c) No constraints are applied.

	a	b	c
x_+	-0.024±0.026	-0.014±0.026	0.005±0.026
y_+	-0.093±0.029	-0.075±0.029	-0.036±0.030
x_-	-0.041±0.027	-0.037±0.026	-0.028±0.026
y_-	-0.075±0.031	-0.057±0.031	-0.010±0.032

Table 5.12: Real and imaginary part of the complex amplitude coefficients, a_i and the fit fractions of each component in the amplitude model found by fitting half of the control channel sample where $x_\pm = y_\pm = 0$ is fixed and the values of a_i are Gaussian constrained to their values in the LASSO model. The uncertainties are statistical. The $\chi^2/ndof$ value is also given.

Decay channel	$\Re(a_i)$	$\Im(a_i)$	$F_i(\%)$
$D^0 \to K^- [K_1(1270)^+ \to \pi^+ K^*(892)^0]$	8.04±0.85	-5.17±0.99	5.3±0.9
$D^0 \to K^- [K_1(1270)^+ \to \pi^+ K^*(1430)^0]$	34.98±2.50	14.84±3.32	7.1±0.8
$D^0 \to K^- [K_1(1270)^+ \to K^+ \rho(770)^0]$	-13.21±1.97	-18.41±1.58	9.7±1.0
$D^0 \to K^+ [\bar{K}_1(1270)^- \to K^- \rho(770)^0]$	9.31±1.09	-10.66±0.94	3.8±0.4
$D^0 \to K^- [K_1(1270)^+ \to K^+ \omega(782)]$	0.47±1.93	-7.88±1.57	0.3±0.1
$D^0 \to K^- [K_1(1400)^+ \to \pi^+ K^*(892)^0]$	3.86±3.69	-42.08±3.09	14.1±2.0
$D^0 \to K^- [K^*(1680)^+ \to \pi^+ K^*(892)^0]$	132.92±9.76	3.72±11.95	3.1±0.4
$D^0[S] \to K^*(892)^0 \bar{K}^*(892)^0$	826.45±58.05	-220.92±69.15	3.8±0.5
$D^0[P] \to K^*(892)^0 \bar{K}^*(892)^0$	-977.56±85.83	-813.74±95.54	4.6±0.5
$D^0[D] \to K^*(892)^0 \bar{K}^*(892)^0$	-4984.75±285.07	1018.25±379.23	4.2±0.4
$D^0[S] \to \phi(1020)\, \rho(770)^0$	5158.65 (fixed)	0.00 (fixed)	26.0±0.7
$D^0[P] \to \phi(1020)\, \rho(770)^0$	-1569.52±122.34	-732.89±218.33	1.7±0.3
$D^0[D] \to \phi(1020)\, \rho(770)^0$	6075.24±429.21	1735.94±593.80	2.2±0.3
$D^0 \to K^*(892)^0 (K^-\pi^+)_S$	48.48±3.12	8.55±4.09	6.7±0.8
$D^0 \to \phi(1020) (\pi^+\pi^-)_S$	46.70±4.24	-52.16±3.95	4.7±0.4
$D^0 \to (K^+K^-)_S (\pi^+\pi^-)_S$	0.35±0.04	0.59±0.03	12.2±0.8
Sum			109.4±2.6
$\chi^2/ndof$			1.22

Table 5.13: Real and imaginary part of the complex amplitude coefficients, a_i and the fit fractions of each component in the amplitude model found by fitting half of the control channel sample where $x_\pm = y_\pm = 0$ is fixed and the values of a_i are Gaussian constrained to their values in the LASSO model where the combined statistical and experimental systematic uncertainty of the LASSO model parameters are used. The uncertainties are statistical. The $\chi^2/ndof$ value is also given.

Decay channel	$\Re(a_i)$	$\Im(a_i)$	$F_i(\%)$
$D^0 \to K^- \, [K_1(1270)^+ \to \pi^+ \, K^*(892)^0]$	8.07±0.90	-5.66±1.00	5.4±0.9
$D^0 \to K^- \, [K_1(1270)^+ \to \pi^+ \, K^*(1430)^0]$	35.83±2.71	13.01±3.64	7.0±0.9
$D^0 \to K^- \, [K_1(1270)^+ \to K^+ \, \rho(770)^0]$	-13.27±2.08	-18.86±1.67	10.4±1.2
$D^0 \to K^+ \, [\bar{K}_1(1270)^- \to K^- \, \rho(770)^0]$	8.14±1.22	-10.39±0.97	3.1±0.4
$D^0 \to K^- \, [K_1(1270)^+ \to K^+ \, \omega(782)]$	0.12±2.01	-7.59±1.75	0.3±0.1
$D^0 \to K^- \, [K_1(1400)^+ \to \pi^+ \, K^*(892)^0]$	4.31±3.86	-43.68±3.35	14.8±2.1
$D^0 \to K^- \, [K^*(1680)^+ \to \pi^+ \, K^*(892)^0]$	132.60±12.35	0.05±12.79	3.0±0.6
$D^0[S] \to K^*(892)^0 \, \bar{K}^*(892)^0$	794.03±69.54	-242.92±70.51	3.5±0.6
$D^0[P] \to K^*(892)^0 \, \bar{K}^*(892)^0$	-1048.65±114.75	-828.51±107.77	4.9±0.6
$D^0[D] \to K^*(892)^0 \, \bar{K}^*(892)^0$	-5091.64±323.69	1305.11±396.64	4.4±0.5
$D^0[S] \to \phi(1020) \, \rho(770)^0$	5158.65 (fixed)	0.00 (fixed)	25.1±0.8
$D^0[P] \to \phi(1020) \, \rho(770)^0$	-1589.84±142.01	-735.00±245.12	1.7±0.3
$D^0[D] \to \phi(1020) \, \rho(770)^0$	6167.99±474.70	2024.73±634.79	2.2±0.3
$D^0 \to K^*(892)^0 \, (K^-\pi^+)_S$	50.68±3.83	8.32±4.17	7.3±1.0
$D^0 \to \phi(1020) \, (\pi^+\pi^-)_S$	50.37±4.84	-50.25±5.04	4.7±0.6
$D^0 \to (K^+K^-)_S \, (\pi^+\pi^-)_S$	0.36±0.04	0.59±0.04	11.3±0.9
Sum			108.9± 3.5
$\chi^2/ndof$			1.23

Table 5.14: Real and imaginary part of the complex amplitude coefficients, a_i and the fit fractions of each component in the amplitude model found by fitting half of the control channel sample where $x_\pm = y_\pm = 0$ is fixed and no constraints are applied to a_i. The uncertainties are statistical. The $\chi^2/ndof$ value is also given.

Decay channel	$\Re(a_i)$	$\Im(a_i)$	$F_i(\%)$
$D^0 \to K^- [K_1(1270)^+ \to \pi^+ K^*(892)^0]$	9.25±1.23	-4.00±1.52	5.3±1.3
$D^0 \to K^- [K_1(1270)^+ \to \pi^+ K^*(1430)^0]$	35.00±4.27	22.26±4.37	7.6±1.2
$D^0 \to K^- [K_1(1270)^+ \to K^+ \rho(770)^0]$	-8.89±3.12	-24.54±2.08	11.9±1.6
$D^0 \to K^+ [\bar{K}_1(1270)^- \to K^- \rho(770)^0]$	7.14±1.54	-9.31±1.23	2.3±0.4
$D^0 \to K^- [K_1(1270)^+ \to K^+ \omega(782)]$	-3.39±2.72	-6.07±2.22	0.2±0.1
$D^0 \to K^- [K_1(1400)^+ \to \pi^+ K^*(892)^0]$	14.77±5.58	-44.54±4.70	15.8±3.0
$D^0 \to K^- [K^*(1680)^+ \to \pi^+ K^*(892)^0]$	124.10±14.76	29.73±17.45	2.6±0.6
$D^0[S] \to K^*(892)^0 \bar{K}^*(892)^0$	760.42±87.31	-148.45±98.81	2.8±0.6
$D^0[P] \to K^*(892)^0 \bar{K}^*(892)^0$	-950.41±149.10	-1115.90±126.22	5.4±0.8
$D^0[D] \to K^*(892)^0 \bar{K}^*(892)^0$	-5624.29±427.11	1319.86±522.72	4.8±0.7
$D^0[S] \to \phi(1020)\,\rho(770)^0$	5158.65 (fixed)	0.00 (fixed)	22.9±0.9
$D^0[P] \to \phi(1020)\,\rho(770)^0$	-1618.20±170.80	-1049.82±274.92	1.9±0.4
$D^0[D] \to \phi(1020)\,\rho(770)^0$	6523.60±520.84	4131.84±839.90	2.8±0.5
$D^0 \to K^*(892)^0 (K^-\pi^+)_S$	55.41±4.64	17.80±6.12	8.6±1.3
$D^0 \to \phi(1020)\,(\pi^+\pi^-)_S$	58.56±5.47	-40.16±6.63	4.2±0.6
$D^0 \to (K^+K^-)_S\,(\pi^+\pi^-)_S$	0.30±0.05	0.66±0.04	12.0±1.1
Sum			111.4±4.0
$\chi^2/ndof$			1.23

5.6 Interpretation of results from work towards γ measurement

A null test of the method to extract γ has been performed using control channel $B^{\pm} \to D(\to K^+K^-\pi^+\pi^-)\pi^{\pm}$ events. For these decays $r_B^{D\pi} \approx 0.027$ and so for the purposes of this analysis we expect to measure x and y parameters that are consistent with zero. Although this is not the case and it seems that the fit is preferring a value of $r_B^{D\pi}$ that is too large the fit shows no observed CP-violation in the decay. The suspicion is that the $D^0 \to K^+K^-\pi^+\pi^-$ amplitude model developed on the much smaller CLEO data set is insufficient to describe the LHCb data. Various fits have been performed to investigate as to why the fit might prefer a larger value of $r_B^{D\pi}$. It is somewhat reassuring to see that the fit to the ϕ region and to the non-ϕ region show the same pattern of results; $y_{\pm}$ parameters significantly different from zero with $x_{\pm}$ parameters closer to those expected, as the fit to the full dataset. This suggests that the issue is not to do with the LASSO model description of the data in one region of phasespace.

As expected, for fits using a model, A_{D^0}, which has been refit to control channel events results are closer to what one would expect, with the results improving the more freedom the A_{D^0} parameters have. This suggests that we need more input from LHCb data to properly describe the data. Given the apparent uniformity of efficiency effects seen across the D decay phasespace it seems unlikely that efficiency effects are affecting the fit to this extent. More likely is that the description of the background is not correct, this background description however would have to affect both the ϕ region and the non-ϕ region.

Chapter 6

Conclusions

An amplitude analysis for the decay $D^0 \to K^+K^-\pi^+\pi^-$ has been performed using 3298 flavour tagged events and 193 CP tagged events collected by the CLEO detector. The CP tagged events are unique to the CLEO-c detector configuration and provide an extra sensitivity to the phase motion over the D decay phasespace. Through the use of a staged, data driven regularisation method an amplitude model containing 16 amplitude components has been developed with dominant contributions from the $D \to VV$ mode $D^0[S] \to \phi(1020)\,\rho(770)^0$; with a fit fraction of 28.1%, and the $D \to AP$ mode $D^0 \to K^-\,[K_1(1400)^+ \to \pi^+\,K^*(892)^0]$ with a fit fraction of 12.4%. The dominance of these two components was also seen in a previous amplitude analysis of this decay performed by the FOCUS experiment. The decay channel $D^0 \to K^-\,[K_1(1270)^+ \to \pi^+\,K^*(1430)^0]$ also contributes significantly to the model. Like the $K_1(1400)^+$ resonance, the $K^*(1430)^0$ resonance peaks outside of the kinematically allowed phasespace. The description of the lineshapes of cascade decays using the energy-dependent width formalism described in this thesis is particularly important for these modes. The largest systematic uncertainty in the analysis arises from the knowledge of mass and width parameters for the resonance particles, in particular, that of the $K_1(1270)^+$ resonance with mass 1272 ± 7MeV and width 90 ± 20MeV that features prominently in the model. With access to far greater statistics, the likes of which are available at LHCb, these parameters can be allowed to float in the amplitude fit reducing this uncertainty. Using this amplitude model a test of CP-violation in the D meson system has been performed both at the global and amplitude component level. No evidence for CP-violation is observed.

The amplitude model for $D^0 \to K^+K^-\pi^+\pi^-$ decays is crucial input to a model-dependent measurement of the CKM phase γ using $B^\pm \to D(\to K^+K^-\pi^+\pi^-)K^\pm$ decays. Significant progress towards this measurement has been made. The LHCb Run 1 dataset yields 362 ± 28 $B^\pm \to D(\to K^+K^-\pi^+\pi^-)K^\pm$ signal events and 4699 ± 82 $B^\pm \to D(\to K^+K^-\pi^+\pi^-)\pi^\pm$ control channel events as determined by fits to m_{Dh} distributions. A toy Monte Carlo study has been performed using the $D^0 \to K^+K^-\pi^+\pi^-$ amplitude model to test for fitter bias in the extraction of γ. The study was run using statistics close the that expected in data and also with ten times these statistics. No significant fitter bias is observed. The control channel $B^\pm \to D(\to K^+K^-\pi^+\pi^-)\pi^\pm$ is used as a null test of method as for this channel we expect to observe no CP-violation at the level of precision attainable. Although the fit to the control channel is not behaving as expected so far, the studies performed suggest that the fault lies with the background description of LHCb data and it is likely that the amplitude model developed in this thesis describes the signal well. Further studies will have to be performed to validate this conclusion. If the problems observed can be overcome, the prospects for this analysis look good. In years 2015 and 2016 of Run 2 LHCb recorded another $\approx 2\text{fb}^{-1}$ of data, within the first few months of data taking in 2017 we can expect to double the available statistics for this analysis.

Appendix A

Appendix

A.1 Spin Amplitudes

The spin factors used for amplitude components in the amplitude analysis are given in Table A.1. The exact spin factor used and the particle ordering for each decay in the final LASSO model is given in A.2.

Table A.1: Spin factors for decay topologies considered in the amplitude analysis where S, P, V, A, and T stand for scalar, pseudoscalar, vector, axial vector and tensor, respectively. If no angular momentum is specified, the lowest angular momentum state permitted is used respecting angular momentum conservation and, where required, parity conservation

Number	Decay chain	Spin amplitude
1	$D \to (P\,P_1),\ P \to (V\,P_2),\ V \to (P_3\,P_4)$	$L_{(1)\alpha}(P)\ L^{\alpha}_{(1)}(V)$
2	$D \to (A\,P_1),\ A \to (V\,P_2),\ V \to (P_3\,P_4)$	$L_{(1)\alpha}(D)\,P^{\alpha\beta}_{(1)}(A)\,L_{(1)\beta}(V)$
3	$D \to (A\,P_1),\ A[D] \to (P_2\,V),\ V \to (P_3\,P_4)$	$L_{(1)\alpha}(D)\,L^{\alpha\beta}_{(2)}(A)\,L_{(1)\beta}(V)$
4	$D \to (A\,P_1),\ A \to (S\,P_2),\ S \to (P_3\,P_4)$	$L_{(1)\alpha}(D)\,L^{\alpha}_{(1)}(A)$
5	$D \to (V_1\,P_1),\ V_1 \to (V_2\,P_2),\ V_2 \to (P_3\,P_4)$	$L_{(1)\mu}(D)\,P^{\mu\alpha}_{(1)}(V_1)\,\epsilon_{\alpha\beta\gamma\delta}\,L^{\beta}_{(1)}(V_1)\,p^{\gamma}_{V_1}\,L^{\delta}_{(1)}(V_2)$
6	$D \to (T\,P_1),\ T \to (V\,P_2),\ V \to (P_3\,P_4)$	$L_{(2)\mu\nu}(D)\,P^{\mu\nu\rho\alpha}_{(2)}(T)\,\epsilon_{\alpha\beta\gamma\delta}\,L^{\beta}_{(2)\rho}(T)\,p^{\gamma}_{T}\,P^{\delta\sigma}_{(1)}(T)\,L_{(1)\sigma}(V)$
7	$D \to (S_1\,S_2),\ S_1 \to (P_1\,P_2),\ S_2 \to (P_3\,P_4)$	1
8	$D \to (V\,S),\ V \to (P_1\,P_2),\ S \to (P_3\,P_4)$	$L_{(1)\alpha}(D)\,L^{\alpha}_{(1)}(V)$
9	$D \to (V_1\,V_2),\ V_1 \to (P_1\,P_2),\ V_2 \to (P_3\,P_4)$	$L_{(1)\alpha}(V_1)\,L^{\alpha}_{(1)}(V_2)$
10	$D[P] \to (V_1\,V_2),\ V_1 \to (P_1\,P_2),\ V_2 \to (P_3\,P_4)$	$\epsilon_{\alpha\beta\gamma\delta}\,L^{\alpha}_{(1)}(D)\,L^{\beta}_{(1)}(V_1)\,L^{\gamma}_{(1)}(V_2)\,p^{\delta}_{D}$
11	$D[D] \to (V_1\,V_2),\ V_1 \to (P_1\,P_2),\ V_2 \to (P_3\,P_4)$	$L_{(2)\alpha\beta}(D)\,L^{\alpha}_{(1)}(V_1)\,L^{\beta}_{(1)}(V_2)$
12	$D \to (V\,T),\ T \to (P_1\,P_2),\ V \to (P_3\,P_4)$	$L_{(1)\alpha}(D)\,L^{\alpha\beta}_{(2)}(T)\,L_{(1)\beta}(V)$
13	$D[D] \to (T\,V),\ T \to (P_1\,P_2),\ V \to (P_3\,P_4)$	$\epsilon_{\alpha\beta\delta\gamma}\,L^{\alpha\mu}_{2}(D)\,L^{\beta}_{2\mu}\,L^{\gamma}_{(1)}(V)\,p^{\delta}_{D}$

Table A.2: Spin factors used for each amplitude component of in the LASSO model, including the particle numbering scheme. The second column refers to the spin factors as numbered in Table A.1, and the particles P_1, P_2, P_3, and P_4 refer to those defined in Table A.1.

Decay channel	Spin factor number	P_1	P_2	P_3	P_4
$D^0 \to K^-\,[K_1(1270)^+ \to \pi^+\,K^*(892)^0]$	2	K^-	π^+	K^+	π^-
$D^0 \to K^-\,[K_1(1270)^+ \to \pi^+\,K^*(1430)^0]$	4	K^-	π^+	K^+	π^-
$D^0 \to K^-\,[K_1(1270)^+ \to K^+\,\rho(770)^0]$	2	K^-	K^+	π^+	π^-
$D^0 \to K^+\,[\bar{K}_1(1270)^- \to K^-\,\rho(770)^0]$	2	K^+	K^-	π^-	π^+
$D^0 \to K^-\,[K_1(1270)^+ \to K^+\,\omega(782)]$	2	K^-	K^+	π^+	π^-
$D^0 \to K^-\,[K_1(1400)^+ \to \pi^+\,K^*(892)^0]$	2	K^-	π^+	K^+	π^-
$D^0 \to K^-\,[K^*(1680)^+ \to \pi^+\,K^*(892)^0]$	5	K^-	π^+	K^+	π^-
$D^0[S] \to K^*(892)^0\,\bar{K}^*(892)^0$	19	K^+	π^-	K^-	π^+
$D^0[P] \to K^*(892)^0\,\bar{K}^*(892)^0$	10	K^+	π^-	K^-	π^+
$D^0[D] \to K^*(892)^0\,\bar{K}^*(892)^0$	11	K^+	π^-	K^-	π^+
$D^0[S] \to \phi(1020)\,\rho(770)^0$	9	K^+	K^-	π^+	π^-
$D^0[P] \to \phi(1020)\,\rho(770)^0$	10	K^+	K^-	π^+	π^-
$D^0[D] \to \phi(1020)\,\rho(770)^0$	11	K^+	K^-	π^+	π^-
$D^0 \to K^*(892)^0\,(K^-\pi^+)_S$	8	K^+	π^-	K^-	π^+
$D^0 \to \phi(1020)\,(\pi^+\pi^-)_S$	8	K^+	K^-	π^+	π^-
$D^0 \to (K^+K^-)_S\,(\pi^+\pi^-)_S$	7	K^+	K^-	π^+	π^-

A.2 Interference Fractions

Table A.3-A.4 lists the interference fractions, ordered by magnitude, for the LASSO model.

Table A.3: Interference fractions ordered by magnitude, for the LASSO $D \to K^+K^-\pi^+\pi^-$ amplitude model. Only the statistical uncertainties are given.

Channel i	Channel j	I_{ij} (%)
(1)$D^0 \to K^-\,[K_1(1270)^+ \to \pi^+\,K^*(1430)^0]$	$D^0 \to K^-\,[K_1(1270)^+ \to K^+\,\rho(770)^0]$	-8.145 ± 1.542
(2)$D^0 \to K^-\,[K_1(1270)^+ \to \pi^+\,K^*(892)^0]$	$D^0 \to K^*(892)^0\,(K^-\pi^+)_S$	-5.650 ± 0.917
(3)$D^0 \to K^-\,[K_1(1400)^+ \to \pi^+\,K^*(892)^0]$	$D^0[S] \to K^*(892)^0\,\bar{K}^*(892)^0$	-3.686 ± 0.838
(4)$D^0[S] \to \phi(1020)\,\rho(770)^0$	$D^0[D] \to \phi(1020)\,\rho(770)^0$	-3.673 ± 0.490
(5)$D^0 \to K^-\,[K_1(1270)^+ \to K^+\,\rho(770)^0]$	$D^0[S] \to \phi(1020)\,\rho(770)^0$	3.338 ± 0.480
(6)$D^0 \to K^-\,[K_1(1270)^+ \to \pi^+\,K^*(892)^0]$	$D^0 \to K^-\,[K_1(1400)^+ \to \pi^+\,K^*(892)^0]$	2.621 ± 1.832
(7)$D^0 \to K^-\,[K_1(1270)^+ \to \pi^+\,K^*(892)^0]$	$D^0 \to K^-\,[K_1(1270)^+ \to K^+\,\rho(770)^0]$	-2.615 ± 0.462
(8)$D^0 \to K^+\,[K_1(1270)^- \to K^-\,\rho(770)^0]$	$D^0[S] \to \phi(1020)\,\rho(770)^0$	2.321 ± 0.335
(9)$D^0 \to K^-\,[K_1(1400)^+ \to \pi^+\,K^*(892)^0]$	$D^0[S] \to \phi(1020)\,\rho(770)^0$	2.211 ± 0.253
(10)$D^0 \to K^-\,[K_1(1270)^+ \to K^+\,\omega(782)]$	$D^0 \to K^-\,[K_1(1270)^+ \to K^+\,\rho(770)^0]$	1.941 ± 0.740
(11)$D^0 \to K^-\,[K_1(1270)^+ \to \pi^+\,K^*(892)^0]$	$D^0[S] \to K^*(892)^0\,\bar{K}^*(892)^0$	1.614 ± 0.426
(12)$D^0 \to K^-\,[K_1(1270)^+ \to K^+\,\rho(770)^0]$	$D^0 \to K^*(892)^0\,(K^-\pi^+)_S$	1.565 ± 0.206
(13)$D^0[S] \to K^*(892)^0\,\bar{K}^*(892)^0$	$D^0[D] \to K^*(892)^0\,\bar{K}^*(892)^0$	1.417 ± 0.145
(14)$D^0 \to K^-\,[K_1(1270)^+ \to \pi^+\,K^*(1430)^0]$	$D^0 \to K^+\,[K_1(1270)^- \to K^-\,\rho(770)^0]$	1.244 ± 0.260
(15)$D^0 \to K^-\,[K_1(1270)^+ \to K^+\,\rho(770)^0]$	$D^0[S] \to K^*(892)^0\,\bar{K}^*(892)^0$	-1.182 ± 0.166
(16)$D^0 \to K^-\,[K_1(1270)^+ \to \pi^+\,K^*(892)^0]$	$D^0[D] \to K^*(892)^0\,\bar{K}^*(892)^0$	-1.144 ± 0.212
(17)$D^0 \to K^-\,[K_1(1270)^+ \to K^+\,\rho(770)^0]$	$D^0 \to K^-\,[K_1(1400)^+ \to \pi^+\,K^*(892)^0]$	1.119 ± 0.516
(18)$D^0 \to K^-\,[K_1(1400)^+ \to \pi^+\,K^*(892)^0]$	$D^0 \to K^*(892)^0\,(K^-\pi^+)_S$	-1.052 ± 1.575
(19)$D^0 \to K^-\,[K_1(1400)^+ \to \pi^+\,K^*(892)^0]$	$D^0[D] \to K^*(892)^0\,\bar{K}^*(892)^0$	-0.966 ± 0.222
(20)$D^0 \to K^-\,[K_1(1270)^+ \to K^+\,\omega(782)]$	$D^0[S] \to \phi(1020)\,\rho(770)^0$	0.849 ± 0.201
(21)$D^0[S] \to K^*(892)^0\,\bar{K}^*(892)^0$	$D^0[S] \to \phi(1020)\,\rho(770)^0$	-0.729 ± 0.164
(22)$D^0 \to K^*(892)^0\,(K^-\pi^+)_S$	$D^0 \to \phi(1020)\,(\pi^+\pi^-)_S$	0.691 ± 0.098
(23)$D^0 \to K^-\,[K^*(1680)^+ \to \pi^+\,K^*(892)^0]$	$D^0[P] \to K^*(892)^0\,\bar{K}^*(892)^0$	-0.689 ± 0.620
(24)$D^0[S] \to \phi(1020)\,\rho(770)^0$	$D^0[D] \to K^*(892)^0\,\bar{K}^*(892)^0$	-0.687 ± 0.055
(25)$D^0 \to K^-\,[K_1(1270)^+ \to \pi^+\,K^*(1430)^0]$	$D^0[S] \to \phi(1020)\,\rho(770)^0$	0.647 ± 0.405
(26)$D^0 \to K^-\,[K_1(1270)^+ \to K^+\,\omega(782)]$	$D^0 \to K^-\,[K_1(1400)^+ \to \pi^+\,K^*(892)^0]$	0.526 ± 0.136
(27)$D^0 \to K^-\,[K_1(1270)^+ \to \pi^+\,K^*(1430)^0]$	$D^0 \to \phi(1020)\,(\pi^+\pi^-)_S$	0.485 ± 0.085
(28)$D^0 \to K^-\,[K_1(1270)^+ \to \pi^+\,K^*(892)^0]$	$D^0 \to K^+\,[K_1(1270)^- \to K^-\,\rho(770)^0]$	0.424 ± 0.061
(29)$D^0 \to K^+\,[K_1(1270)^- \to K^-\,\rho(770)^0]$	$D^0[S] \to K^*(892)^0\,\bar{K}^*(892)^0$	-0.398 ± 0.123
(30)$D^0 \to K^-\,[K_1(1270)^+ \to \pi^+\,K^*(892)^0]$	$D^0 \to \phi(1020)\,(\pi^+\pi^-)_S$	-0.354 ± 0.055
(31)$D^0 \to K^-\,[K_1(1270)^+ \to K^+\,\omega(782)]$	$D^0 \to K^+\,[K_1(1270)^- \to K^-\,\rho(770)^0]$	0.346 ± 0.162
(32)$D^0 \to K^*(892)^0\,(K^-\pi^+)_S$	$D^0[S] \to \phi(1020)\,\rho(770)^0$	-0.341 ± 0.052
(33)$D^0[P] \to K^*(892)^0\,\bar{K}^*(892)^0$	$D^0[P] \to \phi(1020)\,\rho(770)^0$	0.330 ± 0.079
(34)$D^0 \to K^-\,[K^*(1680)^+ \to \pi^+\,K^*(892)^0]$	$D^0[P] \to \phi(1020)\,\rho(770)^0$	0.303 ± 0.126
(35)$D^0 \to K^-\,[K_1(1400)^+ \to \pi^+\,K^*(892)^0]$	$D^0 \to \phi(1020)\,(\pi^+\pi^-)_S$	0.302 ± 0.125
(36)$D^0 \to K^+\,[K_1(1270)^- \to K^-\,\rho(770)^0]$	$D^0 \to K^-\,[K_1(1400)^+ \to \pi^+\,K^*(892)^0]$	0.280 ± 0.110
(37)$D^0 \to K^-\,[K_1(1270)^+ \to \pi^+\,K^*(1430)^0]$	$D^0 \to K^-\,[K_1(1270)^+ \to K^+\,\omega(782)]$	0.225 ± 0.533
(38)$D^0 \to K^-\,[K_1(1270)^+ \to K^+\,\rho(770)^0]$	$D^0 \to K^+\,[K_1(1270)^- \to K^-\,\rho(770)^0]$	-0.220 ± 0.452
(39)$D^0 \to K^-\,[K_1(1270)^+ \to \pi^+\,K^*(1430)^0]$	$D^0 \to (K^+K^-)_S\,(\pi^+\pi^-)_S$	0.218 ± 0.022
(40)$D^0 \to K^+\,[K_1(1270)^- \to K^-\,\rho(770)^0]$	$D^0 \to (K^+K^-)_S\,(\pi^+\pi^-)_S$	-0.207 ± 0.020
(41)$D^0 \to K^+\,[K_1(1270)^- \to K^-\,\rho(770)^0]$	$D^0[D] \to \phi(1020)\,\rho(770)^0$	-0.204 ± 0.031
(42)$D^0 \to K^-\,[K_1(1270)^+ \to K^+\,\rho(770)^0]$	$D^0[D] \to K^*(892)^0\,\bar{K}^*(892)^0$	0.197 ± 0.049
(43)$D^0 \to K^-\,[K_1(1270)^+ \to \pi^+\,K^*(1430)^0]$	$D^0[D] \to \phi(1020)\,\rho(770)^0$	-0.196 ± 0.040
(44)$D^0 \to K^-\,[K_1(1270)^+ \to \pi^+\,K^*(892)^0]$	$D^0[S] \to \phi(1020)\,\rho(770)^0$	0.195 ± 0.149
(45)$D^0 \to K^+\,[K_1(1270)^- \to K^-\,\rho(770)^0]$	$D^0[D] \to K^*(892)^0\,\bar{K}^*(892)^0$	-0.190 ± 0.025
(46)$D^0 \to K^-\,[K_1(1270)^+ \to K^+\,\rho(770)^0]$	$D^0 \to (K^+K^-)_S\,(\pi^+\pi^-)_S$	0.144 ± 0.015
(47)$D^0 \to K^-\,[K_1(1270)^+ \to K^+\,\omega(782)]$	$D^0[S] \to K^*(892)^0\,\bar{K}^*(892)^0$	-0.142 ± 0.054
(48)$D^0 \to K^*(892)^0\,(K^-\pi^+)_S$	$D^0 \to (K^+K^-)_S\,(\pi^+\pi^-)_S$	0.127 ± 0.015
(49)$D^0 \to K^-\,[K_1(1270)^+ \to \pi^+\,K^*(1430)^0]$	$D^0 \to K^*(892)^0\,(K^-\pi^+)_S$	-0.103 ± 0.015
(50)$D^0 \to K^*(892)^0\,(K^-\pi^+)_S$	$D^0[D] \to \phi(1020)\,\rho(770)^0$	-0.095 ± 0.035
(51)$D^0 \to K^-\,[K_1(1270)^+ \to \pi^+\,K^*(892)^0]$	$D^0[D] \to \phi(1020)\,\rho(770)^0$	0.080 ± 0.015
(52)$D^0 \to K^-\,[K_1(1270)^+ \to \pi^+\,K^*(892)^0]$	$D^0 \to (K^+K^-)_S\,(\pi^+\pi^-)_S$	-0.075 ± 0.010
(53)$D^0 \to K^-\,[K_1(1400)^+ \to \pi^+\,K^*(892)^0]$	$D^0[D] \to \phi(1020)\,\rho(770)^0$	-0.075 ± 0.042
(54)$D^0 \to (K^+K^-)_S\,(\pi^+\pi^-)_S$	$D^0[P] \to K^*(892)^0\,\bar{K}^*(892)^0$	-0.066 ± 0.007
(55)$D^0 \to K^+\,[K_1(1270)^- \to K^-\,\rho(770)^0]$	$D^0 \to K^*(892)^0\,(K^-\pi^+)_S$	0.064 ± 0.097
(56) $D^0 \to K^-\,[K^*(1680)^+ \to \pi^+\,K^*(892)^0]$	$D^0[D] \to K^*(892)^0\,\bar{K}^*(892)^0$	0.061 ± 0.009
(57)$D^0 \to K^*(892)^0\,(K^-\pi^+)_S$	$D^0[D] \to K^*(892)^0\,\bar{K}^*(892)^0$	0.057 ± 0.008
(58)$D^0 \to K^-\,[K_1(1400)^+ \to \pi^+\,K^*(892)^0]$	$D^0 \to (K^+K^-)_S\,(\pi^+\pi^-)_S$	0.048 ± 0.019
(59)$D^0 \to K^-\,[K_1(1400)^+ \to \pi^+\,K^*(892)^0]$	$D^0 \to K^-\,[K^*(1680)^+ \to \pi^+\,K^*(892)^0]$	-0.048 ± 0.016
(60)$D^0 \to K^-\,[K_1(1270)^+ \to \pi^+\,K^*(892)^0]$	$D^0 \to K^-\,[K_1(1270)^+ \to K^+\,\omega(782)]$	0.044 ± 0.173
(61)$D^0 \to K^-\,[K_1(1270)^+ \to \pi^+\,K^*(1430)^0]$	$D^0 \to K^-\,[K_1(1270)^+ \to \pi^+\,K^*(892)^0]$	0.044 ± 0.007
(62)$D^0 \to K^-\,[K_1(1270)^+ \to \pi^+\,K^*(892)^0]$	$D^0[P] \to K^*(892)^0\,\bar{K}^*(892)^0$	0.044 ± 0.008
(63)$D^0 \to K^-\,[K_1(1270)^+ \to K^+\,\omega(782)]$	$D^0[D] \to \phi(1020)\,\rho(770)^0$	-0.042 ± 0.015
(64)$D^0 \to K^-\,[K_1(1270)^+ \to K^+\,\rho(770)^0]$	$D^0[P] \to K^*(892)^0\,\bar{K}^*(892)^0$	-0.036 ± 0.004
(65)$D^0 \to K^-\,[K^*(1680)^+ \to \pi^+\,K^*(892)^0]$	$D^0[S] \to K^*(892)^0\,\bar{K}^*(892)^0$	-0.034 ± 0.007
(66)$D^0[S] \to K^*(892)^0\,\bar{K}^*(892)^0$	$D^0[P] \to K^*(892)^0\,\bar{K}^*(892)^0$	-0.033 ± 0.007
(67)$D^0[S] \to \phi(1020)\,\rho(770)^0$	$D^0[P] \to \phi(1020)\,\rho(770)^0$	0.033 ± 0.004
(68)$D^0 \to K^-\,[K_1(1270)^+ \to \pi^+\,K^*(892)^0]$	$D^0 \to K^-\,[K^*(1680)^+ \to \pi^+\,K^*(892)^0]$	-0.033 ± 0.008
(69)$D^0 \to K^-\,[K_1(1270)^+ \to K^+\,\omega(782)]$	$D^0 \to K^*(892)^0\,(K^-\pi^+)_S$	0.027 ± 0.069
(70)$D^0 \to K^-\,[K_1(1270)^+ \to \pi^+\,K^*(1430)^0]$	$D^0[P] \to K^*(892)^0\,\bar{K}^*(892)^0$	0.024 ± 0.003
(71)$D^0 \to K^-\,[K_1(1270)^+ \to K^+\,\omega(782)]$	$D^0[D] \to K^*(892)^0\,\bar{K}^*(892)^0$	-0.023 ± 0.008

Table A.4: Interference fractions, ordered by magnitude, for the LASSO $D \to K^+K^-\pi^+\pi^-$ amplitude model. Only the statistical uncertainties are given.

Channel i	Channel j	I_{ij} (%)
(72)$D^0 \to \phi(1020)\,(\pi^+\pi^-)_S$	$D^0[S] \to \phi(1020)\,\rho(770)^0$	-0.019 ± 0.021
(73)$D^0 \to (K^+K^-)_S\,(\pi^+\pi^-)_S$	$D^0[P] \to \phi(1020)\,\rho(770)^0$	-0.019 ± 0.003
(74)$D^0 \to (K^+K^-)_S\,(\pi^+\pi^-)_S$	$D^0[S] \to \phi(1020)\,\rho(770)^0$	-0.018 ± 0.004
(75)$D^0 \to K^+\,[K_1(1270)^- \to K^-\,\rho(770)^0]$	$D^0[P] \to \phi(1020)\,\rho(770)^0$	0.017 ± 0.003
(76)$D^0 \to K^-\,[K_1(1400)^+ \to \pi^+\,K^*(892)^0]$	$D^0[P] \to K^*(892)^0\,\bar{K}^*(892)^0$	0.017 ± 0.014
(77)$D^0 \to K^-\,[K_1(1270)^+ \to K^+\,\rho(770)^0]$	$D^0[D] \to \phi(1020)\,\rho(770)^0$	0.017 ± 0.064
(78)$D^0[S] \to K^*(892)^0\,\bar{K}^*(892)^0$	$D^0 \to \phi(1020)\,(\pi^+\pi^-)_S$	0.016 ± 0.004
(79)$D^0 \to K^-\,[K_1(1270)^+ \to \pi^+\,K^*(1430)^0]$	$D^0 \to K^-\,[K_1(1400)^+ \to \pi^+\,K^*(892)^0]$	-0.015 ± 0.005
(80)$D^0 \to K^-\,[K_1(1270)^+ \to K^+\,\omega(782)]$	$D^0 \to (K^+K^-)_S\,(\pi^+\pi^-)_S$	0.013 ± 0.008
(81)$D^0 \to (K^+K^-)_S\,(\pi^+\pi^-)_S$	$D^0 \to \phi(1020)\,(\pi^+\pi^-)_S$	-0.013 ± 0.007
(82)$D^0 \to K^-\,[K_1(1270)^+ \to \pi^+\,K^*(1430)^0]$	$D^0[S] \to K^*(892)^0\,\bar{K}^*(892)^0$	0.012 ± 0.007
(83)$D^0[D] \to K^*(892)^0\,\bar{K}^*(892)^0$	$D^0[D] \to \phi(1020)\,\rho(770)^0$	0.012 ± 0.033
(84)$D^0 \to K^+\,[K_1(1270)^- \to K^-\,\rho(770)^0]$	$D^0[P] \to K^*(892)^0\,\bar{K}^*(892)^0$	0.011 ± 0.003
(85)$D^0 \to K^*(892)^0\,(K^-\pi^+)_S$	$D^0[P] \to K^*(892)^0\,\bar{K}^*(892)^0$	0.011 ± 0.002
(86)$D^0 \to K^-\,[K_1(1270)^+ \to K^+\,\rho(770)^0]$	$D^0 \to \phi(1020)\,(\pi^+\pi^-)_S$	-0.010 ± 0.002
(87)$D^0[S] \to K^*(892)^0\,\bar{K}^*(892)^0$	$D^0 \to K^*(892)^0\,(K^-\pi^+)_S$	-0.008 ± 0.001
(88)$D^0[D] \to \phi(1020)\,\rho(770)^0$	$D^0[P] \to \phi(1020)\,\rho(770)^0$	0.008 ± 0.001
(89)$D^0[S] \to K^*(892)^0\,\bar{K}^*(892)^0$	$D^0[P] \to \phi(1020)\,\rho(770)^0$	-0.008 ± 0.001
(90)$D^0 \to K^-\,[K_1(1270)^+ \to \pi^+\,K^*(1430)^0]$	$D^0 \to K^-\,[K^*(1680)^+ \to \pi^+\,K^*(892)^0]$	0.007 ± 0.018
(91)$D^0 \to \phi(1020)\,(\pi^+\pi^-)_S$	$D^0[D] \to K^*(892)^0\,\bar{K}^*(892)^0$	0.007 ± 0.003
(92)$D^0 \to K^-\,[K_1(1270)^+ \to K^+\,\omega(782)]$	$D^0 \to K^-\,[K^*(1680)^+ \to \pi^+\,K^*(892)^0]$	-0.006 ± 0.002
(93)$D^0 \to K^+\,[K_1(1270)^- \to K^-\,\rho(770)^0]$	$D^0 \to K^-\,[K^*(1680)^+ \to \pi^+\,K^*(892)^0]$	0.006 ± 0.006
(94)$D^0 \to K^-\,[K^*(1680)^+ \to \pi^+\,K^*(892)^0]$	$D^0 \to (K^+K^-)_S\,(\pi^+\pi^-)_S$	0.006 ± 0.020
(95)$D^0 \to K^-\,[K^*(1680)^+ \to \pi^+\,K^*(892)^0]$	$D^0 \to K^*(892)^0\,(K^-\pi^+)_S$	-0.006 ± 0.001
(96)$D^0 \to K^-\,[K_1(1400)^+ \to \pi^+\,K^*(892)^0]$	$D^0[P] \to \phi(1020)\,\rho(770)^0$	-0.006 ± 0.002
(97)$D^0 \to (K^+K^-)_S\,(\pi^+\pi^-)_S$	$D^0[D] \to K^*(892)^0\,\bar{K}^*(892)^0$	-0.005 ± 0.008
(98)$D^0 \to K^-\,[K^*(1680)^+ \to \pi^+\,K^*(892)^0]$	$D^0[S] \to \phi(1020)\,\rho(770)^0$	-0.005 ± 0.001
(99)$D^0 \to K^-\,[K_1(1270)^+ \to \pi^+\,K^*(892)^0]$	$D^0[P] \to \phi(1020)\,\rho(770)^0$	-0.005 ± 0.002
(100)$D^0 \to \phi(1020)\,(\pi^+\pi^-)_S$	$D^0[P] \to K^*(892)^0\,\bar{K}^*(892)^0$	0.004 ± 0.001
(101)$D^0 \to K^-\,[K_1(1270)^+ \to \pi^+\,K^*(1430)^0]$	$D^0[D] \to K^*(892)^0\,\bar{K}^*(892)^0$	-0.004 ± 0.004
(102)$D^0 \to K^-\,[K_1(1270)^+ \to K^+\,\rho(770)^0]$	$D^0[P] \to \phi(1020)\,\rho(770)^0$	-0.004 ± 0.007
(103)$D^0 \to K^-\,[K^*(1680)^+ \to \pi^+\,K^*(892)^0]$	$D^0[D] \to \phi(1020)\,\rho(770)^0$	-0.004 ± 0.001
(104)$D^0 \to \phi(1020)\,(\pi^+\pi^-)_S$	$D^0[D] \to \phi(1020)\,\rho(770)^0$	0.003 ± 0.014
(105)$D^0[D] \to K^*(892)^0\,\bar{K}^*(892)^0$	$D^0[P] \to K^*(892)^0\,\bar{K}^*(892)^0$	0.003 ± 0.001
(106)$D^0[D] \to K^*(892)^0\,\bar{K}^*(892)^0$	$D^0[P] \to \phi(1020)\,\rho(770)^0$	0.003 ± 0.001
(107)$D^0 \to K^*(892)^0\,(K^-\pi^+)_S$	$D^0[P] \to \phi(1020)\,\rho(770)^0$	0.002 ± 0.001
(108)$D^0 \to (K^+K^-)_S\,(\pi^+\pi^-)_S$	$D^0[D] \to \phi(1020)\,\rho(770)^0$	-0.002 ± 0.001
(109)$D^0 \to K^-\,[K^*(1680)^+ \to \pi^+\,K^*(892)^0]$	$D^0 \to \phi(1020)\,(\pi^+\pi^-)_S$	0.002 ± 0.002
(110)$D^0 \to K^-\,[K_1(1270)^+ \to K^+\,\omega(782)]$	$D^0[S] \to K^*(892)^0\,\bar{K}^*(892)^0$	-0.002 ± 0.002
(111)$D^0 \to K^-\,[K_1(1270)^+ \to K^+\,\rho(770)^0]$	$D^0 \to K^-\,[K^*(1680)^+ \to \pi^+\,K^*(892)^0]$	0.002 ± 0.007
(112)$D^0[S] \to K^*(892)^0\,\bar{K}^*(892)^0$	$D^0 \to (K^+K^-)_S\,(\pi^+\pi^-)_S$	-0.001 ± 0.001
(113)$D^0[S] \to \phi(1020)\,\rho(770)^0$	$D^0[P] \to K^*(892)^0\,\bar{K}^*(892)^0$	0.001 ± 0.003
(114)$D^0 \to K^-\,[K_1(1270)^+ \to K^+\,\omega(782)]$	$D^0[P] \to \phi(1020)\,\rho(770)^0$	0.001 ± 0.001
(115)$D^0[D] \to \phi(1020)\,\rho(770)^0$	$D^0[P] \to K^*(892)^0\,\bar{K}^*(892)^0$	-0.001 ± 0.001
(116)$D^0 \to K^-\,[K_1(1270)^+ \to \pi^+\,K^*(1430)^0]$	$D^0[P] \to \phi(1020)\,\rho(770)^0$	0.001 ± 0.002
(117)$D^0 \to K^-\,[K_1(1270)^+ \to K^+\,\omega(782)]$	$D^0 \to \phi(1020)\,(\pi^+\pi^-)_S$	0.001 ± 0.001
(118)$D^0 \to K^+\,[K_1(1270)^- \to K^-\,\rho(770)^0]$	$D^0 \to \phi(1020)\,(\pi^+\pi^-)_S$	0.000 ± 0.003
(119)$D^0[S] \to K^*(892)^0\,\bar{K}^*(892)^0$	$D^0[D] \to \phi(1020)\,\rho(770)^0$	0.000 ± 0.010
(120)$D^0 \to \phi(1020)\,(\pi^+\pi^-)_S$	$D^0[P] \to \phi(1020)\,\rho(770)^0$	0.000 ± 0.004

A.3 Fits to $B^\pm$ candidate mass distribution for $B^\pm \to D(\to K^+K^-\pi^+\pi^-)K^\pm$ and $B^\pm \to D(\to K^+K^-\pi^+\pi^-)\pi^\pm$ events

Fit parameter values for the fits to the m_{Dh} distribution of the signal and control channels in the model-dependent measurement of γ are given in tables A.5 and A.6. Also given is whether the parameter is fixed, has a limited range or is allowed to completely float in the fit. The $\chi^2/ndof$ values for the fits are also given where $ndof = (N_{bins} - 1) - N_{par}$ with N_{bins} equal to the number of bins the χ^2 value was evaluated in and N_{par} equal to the number of free parameters in the fit.

Table A.5: Fit parameters for fit to m_{DK} for $B^\pm \to D(\to K^+K^-\pi^+\pi^-)K^\pm$ events

Parameter		Fit value
Signal		
N_{sig}	limited	361.716 $\pm$28.088
Gaussian 1 mean	fixed	5280.320
Gaussian 1 sigma	fixed	12.496
Gaussian 2 fraction	fixed	0.208
Gaussian 2 mean	fixed	-0.893
Gaussian 2 sigma	fixed	1.545
Gaussian 3 fraction	fixed	0.008
Gaussian 3 mean	fixed	-6.369
Gaussian 3 sigma	fixed	2.173
Gaussian 4 fraction	fixed	0.001
Gaussian 4 mean	fixed	-29.752
Gaussian 4 sigma	fixed	3.430
Signal mean cf	free	5.537 $\pm$1.779
Signal sigma cf	limited	1.345 $\pm$0.133
Cross-feed background		
$N_{\text{cross-feed}}$	limited	171.314$\pm$30.818
CB mean	fixed	5324.294
CB sigma	fixed	14.317
CB n	fixed	9.621
CB α	fixed	-0.184
Gaussian fraction 1	fixed	0.692
Gaussian mean 1	fixed	0.000
Gaussian sigma 1	fixed	1.404
Gaussian fraction 2	fixed	0.025
Gaussian mean 2	fixed	130.862
Gaussian sigma 2	fixed	4.253
Gaussian fraction 3	fixed	0.011
Gaussian mean 3	fixed	49.283
Gaussian sigma 3	fixed	2.264
Wrong D background		
$N_{\text{wrong D}}$	fixed	1157.910
Chebyshev c1	fixed	-0.873
Chebyshev c2	fixed	0.296
Chebyshev c3	fixed	0.015
Chebyshev c4	fixed	-0.001
Chebyshev c5	fixed	0.021
Right D background		
$N_{\text{right D}}$	limited	1125.547 $\pm$50.631
Gaussian 1 mean	fixed	5103.507
Gaussian 1 sigma	fixed	22.010
Gaussian 2 fraction	limited	0.627 $\pm$0.103
Gaussian 2 mean	fixed	-72.878
Gaussian 3 fraction	limited	0.334 $\pm$0.060
Gaussian 3 mean	fixed	4893.443
Gaussian 3 sigma	fixed	175.601
Gaussian 4 fraction	limited	0.408 $\pm$0.093
Gaussian 4 mean	free	5167.941 $\pm$4.155
Gaussian 4 sigma	free	16.493 $\pm$3.574
Chebyshev fraction	limited	0.041 $\pm$0.008
Chebyshev c1	fixed	0.172
$\chi^2/ndof$		1.08

Table A.6: Fit parameters for fit to $m_{D\pi}$ for $B^{\pm} \to D(\to K^+K^-\pi^+\pi^-)\pi^{\pm}$ events.

Parameter		Fit value
Signal		
N_{sig}	limited	4699.337 $\pm$82.316
Gaussian 1 mean	fixed	5280.254
Gaussian 1 sigma	fixed	13.529
Gaussian 2 fraction	fixed	0.131
Gaussian 2 mean	fixed	-1.937
Gaussian 2 sigma	fixed	1.719
Gaussian 3 fraction	fixed	0.004
Gaussian 3 mean	fixed	-11.744
Gaussian 3 sigma	fixed	2.599
Gaussian 4 fraction	fixed	0.001
Gaussian 4 mean	fixed	-50.114
Gaussian 4 sigma	fixed	3.026
Signal mean cf	free	3.637 $\pm$0.317
Signal sigma cf	limited	1.180 $\pm$0.021
Wrong D background		
$N_{\text{wrong D}}$	fixed	6070.62
Chebyshev c1	fixed	-1.218
Chebyshev c2	fixed	0.480
Chebyshev c3	fixed	-0.005
Chebyshev c4	fixed	-0.096
Chebyshev c5	fixed	0.056
Right D background		
$N_{\text{right D}}$	limited	9388.869 $\pm$133.079
Gaussian 1 mean	limited	5103.507 $\pm$0.768
Gaussian 1 sigma	limited	22.010 $\pm$0.708
Gaussian 2 fraction	limited	0.775 $\pm$0.038
Gaussian 2 mean	limited	-72.878 $\pm$1.113
Gaussian 3 fraction	limited	0.396 $\pm$0.044
Gaussian 3 mean	free	4893.443 $\pm$74.741
Gaussian 3 sigma	free	175.601 $\pm$39.716
Chebyshev fraction	limited	0.005 $\pm$0.006
Chebyshev c1	limited	0.172 $\pm$1.830
$\chi^2/ndof$		1.32

Bibliography

[1] CLEO collaboration. Amplitude analysis of $\mathrm{D}^0 \to K^+K^-\pi^+\pi^-$. *Phys. Rev.*, D85:122002, 2012.

[2] P. d'Argent, N. Skidmore, J. Benton, J. Dalseno, E. Gersabeck, S. T. Harnew, P. Naik, C. Prouve, and J. Rademacker. Amplitude analyses of $D^0 \to \pi^+\pi^-\pi^+\pi^-$ and $D^0 \to K^+K^-\pi^+\pi^-$ decays. *Journal of High Energy Physics*, 2017(5):1–57, May 2017.

[3] J. Rademacker. Minuit INTerface. *www.phy.bris.ac.uk/people/rademackerj*, 2011.

[4] A. D. Sakharov. Violation of CP Invariance, C Asymmetry, and Baryon Asymmetry of the Universe. *Pisma Zh. Eksp. Teor. Fiz.*, 5:32–35, 1967. [Usp. Fiz. Nauk161,61(1991)].

[5] Antonio Riotto. Theories of baryogenesis. In *Proceedings, Summer School in High-energy physics and cosmology: Trieste, Italy, June 29-July 17, 1998*, pages 326–436, 1998.

[6] Emmy Noether. Invariant Variation Problems. *Gott. Nachr.*, 1918:235–257, 1918. [Transp. Theory Statist. Phys.1,186(1971)].

[7] I.J.R. Aitchison and A.J.G Hey. *Gauge Theories in Particle Physics, Vol. 2: Non-Abelian Gauge Theories: QCD and the Electroweak Theory.* CRC Press, Florida, US, 2003.

[8] University of California, C. Clark. Quantum electrodynamics. QED lecture notes.

[9] Marco Drewes. The Phenomenology of Right Handed Neutrinos. *Int. J. Mod. Phys.*, E22:1330019, 2013.

[10] A. Pich. The Standard model of electroweak interactions. In *2004 European School of High-Energy Physics, Sant Feliu de Guixols, Spain, 30 May - 12 June 2004*, pages 1–48, 2005.

[11] Ludwig-Maximilian University of Munich, K. Nguyen. Lecture notes in the higgs mechanism, July 2009.

[12] Nikhef, I. Vulpen. Lecture notes in the standard model higgs boson, October 2013.

[13] Harvard University, M. Schwartz. Lecture notes in weak interactions, 2012.

[14] ATLAS collaboration. Observation of a new particle in the search for the Standard Model Higgs boson with the ATLAS detector at the LHC. *Phys. Lett.*, B716:1–29, 2012.

[15] CMS collaboration. Observation of a new boson at a mass of 125 GeV with the CMS experiment at the LHC. *Phys. Lett.*, B716:30–61, 2012.

[16] Peter Skands. Introduction to QCD. In *Proceedings, Theoretical Advanced Study Institute in Elementary Particle Physics: Searching for New Physics at Small and Large Scales (TASI 2012): Boulder, Colorado, June 4-29, 2012*, pages 341–420, 2013.

[17] BESIII collaboration. Observation of a Charged Charmonium like Structure in $e^+e^- \to \pi^+\pi^-\ J\psi$ at $\sqrt{s}$ =4.26GeV. *Phys. Rev. Lett.*, 110:252001, 2013.

[18] Belle collaboration. Study of $e^+e^- \to \pi^+\pi^-\ J\psi$ and Observation of a Charged Charmonium like State at Belle. *Phys. Rev. Lett.*, 110:252002, 2013.

[19] LHCb collaboration. Observation of $J/\psi p$ resonances consistent with pentaquark states in $\Lambda_b^0 \to J/\psi K^- p$ decays. *Phys. Rev. Lett.*, 115:072001, 2015.

[20] H. Prez R., P. Kielanowski, and S. R. Jurez W. Cabibbo Kobayashi Maskawa matrix: rephasing invariants and parameterizations. *J. Phys. Conf. Ser.*, 485:012058, 2014.

[21] Nikhef, P. Kooijman. Lecture notes in CP violation, April 2011.

[22] C. Patrignani et al. Review of Particle Physics. *Chin. Phys.*, C40(10):100001, 2016.

[23] K. A. Olive et al. Review of Particle Physics. *Chin. Phys.*, C38:090001, 2014.

[24] J. Charles et al. CKMFitter group. *Eur. Phys. J. C41, 1-131 (2005) [hep-ph/0406184]*. Updated results and plots available at: http://ckmfitter.in2p3.fr.

[25] LHCb collaboration. Test of lepton universality using $B^+ \to K^+\ell^+\ell^-$ decays. *Phys. Rev. Lett.*, 113:151601, 2014.

[26] Sneha Malde. Measurements of the CKM angle gamma using $B^+ \to DK^+$ decays at LHCb. In *7th International Workshop on the CKM Unitarity Triangle (CKM 2012) Cincinnati, Ohio, USA, September 28-October 2, 2012*, 2013.

[27] Alexander L. Kagan and Michael D. Sokoloff. On Indirect CP Violation and Implications for D0 - anti-D0 and B(s) - anti-B(s) mixing. *Phys. Rev.*, D80:076008, 2009.

[28] Fernando Martinez-Vidal. Review on D0 - anti-D0 mixing. In *29th International Conference on Physics in Collision (PIC 2009) Kobe, Japan, August 30-September 2, 2009*, 2009.

[29] Giulia Casarosa and the Babar Collaboration. Studies of CP violation and mixing in the D mesons decays from BABAR. *Journal of Physics: Conference Series*, 335(1):012043, 2011.

[30] Yuval Grossman, Alexander L. Kagan, and Yosef Nir. New physics and CP violation in singly Cabibbo suppressed D decays. *Phys. Rev.*, D75:036008, 2007.

[31] Bhubanjyoti Bhattacharya, Michael Gronau, and Jonathan L. Rosner. Direct CP Violation in D Decays in view of LHCb and CDF Results. 2012.

[32] Roel Aaij et al. Expression of Interest for a Phase-II LHCb Upgrade: Opportunities in flavour physics, and beyond, in the HL-LHC era. Technical Report CERN-LHCC-2017-003, CERN, Geneva, Feb 2017.

[33] Michael Gronau and David London. How to determine all the angles of the unitarity triangle. *Physics Letters B*, 253(3):483 – 488, 1991.

[34] Michael Gronau and Daniel Wyler. On determining a weak phase from CP asymmetries in charged B decays. *Phys. Lett.*, B265:172–176, 1991.

[35] David Atwood, Isard Dunietz, and Amarjit Soni. Enhanced CP violation with $B \to KD^0$ (anti-D^0) modes and extraction of the CKM angle gamma. *Phys. Rev. Lett.*, 78:3257–3260, 1997.

[36] Joachim Brod and Jure Zupan. The ultimate theoretical error on γ from $B \to DK$ decays. *JHEP*, 01:051, 2014.

[37] Anjan Giri, Yuval Grossman, Abner Soffer, and Jure Zupan. Determining γ using $B^\pm \to DK^\pm$ with multibody D decays. *Phys. Rev. D*, 68:054018, Sep 2003.

[38] J. Rademacker and G. Wilkinson. Determining the unitarity triangle γ with a four-body amplitude analysis of $B^\pm \to (K^+K^-\pi^+\pi^-)_D K^\pm$ decays. *Phys.Lett.*, B647:400–404, 2007.

[39] D. ChakrabortyNorthern Illinois University,. Lecture notes in decay widths and scattering cross sections, 2010.

[40] K. Nakamura et al. Review of Particle Physics. *J. Phys.*, G37:075021, 2010.

[41] D.J. Griffiths. *Introduction to Quantum Mechanics.* Pearson Education, Inc., New Jersey, US, 2005.

[42] BaBar collaboration. Measurement of D0-antiD0 mixing parameters using $D^0 \to K(S)^0\pi^+\pi^-$ and $D^0 \to K(S)^0K^+K^- decays$. *Phys. Rev. Lett.*, 105:081803, 2010.

[43] BES collaboration. Resonances in $J/\psi \to \phi\pi^+\pi^-$ and ϕK^+K^-. *Phys. Lett.*, B607:243–253, 2005.

[44] S. U. Chung. General formulation of covariant helicity-coupling amplitudes. *Phys. Rev. D*, 57:431–442, Jan 1998.

[45] William Rarita and Julian Schwinger. On a theory of particles with half-integral spin. *Phys. Rev.*, 60:61–61, Jul 1941.

[46] Charles Zemach. Use of angular-momentum tensors. *Phys. Rev.*, 140:B97–B108, Oct 1965.

[47] Frank von Hippel and C. Quigg. Centrifugal-barrier effects in resonance partial decay widths, shapes, and production amplitudes. *Phys. Rev. D*, 5:624–638, Feb 1972.

[48] A. Papaefstathiou. How to write your own Monte Carlo event generator.

[49] LHCb collaboration. A precise measurement of the B^0 meson oscillation frequency. *Eur. Phys. J.*, C76(7):412, 2016.

[50] LHCb collaboration. Observation of double charm production involving open charm in pp collisions at $\sqrt{s}$ = 7 TeV. *JHEP*, 06:141, 2012. [Addendum: JHEP03,108(2014)].

[51] LHCb collaboration. Precision measurement of D meson mass differences. *JHEP*, 06:065, 2013.

[52] Nazim Hussain. *A study of CP violation in $B \to Dh$ ($h = K, \pi$) with the modes $D \to K\pi\pi^0$ $D \to \pi\pi\pi^0$ and $D \to KK\pi^0$*. PhD thesis, University of Oxford, University College, University of Oxford, Trinity term 2015.

[53] Roy A. Briere et al. CLEO-c and CESR-c: A New frontier of weak and strong interactions. 2001.

[54] M. Artuso et al. The CLEO RICH detector. *Nucl. Instrum. Meth.*, A554:147–194, 2005.

[55] Cornell University. Cornell Electron Storage Ring. https://www.classe.cornell.edu/Research/CESR/WebHome.html, 2016.

[56] Thomas Coan. The CLEO-III upgrade. *Nucl. Instrum. Meth.*, A453:49–53, 2000.

[57] R. Kass et al. The CLEO III silicon vertex detector. *Nuclear Instruments and Methods in Physics Research Section A: Accelerators, Spectrometers, Detectors and Associated Equipment*, 501(1):32 – 38, 2003. Proceedings of the 10th International Workshop on Vertex Detectors.

[58] D. Peterson et al. The CLEO III drift chamber. *Nucl. Instrum. Meth.*, A478:142–146, 2002.

[59] R. Poling. CLEO-c hot topics. *eConf*, C060409:005, 2006.

[60] M. Artuso et al. Construction, pattern recognition and performance of the CLEO III LiF-TEA RICH detector . *Nuclear Instruments and Methods in Physics Research Section A: Accelerators, Spectrometers, Detectors and Associated Equipment*, 502(1):91 – 100, 2003. Experimental Techniques of Cherenkov Light Imaging. Proceedings of the Fourth International Workshop on Ring Imaging Cherenkov Detectors.

[61] D. J. Lange. The evtgen particle decay simulation package. *Nucl. Instrum. Meth.*, A462:152–155, 2001.

[62] CLEO collaboration. QQ-the CLEO event generator. http://www.lns.cornell.edu/public/CLEO/soft/QQ, 1998.

[63] S. Agostinelli et al. Geant - a simulation toolkit. *Nuclear Instruments and Methods in Physics Research Section A: Accelerators, Spectrometers, Detectors and Associated Equipment*, 506(3):250 – 303, 2003.

[64] LHCb collaboration. LHCb Detector Performance. *Int. J. Mod. Phys.*, A30(07):1530022, 2015.

[65] Cinzia De Melis. The CERN accelerator complex. Complexe des acclrateurs du CERN. Jul 2016. General Photo.

[66] Oliver Sim Brning, Paul Collier, P Lebrun, Stephen Myers, Ranko Ostojic, John Poole, and Paul Proudlock. *LHC Design Report*. CERN Yellow Reports: Monographs. CERN, Geneva, 2004.

[67] LHCb collaboration. LHCb Run 2 Trigger Performance. May 2016.

[68] A Augusto Alves et al. The LHCb Detector at the LHC. *JINST*, 3(LHCb-DP-2008-001. CERN-LHCb-DP-2008-001):S08005, 2008. Also published by CERN Geneva in 2010.

[69] LHCb collaboration. $b\bar{b}$ production angle plots. $lhcb.web.cern.ch/lhcb/speakersbureau/html/bb_productionAngles.html$, 2017.

[70] P R Barbosa-Marinho et al. *LHCb VELO (VErtex LOcator): Technical Design Report*. Technical Design Report LHCb. CERN, Geneva, 2001.

[71] R. Aaij et al. Performance of the LHCb Vertex Locator. *JINST*, 9:09007, 2014.

[72] M. Adinolfi et al. Performance of the LHCb RICH detector at the LHC. *Eur. Phys. J.*, C73:2431, 2013.

[73] A. A. Alves, Jr. et al. Performance of the LHCb muon system. *JINST*, 8:P02022, 2013.

[74] S Amato et al. *LHCb RICH: Technical Design Report*. Technical Design Report LHCb. CERN, Geneva, 2000.

[75] P Perret and X Vilasis-Cardona. Performance of the LHCb calorimeters during the period 2010-2012. *J. Phys.: Conf. Ser.*, 587(LHCb-PROC-2014-019. CERN-LHCb-PROC-2014-019. 1):012012. 6 p, Aug 2014. see LHCb-TALK-2014-236.

[76] Eduardo Picatoste Olloqui. LHCb Preshower(PS) and Scintillating Pad Detector (SPD): commissioning, calibration, and monitoring. *J. Phys.: Conf. Ser.*, 160:012046. 8 p, 2009.

[77] Alessandro Cardini, Giovanni Bencivenni, and Patrizia De Simone. The Operational Experience of the Triple-GEM Detectors of the LHCb Muon System: Summary of 2 Years of Data Taking. Technical Report LHCb-PROC-2012-060. CERN-LHCb-PROC-2012-060, CERN, Geneva, Nov 2012.

[78] LHCb collaboration. The LHCb trigger system. *Journal of Instrumentation*, 9(09):C09015, 2014.

[79] Vladimir Gligorov, Christopher Thomas, and Michael Williams. The HLT inclusive B triggers. (LHCb-PUB-2011-016.), Sep 2011. LHCb-INT-2011-030.

[80] D. J. Lange. The EvtGen particle decay simulation package. *Nucl. Instrum. Meth.*, A462:152–155, 2001.

[81] S. Agostinelli et al. GEANT4: A simulation toolkit. *Nucl. Instrum. Meth.*, A506:250, 2003.

[82] John Allison, K. Amako, J. Apostolakis, H. Araujo, P.A. Dubois, et al. Geant4 developments and applications. *IEEE Trans.Nucl.Sci.*, 53:270, 2006.

[83] Torbjorn Sjostrand, Stephen Mrenna, and Peter Z. Skands. PYTHIA 6.4 Physics and Manual. *JHEP*, 05:026, 2006.

[84] Jonathan Pumplin, Daniel Robert Stump, Joey Huston, Hung-Liang Lai, Pavel Nadolsky, and Wu-Ki Tung. New generation of parton distributions with uncertainties from global qcd analysis. *Journal of High Energy Physics*, 2002(07):012, 2002.

[85] M Clemencic, G Corti, S Easo, C R Jones, S Miglioranzi, M Pappagallo, P Robbe, and the LHCb Collaboration. The LHCb simulation application, Gauss: Design, evolution and experience. *Journal of Physics: Conference Series*, 331(3):032023, 2011.

[86] LHCb collaboration. The boole project. http://lhcb-release-area.web.cern.ch/LHCb-release-area/DOC/boole/, 2017.

[87] LHCb collaboration. The moore project. http://lhcb-release-area.web.cern.ch/LHCb-release-area/DOC/moore/, 2017.

[88] LHCb collaboration. The brunel project. http://lhcb-release-area.web.cern.ch/LHCb-release-area/DOC/brunel/, 2017.

[89] LHCb collaboration. The davinci project. http://lhcb-release-area.web.cern.ch/LHCb-release-area/DOC/davinci/, 2017.

[90] FOCUS collaboration. Study of the $D^0 \to K^+K^-\pi^+\pi^-$. *Phys. Lett.*, B610:225–234, 2005.

[91] E791 collaboration. Study of the decay $D^0 \to K^-K^+pi^-pi^+$. *Phys. Lett.*, B423:185–193, 1998.

[92] CLEO collaboration. Determination of the $D^0 \to K^+\pi^-$ relative strong phase using quantum-correlated measurements in $e^+e^- \to D^0$Dbar^0 at CLEO. *Phys. Rev. D*, 78:012001, Jul 2008.

[93] CLEO collaboration. Model-independent determination of the strong-phase difference between D^0 and $\bar{D}^0 \to K^0_{S,L}h^+h^-$ $(h = \pi, K)$ and its impact on the measurement of the CKM angle γ/ϕ_3. *Phys. Rev.*, D82:112006, 2010.

[94] CLEO collaboration. Measurement of absolute hadronic branching fractions of D mesons and $e^+e^- \to$ D anti-D cross-sections at the $\psi(3770)$. *Phys. Rev.*, D76:112001, 2007.

[95] CLEO collaboration. Measurement of Charm Production Cross Sections in e^+e^- Annihilation at Energies between 3.97 and 4.26-GeV. *Phys. Rev. D*, 80:072001, Oct 2009.

[96] CLEO collaboration. Determination of the $D^0 \to K^-\pi^+\pi^0$ and $D^0 \to K^-\pi^+\pi^+\pi^-$ Coherence Factors and Average Strong-Phase Differences Using Quantum-Correlated Measurements. *Phys. Rev.*, D80:031105, 2009.

[97] BaBar collaboration. Evidence for D^0 -anti-D^0 Mixing. *Phys. Rev. Lett.*, 98:211802, 2007.

[98] Baptiste Guegan, John Hardin, Justin Stevens, and Mike Williams. Model selection for amplitude analysis. *JINST*, 10(09):P09002, 2015.

[99] CLEO collaboration. Updated measurements of absolute D^+ and D^0 hadronic branching fractions and $\sigma(e^+e^- \to D\overline{D})$ at $e_{\mathrm{cm}} = 3774$ mev. *Phys. Rev.*, D89(7):072002, 2014. [Erratum: Phys. Rev.D91,no.1,019903(2015)].

[100] CLEO collaboration. Study of exclusive radiative B meson decays. *Phys. Rev. Lett.*, 84:5283–5287, 2000.

[101] BaBar collaboration. Measurements of cp-violating asymmetries in $B^0 \to a^{\pm}(1)(1260)\pi^{\mp}$ decays. *Phys. Rev. Lett.*, 98:181803, 2007.

[102] LHCb collaboration. Measurement of the CKM angle γ from a combination of LHCb results. *JHEP*, 12:087, 2016.

[103] Lucio Anderlini et al. The PIDCalib package. Technical Report LHCb-PUB-2016-021. CERN-LHCb-PUB-2016-021, CERN, Geneva, Jul 2016.

[104] Andrea Contu et al. PID at LHCb and the PIDCalib packages. Online tutorial, 2012.

[105] Kolpin and Tilburg. Tracking efficiencies. https://twiki.cern.ch/twiki/bin/view/LHCb/LHCbTrackingEfficiencies, 2017.

[106] Michel De Cian et al. Measurement of the track finding efficiency. Technical Report LHCb-PUB-2011-025. CERN-LHCb-PUB-2011-025, CERN, Geneva, Apr 2012.

[107] W. D. Hulsbergen. Decay chain fitting with a Kalman filter. *Nuclear Instruments and Methods in Physics Research A*, 552:566–575, November 2005.

[108] A. Hoecker et al. TMVA - Toolkit for Multivariate Data Analysis. *ArXiv Physics e-prints*, March 2007.

[109] Tomasz Skwarnicki. *A study of the radiative cascade transitions between the Upsilon-prime and Upsilon resonances.* PhD thesis, Institute of Nuclear Physics, Krakow, 1986. DESY-F31-86-02.